UNIVERSIDADE FEDERAL DO ESPÍRITO SANTO
CENTRO TÉCNOLÓGICO
PROGRAMA DE PÓS-GRADUAÇÃO EM ENGENHARIA AMBIENTAL

MATHEUS DE ARAUJO SIQUEIRA

INFLUENCE OF THE DESIGN AND OPERATIONAL CONDITIONS ON THE AIRFLOW AND MASS TRANSFER PHENOMENA INSIDE A PORTABLE WIND TUNNEL USED TO ESTIMATE ODORANT COMPOUNDS MEASURED OVER PASSIVE LIQUID SURFACES

Vitória
2022

MATHEUS DE ARAUJO SIQUEIRA

INFLUENCE OF THE DESIGN AND OPERATIONAL CONDITIONS ON THE AIRFLOW AND MASS TRANSFER PHENOMENA INSIDE A PORTABLE WIND TUNNEL USED TO ESTIMATE ODORANT COMPOUNDS MEASURED OVER PASSIVE LIQUID SURFACES

Dissertation submitted to Programa de Pós- Graduação em Engenharia Ambiental, Centro Tecnológico, Universidade Federal do Espírito Santo, for the degree of Master of Science in Environmental Engineering.

Orientador: Profa. Dra. Jane Meri Santos

Coorientador: Prof. Dr. Bruno Furieri

Vitória

2022

Ficha catalográfica disponibilizada pelo Sistema Integrado de
Bibliotecas - SIBI/UFES e elaborada pelo autor

de Araujo Siqueira, Matheus, 1990-
D278i Influence of the design and operational conditions on the airflow and mass transfer phenomena inside a portable wind tunnel used to estimate odorant compounds measured over passive liquid surfaces / Matheus de Araujo Siqueira. - 2022.
170 f. : il.

Orientadora: Jane Meri Santos.
Coorientador: Bruno Furieri.
Tese (Doutorado em Engenharia Ambiental) - Universidade Federal do Espírito Santo, Centro Tecnológico.

1. Poluição do ar. 2. Controle de Odor. 3. Fluidodinâmica Computacional. 4. Transferência de Massa. I. Meri Santos, Jane. II. Furieri, Bruno. III. Universidade Federal do Espírito Santo. Centro Tecnológico. IV. Título.

CDU: 628

UNIVERSIDADE FEDERAL DO ESPÍRITO SANTO
CENTRO TECNOLÓGICO
PROGRAMA DE PÓS-GRADUAÇÃO EM ENGENHARIA AMBIENTAL

INFLUENCE OF THE DESIGN AND OPERATIONAL CONDITIONS ON THE AIRFLOW AND MASS TRANSFER PHENOMENA INSIDE A PORTABLE WIND TUNNEL USED TO ESTIMATE ODORANT COMPOUNDS MEASURED OVER PASSIVE LIQUID SURFACES

Matheus de Araújo Siqueira

Banca Examinadora:

Prof.ª Dr.ª Jane Meri Santos
Orientadora - PPGEA/CT/UFES

BrunoFurieri
Prof. Dr. Bruno Furieri
Coorientador – PPGEA/CT/UFES

Prof. Dr. Neyval Costa Reis Jr.
Examinador Interno – PPGEA/CT/UFES

Igor Braga de Paula
Prof. Dr. Igor Braga de Paula
Examinador Externo – PUC-Rio

ELISA VALENTIM GOULART
Coordenadora do Programa de Pós-Graduação em Engenharia Ambiental
UNIVERSIDADE FEDERAL DO ESPÍRITO SANTO

Vitória/ES, 29 de agosto de 2022

ACKNOWLEDGEMENTS

I thank to God, Father, Son and Holy Spirit, for including me in his plans and nurturing me with faith to move forward.

My mother, Eliane de Araújo Siqueira, for dedicating her life to us, her sons, and being a great example of faith, determination, persistence and love for life.

To my wife, Mariana Rozetti Coelho, for her love, unconditional companionship, and patience throughout these years.

My sisters, Mariana and Mônica, for their great help and companionship. To my dear nephew Giovanni for the friendship and good laughs.

To my advisors Jane Meri Santos and Bruno Furieri, for the opportunities, teachings, and guiding the work.

To all my NQualiar colleagues, people with whom I learned and made my day-by-day in the laboratory more pleasant.

The Federal University of Espírito Santo, for my academic formation.

To all of my great friends, for their companionship and good laughs.

Thanks to everyone who helped me on this journey.

ABSTRACT

The emissions to the atmosphere by liquid passive area sources, that is, extensive liquid surfaces swept by the atmospheric flow in which occurs the emission of a certain chemical, like the tanks and lagoons in wastewater treatment plants are significative sources of odorant compounds, such as the H_2S and the acetic acid. The health effects of these gaseous compounds include eye and throat irritation, and nausea. Different equipments are being used to perform a direct estimation of the emission of the odorant compound on passive surfaces. However, it is well known in the literature that the use of different equipments for the same source is conducing to different results. In general, these equipments are open-bottomed boxes in which is fluxed a clean gas in its inside that enters in contact with the gas-liquid interface and carries the odorant compound, to be posterior sampled at the equipment outlet and analyzed. Thereafter, the results provided by these equipments are straightly connected with the airflow and mass transfer phenomena on its inside. So, to properly assist the answer of the question of which equipment is more adequated to estimate the emission rate of an odorant compound in passive area sources it is first required to understand the airflow and how the mass transfer phenomena occur on its inside occurs. In this way, the present work objectives to analyze, using numerical simulations, the airflow and mass transfer phenomena inside one the of equipments used in the direct estimative of odorant compounds, namely the portable wind tunnel. The turbulent effects were incorporated using the $\kappa - \omega \, SST$ model. The finite volume method was used via the ANSYS Fluent software to numerically solve the involved equations. The analysis of the streamlines, profiles, vectors, and contours of the velocity, turbulent kinetic energy, and concentration showed that the flow inside the device is quite complex and $3D$, with several recirculation zones and thus reversed flow. This feature of the flow have a direct impact on the volatilization process. Nevertheless, the results showed that the geometry configuration of the equipment has a direct impact on the airflow and thus on its mass transfer phenomena, in this way, it seems that small changes in its geometry could lead to an improvement of the flow in its inside.

Keywords: Portable wind tunnel. Odor. Gaseous emissions from passive liquid surfaces. Mass transfer. CFD. Turbulence.

LIST OF FIGURES

1 Schematic configuration of mass transport across stagnant films (PRATA *et al.*, 2018). 31
2 Illustration of the operation of a equipment for direct measurement of odorant compounds in a passive surface (CAPELLI; SIRONI; ROSSO, 2013). 37
3 Enclosure dynamic devices used for sampling odorous compounds in passive surfaces: (a) Dynamic flux chamber (KLENBUSCH, 1986); (b) Portable wind tunnel (JIANG; BLISS; SCHULZ, 1995). 38
4 Summary of the methodology. 49
5 Velocity time series highlighting the averaged value and fluctuation (VERSTEEG; MALALASEKERA, 2007). 51
6 U-Bend geometry used in the present work: (a) Isometric view; (b) Longitudinal dimensions $[mm]$ and (c) Transversal dimensions $[mm]$. . 58
7 Isometric view of the different PWT configurations to be used in the present work: a)Jiang, Bliss and Schulz (1995) geometry; (b) UFES-PWT. 60
8 Dimensions (in mm) of the PWT used to be used in the present work: (a) Extension inlet duct; (b) Device in it self; (c) Modified outlet. . . . 60
9 Input data used to perform the U-bend geometry simulations, obtained experimentally by Benson *et al.* (2020), via the MRV technique: (a) Velocity contour; (b) Velocity profile, plotted at the longitudinal center-line of the inlet plane, normalized in y by the length or radius of the channel (H), equal to $25\,mm$, and in u by the average inlet velocity (U_b), equal to $0.6\,m/s$. 61
10 Contours and profiles, plotted at the longitudinal center-line of the inlet plane, obtained via precursor domain and used as input data to the U-bend geometry simulations using the $\kappa - \omega\,SST$ model: (a) Turbulent kinetic energy - profile; (b) Turbulent kinetic energy - contour; (c) Specific dissipation rate - profile; and (d) Specific dissipation rate - contour. 62

11 Contours and profiles, plotted at the longitudinal center-line of the inlet plane, obtained via precursor domain and used as input data to the U-bend geometry simulations using the $Standard \kappa - \varepsilon$ model: (a) Turbulent kinetic energy - profile; (b) Turbulent kinetic energy - contour; (c) Dissipation rate - profile; and (d) Dissipation rate - contour. 63

12 Profiles obtained via precursor domain and used as input data to the simulations using the Jiang, Bliss and Schulz (1995) geometry: (a) Velocity magnitude; (b) Turbulent kinetic energy and (b) Specific dissipation rate. 65

13 Inlet profiles obtained via precursor domain and used as input data to the simulations with the UFES-PWT geometry for the inlet velocity of $3,82\, m\, s^{-1}$: (a) Velocity magnitude; (b) Turbulent kinetic energy and (b) Specific dissipation rate. 67

14 Inlet profiles obtained via precursor domain and used as input data to the simulations using the UFES-PWT for the inlet velocity of $2,55\, m\, s^{-1}$: (a) Velocity magnitude; (b) Turbulent kinetic energy and (b) Specific dissipation rate. 68

15 Inlet profiles obtained via precursor domain and used as input data to the simulations using the UFES-PWT for the inlet velocity of $1,27\, m\, s^{-1}$: (a) Velocity magnitude; (b) Turbulent kinetic energy and (b) Specific dissipation rate. 69

16 U-bend discretized domain for the simulations with the $Standard\ \kappa - \varepsilon$ model - 280.575 elements: (a) Front vision and (b) Lateral vision. . . 76

17 U-bend discretized domain for the simulations with the $\kappa - \omega\ SST$ model - $3.381.360$ elements: (a) Front vision and (b) Lateral vision. . 76

18 PWT designed by Jiang, Bliss and Schulz (1995) discretized domain - 434.112 elements: (a) Rear view and (b) Lateral vision. 77

19 UFES-PWT geometry discretized domain - 588.924 elements: (a) Rear view and (b) Lateral vision. 77

20 Distribution of the velocity near the wall, in where the dots are experimental data and the solid line represents the wall function approximation (SANTOS, 2000). 79

21 Sampling lines cross-section: (a)Lateral view and (b)Frontal view. . . 80

22 U-bend sampling lines in the four cross-sections - isometric view. . . 80

23 Isometric view of the PWT configuration used by Wu (2007) (modified from source: Wu (2007)). 81

24 Sampling points in the three cross-sections: (a)Isometric view and (b) lateral view. 82

25 Frontal view of the cross-section $[mm]$. 82

26 Sampling lines for the u component of the velocity. 85

27 Benson *et al.* (2020) U bend validation for both turbulence models - u component of the velocity profiles at the positions: (a)$z = 55\ mm$; (b)$z = 75\ mm$; (c) $z = 94\ mm$ and (d) $z = 104\ mm$ 85

28 Sampling lines for the v component of the velocity. 86

29 Benson *et al.* (2020) U bend validation for both turbulence models - v component of the velocity profiles at the positions: (a)$z = 55\ mm$; (b)$z = 75\ mm$; (c) $z = 94\ mm$ and (d) $z = 104\ mm$ 86

30 Sampling lines for the w component of the velocity. 87

31 Benson *et al.* (2020) U bend validation for both turbulence models - w component of the velocity profiles at the positions: (a)$z = 55\ mm$; (b)$z = 75\ mm$; (c) $z = 94\ mm$ and (d) $z = 104\ mm$ 87

32 Vertical profiles for $\overline{u}$ - numerical results compared to the experimental data at the positions: (a) $z = 200\ mm$; (b) $z = 400\ mm$ and (c) $z = 600\ mm$. 88

33 Vertical profiles for $\overline{u}$ - Correlation coefficient for the numerical results compared to the experimental data: (a) $z = 200\ mm$; (b) $z = 400\ mm$ and (c) $z = 600\ mm$. 89

34 Horizontal profiles for $\overline{u}$ - numerical results compared to the Jiang, Bliss and Schulz (1995) and Wu (2007) experimental data at the positions: (a) $z = 200\ mm$; (b) $z = 400\ mm$ and (c) $z = 600\ mm$. 90

35 Vertical velocity profiles for $\overline{u}$ for UFES PWT numerical simulations for the three tested velocities at the positions: (a) $z = 200\ mm$; (b) $z = 400\ mm$ and (c) $z = 600\ mm$. 91

36 Vertical TKE profiles for the UFES PWT numerical simulations for the three tested velocities at the positions: (a) $z = 200\,mm$; (b) $z = 400\,mm$ and (c) $z = 600\,mm$. 92

37 Vertical velocity profiles for $\overline{u}$ normalized by the inlet velocity - UFES PWT numerical simulations for the three tested velocities at the positions: (a) $z = 200\,mm$; (b) $z = 400\,mm$ and (c) $z = 600\,mm$. 92

38 Velocity distribution for $\overline{u}$ top view at half of the PWT height ($y = 125$) - UFES PWT simlations for different inlet velocities: (a) $1.27\,m\,s^{-1}$; (b) $2.55\,m\,s^{-1}$ and (c) $3.82\,m\,s^{-1}$. 93

39 Streamlines side view - UFES PWT simlations for different inlet velocities: (a) $1.27\,m\,s^{-1}$; (b) $2.55\,m\,s^{-1}$ and (c) $3.82\,m\,s^{-1}$. 95

40 TKE distribution side view - UFES PWT simlations for different inlet velocities: (a) $1.27\,m\,s^{-1}$; (b) $2.55\,m\,s^{-1}$ and (c) $3.82\,m\,s^{-1}$. 96

41 Location of the lines used to study the size of the recirculation zone, red line: velocity and blue line: friction velocity: (a) Isometric view and (b) Lateral view. 97

42 Graphics used to analyze the size of a recirculation zone and its influence of the friction velocity: (a) Component w of the velocity for a line placed at the center of the main section; (b) Friction velocity for a line placed at the center of the gas-liquid interface. 97

43 Velocity distribution for $\overline{u}$ at the outlet of the UFES PWT for different inlet velocities: (a) $1.27\,m\,s^{-1}$; (b) $2.55\,m\,s^{-1}$ and (c) $3.82\,m\,s^{-1}$. . . . 98

44 Friction velocity distribution in the gas-liquid interface and velocity vectors in a side view plane - UFES PWT simulations for different inlet velocities: (a) $1.27\,m\,s^{-1}$; (b) $2.55\,m\,s^{-1}$ and (c) $3.82\,m\,s^{-1}$. 100

44 Friction velocity distribution in the gas-liquid interface and velocity vectors in a side view plane - UFES PWT simulations for different inlet velocities: (a) $1.27\,m\,s^{-1}$; (b) $2.55\,m\,s^{-1}$ and (c) $3.82\,m\,s^{-1}$. 101

45 $3D$ Streamlines isometric view - UFES PWT simulations for different inlet velocities: (a) $1.27\,m\,s^{-1}$; (b) $2.55\,m\,s^{-1}$ and (c) $3.82\,m\,s^{-1}$. . . . 103

45 $3D$ Streamlines isometric view - UFES PWT simlations for different inlet velocities: (a) $1.27\,m\,s^{-1}$; (b) $2.55\,m\,s^{-1}$ and (c) $3.82\,m\,s^{-1}$. . . . 104

46 $3D$ Streamlines bottom view - UFES PWT simlations for different inlet velocities: (a) $1.27\,m\,s^{-1}$; (b) $2.55\,m\,s^{-1}$ and (c) $3.82\,m\,s^{-1}$. 104
47 $3D$ Streamlines top view - UFES PWT simlations for different inlet velocities: (a) $1.27\,m\,s^{-1}$; (b) $2.55\,m\,s^{-1}$ and (c) $3.82\,m\,s^{-1}$. 105
48 Velocity vectors in a side view plane - UFES PWT simlations for different inlet velocities: (a) $1.27\,m\,s^{-1}$; (b) $2.55\,m\,s^{-1}$ and (c) $3.82\,m\,s^{-1}$.106
48 Velocity vectors in a side view plane - UFES PWT simlations for different inlet velocities: (a) $1.27\,m\,s^{-1}$; (b) $2.55\,m\,s^{-1}$ and (c) $3.82\,m\,s^{-1}$.106
49 Difference in the outlet duct for the PWT geometries: (a) Jiang, Bliss and Schulz (1995) and (b) UFES PWT. 107
50 Detail of the joint that connects the inlet duct and the expanse section of the PWT: (a) Jiang, Bliss and Schulz (1995) ; (b) Jiang, Bliss and Schulz (1995); (c) UFES pwt and (d) UFES PWT. 108
51 Detail of the streamline in the main section for the: (a) Jiang, Bliss and Schulz (1995) PWT simulation and (b) UFES PWT simulation. . 109
52 Point selected to analyse the stabilization time for the mass-fraction numerical simulations. 110
53 Mass fraction variation for point shown in the Figure using the three different velocities for: (a) H_2S and (b) Acetic acid. 112
54 $H2S$ mass fraction profiles for the UFES PWT numerical simulations for the three tested velocities at the positions: (a) $z = 200\,mm$; (b) $z = 400\,mm$ and (c) $z = 600\,mm$. 113
55 Acetic acid mass fraction profiles for the UFES PWT numerical simulations for the three tested velocities at the positions: (a) $z = 200\,mm$; (b) $z = 400\,mm$ and (c) $z = 600\,mm$. 113
56 H_2S mass fraction distribution side view - UFES PWT simlations: (a) $1.27\,m\,s^{-1}$; (b) $2.55\,m\,s^{-1}$ and (c) $3.82\,m\,s^{-1}$. 115
57 Acetic acid mass fraction distribution side view - UFES PWT simlations: (a) $1.27\,m\,s^{-1}$; (b) $2.55\,m\,s^{-1}$ and (c) $3.82\,m\,s^{-1}$. 116
58 H_SS gradient mass fraction contour side by side with the friction velocity - UFES PWT simlations: (a) $1.27\,m\,s^{-1}$; (b) $2.55\,m\,s^{-1}$ and (c) $3.82\,m\,s^{-1}$. 118

58 H_SS gradient mass fraction contour side by side with the friction velocity - UFES PWT simlations: (a) $1.27\,m\,s^{-1}$; (b) $2.55\,m\,s^{-1}$ and (c) $3.82\,m\,s^{-1}$. 119
59 Acetic acid gradient mass fraction contour side by side with the friction velocity - UFES PWT simlations: (a) $1.27\,m\,s^{-1}$; (b) $2.55\,m\,s^{-1}$ and (c) $3.82\,m\,s^{-1}$. 120
59 Acetic acid gradient mass fraction contour side by side with the friction velocity - UFES PWT simlations: (a) $1.27\,m\,s^{-1}$; (b) $2.55\,m\,s^{-1}$ and (c) $3.82\,m\,s^{-1}$. 121
60 Lines selected to analyze the mass fraction behavior at the outlet duct.122
61 $H2S$ mass fraction profiles for the UFES PWT numerical simulations at the outlet duct: (a) and (b): group one; (c) and (d) group two. . . . 122
62 Acetic acid mass fraction profiles for the UFES PWT numerical simulations at the outlet duct: (a) and (b): group one; (c) and (d) group two. 123
63 H_2S mass fraction at the outlet section of the UFES PWT for different inlet velocities: (a) $1.27\,m\,s^{-1}$; (b) $2.55\,m\,s^{-1}$ and (c) $3.82\,m\,s^{-1}$. . . . 123
64 Acetic acid mass fraction at the outlet section of the UFES PWT for different inlet velocities: (a) $1.27\,m\,s^{-1}$; (b) $2.55\,m\,s^{-1}$ and (c) $3.82\,m\,s^{-1}$.124
65 H_2S mass fraction distribution side view when using a constant mass flux as interface boundary condition - UFES PWT simlations: (a) $1.27\,m\,s^{-1}$; (b) $2.55\,m\,s^{-1}$ and (c) $3.82\,m\,s^{-1}$. 126
66 H_2S mass fraction for the UFES PWT numerical simulations using a constant mass flux as interface boundary condition for the three tested velocities at the positions: (a) $z = 200\,mm$; (b) $z = 400\,mm$ and (c) $z = 600\,mm$. 127
67 Ratio of H_2S mass fraction obtained by the use of two boundary conditions for the UFES PWT numerical simulations for the three tested velocities at the positions: (a) $z = 200\,mm$; (b) $z = 400\,mm$ and (c) $z = 600\,mm$. 127

68 H_2S gradient mass fraction distribution side by side with the friction velocity for the simulations with constant mass flux boundary condition - UFES PWT: (a) $1.27\,m\,s^{-1}$; (b) $2.55\,m\,s^{-1}$ and (c) $3.82\,m\,s^{-1}$. 128
68 H_2S gradient mass fraction distribution side by side with the friction velocity for the simulations with constant mass flux boundary condition - UFES PWT: (a) $1.27\,m\,s^{-1}$; (b) $2.55\,m\,s^{-1}$ and (c) $3.82\,m\,s^{-1}$. 129
69 H_2S mass fraction distribution side view in the outlet duct when using a constant mass flux as interface boundary condition - UFES PWT simlations: (a) $1.27\,m\,s^{-1}$; (b) $2.55\,m\,s^{-1}$ and (c) $3.82\,m\,s^{-1}$. 129
70 Different views of the coarser mesh (150.968) used to perform the mesh sensitivity test of the Jiang, Bliss and Schulz (1995) pwt simulations: (a)Lateral, (b)Back and (c)Inlet duct zoom. 141
71 Different views of the coarse mesh (282.576) used to perform the mesh sensitivity test of the Jiang, Bliss and Schulz (1995) pwt simulations: (a)Lateral, (b)Back and (c)Inlet duct zoom. 142
72 Different views of the medium mesh (434.112) used to perform the mesh sensitivity test of the Jiang, Bliss and Schulz (1995) pwt simulations: (a)Lateral, (b)Back and (c)Inlet duct zoom. 142
73 Different views of the fine mesh (932.640) used to perform the mesh sensitivity test of the Jiang, Bliss and Schulz (1995) pwt simulations: (a)Lateral, (b)Back and (c)Inlet duct zoom. 142
74 Different views of the finer mesh $(1.808.940)$ used to perform the mesh sensitivity test of the Jiang, Bliss and Schulz (1995) pwt simulations: (a)Lateral, (b)Back and (c)Inlet duct zoom. 142
75 Quality spectrum for the mesh metrics: (a) Skewness and (b) Orthogonal quality Fluent (2005). 144
76 Velocity distribution - central plane - top view: (a) Coarser mesh; (b) Coarse mesh (c) Medium mesh; (d) Fine mesh and (e) Finer mesh. 145
77 Friction velocity distribution - gas liquid-interface: (a) Coarser mesh; (b) Coarse mesh (c) Medium mesh; (d) Fine mesh and (e) Finer mesh.146
78 Velocity vertical profiles - mesh sensitivity test at the positions: (a)$z = 200\,mm$; (b)$z = 400\,mm$ and (c) $z = 600\,mm$. 147

79 TKE vertical profiles - mesh sensitivity test at the positions: (a)$z = 200\,mm$; (b)$z = 400\,mm$ and (c) $z = 600\,mm$. 147

80 $H_2Smassfraction$ vertical profiles - mesh sensitivity test at the positions: (a)$z = 200\,mm$; (b)$z = 400\,mm$ and (c) $z = 600\,mm$. 147

81 Different views of the meshes used to perform the mesh sensitivity test of the Benson *et al.* (2020) U bend using the $\kappa - \omega \; SST$ model: Coarsest mesh:(a)Lateral and (b)Frontal; Coarser mesh:(c)Lateral and (d)Frontal; Coarse mesh:(e)Lateral and (f)Frontal; Medium mesh:(g)Lateral and (h)Frontal; Fine mesh:(i)Lateral and (j)Frontal; Finer mesh:(k)Lateral and (l)Frontal;. 149

81 Different views of the meshes used to perform the mesh sensitivity test of the Benson *et al.* (2020) U bend using the $\kappa - \omega \; SST$ model: Coarsest mesh:(a)Lateral and (b)Frontal; Coarser mesh:(c)Lateral and (d)Frontal; Coarse mesh:(e)Lateral and (f)Frontal; Medium mesh:(g)Lateral and (h)Frontal; Fine mesh:(i)Lateral and (j)Frontal; Finer mesh:(k)Lateral and (l)Frontal;. 150

82 Different views of the meshes used to perform the mesh sensitivity test of the Benson *et al.* (2020) U bend using the $\kappa - \varepsilon$ model: Coarse mesh:(a)Lateral and (b)Frontal; Medium mesh:(c)Lateral and (d)Frontal; Fine mesh:(e)Lateral and (f)Frontal. 151

83 Velocity distribution - Lateral view ($\kappa - \omega \; SST$ model): (a) Coarsest mesh; (b) Coarser mesh; (c) Coarse mesh (d) Medium mesh; (e) Fine mesh and (f) Finer mesh. 153

83 Velocity distribution - Lateral view ($\kappa - \omega \; SST$ model): (a) Coarsest mesh; (b) Coarser mesh; (c) Coarse mesh (d) Medium mesh; (e) Fine mesh and (f) Finer mesh. 154

84 Velocity distribution - Lateral view ($\kappa - \varepsilon$ model): (a) Coarse mesh (b) Medium mesh and (c) Fine mesh. 155

85 Benson *et al.* (2020) U bend mesh sensitivity test ($\kappa - \omega \; SST$ model) - u component of the velocity profiles at the positions: (a)$z = 55\,mm$; (b)$z = 75\,mm$; (c) $z = 94\,mm$ and (d) $z = 104\,mm$ 157

86 Benson *et al.* (2020) U bend mesh sensitivity test ($\kappa-\omega\ SST$ model) - u component of the velocity profiles at the positions: (a)$z = 55\ mm$; (b)$z = 75\ mm$; (c) $z = 94\ mm$ and (d) $z = 104\ mm$ 158
87 Benson *et al.* (2020) U bend mesh sensitivity test ($\kappa-\omega\ SST$ model) - u component of the velocity profiles at the positions: (a)$z = 55\ mm$; (b)$z = 75\ mm$; (c) $z = 94\ mm$ and (d) $z = 104\ mm$ 159
88 Benson *et al.* (2020) U bend mesh sensitivity test ($\kappa-\omega\ SST$ model) - TKE line 1 at posisions: (a)$z = 55\ mm$; (b)$z = 75\ mm$; (c) $z = 94\ mm$ and (d) $z = 104\ mm$ 160
89 Benson *et al.* (2020) U bend mesh sensitivity test ($\kappa-\omega\ SST$ model) - TKE line 2 at posisions: (a)$z = 55\ mm$; (b)$z = 75\ mm$; (c) $z = 94\ mm$ and (d) $z = 104\ mm$ 161
90 Benson *et al.* (2020) U bend mesh sensitivity test ($\kappa-\omega\ SST$ model) - TKE line 3 at posisions: (a)$z = 55\ mm$; (b)$z = 75\ mm$; (c) $z = 94\ mm$ and (d) $z = 104\ mm$ 162
91 Benson *et al.* (2020) U bend mesh sensitivity test ($\kappa-\varepsilon$ model) - u component of the velocity profiles at the positions: (a)$z = 55\ mm$; (b)$z = 75\ mm$; (c) $z = 94\ mm$ and (d) $z = 104\ mm$ 163
92 Benson *et al.* (2020) U bend mesh sensitivity test ($\kappa-\varepsilon$ model) - v component of the velocity profiles at the positions: (a)$z = 55\ mm$; (b)$z = 75\ mm$; (c) $z = 94\ mm$ and (d) $z = 104\ mm$ 164
93 Benson *et al.* (2020) U bend mesh sensitivity test ($\kappa-\varepsilon$ model) - w component of the velocity profiles at the positions: (a)$z = 55\ mm$; (b)$z = 75\ mm$; (c) $z = 94\ mm$ and (d) $z = 104\ mm$ 165
94 Benson *et al.* (2020) U bend mesh sensitivity test ($\kappa-\varepsilon$ model) - - TKE line 1 at posisions: (a)$z = 55\ mm$; (b)$z = 75\ mm$; (c) $z = 94\ mm$ and (d) $z = 104\ mm$ 166
95 Benson *et al.* (2020) U bend mesh sensitivity test ($\kappa-\varepsilon$ model) - - TKE line 2 at posisions: (a)$z = 55\ mm$; (b)$z = 75\ mm$; (c) $z = 94\ mm$ and (d) $z = 104\ mm$ 167

96 Benson *et al.* (2020) U bend mesh sensitivity test ($\kappa - \varepsilon$ model) - - TKE line 3 at posisions: (a)$z = 55\,mm$; (b)$z = 75\,mm$; (c) $z = 94\,mm$ and (d) $z = 104\,mm$ 168

LIST OF TABLES

6 Extra examples of works that study the influence of the operational parameters on the flow inside the PWT. 43

7 Extra examples of works that study the influence of the operational parameters on the flow inside the flux chamber. 43

8 Extra examples of works that use the direct methods to sample odorant compounds emitted from solid surfaces. 45

9 Summary of the geometries used to conduce the present work. . . . 57

10 Boundary conditions used for the U-bend geometry simulations using the $\kappa - \omega\, SST$ turbulence model. 63

11 Boundary conditions used for the U-bend geometry simulations using the $Standard \kappa - \varepsilon$ turbulence model. 64

12 Jiang, Bliss and Schulz (1995) boundary conditions. 65

13 UFES PWT boundary conditions. 66

14 Interface boundary conditions used for the PWT simulations. 72

15 Solution Methods. 74

16 Boundary conditions 75

17 Mesh first element height according to its respective geometry and turbulence model. 78

18 Average friction velocity ($\overline{u}^{*}$) in the gas-liquid interface for the different inlet velocities. 101

19 Average mass fraction in the outlet section for both odorant compounds and inlet velocities. 124

20 Number of elements and nodes of the meshes used to perform the mesh sensitivity test of the Jiang, Bliss and Schulz (1995) pwt simulations. 141

21 Number of elements and nodes of the meshes used to perform the mesh sensitivity test of the Jiang, Bliss and Schulz (1995) pwt simulations. 143

22 Number of elements and nodes of the meshes used to perform the mesh sensitivity test of the Jiang, Bliss and Schulz (1995) pwt simulations. 144

23 Average friction velocity ($\overline{u}^{*}$) in the gas-liquid interface for the different mesh resolutions. 148

24 Number of elements and nodes of the meshes used to perform the mesh sensitivity test of the Benson *et al.* (2020) U bend simulations using the $\kappa-\omega\ SST$ model. 148

25 Number of elements and nodes of the meshes used to perform the mesh sensitivity test of the Benson *et al.* (2020) U bend simulations using the $\kappa-\varepsilon$ model. 149

26 Number of elements and nodes of the meshes used to perform the mesh sensitivity test of the Benson *et al.* (2020) U bend using the $\kappa-\omega\ SST$ model. 152

27 Number of elements and nodes of the meshes used to perform the mesh sensitivity test of the Benson *et al.* (2020) U bend using the $\kappa-\varepsilon$ model. 152

LIST OF SYMBOLS

Acronyms

CAPES	Coordenação de Aperfeicoamento de Pessoal de Nível Superior
CFD	Computational fluid dynamics
CV	Control volume
DFC	Dynamic flux chamber
FAPES	Fundação de Amparo à Pesquisa e Inovação do Espírito Santo
LES	Large eddy simulation
NQualiAr	Núcleo de Qualidade do Ar
PUC RJ	Pontifícia Universidade Católica do Rio de Janeiro
PWT	Portable wind tunnel
RANS	Reynolds averaged Navier-Stokes
RSM	Reynolds stress model
SST	Shear stress transport
UFES	Universidade Federal do Espírito Santo
UNSW	University of New South Wales
US-EPA	United States Environmental Protection Agency
VOC	Volatile organic Compound
WWPT	Wastewater treatment plant

Roman symbols

A	Surface area of the source covered by the sampling device (m^2)
a_1	Inner radius of the cross section area (m)
a_2	Outer radius of the cross section area (m)
C	Concentration of the solute in the medium $(kg\, m^{-3})$
C_o	Gas-phase concentration of the odorant compound in air $(kg\, m^{-3})$
C_μ	Dimensionless constant of the $k-\varepsilon$ model
C_{A1}	Concentration of the opposite side of the slab $(kg\, m^{-3})$
C_{A2}	Concentration of the opposite side of the slab $(kg\, m^{-3})$
$C_{G,i}$	Concentration of the solute in the gaseous interface $(kg\, m^{-3})$
$C_{L,i}$	Concentration of the solute in the liquid interface $(kg\, m^{-3})$
C_{od}	Concentration of the odorant $(kg\, m^{-3})$
C_{onc}	Concentration of H_2S $(kg\, m^{-3})$
C_A	Concentration of the compound A $(kg\, m^{-3})$
$CD_{\kappa\omega}$	Positive portion of the cross-diffusion term of the auxiliary function F_1
C_G	Concentration of the solute in the gas phase $(kg\, m^{-3})$
C_L	Concentration of the solute in the liquid phase $(kg\, m^{-3})$
d	Perpendicular distance from the first nodal point to the wall (m)
D	Molecular diffusivity of the solute in the medium $(m^2\, s^{-1})$
D_{AB}	Diffusivity of the compound A in the medium B $(m^2\, s^{-1})$
D_A	Diffusivity of the material through the solid $(m^2\, s^{-1})$
D_G	Diffusivity of the solute in the gaseous phase $(m^2\, s^{-1})$

d_G	Thickness of the gaseous film (m)
D_L	Diffusivity of the solute in the liquid phase $(m^2\, s^{-1})$
d_L	Thickness of the liquid film (m)
E	Emission rate $(kg\, s^{-1}\, m^{-2})$
F_1, F_2	Auxiliary functions of the $k-\omega\, SST$ model
GMF	Gradient mass fraction (m^{-1})
H	Channel height (mm)
I	Turbulence intensity $(\%)$
J	Mass flux of a specific solute $(kg\, s^{-1}\, m^{-2})$
J_{H_2S}	Mass flux of H_2S $(m^3\, s^{-1})$
J_w	Water evaporation rate $(kg\, s^{-1}\, m^{-2})$
J_G	Mass flux of the solute that cross the gas surface $(kg\, s^{-1}\, m^{-2})$
J_L	Mass flux of the solute that cross the liquid surface $(kg\, s^{-1}\, m^{-2})$
k_G	Mass transfer coefficient of the gaseous film $(m\, s^{-1})$
K_H	Dimensionless Henry's law constant
K_L	Liquid-phase overall mass transfer coefficient $(m\, s^{-1})$
k_L	Mass transfer coefficient of the liquid filme $(m\, s^{-1})$
m_0 ,m_f	Initial and final mass of the filled tank (kg)
N_A	Rate of diffusion of a certain compound crossing the solid-gas interface $(kg\, s^{-1}\, m^{-2})$
P	Pressure $(kg\, t^{-2}\, m^{-1})$
Q	Flow rate of the carrier gas $(m^3\, s^{-1})$

s	Stream-wise distance (mm)
S_{av}	Cross section area of the surface (m^2)
S_C	Schmidt number
TVR	Turbulent viscosity ratio $(kg\,t^{-2}\,m^{-1}/kg\,t^{-2}\,m^{-1})$
t	Time (s)
u	Velocity in the x direction $(m\,s^{-1})$
U	Magnitude of the velocity $(m\,s^{-1})$
u^*	Friction velocity $(m\,s^{-1})$
u_i, u_j	Velocity in i and j direction $(m\,s^{-1})$
v	Velocity in the y direction $(m\,s^{-1})$
v_{in}	Inlet velocity $(m\,s^{-1})$
v_{out}	Outlet velocity $(m\,s^{-1})$
w	Velocity in the z direction $(m\,s^{-1})$
y^+	Non-dimensional distance from the wall based on the influence of the shear stress

Greek symbols

α_1, $\beta*$, σ_κ, γ, β, σ_ω	Constants of the $\kappa-\omega$ SST model
β_1, γ_1, $\sigma_{\kappa,1}$,$\sigma_{\omega,1}$	Constants of the original Wilcox $\kappa-\omega$ model
β_2, γ_2, $\sigma_{\kappa,2}$,$\sigma_{\omega,2}$	Constants of the transformed $\kappa-\varepsilon$ model
ε	Dissipation of the turbulent kinetic energy $(m^2\,s^{-3})$

η	Mass fraction of the solute in the medium $(kg\, kg^{-1})$
κ	Turbulent kinetic energy $(m^2\, s^{-2})$
μ	Dynamic viscosity $(kg\, t^{-2}\, m^{-1})$
μ_T	Turbulent viscosity $(kg\, t^{-2}\, m^{-1})$
ν	Kinematic viscosity $(m^2\, s^{-1})$
ρ	Specific mass $(kg\, m^{-3})$
τ	Turbulent stress tensor $(kg\, t^{-2}\, m^{-1})$
υ	Kinematic eddy viscosity $(m^2\, s^{-2})$
υ_t	Turbulent eddy viscosity $(m^2\, s^{-2})$
ϕ, ϕ_1, ϕ_2	Variable that represents any constant of the $\kappa - \omega$ SST model, original Wilcox $\kappa - \omega$ model and transformed $\kappa - \varepsilon$ model, respectively
ω	Specific dissipation rate (s^{-1})

Subscript

i, j, k	Indicial notation

Superscript

$'$	Fluctuations
$-$	Average value

CONTENTS

1 INTRODUCTION 24

2 OBJECTIVES 29

2.1 GENERAL OBJECTIVE 29

2.2 SPECIFIC OBJECTIVES 29

3 LITERATURE REVIEW ON ODOROUS GASES EMISSION FROM PASSIVE SURFACES 30

3.1 THEORETICAL APPROACH TO ESTIMATE VOLATILIZATION RATE FROM PASSIVE SURFACES 30

3.2 MEASUREMENT METHODS OF ODOROUS GASES EMISSION RATE 35

3.2.1 Assessment of direct methods to sample odorant gases from passive surfaces 39

3.2.1.1 Operational parameters for direct methods 39

3.2.1.2 Specificities on sampling odorant from solid surfaces: applied works . 43

3.2.1.3 Numerical Simulations 45

4 METHODOLOGY 48

4.1 GOVERNING EQUATIONS 49

4.2 TURBULENCE MODELING 52

4.3 DOMAINS OF INTEREST 56

4.3.1 U-bend configurations 57

4.3.2 Portable wind tunnel configurations 59

4.4 BOUNDARY CONDITIONS 60

4.4.1 U-bend 60

4.4.2 Portable Wind Tunnel 64

4.4.3 Interface boundary conditions 69

4.5 NUMERICAL SOLUTION OF THE GOVERNING EQUATIONS 73

4.6 DISCRETIZATION OF THE COMPUTATIONAL DOMAIN 76

4.7 EXPERIMENTAL VALIDATIONS 79

4.7.1 U-bend 79

4.7.2 Portable wind tunnel 80

5 RESULTS 83

5.1 VALIDATION AND COMPARISON OF THE NUMERICAL SIMULATIONS RESULTS AGAINST EXPERIMENTAL DATA 83
5.1.1 Validation and analysis of the turbulence model on the U-bend simulations 83
5.1.2 Comparison between the numerical simulations results and JIANG, BLISS E SCHULZ (1995) and WU (2007) portable wind tunnel data 88
5.2 ANALYSIS OF THE AIRFLOW PATTERNS INSIDE THE UFES-PWT FOR DIFFERENT INLET VELOCITIES 90
5.3 ANALYSIS OF THE MASS FRACTION PATTERNS INSIDE THE UFES-PWT FOR DIFFERENT INLET VELOCITIES 109
5.3.1 Analyze of a different boundary condition at the gas-liquid interface 124
6 CONCLUSIONS 130
6.1 CONCLUSIONS 130
6.2 RECOMMENDATIONS FOR FUTURE WORKS 131
BIBLIOGRAPHY 133
APPENDIX A – MESH SENSITIVITY TEST **. 141**
A.1 PORTABLE WIND TUNNEL 141
A.2 U-BEND 148

1 INTRODUCTION

Gaseous compounds emitted to the atmosphere by wastewater treatment plants (WWTP) or landfills can cause health effects, like eye, nose, and throat irritation, headache, nausea, diarrhea, hoarseness, sore throat, cough, among others (GODOI *et al.*, 2018; HU; DU; LONG, 2017; BEGHI *et al.*, 2012; YANG *et al.*, 2012; SCHIFFMAN; WILLIAMS, 2005); greenhouse gases effect (GLAZ *et al.*, 2016; DAELMAN *et al.*, 2012) and also annoyance to the nearby population leading to a number of complaints due to malodorous (HAYES; STEVENSON; STUETZ, 2014; GOSTELOW; PARSONS; STUETZ, 2001). That problem became sharper with the rapidly growth and encroachment of population living close to the emitting sites (SANTOS *et al.*, 2012; BEGHI *et al.*, 2012; LEBRERO *et al.*, 2011; CAPELLI *et al.*, 2009b; CHENG; HSU; CHOU, 2008).

Odour is a complex mixture of many inorganic and organic chemicals depending on its source (HUDSON; AYOKO, 2008a) perceived by the olfactory system. Common odorous gases emitted by WWTP and landfills are hydrogen sulfide (H_2S) and volatile organic compounds (VOCs) (SANTOS *et al.*, 2006; SANTOS *et al.*, 2009; SANTOS *et al.*, 2012). However, one odorous gas is usually chosen as a marker to assess the environmental impact of these sources. For instance, H_2S is used as a marker for WWTP due mainly to the strong rotten-egg smell present even in very low environmental concentrations of this gas (SANTOS *et al.*, 2012). The odor threshold for H_2S is in the range between 0.008 and $0.13\ ppm$, and the fatigue of the olfactory nerves may occurs at $100\ ppm$ (National Research Council *et al.*, 2010). Moreover, Gostelow and Parsons (2000) presented a series of advantages of using H_2S as a marker of the overall odour impact caused by a WWTP: it is easily and rapidly measured down to low ppb levels by hand-held equipment; gas-phase concentrations can be related to liquid phase measurements and theoretical models of sulphide formation are available in the literature.

Passive surfaces are the major sources of H_2S in WWTP. They can be defined as liquid surfaces classified as area sources swept by the atmospheric airflow (BOCKREIS; STEINBERG, 2005; CAPELLI *et al.*, 2009b; LEBRERO *et al.*, 2011). Examples of passive surfaces in WWTP includes: primary and secondary settlement tanks and stabilisation ponds. The term "quiescent" is also often used to refer to these surfaces, but this implies an undisturbed surface which does not commonly happen as the wind is likely to disturb the water surface and generate waves (Prata Jr, 2017).

The mass transfer phenomena in passive surfaces are formulated by using the two-resistance hypothesis in which two films of gas and liquid are in equilibrium and exchange mass at the interface due to molecular diffusion. Therefore, the Fick's law can be applied and the mass transfer coefficient can be written as a function of the molecular diffusion coefficient and the thickness of the film in each phase. Thus, the mass transfer rate or emission rate can be determined based on the Fick's law and on the experimentally determined mass transfer coefficients. It is important to note that some aspects used to elaborate the two-film theory are not observed in passive liquid surfaces in WWTPs, however, the idea of the two films, film thickness and a resistance associated is used to propose mass transfer calculation methodologies, given its simplicity.

Another approach to determine emission rate from passive surfaces consists of experimental measurements. Conceptually, this approach are divided into two classes: the indirect techniques, which do not use an enclosure device to perform the measurement and the direct techniques, which uses a enclosure device to perform the measurements (CAPELLI; SIRONI; ROSSO, 2013). The indirect techniques despite its higher accuracy (HARPER; DENMEAD; FLESCH, 2011), are associated with a greater time/cost. That is due mainly because of the large number of samples required (HUDSON; AYOKO, 2008a). In the direct techniques a part of the emitting surface is confined in a device with controlled air flow rate. The emission rate is a function of the gas-phase concentration and the air flow rate (JIANG; BLISS; SCHULZ, 1995). The direct measurement is simpler, less costly and faster (HUDSON; AYOKO, 2008a).

In order to estimate the emission rates of passive area sources, mathematical emission models have also been used. All these models are based on the contribution of the removal process modelled through empirical algebraic expressions, on the mass balance of the odorant compound. In the literature there are several models accessible to do such a task, as the WATER9(U.S.EPA, 2001), TOXCHEM+(ENVIROMEGA, 2004) and Gostelow, Parsons and Stuetz (2001). The advantage and usefulness of the mathematical emission models are the possibility to estimate the emission rate in

WWTP sites that were not yet constructed. Also, these models provides a cheaper and rapidly solution to already constructed sites (SANTOS *et al.*, 2006; SANTOS *et al.*, 2009).

Enclosure devices used in the direct measurement techniques have been studied and improved by many researchers. The two most commonly used ones are the Dynamic Flux Chamber (DFC) and the Portable Wind Tunnel (PWT) (PI; SHARRATT, 2017; MARTINS *et al.*, 2018; PRATA JR *et al.*, 2018; CAPELLI; SIRONI, 2018; ANDREÃO *et al.*, 2019; PERTA *et al.*, 2019; KIM *et al.*, 2020). They are both open bottom equipments which are placed over the emitting surface from which the volatilized compound is transported through a carrier gas to a bag or sorbent tube for posterior chemical analysis or directly quantified using a gas-specific sensor (HUDSON *et al.*, 2009). The most important difference between these two devices are the magnitude of the sweep air flow rate (in the DFC they are are much lower (STUETZ; FRECHEN, 2001)) and the aerodynamics inside these devices due to their different geometrical designs. Studies have shown that the use of these two devices results in different measurements raising some discussions about their use (HUDSON; AYOKO, 2009; PARKER *et al.*, 2013).

Although there are standards for the use of DFC in the USA and Europe, Capelli, Sironi and Rosso (2013) pointed out that in the recent years its use has been largely replaced by a PWT. This is due to the better characterization of the natural ventilation effects on the emitting surface in comparison with the DFC (JIANG; KAYE, 1996; HUDSON; AYOKO, 2008b). Given the fact that wind velocity (atmospheric turbulence) and emission rate are clearly related, the devices that operate using a dynamic principle (i.e. using a carrier gas) and showing a turbulent flow, such as the PWT, are more likely to model natural processes of emission (HUDSON; AYOKO, 2008b).

Bliss, Jiang and Schulz (1995) studied the mass transfer of ammonia (NH_3) within the PWT. They compared convective mass transfer coefficients obtained by theoretical calculation using the Prandtl boundary layer theory with those obtained experimentally using the PWT. The difference between the theoretical and experimental values was found to be 10%. The authors believe that this occurred due to ammonia trapping in the impingers and the experimental techniques employed. The impingers makes the use of a reaction between the ammonia and sulfuric acid which is not complete and have a 5 to 10 % of bias interference inherent to it.

According to Hudson *et al.* (2009), despite its advantages, the PWT aerodynamic performance is still a matter of discussions and clearly motivates further investigations. The evaluation of the aerodynamic performance of the PWT can be performed by assessing the mixing of the pollutant inside the apparatus and by comparing the values of friction velocity on the surface with those found in the atmospheric flow. In order to obtain a representative sample, the odorous gas should be uniformly distributed inside the equipment, i.e. well mixed at the exit where the sampling probe is located (JIANG; BLISS; SCHULZ, 1995). The friction velocity is straightly related with the mass transfer coefficients (SANTOS *et al.*, 2012; PRATA *et al.*, 2018). To better represent the atmospheric flow, and thus the mass transfer phenomena, the friction velocity values must match the values found in the atmospheric flow . Recent studies using Computational Fluid Dynamics (CFD) showed that the flow inside the main section of the device are quite complex and is not as well behaved as expected (PERTA *et al.*, 2016; MARTINS *et al.*, 2018) and, the friction velocity on the liquid surface does not match typical values found in atmospheric flow (SANTOS *et al.*, 2019).

About the geometrical aspects of the PWT, there is no universal consensus yet and several different designs have been studied (BRASCHKAT *et al.*, 1993; JIANG; BLISS; SCHULZ, 1995; CAPELLI *et al.*, 2009a; PERTA *et al.*, 2016; MARTINS *et al.*, 2018) . The variations between them include differences in the material used in the construction of the tunnel, the length/width ratio, the surface area sampled, the height, the use of flow conditioners and the length/shape/position of the inlet tube (of clean air). (SMITH; WATTS, 1994; HUDSON; AYOKO, 2008b; CAPELLI; SIRONI; ROSSO, 2013).

In order to improve the aerodynamic performance of the PWT, several efforts have been made. Generally the studies can be divided into two groups. First, the experimental studies that include laboratory and field experiments. Second, the computational studies that include the numerical simulation of the flow and the mass transfer inside the devices using a CFD technique. For instance, Perta *et al.* (2016) and Martins *et al.* (2018) conduced numerical simulations to evaluate the effects of small modifications in the PWT geometry on the air flow inside the apparatus. Furthermore, Santos *et al.* (2019) also performed numerical simulations to investigate the effects of small modifications plus different surface roughness on the volatilization of odorous compounds. In general, the results of both studies showed that small modifications in the inlet flow tube, for instance the replacement of the 180° elbow by a extended straight inlet duct, can lead to a better aerodynamic performance of the device. However, despite some works devoted to the investigation of aerodynamics, studies that focus on the mass transfer and the concentration distribution inside this device are very scarce. In this way, there is still a lack of experimental data and detailed information regarding the mass transfer phenomena occurring inside the PWT.

The present work investigated the air-flow and mass transfer process inside the PWT using a numerical approach. It was conduced numerical simulations of the air-flow and mass transfer inside two different geometries of the apparatus, the PWT designed by Jiang, Bliss and Schulz (1995) and another based on the Jiang, Bliss and Schulz (1995) design and presenting the extension outlet duct proposed by Wang, Jiang and Kaye (2001), called UFES PWT. The simulations was validated using the Jiang, Bliss and Schulz (1995) experimental data. Moreover, as a parallel validation in order to show that the air-flow in the 180° are being well simulated, it was conduced the simulations of a U-bend geometry using the experimental data presented by Benson *et al.* (2020).

2 OBJECTIVES

2.1 GENERAL OBJECTIVE

Evaluate the influence of the design and operational conditions on the airflow and mass transfer phenomena inside a portable wind tunnel used to estimate odorant compounds measured over passive liquid surfaces

2.2 SPECIFIC OBJECTIVES

- Analyse the influence of the inlet flow rate on the airflow pattern inside the Portable Wind tunnel through Computational Fluid Dynamics;
- Investigate the influence of the inlet air flow rate on the mass transfer phenomena inside the portable wind tunnel performing numerical simulations;
- Investigate the influence of the geometry changes between the Jiang, Bliss and Schulz (1995) PWT and a PWT designed based on the Jiang, Bliss and Schulz (1995) and including the outlet extension duct proposed by Wang, Jiang and Kaye (2001) on the airflow inside the portable wind tunnel performing numerical simulations;
- Analyse the influence of the use of two different boundary conditions, a prescribed concentration, and mass flux, on the flow pattern inside the Portable Wind tunnel through Computational Fluid Dynamics.

3 LITERATURE REVIEW ON ODOROUS GASES EMISSION FROM PASSIVE SURFACES

In the literature review chapter, it will be covered first the theoretical approach to estimating the volatilization rate from passive surfaces, i.e. its basis, considerations, and calculations. In the following, it will be discussed the measurement methods of odorous gases emission rate, covering articles that discuss the operational parameters, sampling on solid surfaces, and the application of numerical simulations to model airflow and/or the mass transfer inside the apparatus used in the direct methods. A different perspective of the literature review addressing similar topics can be found in the work of Siqueira (2022).

3.1 THEORETICAL APPROACH TO ESTIMATE VOLATILIZATION RATE FROM PASSIVE SURFACES

Volatilization is the process of mass transfer of a compound dissolved in a liquid or solid medium to an adjacent gaseous one.

According to the two-films theory, proposed by Lewis and Whitman (1924), in a liquid-gas interface occurs the formation of two thin layers at each phase side. These two thin layers are considered stationary. In the inner region of either gas or liquid phase (i.e. in the bulk region of the phases, outside the thin layers) the mixing due to convection is so rapid that the concentration of a solute in the fluid is essentially uniform at all points. Since the stationary layers are practically free of convection currents, any transport of solute through these films will occur by diffusion. The rate of mass transfer by diffusion through the films and its direction are dependent on the gradient of concentrations along the films. Figure 1 presents a schematic view of the two-films theory, where J is the mass flux of a specific solute $(kg\, s^{-1}\, m^{-2})$, C_G is the concentration of the solute in the gas phase $(kg\, m^{-3})$, $C_{G,i}$ is the concentration of the solute in the gaseous interface $(kg\, m^{-3})$, $C_{L,i}$ is the concentration of the solute in the liquid interface $(kg\, m^{-3})$, C_L is the concentration of the solute in the liquid phase $(kg\, m^{-3})$, d_G is the thickness of the gaseous film (m) and d_L is the thickness of the liquid film (m). It can be noted that a constant concentration in the bulk region of both phases is represented, as well as the linear gradient of concentration within the two films and the emission direction.

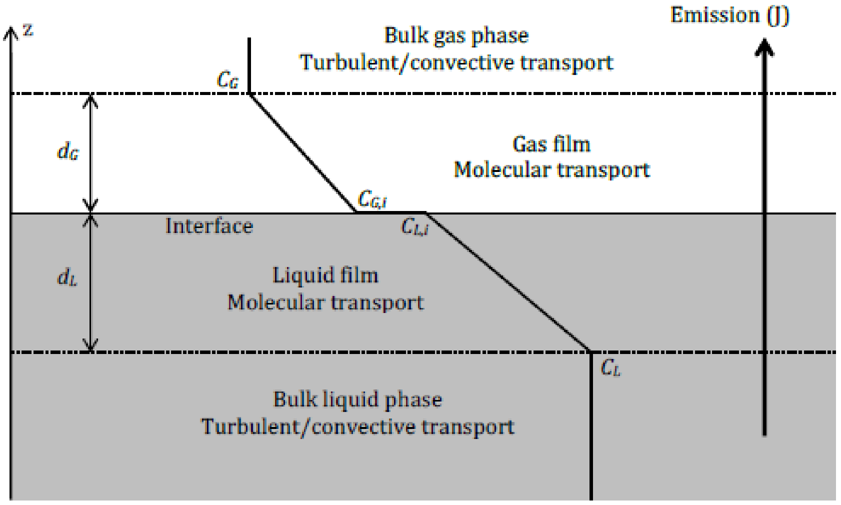
z
Emission (J)
Bulk gas phase
Turbulent/convective transport
C_G
d_G
Gas film
Molecular transport
$C_{G,i}$
Interface
$C_{L,i}$
d_L
Liquid film
Molecular transport
C_L
Bulk liquid phase
Turbulent/convective transport

Figure 1 – Schematic configuration of mass transport across stagnant films (PRATA *et al.*, 2018).

Since the transport in the stagnant films occurs predominantly by diffusion, it can be described using the Fick's law, as shown in Equation 3.1.

$$J = -\rho D \frac{\partial \eta}{\partial z} = -D \frac{\partial C}{\partial z} \tag{3.1}$$

where ρ is the specific mass of the mixture $(kg\, m^{-3})$; D is the molecular diffusivity of the solute in the medium $(m^2\, s^{-1})$; η is the mass fraction of the solute in the medium $(kg\, kg^{-1})$ and C is the concentration of the solute in the medium $(kg\, m^{-3})$. The negative sign represents that the mass flux occurs in the opposite direction of the concentration gradient.

It is also assumed that the films are so thin that the concentration distribution can be approximated as a linear profile along the surface, as shown in Figure 1. Given that, Equation 3.1 can be rewritten for the gaseous and liquid film as: $J_G = D_G{}^{(C_G - C_{G,i})}/_{d_G}$ and $J_L = D_L{}^{(C_L - C_{L,i})}/_{d_L} =$. In where J_G and J_L are mass fluxes of the solute that crosses the gas and liquid phases $(kg\, s^{-1}\, m^{-2})$, respectively; D_G and D_L are the diffusivities of the solute in the gaseous and liquid phases $(m^2\, s^{-1})$, respectively. It should be noted that this is equal to calculate the mass transfer coefficients as: $k_G = D_G/d_G$ and $k_L = D_L/d_L$, respectively.

However, some assumptions used to elaborate the two-film theory are not observed in many of the situations of interest, such as the passive liquid surfaces in WWTPs. In these surfaces is expected that the air-liquid interface to be sheared turbulent boundary layers and thus the films not remain stagnant and with constant thickness. Despite that, given the relative simplicity of the theory, the idea of two films, film thickness and a resistance associated with each one is used to propose new methodologies to calculate the mass transfer in the gas-liquid interface (PRATA *et al.*, 2018).

In this way, two resistance volatilization models are proposed. Although the models uses the idea of two films in the gas-liquid interface and a resistance associated with each one, the films do not need to be stagnant, and neither the mass transfer occurs solely by molecular diffusion. Thus, the films are theoretical layers adjoined to the interface that contain the most important restraints to the mass transfer process (PRATA *et al.*, 2018). The models differ in the manner used to estimate k_L and k_G. Examples are: Lewis and Whitman (1924), Deacon (1977), Mackay and Yeun (1983), Springer, Lunney and Valsaraj (1984) and Gostelow, Parsons and Cobb (2001). It should be noted that the Lewis and Whitman (1924) model is also a two-resistance model.

Given that, Equation 3.1 can be rewritten as Equation 3.2a and 3.2b, for the gaseous and liquid films, respectively. In where the approach used to calculate k_L and k_G will vary according to the mass transfer model.

$$J_G = k_G(C_{G,i} - C_G) \tag{3.2a}$$

$$J_L = k_L(C_L - C_{L,i}) \tag{3.2b}$$

Nonhappening chemical reactions inside the films, there is no consumption or production of the solute in its inside. In this case, the mass flux that crosses the gaseous film (J_G) is equal to that crossing the liquid film (J_L). Thus, equalizing Equations 3.2a and 3.2b, Equation 3.3 is obtained.

$$J = k_G(C_{G,i} - C_G) = k_L(C_L - C_{L,i}) \tag{3.3}$$

According to the Henry's law, in equilibrium conditions, the concentration ratio between the gas and liquid phases obeys a specific proportion, as shown in Equation 3.4 which depends on several factors (for instance, temperature and pressure).

$$K_H = \frac{C_G}{C_L} \tag{3.4}$$

where K_H is the dimensionless Henry's law constant.

The situation in which equation 3.4 is obeyed is called dynamic equilibrium. The transport from the gas to the liquid phase is compensated by the transport from the liquid to the gas phase, thus, there is not net mass transfer. However, there are situations in which that equilibrium are not obeyed and there is effective mass transfer between phases. Even in such situations, its assumed that the in the gas-liquid interface the equilibrium are reached instantaneously (CHAO *et al.*, 2005). The Henry's law in such situations assumes the form shown in Equation 3.5.

$$K_H = \frac{C_{G,i}}{C_{L,i}} \tag{3.5}$$

Through the Henry's law (Equation 3.5), the following expression are obtained: $C_{G,i} = K_H C_{L,i}$. Replacing that expression in the Equation 3.3, the Equation 3.6 is obtained.

$$C_{L,i} = \frac{k_g C_g + k_L C_L}{k_g K_H + k_L} \tag{3.6}$$

Replacing the Equation 3.6 in Equation 3.2b, the Equation 3.7 is obtained. In where the K_L is presented in Equation 3.8.

$$J_L = K_L \left(C_L - \frac{C_g}{K_H} \right) \tag{3.7}$$

$$\frac{1}{K_L} = \frac{1}{k_L} + \frac{1}{k_g K_H} \tag{3.8}$$

where K_L is the liquid-phase overall mass transfer coefficient.

The terms in Equation 3.8 can be understood as the resistances to the mass transfer process. In this way, the terms $1/k_L$ and $1/k_G K_H$ represent the resistances of the liquid and gaseous films, respectively. Therefore, the term $1/K_L$ represents the global resistance to the mass transfer between the phases. The liquid-phase overall mass transfer coefficient (K_L) is limited by the conditions of the liquid, gaseous or both phases, according to the solubility of the compound. Moreover, it should be noted that, in the absence of physical barriers, the conditions required to use the Equation 3.8 are normally found in passive liquid surfaces in WWTPs (HUDSON; AYOKO, 2008a).

By analyzing the Equation 3.8, it can be inferred that the overall mass transfer coefficient (K_L) and thus the overall mass transfer in it self, is conditioned by the dimensionless Henry's law constant value (K_H). Being K_H a characteristic of the chemical compound. Smith, Bomberger and Haynes (1980) and Dilling (1977) presented similar results as Hudson and Ayoko (2008a), that using data presented by Schwarzenbach, Gschwend and Imboden (2003), summarizes that:

- For compounds that presents $K_H \gg 10^{-3}$, that is high volatile compounds, $K_L \approx k_L$. Therefore, the overall mass transfer is strongly dependent on the condition of transport in the liquid film (liquid-phase dominated);
- For compounds that presents $K_H \ll 10^{-3}$, that is less volatile compounds, $K_L \approx k_g K_H$. Therefore, the overall mass transfer is strongly dependent on the condition of transport in the gas film (gas-phase dominated);
- For compounds that presents $K_H \approx 10^{-3}$, no term can be disregarded and the overall mass transfer is dependent on both phases.

For the case of a solid surface, the mass transfer of a diffusing substance through the solid-gas interface can be described also by the Fick's law, as shown in Equation 3.9.

$$N_A = -D_A \frac{\partial C_A}{\partial z} \tag{3.9}$$

Where N_A is the rate of diffusion of a certain compound crossing the solid-gas interface ($kg\ s^{-1}\ m^{-2}$), D_A is the diffusivity of the material through the solid ($m^2\ s^{-1}$) and C_A is the concentration of the compound ($kg\ m^{-3}$).

Integrating the Equation 3.9 for a thin flat slab of thickness Δz, and considering D_A constant the Equation 3.10 are founded.

$$N_A = D_A \frac{(C_{A1} - C_{A2})}{\Delta z} \tag{3.10}$$

Where C_{A1} and C_{A2} are the concentrations at the opposite sides of the slab.

For other solid shapes, the cross section area (S_{av}) is considered, as shown in Equation 3.11.

$$w = N_A S_{av} = \frac{D_A S_{av}(C_{A1} - C_{A2})}{\Delta z} \tag{3.11}$$

Where w is the rate of mass transfer expressed in $(kg\, s^{-1})$.

For example, the diffusion can be spherical, such as in a micro-organism colony in the soil. In this case, $S_{av} = 4\pi a_1 a_2$ and $\Delta z = a_2 - a_1$, in where a_1 and a_2 are the inner and outer radius, respectively.

3.2 MEASUREMENT METHODS OF ODOROUS GASES EMISSION RATE

Several approaches have been developed and studied in order to measure the emission rate of an odorous gas from area sources, such as the passive surfaces. Conceptually, this can be divided into two categories (WILSON *et al.*, 1982; PARKER *et al.*, 2013; HUDSON; AYOKO, 2008b): indirect (device independent) and direct techniques (using an enclosure device).

- The device-independent micrometeorological techniques in which concentration is measured in several locations downstream the source and emission rate is calculated using a dispersion mathematical model reversely (BAI *et al.*, 2017; NI *et al.*, 2015; LAUBACH *et al.*, 2014; BARCLAY; BORISSOVA, 2013; LAUBACH; KELLIHER, 2004), and;
- The direct measurement in which a portion of the emitting area is enclosed by an equipment and a sweep clean air is injected inside the equipment with a known flow rate. The emission rate is then obtained as a function of the gas-phase concentration and the air flow rate (KLENBUSCH, 1986; EKLUND, 1992; JIANG; BLISS; SCHULZ, 1995; WANG; JIANG; KAYE, 2001).

The device-independent technique has the advantage of not being intrusive to the emission process, once no enclosure equipment is used (HUDSON; AYOKO, 2008a). However, for odour assessment, a large number of samples would be needed and the high time/cost involved would make this technique unfeasible for many applications due to its expensiveness. On the other hand, the direct measurement technique is easier to handle and cheaper/faster.

The direct measurement approach can also be divided based on two operation principles: static and dynamic. The last principle uses a carrier gas inside the apparatus. This gas is odorless and has the propose to carry the odorous compound from the emitting surface to the sampling port in which a bag or a canister can be used, as shown in Figure 2. The two most commonly used devices for sampling in passive surfaces operates using the dynamic principle are the flux chamber and the portable wind tunnel (PWT) (CAPELLI; SIRONI; ROSSO, 2013).

The main idea is that the equipment should be able to simulate the effects of the atmospheric flow in the emitting surface (EKLUND, 1992; JIANG; BLISS; SCHULZ, 1995; HUDSON; AYOKO, 2008b) which is called as aerodynamic performance that aims a well mixed flow and a friction velocity on the surface consistent to that of the atmospheric flow. A good mixture it is important because to assure that the samples are representative, the odorous gas should be uniformly distributed inside the equipment. The friction velocity is straightly related with the mass transfer coefficient as the first is also straightly connected with the turbulent transport and the shear stress caused by the wind at the surface (GOSTELOW, 2002).

However, it is important to note that matching the friction velocity values between the open-field and inside the micro-environment created by the equipment is not a guarantee that the mass transfer coefficient will be the same in these two scenarios. For compounds whose emission is dominated by the liquid phase conditions, is expected that the dynamic of the interface would be very different from the open-field, mainly due to currents and waves. On the other hand, for compounds whose emission is dominated by the gas phase, including solid/land surfaces, the same mass transfer coefficient can be observed in the interfacial sub-layer. Nonetheless, the length of the mass transfer boundary layer will be very different, considerably thicker than in the open field, which would conduce to a considerably smaller mass transfer coefficient (from the surface to the boundary layer edge), due to the additional resistance above the interfacial sub-layer (PRATA *et al.*, 2018).

Figure 2 shows a general illustration of the operation of a dynamic flux chamber (DFC) and a PWT. The odorless carrier gas enters in the device with a predefined velocity and carries the odorous compounds emitted by the surface to the outlet to be sampled using an appropriate apparatus for further analysis (CAPELLI; SIRONI; ROSSO, 2013). The main difference between those two devices (i.e. the wind tunnel and flux chamber) regards the flow rate and the directionality of the carrier gas (JIANG; KAYE, 1996; STUETZ; FRECHEN, 2001; CAPELLI; SIRONI; ROSSO, 2013).

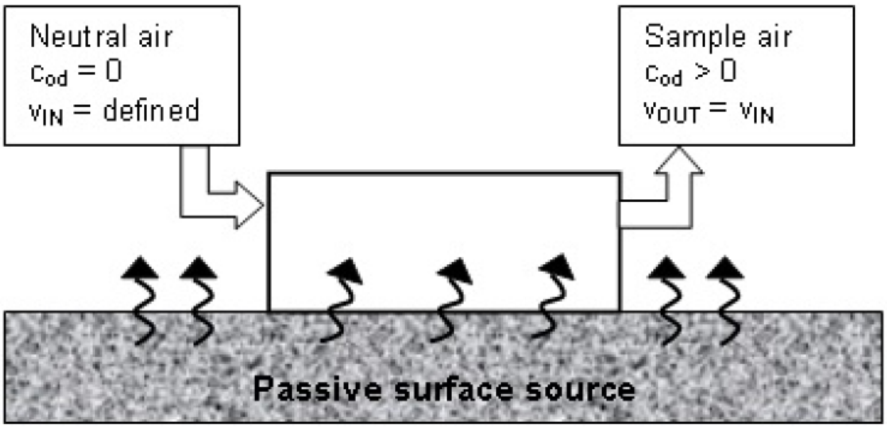

Figure 2 – Illustration of the operation of a equipment for direct measurement of odorant compounds in a passive surface (CAPELLI; SIRONI; ROSSO, 2013).

In Figure 3-a is shown a DFC, specifically developed required by the US-EPA. The aim was to create a method that it is standardized for measuring the emission rate of industrial chemicals from soils and liquid storage facilities. DFCs geometries can vary. Despite the PWT that aims to promote a flow parallel to the liquid surface, the mix between the carrier gas and the emission are in the DFC are non-directional and the rate of carrier gas required are at the range of 5 to 24 $l\ min-1$. The operational parameters that are critical for its use are the mixing of the chemicals and the carrier gas (KLENBUSCH, 1986; GHOLSON; ALBRITTON; JAYANTY, 1989; GHOLSON *et al.*, 1991; CAPELLI; SIRONI; ROSSO, 2013).

Figure 3-b shows a PWT designed by researchers at the University of New South Wales (JIANG; BLISS; SCHULZ, 1995). Their aim was to create a equipment that has a well defined aerodynamic characteristics and a solid and manageable relation between air velocity and measured odor emission rates (JIANG; BLISS; SCHULZ, 1995; JIANG; KAYE, 1996; WANG; JIANG; KAYE, 2001). That is, should be well known the behavior of the flow inside the equipment and the response, in terms of odor emission rate, if varying the inlet flow rate for the same odor source. Like the DFCs to produce air velocity between 0.3 and $1.0\ m\,s^{-1}$ above the emitting surface.

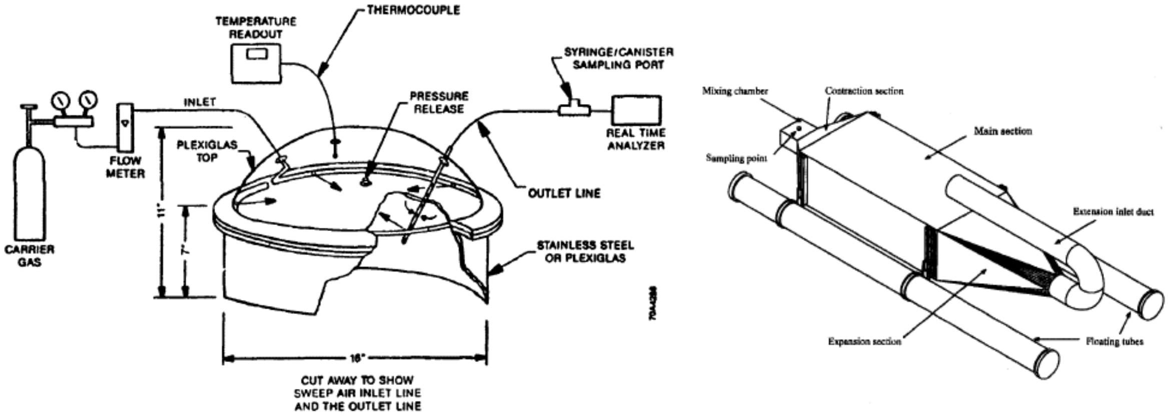
TEMPERATURE READOUT
THERMOCOUPLE
SYRINGE/CANISTER SAMPLING PORT
INLET
PRESSURE RELEASE
REAL TIME ANALYZER
PLEXIGLAS TOP
FLOW METER
OUTLET LINE
CARRIER GAS
11"
7"
STAINLESS STEEL OR PLEXIGLAS
16"
CUT AWAY TO SHOW SWEEP AIR INLET LINE AND THE OUTLET LINE
Mixing chamber
Contraction section
Main section
Sampling point
Extension inlet duct
Expansion section
Floating tubes

(a) (b)

Figure 3 – Enclosure dynamic devices used for sampling odorous compounds in passive surfaces: (a) Dynamic flux chamber (KLENBUSCH, 1986); (b) Portable wind tunnel (JIANG; BLISS; SCHULZ, 1995).

For both devices, the emission rate is calculated using the expression shown in Equation 3.12 where E is the emission rate $(kg\,s^{-1}\,m^{-2})$, C is the gas-phase concentration of the odorous compound in air $(kg\,m^{-3})$, Q is the flow rate of carrier gas $(m^3\,s^{-1})$ and A is the surface area covered by the sampling device (m^2).

$$E = \frac{C.Q}{A} \tag{3.12}$$

Despite the apparently uncomplicated application of both devices, studies regarding the physical-chemistry and aerodynamic (HUDSON; AYOKO, 2008b) characteristics of these devices, Hudson and Ayoko (2008a) concluded that different devices provides different results. Hudson and Ayoko (2008a) compared the data of odor emission rate from feedlot pens, feedlot runoff holding ponds and anaerobic piggery waste treatment ponds provided by these two devices and concluded that they varied by a factor of up to 100 for the same odour source.

Several authors have raised concerns about the use of the DFC. Conen and Smith (1998) showed that a sample collected using DFCs may have its representativiness affected due to an alteration on the gas exchange caused mainly because of the absence of the mixing of soil air with the atmosphere caused by the wind turbulence. In the recent work of Andreão *et al.* (2019), the authors pointed out that a bad mixing inside the chamber affect the overall mass transfer and the sampling recovery efficiency (i.e., a measure of the quantity of gas recovered in relation to the amount released (FANCHI, 2002)). About the PWT, studies indicate that this device may better characterize the effects of the atmospheric flow on the emitting surface making its use a better option to measure the emission rate on passive surfaces (JIANG; KAYE, 1996; HUDSON; AYOKO, 2008a; CAPELLI; SIRONI; ROSSO, 2013). However, as mentioned earlier, the use of the PWT also raises concerns about the representation of some relevant aspects of the open-field atmospheric flow, as the boundary layer and the development of the wave field. Therefore, further investigation is necessary to better understand the physical processes ocurring inside the PWT.

3.2.1 Assessment of direct methods to sample odorant gases from passive surfaces

In this section it will be discussed, via literature review, the operational parameters for direct methods, the measurement of odorant compounds on solid surfaces and the numerical modeling of the flow inside these apparatus.

3.2.1.1 Operational parameters for direct methods

Prata Jr *et al.* (2018) conducted a study to evaluate the mass transfer of compounds inside the Klenbusch (1986) DFC. The laboratory experiments included the evaporation of water and the volatilization of VOC for different air velocities. Particular attention was given to the mass transfer coefficient inside the chamber and the effect of concentration build-up in the hood's headspace. The authors compared the results found for the DFC with those reported in the literature for PWT. It was found that k_G values were in the same order of magnitude, although the measurements using the DFC were expected to produce lower values due to the concentration build-up. A comparison was also performed with the results obtained using an emission model for passive surfaces in WWTPs. The theoretical and experimental results were well correlated for a gas-phase-dominated compound and low wind speeds. For the conditions of the field that differ from the micro-environment created by the DFC a procedure to scale the emission rate measurements by the DFC was proposed. This procedure takes into account the concentration build-up in the hood's headspace, which did not happen for other scaling methods as the water evaporative ratio correction factor presented by Parker *et al.* (2013).

Perta *et al.* (2016) studied, through CFD simulations and wind speed measurements, the effect of different geometry configurations and inlet flow rates on the flow inside a PWT design based on the Jiang, Bliss and Schulz (1995) geometry. Its simulations were validated using the experimental data presented by Jiang, Bliss and Schulz (1995). Despite the good results presented in the paper, informations regarding the geometrical configuration and the numerical methods are not clear. Making difficult the use of the methodology in the present work.

Capelli *et al.* (2009a) designed a new PWT for the collection of gaseous samples on passive area sources. Its design aims to simulate the wind action on the surface to be monitored. The flow behavior inside the device was evaluated via velocity profiles. Whereas the sampling system was validated by comparing the odor concentration of samples collected using the PWT and measured by dynamic olfactometry with the odor concentration predicted using a volatilization model, based on the Prandtl boundary layer theory. Capelli *et al.* (2009a) reports that the velocity profiles showed that the flow inside the device is uniform and homogenous. About the sampling system, the author reports that was observed a good correspondence between the odor concentration measured at the PWT outlet and the value predicted by the volatilization model. Comparing the Capelli *et al.* (2009a) design and the PWT that is used in the present work, based on the Jiang, Bliss and Schulz (1995) configuration and presenting the outlet modification presented by Wang, Jiang and Kaye (2001), the Capelli *et al.* (2009a) design does not present a curve in its inlet pipe, a vertical expansion or contraction and to uniform the flow the new geometry includes three baffles in the expansion section and a flow conditioner in its inlet pipe. According to the author, those modifications result in better uniformity of the flow inside the main section, when compared to the Jiang, Bliss and Schulz (1995) design. However, the data that is presented in the paper does not allow a critical analysis regarding the effects of these alterations. It is not given information about the experimental method, the frequency of data acquisition, and the distribution of friction velocity after the insertion of the flow conditioner.

Using a different wind tunnel, designed to simulate some physical aspects of Klenbusch (1986) flux chamber (i.e. the air enters the device through small, equally-spaced holes), Parker *et al.* (2008) conduced laboratory experiments to study the effects of wind tunnel airflow velocity on VOC emission rates. The VOC emission rates were evaluated on manure, wastewater from beef cattle, dairy animal feeding operations, and water using a standard solution. The wind tunnel air inlet velocity ranged from 0.003 to $0.2\,ms^{-1}$. The results showed that the VOC emission rate increases in a linear manner with the increase of the air velocity. In this way, the air velocity has a major effect on the measured VOC emission, which makes its selection a crucial step when using a wind tunnel to estimate its emission. It is important to note that this result is not valuable for all kinds of VOCs, but just for ones typically found in animal feeding operations. The present work asses the H_2S emission rate through numerical simulation, with the variation of the inlet air velocity, in a PWT designed based on the Jiang, Bliss and Schulz (1995) model with the geometry improvements presented by Wang, Jiang and Kaye (2001).

Baléo and Cloirec (2006) studied, via numerical simulations, the flow inside a PWT design based on the NF X 43-104 (1995) geometry and proposed geometrical modifications to improve it. The author noticed that the presence of a sudden expansion and contraction in the junction of the inflow and outflow pipe with the main section was causing low-velocity zones above the surface to be sampled, reducing the mass transfer and leading to an underestimation of the actual medium emissivity. These problems were mainly caused by a recirculation zone caused by the sudden expansion and contraction. To solve the problem, the author suggested the replacement of the sudden expansion and contraction by an expansion and contraction angled with 7°, similar to that found in the Jiang, Bliss and Schulz (1995) PWT. The introduction of this geometry modification helped to solve the problem by reducing the size of the inflow recirculation zone.

Bliss, Jiang and Schulz (1995) conducted a laboratory study to assess the suitability of the PWT designed by Jiang, Bliss and Schulz (1995) to measure ammonia (NH_3) mass transfer for different inlet flow rates. The author compared the ammonia convective mass transfer coefficients obtained theoretically predicted by the boundary layer theory considering a laminar flow and experimentally using the PWT. It was found a difference of 10% between them. Impingers were used to withdraw the NH_3 samples and were analyzed by a colorimetric method. Impingers uses a reaction between the ammonia and sulfuric acid which is not complete and have a 5 to 10% bias interference inherent to it. The authors credit this difference to ammonia trapping in the impingers and the measurement techniques used in general. It should be noted that the airflow inside the PWT designed by Jiang, Bliss and Schulz (1995) is expected to be turbulent.

Efforts were also performed to understand the influence of the operational parameters on the flow inside the DFC. It can be highlighted the recent works of (ANDREÃO *et al.*, 2019) and Prata Jr *et al.* (2016).

Andreão *et al.* (2019) performed a numerical simulation of the airflow and odorous compounds transport (with different Henry's law constants) in the Klenbusch (1986) DFC. The authors investigated the effect of different inlet air flow rates ($2,5$ and 10 $l\ min^{-1}$), the number of inlet holes (4, 6 and 8), and the inclusion of an internal fan, on the surface friction velocity and emission rate. The results showed that the flow inside the chamber is quite complex and the concentration field reaches a steady state after six residence times. About the presence of the fan, its utilization considerably improved the mixture. The values of friction velocity found with its use were close to those found in an atmospheric flow, which does not happen for all the other configurations. Given that, the authors recommend the use of a fan to improve the mixing inside the DFC and, especially, to reach the values of friction velocity found in the atmospheric flow.

Prata Jr *et al.* (2016) carried out numerical simulations to analyze the influence of the fluid flow features inside the Klenbusch (1986) DFC on its measurements of hydrogen sulfide emission at quiescent liquid surfaces. The results showed that there is a tendency to stagnation and consequent accumulation of the compound near the chamber walls. It indicates that the position of the sampling tube and inlet orifices are probably leading to deviation in the measurements. It was also shown that the friction velocity values do not match the typical values found for atmospheric flow.

More examples of works that study the influence of the operational parameters on the flow inside the PWT and the DFC are shown at the Tables 6 and 7, respectively.

Author	Brief description
Invernizzi *et al.* (2019)	Evaluation of how the change of the inlet air flow rate, the temperature in the liquid phase and the temperature of the sweep air flow affects the emission process of VOC and other odorant compounds in the PWT designed by Capelli *et al.* (2009a) compared to a new theoretical model. It was found a good agreement between the emission rates obtained theoretically and experimentally. The liquid temperature affects signicantly the outlet concentrations.
Perta *et al.* (2019)	Compared two methods for measure ammonia emissions by agricultural sites, a micrometeorological one called the Integrated Horizontal Flux used with glass tubes and the Jiang, Bliss and Schulz (1995) PWT with acid traps. The tests was conduced in field. The measured volatilization by the micrometeorological method differ from the PWT by approximately $40\ \%$, a better correlation was found increasing the exposition time to a minimum of 3 hours.

Table 6 – Extra examples of works that study the influence of the operational parameters on the flow inside the PWT.

Author	Brief description
Aneja *et al.* (2006)	Development of a flux chamber for measure emissions of nitrogen, sulphur and carbon compounds for a variety of field applications. The chamber measurements was validated with theoretical models.
Christensen *et al.* (1996)	A comparison between the measurements of N_2O by an agricultural field made with a flux chamber and micrometereological techniques. The results confirms that emission rates obtained with the different methods can be meaningfully compared.
Gholson *et al.* (1991)	Stutied the use of a Klenbusch (1986) flux chamber to measure VOC from passive water sufaces, at the laboratory and field. The results indicate the capability to use this equipment for this kind of measurement.

Table 7 – Extra examples of works that study the influence of the operational parameters on the flow inside the flux chamber.

3.2.1.2 Specificities on sampling odorant from solid surfaces: applied works

Using a wind tunnel sampler, Qiang, Li and Liu (2019) investigated the emission rate of odorant compounds in a municipal solid waste landfill working area in China. It was measured the emission rate of H_2S, VOCs, and odor units. The author finds that in the high-temperature season (summer), the emission rate was nearly 6 times higher than that in the low-temperature season. It was also tested the variation of the wind sweeping velocity from a range of $0,6$ to $4\,m/s$, and a linear relationship between the wind velocity and the measured emission rate was reported. The present work tested the variation of the wind speed inside a PWT based on the geometry presented by Jiang, Bliss and Schulz (1995) and improved by Wang, Jiang and Kaye (2001) for the emission of H_2S, via numerical simulation.

Capelli *et al.* (2012) conduced a study to assess the use of the PWT designed by Capelli *et al.* (2009a) to sample odorous compounds emitted by solid area sources. The assessment was performed by confronting the data obtained using the PWT to sample odorant compounds from a solid surface in laboratory conditions with data obtained using a suitable theoretical volatilization model. In general, the results of the tests showed a good agreement between the volatilization model and the experimental tests.

Wang *et al.* (2011) conduced measurements of odor and odor emission rates from freshly dewatered biosolids in a dewatering building of a Water Reclamation Plant (WRP) using the US-EPA DFC and the PWT designed by Gao *et al.* (1996). To test with the use of the two methods results in similar emission rates under field conditions, the results were statistically compared. To control the field pertinent conditions, i.e., the wind velocity and air exchange rate, the tests were conduced indoors. The measured emission rates, of odor and H_2S, do not present any statistically significant difference. The same equivalence between the measurements using samples collected using the Jiang, Bliss and Schulz (1995) PWT and the US-EPA DFC is not observed, as shown by Hudson and Ayoko (2008b). It should be noted that the PWT designed by Gao *et al.* (1996) differs greatly from the PWT designed by Jiang, Bliss and Schulz (1995), mainly in terms of creative purpose, operational conditions, and design. About the creative purpose, while the Jiang, Bliss and Schulz (1995) PWT was firstly designed to sample odorous compounds emitted from liquid surfaces, the Gao *et al.* (1996) was designed with soil surfaces in mind. It should be noted that this does not state that either geometry can't be used to sample in different mediums. About the operational parameters, the inlet airflow rate of the Jiang, Bliss and Schulz (1995) PWT, pointed by the author as of its ideal, is about $1300\,L/min$, and of the Gao *et al.* (1996) PWT is $24,6\,L/min$, that is, the Gao *et al.* (1996) PWT inlet air flow rate is about 53 times slower than the Jiang, Bliss and Schulz (1995) PWT. The design of the geometries also varies, the Gao *et al.* (1996) design does not present a curve in its inlet pipe, a vertical expansion, or contraction and to uniform the flow the geometry includes five baffles in the expansion and contraction section. The height of the equipment and its open-bottom area also differ, being $0,08\,m$ and $1,6\,m^2$, respectively. To compare, the height of the Jiang, Bliss and Schulz (1995) PWT is 3 times higher and the area 2 times bigger. The present work aims to elucidate more clearly what occurs inside the PWT proposed by Jiang, Bliss and Schulz (1995), both in terms of flow and mass transfer. Thus, helping to explain the differences that occur in the odor measurements using a PWT build based on the Jiang, Bliss and Schulz (1995) design in relation to other equipment, such as the US-EPA DFC.

More examples of works that use the direct methods to sample odorant compounds emitted from solid surfaces are shown at the Table 8.

Author	Brief description
Capelli and Sironi (2018)	Using the PWT designed by Capelli *et al.* (2009a), the author made measurements of the specific odour emission rate in a landfill. The author used this data as input to a dispersion model, in order to compare two different modeling approaches to estimate the odour emission from landfills.
Borhan *et al.* (2013)	Using a PWT, the author collected air samples from feedlot pen surfaces, to study the effects of dietary crude protein levels fed to beef steers in pens with or without corn stover bedding.
Henry, Watts and Nicholas (2008)	Outlined and summarized the unpublished reports of a collective effort to develop industry-specific odor impact criteria for Australian feedlots. It was used 250 olfactometry samples collected using a PWT.

Table 8 – Extra examples of works that use the direct methods to sample odorant compounds emitted from solid surfaces.

3.2.1.3 Numerical Simulations

Andreão and Feroni (2021) performed several numerical simulations of the mass transfer inside the DFC using algebraic models to calculate the liquid-phase mass transfer coefficient (k_L). In total, it was used ten different models to calculate the gas-liquid interface boundary condition. Despite the contributions of the paper in the understanding of the mass transfer process inside the DFC, as the author state, none of these models are capable of representing the simulated friction velocity ranges. Furthermore, a closer look into these algebraic models shows that they weren't developed to cases with a mass flow in a confined space. Unfortunately, this is the scenario inside of the apparatus commonly used by the direct methods e.g. dynamic flux chambers or portable wind tunnels. In this way, the present work does not make use of algebraic models to calculate k_L. For the H_2S case, it was used the Siqueira (2022) experimental results and for the acetic acid, it was used the same concentration as Prata Jr *et al.* (2018) used for the liquid phase. More details can be found in the Methodology (Section 4.4.3).

The simulations conduced by Martins *et al.* (2018), showed that the flow inside the PWT designed by Jiang, Bliss and Schulz (1995) is quite different from what it was designed to be. To lead to better predictions, that PWT was first designed aiming to present a fully developed boundary layer in its main section (JIANG; BLISS; SCHULZ, 1995). However, according to the simulations, the flow inside the equipment is quite complex and not as well behaved as expected. To make the flow close to a fully developed boundary layer, as initially thought, Martins *et al.* (2018) proposed some modifications in the geometry of the PWT. It was proposed two modifications, a first that uses an extra flow conditioner between the 90° curve and the expansion section, and a second, that substitute the 90° curve by a straight duct. The aerodynamic performance of the modified geometries was assessed via numerical simulation. Although the modifications did not conduce the flow inside the main section to behave as a fully developed boundary layer, they showed that small modifications in the geometry can lead to considerable modifications in the flow behavior.

Prata Jr *et al.* (2016) carried out numerical simulations to analyze the influence of the fluid flow features inside the Klenbusch (1986) DFC on its measurements of hydrogen sulfide emission at quiescent liquid surfaces. The results showed that there is a tendency to stagnation and consequent accumulation of the compound near the chamber walls. It indicates that the position of the sampling tube and inlet orifices are probably leading to deviation in the measurements. It was also shown that the friction velocity values do not match the typical values found for atmospheric flow.

Prata Jr *et al.* (2014) has simulated the flow in a $2D$ sagittal plane longitudinal to the flow direction of the PWT designed by Jiang, Bliss and Schulz (1995). Although is not possible to conduce a detailed analysis of the airflow inside the device using the data provided by the author, because of the geometry simplification that was used, it is shown the potential of the CFD simulations to assess the airflow in such devices.

Based on previous works found in the recent literature, it can be observed that there are still open questions concerning the best numerical methodology to perform and validate the numerical simulation of the airflow inside the Jiang, Bliss and Schulz (1995) PWT, how the geometry of the apparatus influence the airflow in its inside and the influence of the inlet air flow rate on the airflow pattern and on the mass transfer phenomena inside the device.

4 METHODOLOGY

Figure 4 summarizes the methodology. To validate the numerical simulations of the airflow inside the PWT it was used the velocity data presented by Jiang, Bliss and Schulz (1995), obtained through hot wire anemometry. Therefore in this step, it was simulated the airflow inside the PWT designed by Jiang, Bliss and Schulz (1995). As the configuration of the PWT chosen to be simulated in this work includes an inlet tube in the shape of a U-bend, the airflow in a 90° curve with square shape was simulated and validated using the velocity experimental data presented by Benson *et al.* (2020), obtained through magnetic resonance velocimetry. Furthermore, it was used the velocity data presented by Wu (2007) for the PWT to perform a general comparison with the numerical data obtained when simulating the airflow inside the apparatus. That data couldn't be used to a validation due to geometrical changes with the Jiang, Bliss and Schulz (1995) PWT. The mesh sensitivity test was conduced for the U-bend, considering the tree velocity components and turbulent kinetic energy, and for the Jiang, Bliss and Schulz (1995) PWT considering the velocity, turbulent kinetic energy, and H_2S mass fraction. It should be noted that the application of two different turbulence models, the $Standard\ \kappa-\varepsilon$ and $\kappa-\omega\ SST$, was analyzed for the U-bend simulations. The variation of the velocity, odorant compound, and boundary condition methodology was studied using a PWT design based on the Jiang, Bliss and Schulz (1995) geometry and including the outlet extension duct presented by Wang, Jiang and Kaye (2001), namely the UFES PWT.

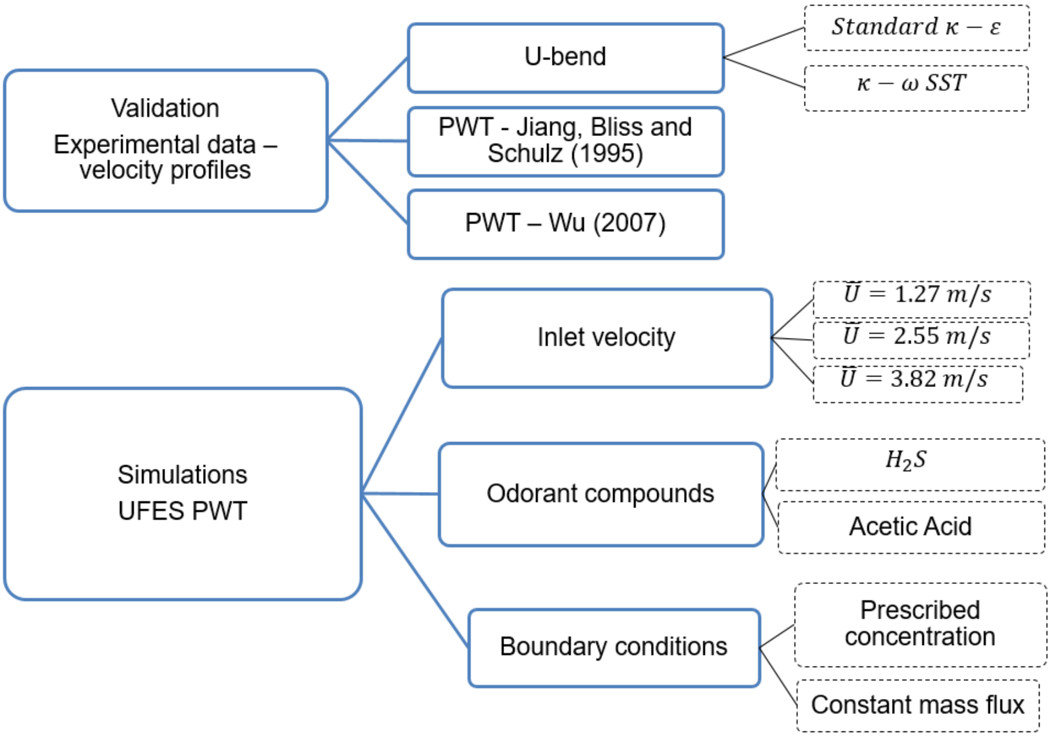
Validation
Experimental data – velocity profiles
U-bend
$Standard\ \kappa-\varepsilon$
$\kappa-\omega\ SST$
PWT - Jiang, Bliss and Schulz (1995)
PWT – Wu (2007)
Simulations
UFES PWT
Inlet velocity
$\bar{U}=1.27\ m/s$
$\bar{U}=2.55\ m/s$
$\bar{U}=3.82\ m/s$
Odorant compounds
H_2S
Acetic Acid
Boundary conditions
Prescribed concentration
Constant mass flux

Figure 4 – Summary of the methodology.

4.1 GOVERNING EQUATIONS

The airflow and the transport of the odorous compound (in this case H_2S) inside the portable wind tunnel (PWT) is modelled using the differential equations of continuity (Equation 4.1a), momentum conservation (Equation 4.1b) and chemical species mass conservation (Equation 4.1c) for an incompressible Newtonian fluid in a uniform temperature media.

$$\frac{\partial u_i}{\partial x_i}=0 \tag{4.1a}$$

where u is the velocity component $(m\,s^{-1})$ and i,j are the indexes, being $(i,j)=(1,2,3)$ and, consequently, $(u_1,u_2,u_3)=(u,v,w)$ and $(x_1,x_2,x_3)=(x,y,z)$.

$$\rho\frac{\partial u_i}{\partial t}+\rho u_j\frac{\partial u_i}{\partial x_j}=-\frac{\partial P}{\partial x_i}+\mu\frac{\partial^2 u_i}{\partial x_j\partial x_j} \tag{4.1b}$$

where ρ is the specific mass $(kg\,m^{-3})$, P is the thermodynamic pressure $(kg\,m^{-1}\,t^{-2})$ and μ the dynamic viscosity of the fluid $(kg\,m^{-1}\,t^{-1})$.

$$\frac{\partial C_A}{\partial t} + u_j \frac{\partial C_A}{\partial x_j} = D_{AB} \frac{\partial^2 C_A}{\partial x_j \partial x_j} \tag{4.1c}$$

where C_A is the compound concentration $(kg\, m^{-3})$ and D_{AB} is the diffusivity coefficient of the compound A in the medium B $(m^2\, s^{-1})$.

The term $\frac{\partial u_i}{\partial t}$ in the Equation 4.1b represents the rate of local temporal variation of velocity. In Equation 4.1b, $\rho u_j {}^{\partial u_i}/_{\partial x_j}$ is the advective term, $\mu {}^{\partial^2 u_i}/_{\partial x_j \partial x_j}$ is the influence of the viscous stress tensor and ${}^{\partial P}/_{\partial x_i}$ is the influence of the pressure forces. The term ${}^{\partial C_A}/_{\partial t}$, in Equation 4.1c, is the variation of the concentration with time, $u_j {}^{\partial C_A}/_{\partial x_j}$ is the advective transport and $D_{AB} {}^{\partial^2 C_A}/_{\partial x_j \partial x_j}$ is the diffusive term.

All these equations are valid for a differential control volume CV. Equation 4.1a establishes that the mass within (CV) remains constant. With respect to Equation 4.1b, it establishes that the total force acting on CV drives to a rate of change of momentum within the CV and/or to the net rate in which momentum are withdrawing or coming to the CV through its control surfaces (BATCHELOR; BATCHELOR, 2000). Equation 4.1c states that the local variation of the chemical species mass with time are due to advection and/or diffusion (BERGMAN *et al.*, 2011).

The airflow inside the PWT appears to be turbulent, once that it possesses a Reynolds number of approximately 2.10^4 $(Re = {}^{U[m\, s^{-1}]*D[m]}/_{\nu[m^2\, s^{-1}]} = {}^{2.82*0.1}/_{1.45e^{-06}})$, in where U is the average inlet velocity and D is the inlet tube diameter. Therefore, it is necessary to consider all the spectrum of frequencies involved in the problem. This consideration makes the numerical simulation extremely expensive in terms of computational cost. Thus, the present work will use a Reynolds Averaged Navier Stokes (RANS) modeling which solves only the equations for the average flow and considers the influence of the turbulent effects as described only by one term of the equation to be modeled. For this purpose, it uses the Reynolds postulates which consider that the properties involved in the problem can be modeled as an average value and its fluctuation, as shown in Equation 4.2 for the velocity (VERSTEEG; MALALASEKERA, 2007; PATANKAR, 2018).

$$u(t) = \overline{u} + u'(t) \tag{4.2}$$

where $\overline{u}$ are the average velocity and $u'(t)$ describes the velocity turbulent fluctuation. Figure 5 shows the temporal variation of velocity for a given case (VERSTEEG; MALALASEKERA, 2007).

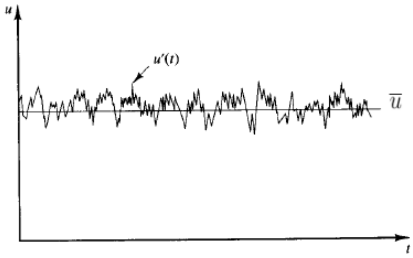

Figure 5 – Velocity time series highlighting the averaged value and fluctuation (VERSTEEG; MALALASEKERA, 2007).

All variables that appear in Equations 4.1a, 4.1b and 4.1c can be expressed as a function of the averaged value and fluctuation. After carrying out this decomposition and applying a temporal average in each one of the terms, Equations 4.3a, 4.3b and 4.3c are obtained (VERSTEEG; MALALASEKERA, 2007; PATANKAR, 2018).

$$\frac{\partial \overline{u}}{\partial x_i} = 0 \tag{4.3a}$$

$$\rho \frac{\partial \overline{u}_i}{\partial t} + \rho \overline{u}_j \frac{\partial \overline{u}_i}{\partial x_j} = -\frac{\partial \overline{P}}{\partial x_i} + \frac{\partial}{\partial x_j}\left[\mu\left(\frac{\partial \overline{u}_i}{\partial x_j} + \frac{\partial \overline{u}_j}{\partial x_i}\right) - \rho\overline{u'_i u'_j}\right] \tag{4.3b}$$

$$\frac{\partial \overline{C}_A}{\partial t} + \overline{u}_j \frac{\partial \overline{C}_A}{\partial x_j} = \frac{\partial}{\partial x_j}\left[D_{AB}\frac{\overline{C}_A}{\partial x_j} - \overline{u'_j C'_A}\right] \tag{4.3c}$$

These equations express the averaged behavior of the fluid motion and mass tranfer described by Equations 4.1a, 4.1b and 4.1c. The term $\rho\overline{u'_i u'_j}$ that appear in Equation 4.3b is called Reynolds stress tensor and is related with the influences of the fluctuations of velocity on the average flow (VERSTEEG; MALALASEKERA, 2007; PATANKAR, 2018).

The new terms that appear in Equations 4.3b and 4.3c insert new variables to the problem. Thus, it is necessary to use new equations to model the Reynolds stress tensor components.

4.2 TURBULENCE MODELING

One of the approaches consists in deriving and solving the transport equations for all the tensor components, this is what the Reynolds stress model (RSM) proposes. However, this alternative is more computationally expensive, once that six new equation are added to the problem (VERSTEEG; MALALASEKERA, 2007; PATANKAR, 2018) just for the turbulent momentum flux.

An expanded form of the Reynolds stress tensor is shown in Equation 4.4. As can be seen, the matrix that represents the tensor is symmetric, thus in order to model its behavior six new equations are required (VERSTEEG; MALALASEKERA, 2007; PATANKAR, 2018).

$$\overline{u_i'u_j'} \equiv \begin{bmatrix} \overline{u'u'} & \overline{u'v'} & \overline{u'w'} \\ \overline{v'u'} & \overline{v'v'} & \overline{v'w'} \\ \overline{w'u'} & \overline{w'v'} & \overline{w'w'} \end{bmatrix} \tag{4.4}$$

Another approach consists in using the Boussinesq hypothesis. That hypothesis is based on the experimental observation that the turbulence decays unless there is a shear stress in the incompressible averaged flow. Moreover, it was observed that the turbulent shear increases as long the averaged deformation rate increases as well. In this way, Boussinesq proposed in 1877 that the Reynolds stress could be related with the average rate of deformation, as indicated by Equation 4.5a (VERSTEEG; MALALASEKERA, 2007; PATANKAR, 2018).

$$\rho\overline{u_i'u_j'} = \tau^T = \mu_T\left(\frac{\partial\overline{u}_i}{\partial x_j} + \frac{\partial\overline{u}_j}{\partial x_i}\right) \tag{4.5a}$$

Being the stresses shown in Equation 4.5b.

$$\overline{\tau}_{ij} = \mu\left(\frac{\partial\overline{u}_i}{\partial x_j} + \frac{\partial\overline{u}_j}{\partial x_i}\right) \tag{4.5b}$$

where μ_T it is the turbulent viscosity $(kg\, t^{-2}\, m^{-1})$.

Replacing Equations 4.5a and 4.5b on 4.3b, Equation 4.6 can be obtained.

$$\rho\frac{\partial \overline{u}_i}{\partial t}+\rho\overline{u}_j\frac{\partial \overline{u}_i}{\partial x_j}=-\frac{\partial \overline{P}}{\partial x_i}+\frac{\partial}{\partial x_j}\left[(\mu_T+\mu)\left(\frac{\partial \overline{u}_i}{\partial x_j}+\frac{\partial \overline{u}_j}{\partial x_i}\right)\right] \tag{4.6}$$

Therefore, arises the necessity to model a new property, the turbulent viscosity (μ_T).

In order to model the new variable, i.e. the turbulent viscosity (μ_T), that appears in Equation 4.6, several models have been proposed. Generally, the models vary in the number of equations used to describe the phenomenon. Two well-known and widely used models are the $\kappa-\varepsilon$ and the $\kappa-\omega$ which are based on the solution of two additional equations (VERSTEEG; MALALASEKERA, 2007; PATANKAR, 2018).

The $\kappa-\varepsilon$ model calculates the turbulent viscosity using the turbulent kinetic energy (κ) ($m^2\ s^{-2}$) and the dissipation of the turbulent kinetic energy (ε) ($m^2\ s^{-3}$), as shown in Equation 4.9. In the case of the $\kappa-\omega$ model, turbulent viscosity is calculated using Equation 4.10, that involves the turbulent kinetic energy (κ) and the specific dissipation rate (ω) (s^{-1}). This way, the models add two additional transport equations to the problem (VERSTEEG; MALALASEKERA, 2007; PATANKAR, 2018).

From a dimensional point of view, the kinetic turbulent viscosity can be expressed as a function of the scale of velocity (ϑ $[m/s]$) and length (ℓ $[m]$). Therefore, through dimensional analysis and multiplying it by the mass specific (ρ) to express the dynamic turbulent viscosity, Equation 4.7 is obtained. In which C is a proportionality constant. To the $\kappa-\varepsilon$ model, the velocity and length scales are defined in function of κ and ε, as shown respectively, in Equations 4.8a and 4.8b. Replacing Equations 4.8a and 4.8b in Equation 4.7, the Equation for the turbulent viscosity is obtained, as shown in Equation 4.9.

$$\mu_T=C\rho\vartheta\ell \tag{4.7}$$

$$\vartheta=\kappa^{1/2} \tag{4.8a}$$

$$\ell = \frac{\kappa^{3/2}}{\varepsilon} \tag{4.8b}$$

$$\mu_T = \rho C_\mu \frac{\kappa^2}{\varepsilon} \tag{4.9}$$

In where C_μ, equal to C, is a dimensionless constant. Its value is obtained by a comprehensive data fitting for a wide range of turbulent flows (VERSTEEG; MALALASEKERA, 2007).

$$\mu_T = \rho \frac{\kappa}{\omega} \tag{4.10}$$

Both models, $\kappa - \varepsilon$ and $\kappa - \omega$, present good results, are widely tested and require considerably less computation effort if compared to others models (FLUENT *et al.*, 2011). However, despite the reliability and simplicity of the model $\kappa - \omega$ model, it presents an undesirable freestream dependency (MENTER, 1993). This way, it presents good results near the wall and not so good in the free flow region. On the other hand, the model $\kappa - \varepsilon$ presents good results in the free flow region and not so good close to walls (MENTER, 1994). After analyzing this problem, Menter (1994) proposed a new model that maintain the good characteristics of the $\kappa - \varepsilon$ without its undesirable effects near the wall. The author used a function to discriminate the near wall region (about 50%) in the boundary layer and the rest of the flow. In the near wall region, the $\kappa - \omega$ model is used and gradually changed to the $\kappa - \varepsilon$ model as the solution moves to the edge of the boundary layer. That new model is named $\kappa - \omega \; SST$ (*SST - Shear Stress Transport*) and has also the capability to consider the transport of the turbulent shear stresses in adverse pressure gradients in the boundary layer (MENTER, 1993; MENTER, 1994).

The $\kappa - \omega \; SST$ model uses Equations 4.11a and 4.11b to model the transport of κ and ω, respectively (MENTER, 1993; MENTER, 1994).

$$\frac{\partial \rho \kappa}{\partial t} + u_j \frac{\partial \rho \kappa}{\partial x_j} = \tau_{i,j} \frac{\partial u_i}{\partial x_j} - \beta^* \rho \omega \kappa + \frac{\partial}{\partial x_j} \left[(\mu + \sigma_\kappa \mu_T) \frac{\partial \kappa}{\partial x_j} \right] \tag{4.11a}$$

$$\frac{\partial \rho \omega}{\partial t}+u_j\frac{\partial \rho \omega}{\partial x_j}=\frac{\gamma}{\upsilon_t}\tau_{i,j}\frac{\partial u_i}{\partial x_j}-\beta\rho\omega^2+\frac{\partial}{\partial x_j}\left[(\mu+\sigma_w\mu_T)\frac{\partial \omega}{\partial x_j}\right]+2(1-F_1)\rho\sigma_\omega 2\frac{1}{\omega}\frac{\partial k}{\partial x_j}\frac{\partial \omega}{\partial x_j} \tag{4.11b}$$

where $\beta*$, σ_κ, γ, β, σ_ω are the constants of the model, υ_t is the turbulent eddy viscosity $(m^2\ s^{-2})$ and F_1 is an auxiliary function (Equation 4.13).

The $\kappa-\omega\ SST$ model uses an expression to adapt the constants of the original Wilcox $\kappa-\omega$ model and the modified $\kappa-\varepsilon$ to its use. Being ϕ_1 any constant of the original Wilcox $\kappa-\omega$ model, ϕ_2 any of the transformed $\kappa-\varepsilon$ model and ϕ any of the new model, the relation between them are expressed in Equation 4.12 (MENTER, 1993; MENTER, 1994).

$$\phi=F_1\phi_1+(1-F_1)\phi_2 \tag{4.12}$$

The first set of constants (ϕ_1) - original Wilcox $\kappa-\omega$ model, are (MENTER, 1993; MENTER, 1994):

$$\sigma_{k,1}=0,5,\ \sigma_{\omega,1}=0,5,\ \beta_1=0,0750$$

$$\beta*=0,09\ ,\ \kappa=0,41,\ \gamma_1={}^{\beta_1}/_{\beta*}-\sigma_{\omega,1}{}^{\kappa^2}/\sqrt{\beta*}$$

The second set of constants (ϕ_2) - modified $\kappa-\varepsilon$, are (MENTER, 1993; MENTER, 1994):

$$\sigma_{k,2}=1,0,\ \sigma_{\omega,2}=0,856,\ \beta_2=0,0828$$

$$\beta*=0,09\ ,\ \kappa=0,41,\ \gamma_2={}^{\beta_2}/_{\beta*}-\sigma_{\omega,2}{}^{\kappa^2}/\sqrt{\beta*}$$

The F_1 auxiliary function is defined as Equation 4.13 where $CD_{\kappa\omega}$ is the positive portion of the cross-diffusion term of Equation 4.11b and is defined as Equation 4.14 (MENTER, 1993; MENTER, 1994).

$$F_1=tanh\left\{\left[min\left(max\left(\frac{2\sqrt{\kappa}}{\beta*\gamma y},\frac{500\nu_t}{y^2\gamma}\right),\frac{4\sigma_{\omega,2}\kappa}{CD_{\kappa\omega}}y^2\right)\right]\right\} \tag{4.13}$$

$$CD_{\kappa\omega} = max\left(2\rho\sigma_{\omega,2}\frac{1}{\omega}\frac{\partial\kappa}{\partial x_j}\frac{\partial\omega}{\partial x_j}, 10^{-20}\right) \tag{4.14}$$

The turbulent eddy viscosity (υ_t) $(m^2\ s^{-2})$ is calculated as Equation 4.15 (MENTER, 1993; MENTER, 1994).

$$\upsilon_t = \frac{a_1 k}{\max(\alpha_1 \omega; \Omega F_2)} \tag{4.15}$$

where the constant $\alpha_1 = 0,31$, Ω is absolute value of the vorticity and the term F_2 is defined as Equation 4.16 (MENTER, 1993; MENTER, 1994).

$$F_2 = \tanh\left(\max\left(\frac{2\sqrt{k}}{0,09\omega y}; \frac{500\upsilon}{y^2\omega}\right)\right) \tag{4.16}$$

where υ is the eddy viscosity $(m^2\ s^{-2})$.

4.3 DOMAINS OF INTEREST

There will be used in the present work three different configurations of the portable wind tunnel and a relatively simple u-bend geometry as a complementary validation. All the simulated geometries and its purpose are summarized in Table 9.

Geometry	Image	Brief description of its usage
Benson *et al.* (2020) U-bend	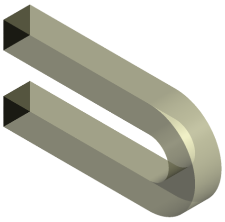	Complementary validation and compare the response of two turbulence models to model the flow in the curve, the $Standard\ \kappa-\varepsilon$ and the $\kappa-\omega\ SST$.
Jiang, Bliss and Schulz (1995) PWT U-bend	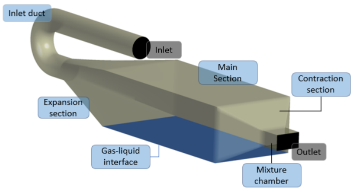 Inlet duct Inlet Main Section Contraction section Expansion section Gas-liquid interface Outlet Mixture chamber	Validation and comparison of the numerical simulations against the experimental data and analysis of the geometrical influence on the PWT airflow and mass transfer phenomena.
UFES PWT	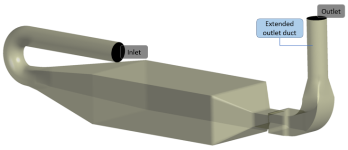 Outlet Extended outlet duct Inlet	Analysis of the airflow and the mass transfer phenomena using different inlet velocities, odorant compounds and gas-liquid interface boundary conditions.

Table 9 – Summary of the geometries used to conduce the present work.

4.3.1 U-bend configurations

There is in the literature a lack of robust experimental data concerning the airflow inside the PWT. Jiang, Bliss and Schulz (1995) presented velocity profiles for the flow inside the main section of the PWT, however, little information is provided regarding the inlet air flow rate and the exact configuration of the hot-wire anemometer used in its experiments.

Duo to that, in the present work, validation is conducted in two manners. The first one uses the experimental data provided by Jiang, Bliss and Schulz (1995), and the second uses a relatively simple geometry that presents a good experimental database concerning the airflow and that regards similarities with the physics presented by the PWT airflow. That relatively simple geometry is the U-bend presented by Benson *et al.* (2020), its isometric view and dimensions are shown in Figure 6, respectively. These authors present experimental data concerning the three components of the velocity (i.e. u, v, and w) distributed through the domain obtained via magnetic resonance velocimetry.

One of the challenges to simulate the flow inside the PWT is to correctly predict the airflow after the inlet curve, specifically the boundary layer separation. In this way, the simulation of the airflow inside the U-bend geometry enables a good evaluation of the calculations provided by two different turbulent models, the $Standard\ \kappa-\varepsilon$ and the $\kappa-\omega\ SST$. It is important to note that the Reynolds number of both flows presents values of the same order of magnitude, $1,5.10^4$ for the U-bend and $1,9.10^4$ for the PWT.

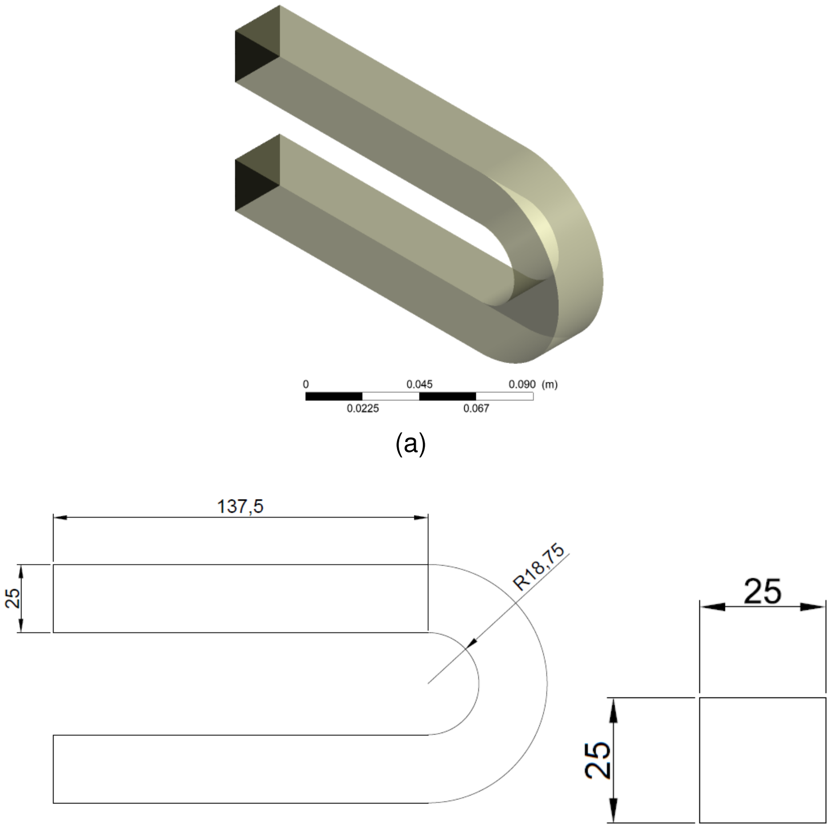

(a)

(b) (c)

Figure 6 – U-Bend geometry used in the present work: (a) Isometric view; (b) Longitudinal dimensions $[mm]$ and (c) Transversal dimensions $[mm]$.

4.3.2 Portable wind tunnel configurations

Two different PWT configurations are tested in the present work. The PWT configuration presented by Jiang, Bliss and Schulz (1995) is used to validate the numerical simulations as it is the only PWT configuration that has experimental data concerning the airflow presented in the literature. Then, to perform the airflow and mass transfer analysis, another configuration based on the Jiang, Bliss and Schulz (1995) design and containing the modified outlet duct presented by Wang, Jiang and Kaye (2001), namely the UFES-PWT, is used.

The PWT built based on the design presented by Jiang, Bliss and Schulz (1995) is shown in Figure 7-a . The airflow enters the inlet duct and then to the expansion section. The idea of these two parts is to establish a stable and reproducible flow in the region close to the emitting surface, i.e. the main section. After the main section, the flow now containing the odorous compound goes to the contraction section which has the objective to improve the mixture between the clean air and the odorous compounds. Finally, it flows to the mixture chamber to be sampled. The shape of the mixture chamber was designed to avoid interferences of compounds coming from outside of the device (JIANG; BLISS; SCHULZ, 1995).

The difference between this PWT (first configuration) and the UFES-PWT (second configuration) is in the outlet section as can be seen in Figure 7. Studying the gas recovery efficiency in wind tunnel systems, using carbon monoxide as a tracer gas, Wang, Jiang and Kaye (2001) showed that the PWT presented as the first configuration showed low recovery rates, in the order of 42%. By analyzing the aerodynamic character of air movement and the compound transportation inside the apparatus, the poor recoveries appeared to occur as a result of an uneven mixing at the sample collection point, and thus, the presence of the modified outlet should help to improve the mixing at the outlet. The new outlet configuration showed a recovery rate of an average 90% (WANG; JIANG; KAYE, 2001).

The isometric views and dimensions of the different PWT configurations to be used in the present work are shown in Figures 7 and 8, respectively. Its main section has 250 mm in height, 800 mm in length, and 400 mm in width.

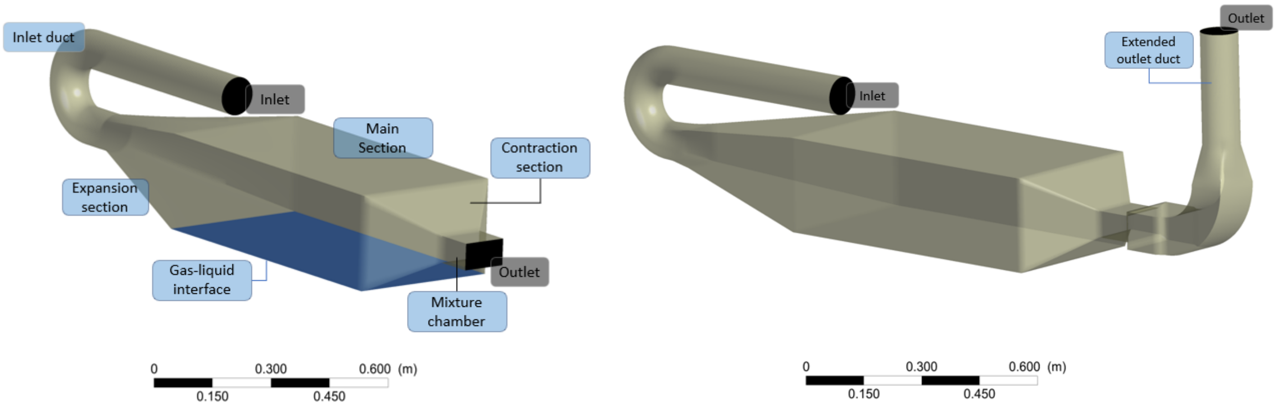
Inlet duct
Inlet
Main Section
Contraction section
Expansion section
Gas-liquid interface
Outlet
Mixture chamber
0
0.300
0.600 (m)
0.150
0.450
Outlet
Extended outlet duct
Inlet
0
0.300
0.600 (m)
0.150
0.450

(a) (b)

Figure 7 – Isometric view of the different PWT configurations to be used in the present work: a)Jiang, Bliss and Schulz (1995) geometry; (b) UFES-PWT.

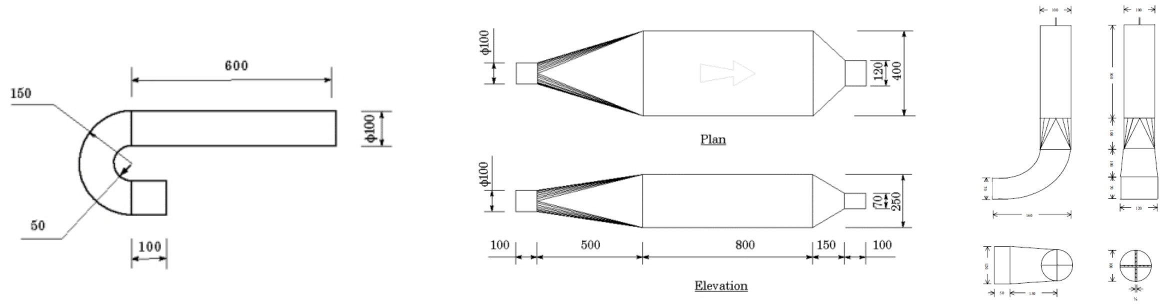
600
150
50
100
ϕ100
ϕ100
120
400
Plan
ϕ100
70
250
100
500
800
150
100
Elevation

(a) (b) (c)

Figure 8 – Dimensions (in mm) of the PWT used to be used in the present work: (a) Extension inlet duct; (b) Device in it self; (c) Modified outlet.

4.4 BOUNDARY CONDITIONS

4.4.1 U-bend

The boundary conditions used in the U-bend simulations is presented for two different geometry shapes (squared and circular) and two different used turbulence models ($\kappa-\omega\ SST$ and $Standard\ \kappa-\varepsilon$) followed by the boundary conditions applied to its precursor domain.

In the U-bend geometry simulations, a fully developed velocity profile with an average value of $0.6\ m/s$ was set at the inlet. This velocity profile was experimentally obtained using the magnetic resonance velocimetry (MRV) technique, the data is presented by Benson *et al.* (2020). Figure 9 shows the velocity contour used as inlet input data and also the velocity profile plotted at the longitudinal center-line of the inlet plane, normalized in y by the length or radius of the channel (H), equal to $25\,mm$, and in u by the average inlet velocity (U_b), equal to $0.6\,m/s$. The no-slip condition was used on the walls. At the outlet, the atmospheric pressure condition was set. All boundary conditions are summarized in Tables 10 and 11, for the $\kappa-\omega\,SST$ and $Standard\kappa-\varepsilon$ model, respectively.

The profiles for the turbulence variables (κ, ω and ε) in the inlet were obtained using a precursor domain, the contours and the profiles, plotted at the longitudinal center-line of the inlet plane, are shown in the Figures 11 and 10, for the $\kappa-\omega\,SST$ and $Standard\kappa-\varepsilon$ model, respectively.

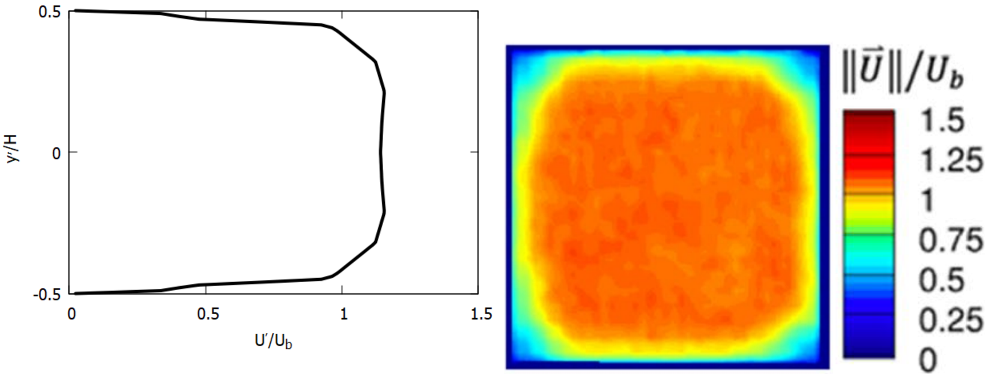

(a) (b)

Figure 9 – Input data used to perform the U-bend geometry simulations, obtained experimentally by Benson *et al.* (2020), via the MRV technique: (a) Velocity contour; (b) Velocity profile, plotted at the longitudinal center-line of the inlet plane, normalized in y by the length or radius of the channel (H), equal to $25\,mm$, and in u by the average inlet velocity (U_b), equal to $0.6\,m/s$.

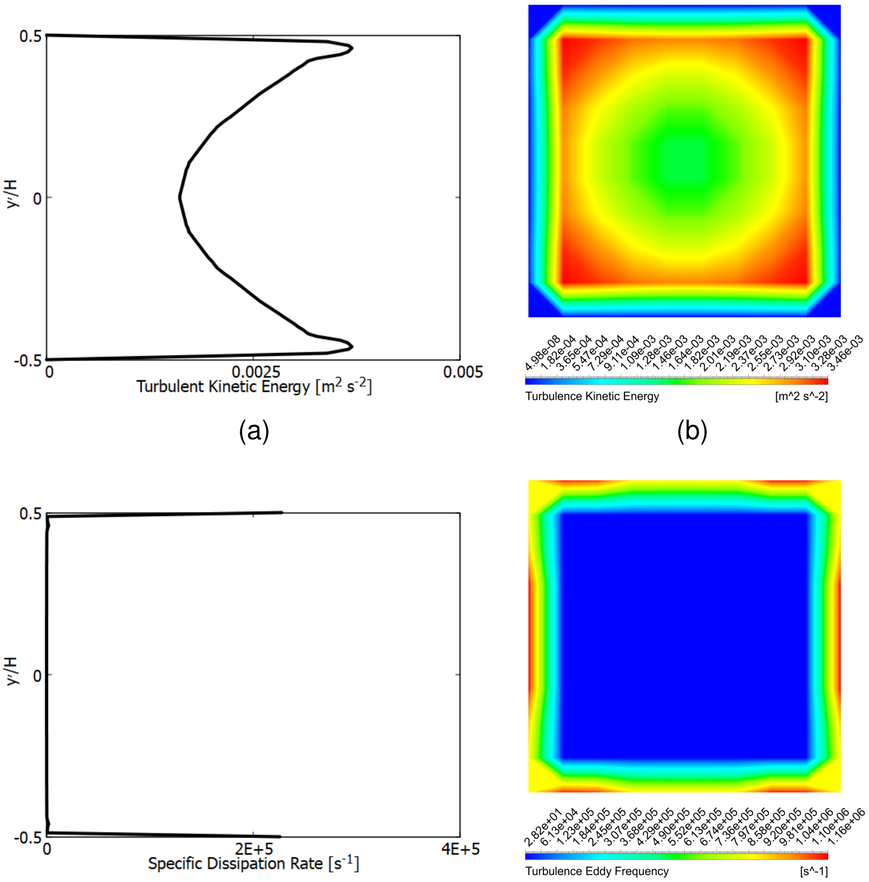

(a) (b)

(c) (d)

Figure 10 – Contours and profiles, plotted at the longitudinal center-line of the inlet plane, obtained via precursor domain and used as input data to the U-bend geometry simulations using the $\kappa - \omega\ SST$ model: (a) Turbulent kinetic energy - profile; (b) Turbulent kinetic energy - contour; (c) Specific dissipation rate - profile; and (d) Specific dissipation rate - contour.

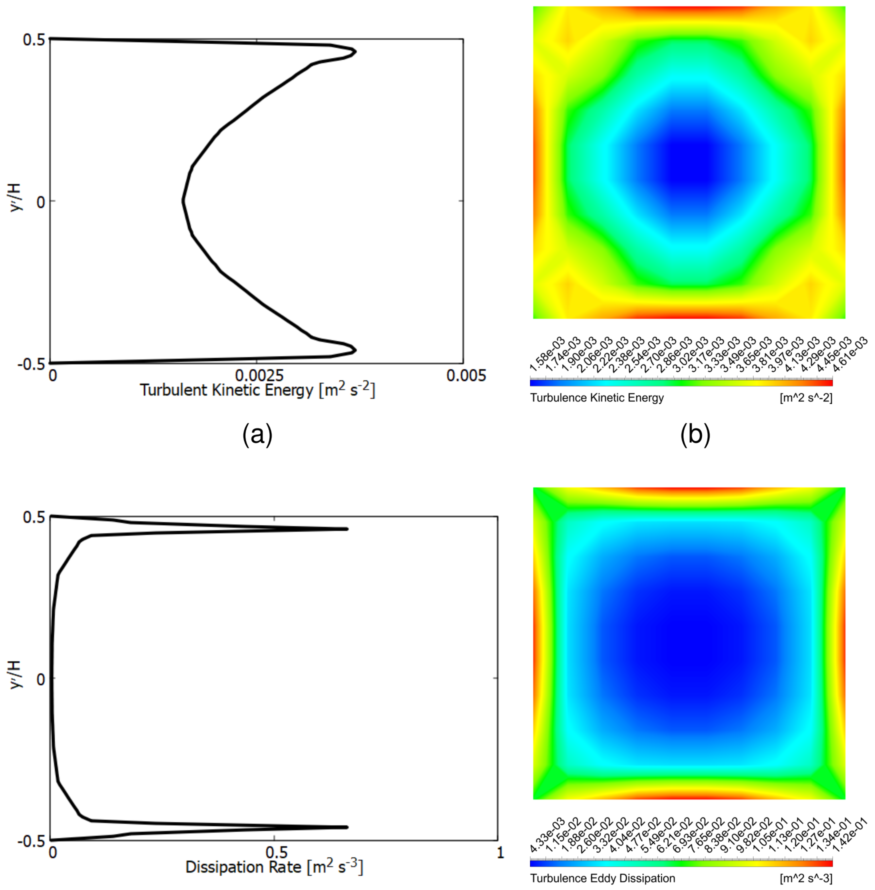

(a) (b)

(c) (d)

Figure 11 – Contours and profiles, plotted at the longitudinal center-line of the inlet plane, obtained via precursor domain and used as input data to the U-bend geometry simulations using the $Standard \kappa - \varepsilon$ model: (a) Turbulent kinetic energy - profile; (b) Turbulent kinetic energy - contour; (c) Dissipation rate - profile; and (d) Dissipation rate - contour.

Location	Boundary conditions Momentum	Boundary conditions TKE	Boundary conditions Specific Dissipation Rate
Inlet	$\overline{U} = 0,6\, m\, s^{-1}$	$\overline{TKE} = 0,0027\, m^2\, s^2$	$\overline{\varpi} = 237,55\, s^{-1}$
Outlet	$P = 0\, Pa$	$\partial\kappa/\partial x_3 = 0$	$\partial\omega/\partial x_3 = 0$
Wind tunnel walls	$u_1 = u_2 = u_3 = 0$	$\kappa = 0$	$\omega = 0$
Liquid-gas interface	$u_1 = u_2 = u_3 = 0$	$\kappa = 0$	$\omega = 0$

Table 10 – Boundary conditions used for the U-bend geometry simulations using the $\kappa - \omega\, SST$ turbulence model.

Location	Boundary conditions Momentum	Boundary conditions TKE	Boundary conditions Dissipation Rate
Inlet	$\overline{U} = 0,6\, m\, s^{-1}$	$\overline{TKE} = 0.0031\, m^2\, s^2$	$\overline{\varepsilon} = 0.054\, m^2\, s^{-3}$
Outlet	$P = 0\, Pa$	$\partial\kappa/\partial x_3 = 0$	$\partial\varepsilon/\partial x_3 = 0$
Wind tunnel walls	$u_1 = u_2 = u_3 = 0$	$\kappa = 0$	$\varepsilon = 0$
Liquid-gas interface	$u_1 = u_2 = u_3 = 0$	$\kappa = 0$	$\varepsilon = 0$

Table 11 – Boundary conditions used for the U-bend geometry simulations using the $Standard \kappa - \varepsilon$ turbulence model.

4.4.2 Portable Wind Tunnel

In the PWT simulations, the boundary conditions are presented according to the different geometries and followed by the boundary conditions applied to the precursor domain.

For the validation step, using the geometry shown in Figure 7-a (Jiang, Bliss and Schulz (1995)), at the inlet a full developed profile with an average value of $2,82\, m/s$ was set in order to achieve $0,3\, m/s$ as a mean velocity over the cross-section area in the main section of the tunnel. The no-slip condition was used on the walls and at the outlet, and the atmospheric pressure condition. To the turbulence inlet parameters, i.e. the turbulent kinetic energy (κ) and its specific dissipation rate (ω), full developed profiles of both variables were set at the inlet. The average value of κ were equal to $0,056\, m^2\, s^{-2}$ and of ω were equal to $1530,28\, s^{-1}$. In the liquid-gas interface, a fixed H_2S mass fraction of $1.45E-06$ was used. More details of the fixed mass fraction methodology and its calculations are provided in Section 4.4.3.

All the boundary conditions used in the validation step are summarized in Table 12. The fully developed profiles of velocity magnitude, turbulent kinetic energy, and its specific dissipation, obtained via precursor domain, are shown in Figure 12.

Location	Boundary conditions Momentum	Boundary conditions TKE	Boundary conditions Specific Dissipation	Boundary conditions Concentration
Inlet	$\overline{U} = 2,82\,m\,s^{-1}$	$\overline{TKE} = 0,056\,m^2\,s^{-2}$	$\overline{\omega}1530,28\,s^{-1}$	$C_{onc} = 0$
Outlet	$P = 0\,Pa$	$\partial\kappa/\partial x_3 = 0$	$\partial\omega/\partial x_3 = 0$	-
Wind tunnel walls	$u_1 = u_2 = u_3 = 0$	$\kappa = 0$	$\omega = 0$	$C_{onc} = 0$
Liquid-gas interface	$u_1 = u_2 = u_3 = 0$	$\kappa = 0$	$\omega = 0$	Fixed H_2S Mass Fraction equal to $1.45e^{-06}$

Table 12 – Jiang, Bliss and Schulz (1995) boundary conditions.

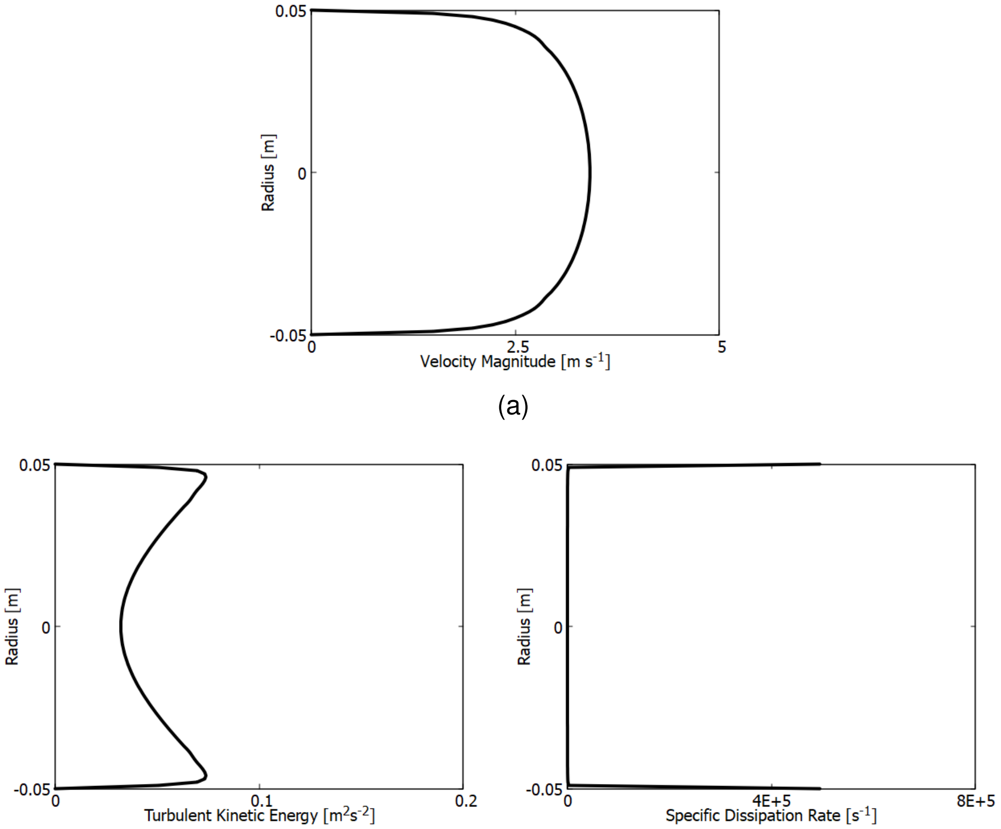

(a)

(b) (c)

Figure 12 – Profiles obtained via precursor domain and used as input data to the simulations using the Jiang, Bliss and Schulz (1995) geometry: (a) Velocity magnitude; (b) Turbulent kinetic energy and (b) Specific dissipation rate.

For the UFES-PWT (presented in the Figure 7-b), at the inlet, a full developed velocity profile with average values of $1,27$; $2,55$ and $3,82\,m\,s^{-1}$ were set. The no-slip condition was used on the walls and at the outlet, and the atmospheric pressure condition. To the turbulence inlet parameters, i.e. the turbulent kinetic energy (κ) and its specific dissipation rate (ω), full developed profiles of both variables were set at the inlet. In the liquid-gas interface, it was used two different boundary conditions and two different chemical compounds. For H_2S, a fixed mass fraction and a fixed mass flux were used. While for acetic acid, a fixed mass flux was used. More details of these two different boundary conditions are provided in Section 4.4.3.

All the boundary conditions are summarized in Table 13. The full developed profiles of velocity magnitude, turbulent kinetic energy and specific dissipation rate are shown in Figures 13, 14 and 15, for the inlet velocities of $3,82\,m\,s^{-1}$, $2,55\,m\,s^{-1}$ and $1,27\,m\,s^{-1}$, respectively.

Location	Boundary conditions Momentum	Boundary conditions TKE	Boundary conditions Specific Dissipation	Boundary conditions Concentration
Inlet	$\overline{U} = 1,27;\ 2,55\ \&\ 3,82\,m\,s^{-1}$	$\overline{TKE}$	$\overline{\omega}$	$C_{onc} = 0$
Outlet	$P = 0\,Pa$	$\partial\kappa/\partial x_3 = 0$	$\partial\omega/\partial x_3 = 0$	-
Wind tunnel walls	$u_1 = u_2 = u_3 = 0$	$\kappa = 0$	$\omega = 0$	$C_{onc} = 0$
Liquid-gas interface	$u_1 = u_2 = u_3 = 0$	$\kappa = 0$	$\omega = 0$	Mass flux (J_{H_2S}) or a Fixed concentration (C_{onc})

Table 13 – UFES PWT boundary conditions.

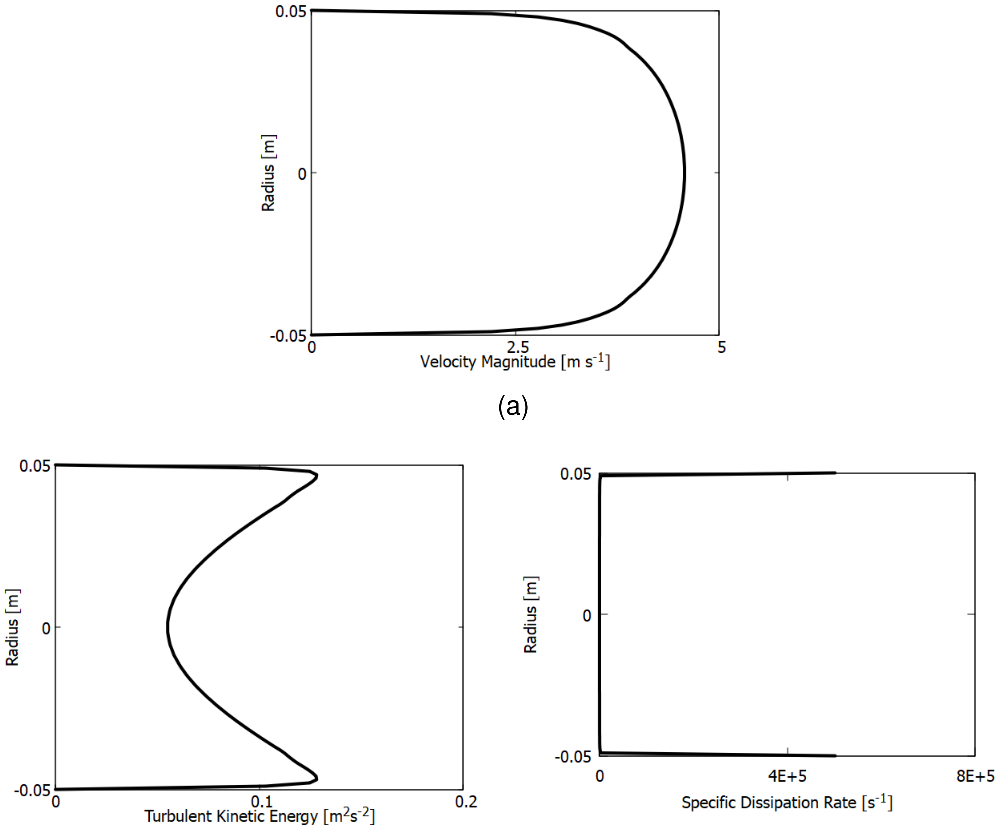

(a)

(b)

(c)

Figure 13 – Inlet profiles obtained via precursor domain and used as input data to the simulations with the UFES-PWT geometry for the inlet velocity of $3,82\,m\,s^{-1}$: (a) Velocity magnitude; (b) Turbulent kinetic energy and (b) Specific dissipation rate.

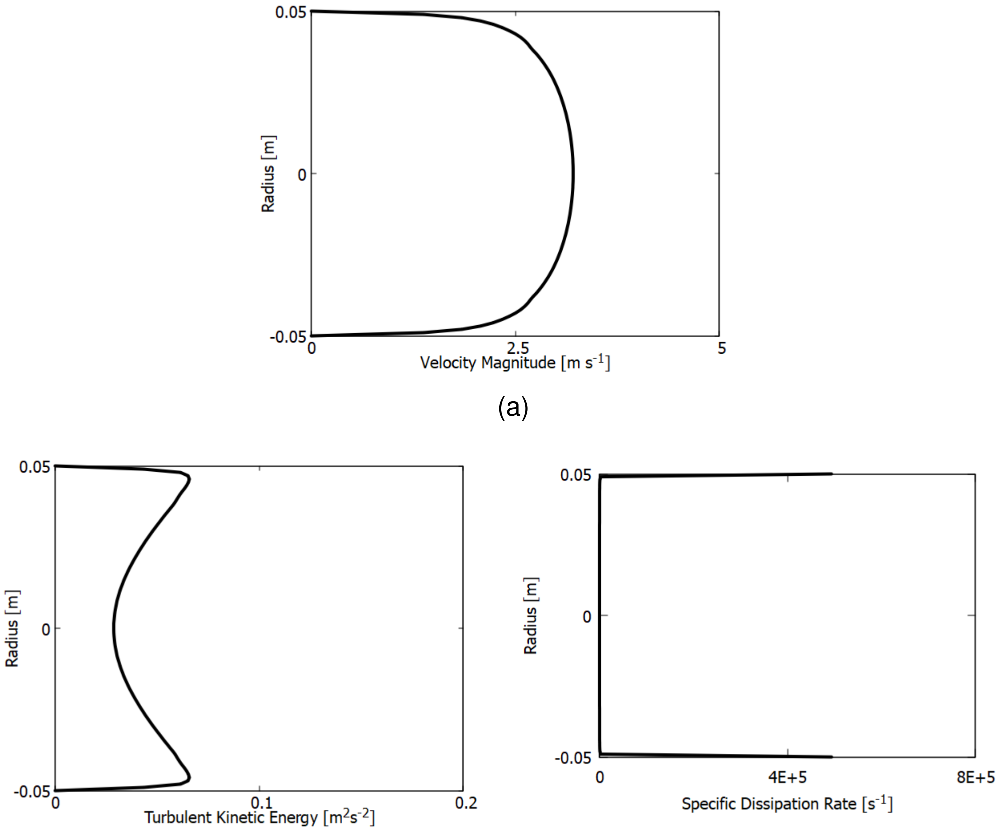

(a)

(b)

(c)

Figure 14 – Inlet profiles obtained via precursor domain and used as input data to the simulations using the UFES-PWT for the inlet velocity of $2,55\,m\,s^{-1}$: (a) Velocity magnitude; (b) Turbulent kinetic energy and (b) Specific dissipation rate.

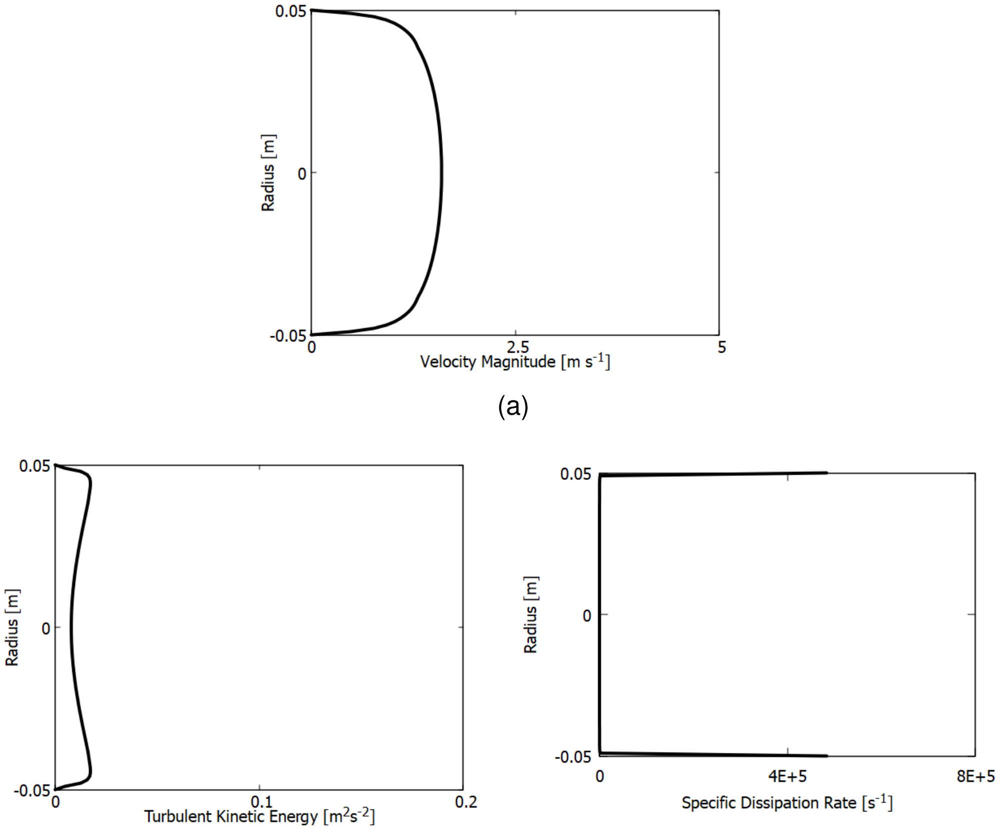

(a)

(b)

(c)

Figure 15 – Inlet profiles obtained via precursor domain and used as input data to the simulations using the UFES-PWT for the inlet velocity of $1,27\,m\,s^{-1}$: (a) Velocity magnitude; (b) Turbulent kinetic energy and (b) Specific dissipation rate.

4.4.3 Interface boundary conditions

Two odorant compounds were chosen to study the mass transfer phenomena inside the apparatus, with different characteristics concerning their volatilization process. As explained in item 3.1, the emission of an odorant compound can be dominated by the conditions of the gas phase, liquid phase, or both phases. In the present work, hydrogen sulfide (H_2S) was used to represent a compound that has its volatilization process dominated by the liquid phase, and acetic acid (CH_3COOH) to represent a compound dominated by the gas phase.

The interface boundary conditions were set by using two different approaches, a prescribed concentration or a constant mass flux of the odorant compound. Both boundary conditions were set at the open bottom of the PWT, represented by the gas-liquid interface shown in Figure 7.

The prescribed concentration was calculated by assuming a well-mixed gas phase inside the apparatus. So that the concentration of the odorant compound in the outlet section of the PWT is all due to its emission in the gas-liquid interface, i.e. the air enters the apparatus clean and recovery rate is 100%. The mass flux of the odorant compound in the outlet section of the PWT is given by $Q\,x\,C_g$, in which Q is the air flow rate $[m^3/s]$. In the gas-liquid interface, the emission rate of the odorant compound is given by the product of the mass flux through the interface and its respective area ($A\ [m^2]$). In this way, the mass balance of the odorant compound inside the PWT can be expressed by Equation 4.17.

$$Q\,x\,C_g = J\,x\,A \tag{4.17}$$

The mass flux can be written as a function of the liquid-phase overall mass transfer coefficient (K_L) by replacing the Equation 3.7 in Equation 4.17, Equation 4.18 is obtained.

$$Q\,x\,C_g = \left[K_L\left(C_L - \frac{C_g}{K_H}\right)\right]\,x\,A \tag{4.18}$$

Re-writing Equation 4.19 with C_g in evidence, equation 3.17 is obtained.

$$C_g = \frac{K_L C_L A}{\left(Q + \frac{K_L A}{K_H}\right)} \tag{4.19}$$

As presented by the two-resistance models, Section 3.1, the mass flux that cross the gas-liquid interface is the same that cross the liquid film, and thus, can be equalized as shown in Equation 4.20.

$$\left[K_L\left(C_L - \frac{C_g}{K_H}\right)\right]\,x\,A = k_L(C_L - C_{L,i}) \tag{4.20}$$

For H_2S, volatilization is strongly dependent on the liquid phase conditions, i.e. its resistance to the global process of mass transfer is mainly due to the liquid film resistance. This can be seen through its Henry constant (SANTOS *et al.*, 2012; HUDSON; AYOKO, 2008a). Thus, its overall mass transfer coefficient can be approximated as the liquid-phase mass transfer coefficient ($K_L \approx k_L$) citesantos2012,andreao2019. In this sense, by rewriting Equation 4.20, Equation 4.21 is obtained.

$$C_g = C_{L,i} K_H \tag{4.21}$$

Inserting the Henry Law (Equation 3.5) into Equation 4.21, it is concluded that C_g can be aproximated as $C_{g,i}$, as shown in Equation 4.22. In this way the Equation 4.19 can be rewrite as the Equation 4.23.

$$C_g = C_{L,i} K_H = C_{L,i} \frac{C_{g,i}}{C_{L,i}} \therefore C_g = C_{g,i} \tag{4.22}$$

$$C_{g,i} = \frac{K_L C_L A}{\left(Q + \frac{K_L A}{K_H}\right)} \tag{4.23}$$

The H_2S concentration at the gas interface was calculated through the Equation 4.23. Being the Henry constant (K_H) equal to 0.36, the liquid phase H_2S concentration (C_L) equal to $5\ mg\ L^{-1}$, the area interface (A) equal to $0.32\ m^2$, the overall mass transfer coefficient (K_L) equal to $2.46E-05 ms^{-1}$ and varying the air-flow rate according to the inlet air-flow rate ($Q = 0.009975,\ 0.020028\ or\ 0.03 m^3/s$).

The referred K_L data was experimentally obtained by Siqueira (2022) using the UFES-PWT, with the liquid phase H_2S concentration (C_L) equal to $5\ mg\ L^{-1}$. Siqueira (2022) experiments showed that the K_L values didn't change for the tested inlet air-flow rates, the same as the ones used here. Santos *et al.* (2012) presented similar findings.

The data used as input into the simulations is the mass fraction, therefore the concentrations calculated using Equation 4.23 were divided by the H_2S specific mass to obtain it.

The H_2S mass flux at the interface for each inlet air-flow rate was calculated by putting J in evidence in Equation 4.17, generating Equation 4.24.

$$J = \frac{Q C_{g,i}}{A} \tag{4.24}$$

For the acetic acid, a different methodology was used to obtain its gas-phase concentration to calculate the interface boundary conditions i.e. a prescribed concentration. Unlike the H_2S no work that evaluates the acetic acid mass transfer coefficients (k_l or k_g) for the PWT was found in the literature. Recent works have applied empirical models to calculate mass transfer coefficients to be used as input data in numerical simulations, an example is Andreão *et al.* (2019) that applied the models of Smith, Bomberger and Haynes (1980) and Dilling (1977) to calculate mass transfer coefficients to study the mass transfer inside a dynamic flux chamber. A similar work was carried out by Andreão and Feroni (2021). However, these models were not developed to be applied to a mass flow in a confined space as happens inside of the apparatus commonly used by the direct methods e.g. dynamic flux chambers or portable wind tunnels.

In this way, it was used the same acetic acid concentration that was used by Prata Jr *et al.* (2018) for the liquid phase, i.e. $50\,mL\,L^{-1}$, and thus, through Equation 3.5 the interface gas-phase concentration is obtained:

$$C_{g,i} = K_H C_{L,i} = 3,79E-04\,kg\,m^{-3}$$

in where the dimensionless Henry's law constant (K_H) is equal to $7,19E-06$. It should be noted that for a gas-phase controlled compound, as it is the acetic acid, $C_{L,i} = C_L$.

The mass flux for acetic acid was calculated through the same methodology as for the H_2S, that is, by using the Equation 4.24 for each inlet air-flow rate.

All boundary conditions for both odorant compounds are summarized in Table 14.

Spatial average inlet velocity $m\,s{-}1]$	Inlet air-flow rate $[m^3\,s{-}1]$	H_2S		$Acetic\ acid$
		Prescribed Concentration $[kg\,m^{-3}]$	Mass Flux $[kg\,m^{-2}\,s^{-1}]$	Prescribed Concentration $[kg\,m^{-3}]$
3.82	0.03000	$1.31E-06$	$1.23010E-07$	$3,79E-04$
2.82	0.02215	$1.78E-06$	–	–
2.55	0.02003	$1.97E-06$	$1.22965E-07$	$3,79E-04$
1.27	0.00998	$3.95E-06$	$1.22831E-07$	$3,79E-04$

Table 14 – Interface boundary conditions used for the PWT simulations.

It should be noted that the inlet velocity corresponding to $2.82m\,s^{-1}$ was used in the validation step.

4.5 NUMERICAL SOLUTION OF THE GOVERNING EQUATIONS

To solve the transport equations shown along Sections 4.1 and 4.2, the software *ANSYS Fluent* version 19.0 was used. This software is based on the finite volume method (FLUENT, 2005), which is used mainly for the numerical solution of problems in fluid mechanics (SCHÄFER, 2006).

Schäfer (2006) summarizes the finite volume method into the following steps:

1. Decomposition of the problem domain into control volumes - subsection 4.6;
2. Formulation of integral balance equations for each control volume;
3. Approximation of integrals by numerical integration;
4. Approximation of function values and derivatives by interpolation of nodal values;
5. Assemblage and solution of discrete algebraic system.

The discretization leads to a linear system of algebraic equations solved through incomplete LU decomposition together with the Multigrid method in order to accelerate the solution (FLUENT, 2005). In general, the Multigrid technique involves the solution of preliminary interactions in finer meshes followed by posterior interactions in progressively coarse meshes. In this way, the results obtained in the coarse mesh are transferred to the finer original mesh (WESSELING, 1993; FLUENT, 2005; HACKBUSCH, 2013).

The second-order upwind scheme is used to interpolate the convective terms of the equations of momentum, turbulent kinetic energy, and its specific dissipation rate and mass conservation of the chemical species. The gradients are solved using the least square cell-based method and the pressure terms using a second-order approach. The transient formulation was solved using a first-order implicit scheme, that method is recommended by the *ANSYS Fluent* User's Guide for most of the problems (FLUENT *et al.*, 2011). I.e. it presents a lower computational cost when compared to the second-order version and presents reliable results. All the used schemes are shown in Table 15. The pressure-velocity coupling is solved using the SIMPLE scheme.

Pressure-velocity coupling	SIMPLE scheme
Gradient	Least square cell based
Pressure	Second order approach
Momentum	Second order upwind
Turbulent kinetic energy	Second order upwind
Specific dissipation rate	Second order upwind
Concentration	Second order upwind
Transient formulation	First order implicit

Table 15 – Solution Methods.

A convergence problem was faced when simulating the airflow inside the PWT using second-order schemes. It seems to happen due to the airflow complexity, (i.e. $3D$ and with several re-circulation zones, for instance), which is caused by the PWT geometry, especially by the presence of curves, walls, expansions, and contraction. On the other hand, the results when using first-order schemes although producing a good convergence weren't showing great accuracy when compared to the experimental results, presented by Jiang, Bliss and Schulz (1995). In summary, although the results obtained when using the second-order schemes presents great accuracy, it also leads to convergence problems. For the first-order schemes was the opposite, with great convergence and a lack of accuracy. In such cases, the *ANSYS Fluent* User's Guide recommends the use of a discretization blending factor (FLUENT *et al.*, 2011).

For each cell face, this methodology obtains a blending of the flux from a low order scheme ($\varphi_{1st\ order}$) and a more accurate higher-order scheme ($\varphi_{2nd\ order}$). As shown in Equation x, the use of a blending factor (B) of 0 reduces the gradient reconstruction to a low order discretization scheme and a value of 1 recovers the high order scheme (PAPADAKIS; BERGELES, 1995). The *ANSYS Fluent* User's Guide recommends the of a blending factor typically equal to 0.75 or 0.5 (FLUENT *et al.*, 2011). For the present work, the use of a blending factor equal to 0.75 led to the convergence. The low-order scheme was first-order and the high-order scheme, a second-order.

$$\varphi = \varphi_{1st\ order} - B(\varphi_{2nd\ order} - \varphi_{1st\ order}) \tag{4.25}$$

To determine the time step size, it was used the adaptive time-stepping technique. In where there is no specification of a singular time step, but an interval (10^{-6} to 10^{-2}) and the time step is automatically determined based on the truncation error associated with the integration scheme. If the truncation error is smaller than a specified tolerance the time step is increased and on the other side, if the truncation error is higher than the tolerance the time step is decreased. It used the default truncation tolerance error that is equal to 0.01.

The convergence criteria are the root mean square of the residual of each equation, which should be lower than 10^{-4}. This value is considered reasonable for many applications (FLUENT, 2005).

The time of simulation was calculated based on a characteristic length (L^* $[m]$) and a characteristic velocity (u^* $[m\,s^{-1}]$). By means of these parameters a characteristic time (t^* $[s]$) was calculated using the Equation 4.26.

$$t^* = \frac{L^*}{u^*} \tag{4.26}$$

where L^* is equal to the PWT main section height ($0.25\,m$) and u^* is an average velocity in the main section, equal to $0,2\,m\,s^{-1}$. Therefore, the characteristic time was equal to $1,25\,s$.

For the air flow, to guarantee its development it was calculated $200t^*$ as a stabilization time and more $200t^*$ to collect data for time statistics. Once the average air flow was calculated, it was performed the calculations including mass transfer for $120t^*$.

		Simulation time
Air-flow	Stabilization time	$200t^*$ $(250\,s)$
	Data sampling for time statistics	$200t^*$
Mass transfer		$120t^*$ $(125\,s)$

Table 16 – Boundary conditions

It should be noted that all studied variables have achieved constant or periodic values in much less time than the simulated.

4.6 DISCRETIZATION OF THE COMPUTATIONAL DOMAIN

The domains shown along the section 4.3 were all discretized into structured meshes. In the regions where occurs the larger gradients, i.e. the walls and the gas-liquid interface (bottom of the main section for the pwt), the domains were discretized using finer elements with the height varying according to the turbulence model. This procedure is important to capture the intense gradients close to the wall and to enable the turbulence model to capture the characteristics of the flow as it was designed to work. The Figures 16, 17, 18 and 19 shows the meshes for all the studied domain.

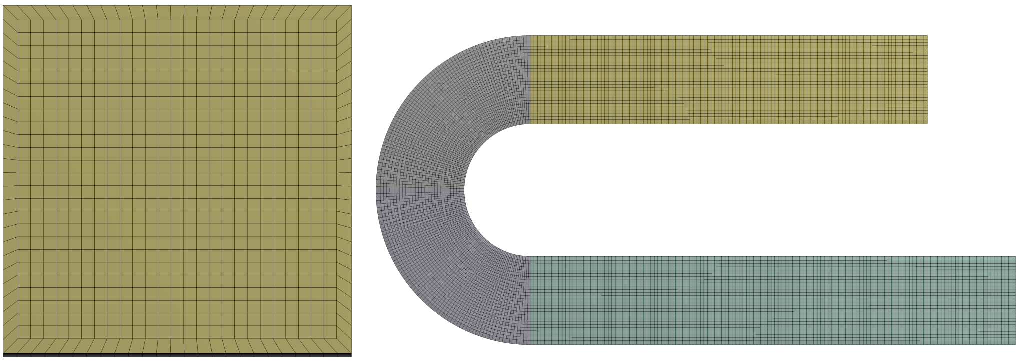
(a) (b)

Figure 16 – U-bend discretized domain for the simulations with the *Standard* $\kappa-\varepsilon$ model - 280.575 elements: (a) Front vision and (b) Lateral vision.

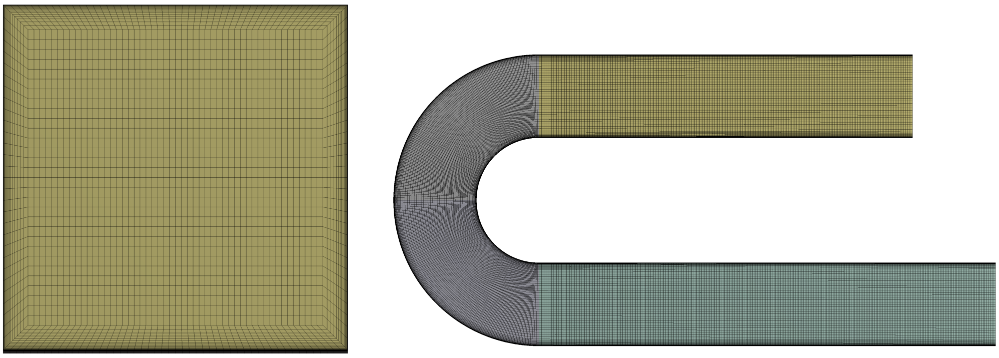
(a) (b)

Figure 17 – U-bend discretized domain for the simulations with the $\kappa-\omega$ *SST* model - 3.381.360 elements: (a) Front vision and (b) Lateral vision.

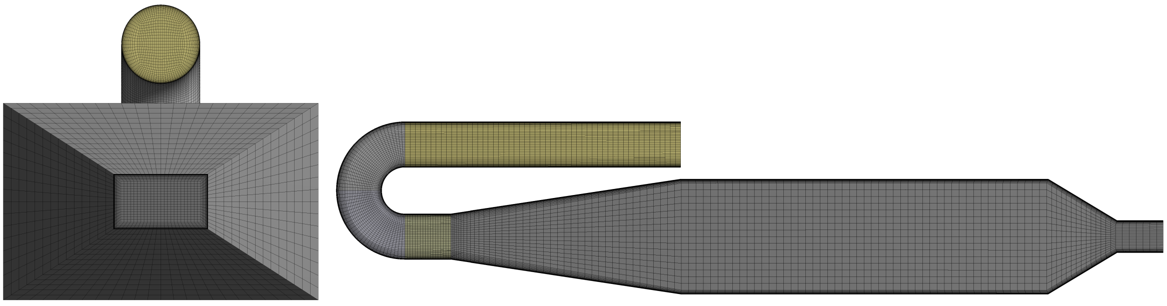
(a) (b)

Figure 18 – PWT designed by Jiang, Bliss and Schulz (1995) discretized domain - 434.112 elements: (a) Rear view and (b) Lateral vision.

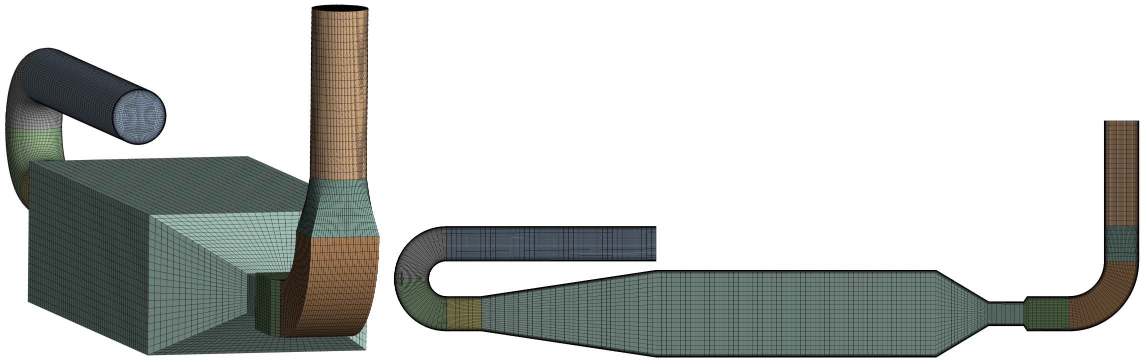
(a) (b)

Figure 19 – UFES-PWT geometry discretized domain - 588.924 elements: (a) Rear view and (b) Lateral vision.

The $Standard\ \kappa-\varepsilon$ model uses wall functions to describe the flow in the near-wall region inside the viscous sub-layer and the $\kappa-\omega\ SST$ not. Therefore, the first requires a more coarse element near the wall, and the second, a more refined element to capture the flow details in this region. A way of controlling the accuracy of the results in the near-wall regions is by monitoring the y^+ value, that is the non-dimensional distance from the wall based on the influence of the shear stress, as shown in Equation 4.27.

$$y^+ = \frac{u^* d}{\upsilon} \tag{4.27}$$

where u^* is the friction velocity $(m\,s^{-1})$ and d is the perpendicular distance from the first nodal point to the wall (m). The value of y^+ should be within a certain range. For the case of the $\kappa-\omega\ SST$, Cao and Meyers (2013) believes that a value under 5 should resolve most of the cases, and Pope (2001) also points to 5 as a theoretical value to resolve the flow in the near-wall region i.e. in the viscous sub-layer. For the $Standard\ \kappa - \varepsilon$ model the Fluent (2005) recommends the use of a $y^+ < 11.25$ for the scalable wall function.

To obey this value the first element height was set according to the geometry and turbulence model. For the simulations using the PWT it was used the $\kappa - \omega\ SST$ model, in this case, the first element height was equal to $1.10^{-4}\ m$. To the simulations using U-Bend it was used both the $\kappa - \omega\ SST$ and the $Standard\ \kappa - \varepsilon$ models, in this cases the first element height was equal to $1,5.10^{-3}\ m$ and $2x10^{-5}\ m$, respectively. The Table 17 summarizes all the first elements height to its respective geometry, turbulence model and y^+ requirement.

Geometry	Turbulence model	y^+ requirement	Average inlet velocity	First element height
Benson *et al.* (2020) U-bend geometry	$Standard\ \kappa - \varepsilon$	$y^+ < 11.25$	$\overline{U} = 0,6\, m\, s^{-1}$	$1,5.10^{-3}\, m$
Benson *et al.* (2020) U-bend geometry	$\kappa - \omega\ SST$	$y^+ < 5$	$\overline{U} = 0,6\, m\, s^{-1}$	$2.10^{-5}\, m$
Jiang, Bliss and Schulz (1995) PWT	$\kappa - \omega\ SST$	$y^+ < 5$	$\overline{U} = 2,82\, m\, s^{-1}$	$1.10^{-4}\, m$
UFES PWT			$\overline{U} = 3,82\, m\, s^{-1}$	
			$\overline{U} = 2,55\, m\, s^{-1}$	
			$\overline{U} = 1,55\, m\, s^{-1}$	

Table 17 – Mesh first element height according to its respective geometry and turbulence model.

Because of the friction velocity (u^*), the value of y^+ is straightly dependent on the inlet velocity. Therefore, for the simulations using the PWT geometries the value of $1.10^{-4}\ m$ was valid for the worst-case scenario (highest tested velocity), i.e., for the case in which the inlet velocity is equal to $3.82\, m\, s^{-1}$ and in consequence was valid for the lower inlet velocities to be simulated (the y^+ requirement (bellow 5) was obtained for all cases).

The viscous sub-layer is a thin region, in direct contact with the wall, that is defined by the absence of turbulent shear stresses. That is because the flow is stationary at the walls and so on, the fluid in this region is dominated by the viscous shear. The Figure 20 shows the near-wall velocity distribution, where the dots are experimental data and the solid line represents the wall function approximation - used in the present work (SANTOS, 2000; VERSTEEG; MALALASEKERA, 2007).

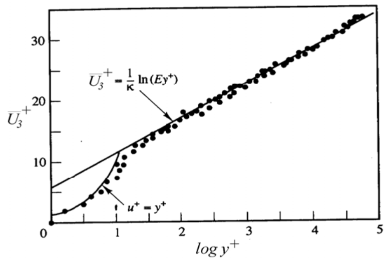

Figure 20 – Distribution of the velocity near the wall, in where the dots are experimental data and the solid line represents the wall function approximation (SANTOS, 2000).

4.7 EXPERIMENTAL VALIDATIONS

To validate the numerical simulations, i.e., to make sure that the model is correctly simulating the flow inside the PWT, comparison with experimental data were performed.

4.7.1 U-bend

The flow inside a U-bend is validated as a complementary validation using the Benson *et al.* (2020) experimental data. The purpose behind the U-bend simulations is to show that a critical part of the PWT configuration, i.e., its curve, is being well simulated. The U-bend configuration used by the author is shown in Figure 6. Although the fluid used in the Benson *et al.* (2020) experiments was water and the fluid used in the PWT experiments is air, the Reynolds number ($Re = {}^{U*L}/_{\nu}$) of both cases is similar and equal to $1.5x10^4$ and $1.9x40^4$, respectively. The experimental data were obtained using magnetic resonance velocimetry.

The velocity profiles were presented by Benson *et al.* (2020) in the four cross-sections presented at the 21-a and 22, being $H = 25\ mm$. Each cross-section were divided into three lines (Figure 21-b), the u component of the velocity were present at the $z'/H = 0$, the v component at the $y'/H = -0.4$ and w component at the $y'/H = -0.3$. The numerical results to be compared with the experimental data were taken following the same methodology.

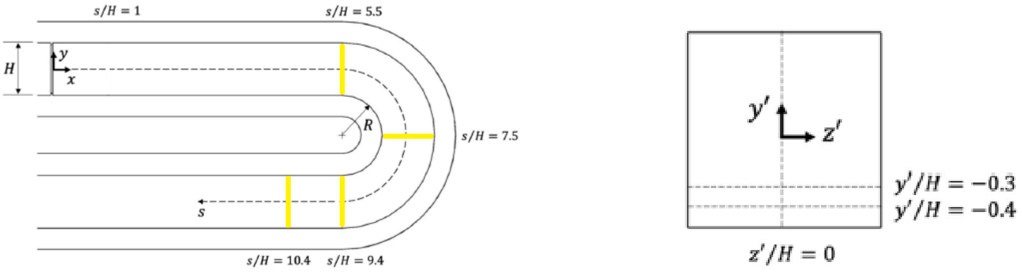

(a) (b)

Figure 21 – Sampling lines cross-section: (a)Lateral view and (b)Frontal view.

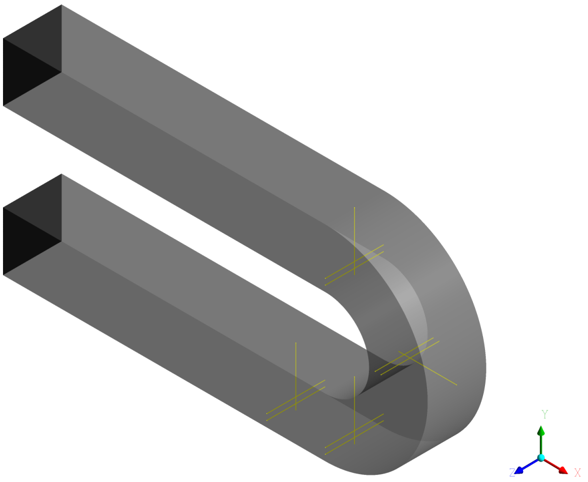

Figure 22 – U-bend sampling lines in the four cross-sections - isometric view.

4.7.2 Portable wind tunnel

The flow inside the PWT is validated using the Jiang, Bliss and Schulz (1995) data.

The PWT geometry used by Jiang, Bliss and Schulz (1995) in their experiments is the same shown in Figure 7-a. The mean velocity used by the authors it is equal to $0,33\,m\,s^{-1}$, this value is presented as an operating velocity through the hood. Although the authors have not elucidated where this value was measured, in the present work this value is assumed to be an average mean velocity through the main section measurement points. Another source of experimental data is the work done by Wu (2007). Although the author has used in general the same PWT geometry as the Jiang, Bliss and Schulz (1995), some specific configurations are not the same, Wu (2007) used a flow conditioner, similar to the one tested by Jiang, Bliss and Schulz (1995), between the expanse and the main section, the inlet velocity used by the author was slightly higher (equal to $3,82\,m\,s^{-1}$) and the general configuration of the PWT inlet duct was different, there is a difference in the placement and configuration of the inlet duct. The geometry used by Wu (2007) is shown in Figure 23. Thus, the data available in the work of Wu (2007) are used only to evaluate the similarities between the general characteristics of the flow and not as validation in itself. Both works (Jiang, Bliss and Schulz (1995) and Wu (2007)) used hot-wire anemometers to measure the velocity inside the PWT main section and followed the same methodology to present the data.

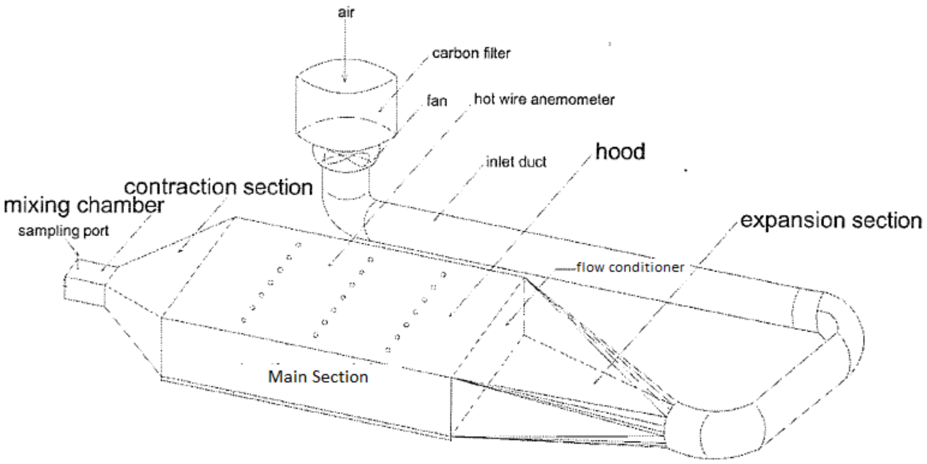
air
carbon filter
fan
hot wire anemometer
inlet duct
hood
contraction section
mixing chamber
sampling port
expansion section
flow conditioner
Main Section

Figure 23 – Isometric view of the PWT configuration used by Wu (2007) (modified from source: Wu (2007)).

The velocity measurements were taken at three different cross-sections ($z = 200$, 400 and $600\,mm$) shown in Figure 24, in where the reference ($z = 0$) it is located at the starting point of the main section. Each cross-section was divided into 40 equally distant points, distant $50\,mm$ from each other (Figure 25). The horizontal velocity profile was calculated by averaging the velocities at 5 different heights for each horizontal level at each position. Following the same methodology the vertical profile was calculated, i.e., by averaging the velocities at 8 different horizontal positions for each vertical level at each position.

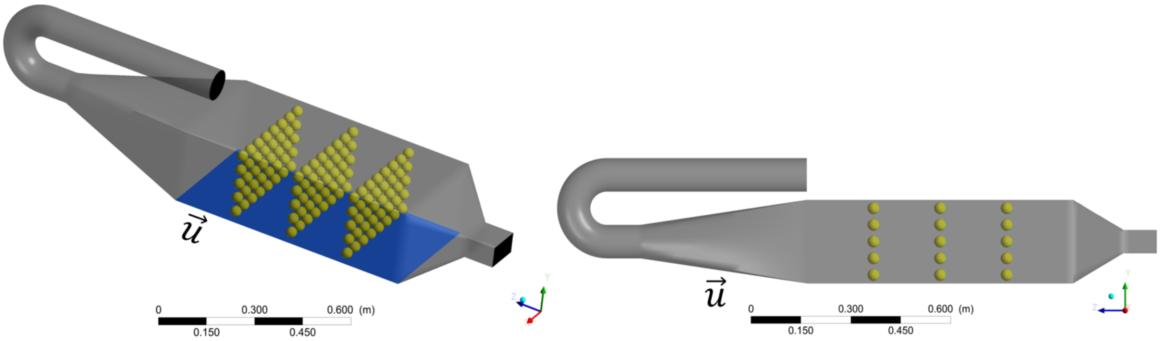
$\vec{u}$
0
0.150
0.300
0.450
0.600 (m)
$\vec{u}$
0
0.150
0.300
0.450
0.600 (m)

(a) (b)

Figure 24 – Sampling points in the three cross-sections: (a)Isometric view and (b) lateral view.

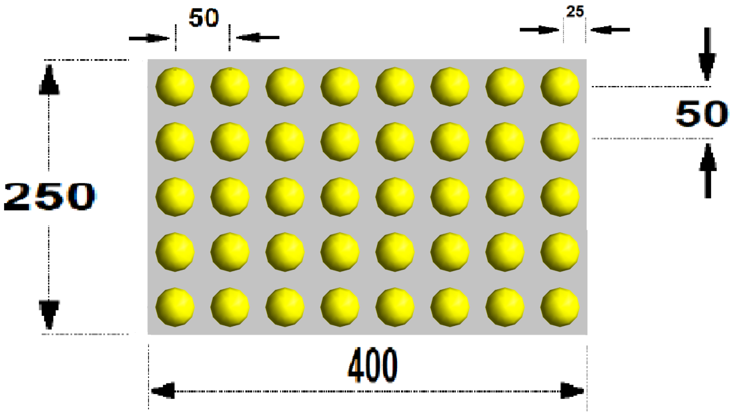
50
25
250
50
400

Figure 25 – Frontal view of the cross-section $[mm]$.

It is important to note that all the numerical results was presented using the same methodology.

Both Jiang, Bliss and Schulz (1995) and Wu (2007) did not clarify which velocity component they used to present their results nor the number of tests that were done. Considering that it was used hot wire anemometers measurements in both works, it was used the main component of the velocity (u) to compare with the experimental results.

5 RESULTS

In this chapter it will be presented and analyzed the results obtained from the numerical simulations following the methodologies presented at Section 4. First, the validation of the flow inside the U-bend and the PWT designed by Jiang, Bliss and Schulz (1995) and them, the UFES-PWT results in itself, first it will be analyzed the airflow and them the mass fraction.

5.1 VALIDATION AND COMPARISON OF THE NUMERICAL SIMULATIONS RESULTS AGAINST EXPERIMENTAL DATA

In this section, it will be validated and compared the results obtained for the Benson *et al.* (2020) numerical simulations obtained from two different turbulence models ($\kappa - \omega\ SST$ and the $\kappa - \varepsilon$). The turbulence model that better reproduces the flow inside the Benson *et al.* (2020) U-bend is used to simulate the PWT airflow. The validation and comparison of the Jiang, Bliss and Schulz (1995) PWT numerical results is performed using the Jiang, Bliss and Schulz (1995) and Wu (2007) experimental data is presented in Section 5.1.2.

5.1.1 Validation and analysis of the turbulence model on the U-bend simulations

The validation of the U-bend simulations is conducted using the Benson *et al.* (2020) experimental data, to make sure that the turbulence model is correctly representing the effects of turbulence on the flow patterns inside a U-bend structure. A comparison between two turbulence models is performed ($\kappa - \omega\ SST$ and the $\kappa - \varepsilon$) to identify which model better describes the turbulent airflow inside a U-bend. Furthermore, it was conducted a mesh sensitivity test to make sure that the mesh resolution isn't impending the correct application of the turbulence models, the test is presented in Appendix A.

Figures 27, 29 and 31 show, for both turbulence models, the velocity profiles obtained using the methodology shown in the Section 4.7, and the Figures 26, 28 and 30 shows the lines in where each profile was obtained according to the velocity component. Analyzing the $\kappa - \varepsilon$ results in the region before the U-bend curve ($z = 55\ mm$) and far from the walls, y'/H approximately between -0.35 and 0.35, this model showed a good correspondence with the $\kappa - \omega\ SST$ and experimental results. However, the results in the middle of the U-bend curve ($z = 75\,mm$) and after it ($z = 94$ and $104\,mm$, respectively), do not show the same good correspondence. There was a lack of accuracy in all the velocity directions, far and close to the walls. On the other hand, by analyzing the $\kappa - \omega\ SST$ results, it can be seen that, in general, and especially for the main component of the velocity (u), this model is able to capture all the tendencies of the flow with considerable accuracy. Furthermore, the $\kappa - \varepsilon$ results show a considerable difference between numerical and experimental data in the near-wall region for all the the studied velocity profiles. In this region, close to the walls, there is a considerable difference between the two models results accuracy, which can be explained by the fundamental differences in the models to account for the near-wall region flow characteristics. As explained in Section 4.2, the $\kappa - \omega\ SST$ model directly apply the no-slip condition and therefore directly calculate the near-wall flow, while the $\kappa - \varepsilon$ model uses wall functions to describe the flow in this region. As explained by Eça *et al.* (2015), the advantage of the use of these models is purely numerical. In addition, the use of the $\kappa - \varepsilon$ model is not adequate to simulate the flow in adverse pressure gradients and close to walls (SANTOS *et al.*, 2009; WILCOX *et al.*, 1998; MENTER, 1994), such as the characteristic of the flow and geometry of the U-bend. Therefore, in view of the results obtained for the U-bend simulations and the literature review, the $\kappa - \omega\ SST$ model was chosen to perform the PWT simulations.

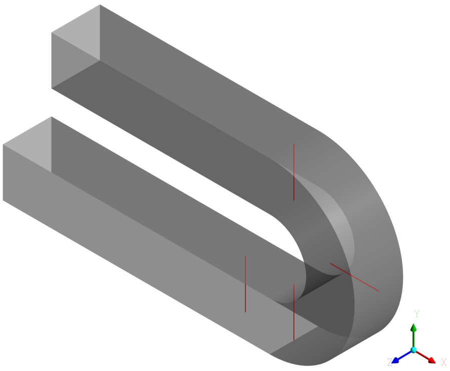

Figure 26 – Sampling lines for the u component of the velocity.

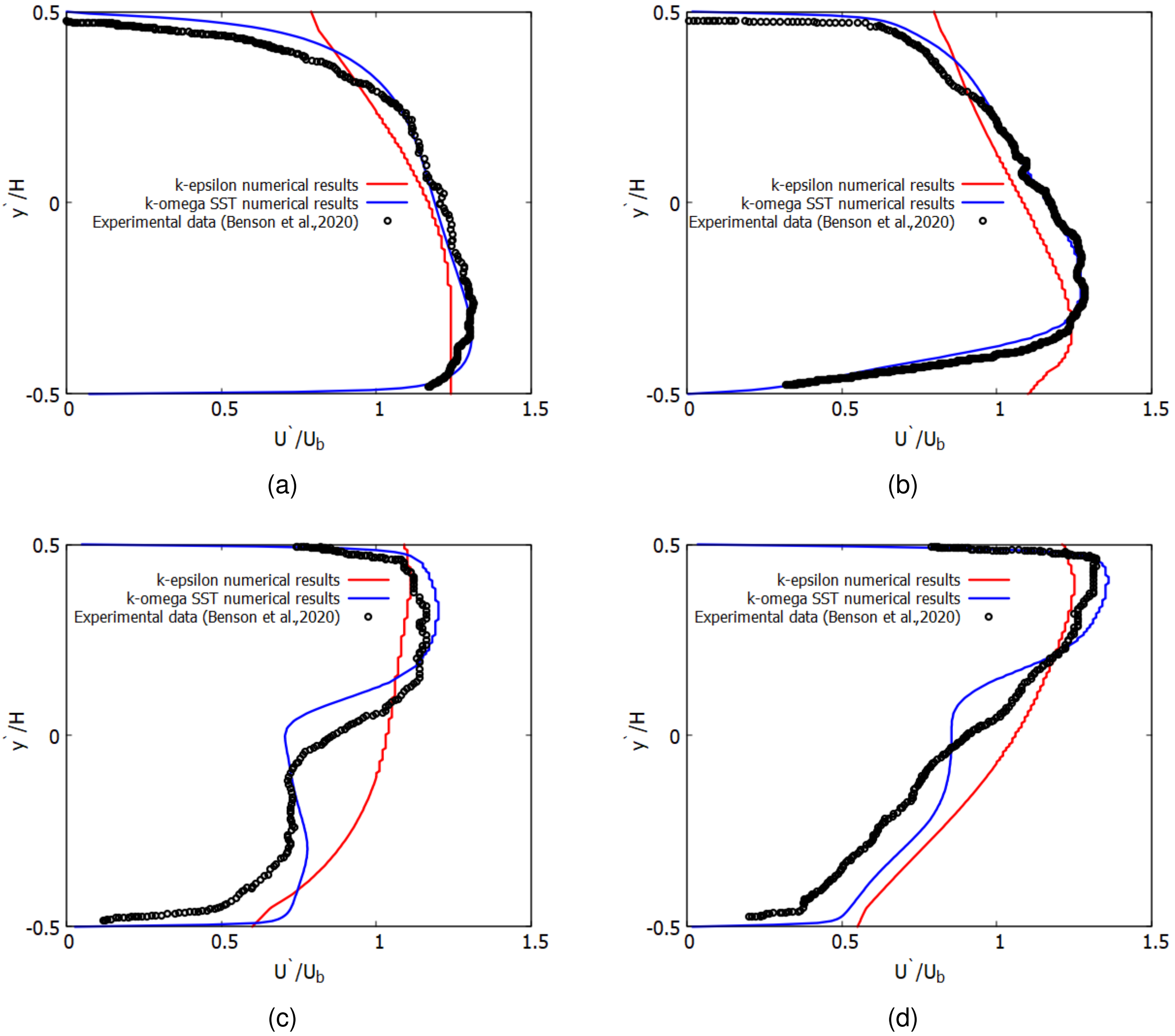

Figure 27 – Benson *et al.* (2020) U bend validation for both turbulence models - u component of the velocity profiles at the positions: (a)$z = 55\ mm$; (b)$z = 75\ mm$; (c) $z = 94\ mm$ and (d) $z = 104\ mm$

.

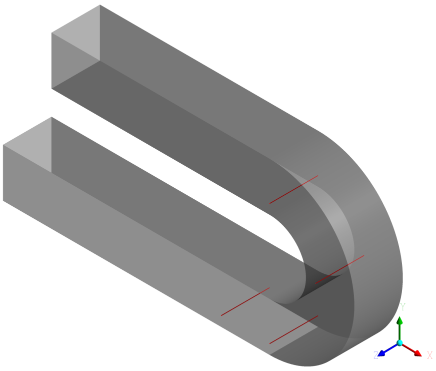

Figure 28 – Sampling lines for the v component of the velocity.

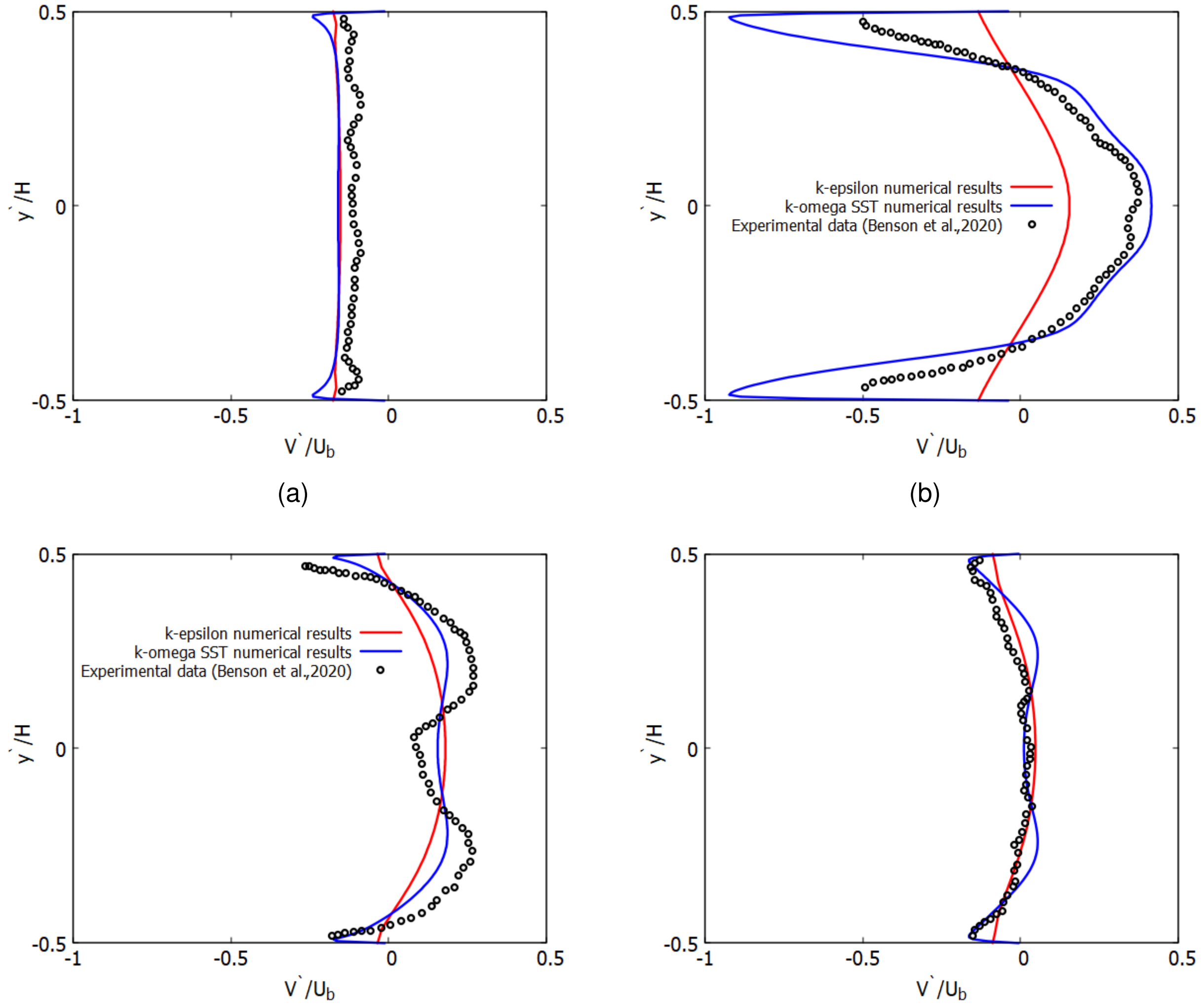

(a) (b) (c) (d)

Figure 29 – Benson *et al.* (2020) U bend validation for both turbulence models - v component of the velocity profiles at the positions: (a)$z = 55\ mm$; (b)$z = 75\ mm$; (c) $z = 94\ mm$ and (d) $z = 104\ mm$.

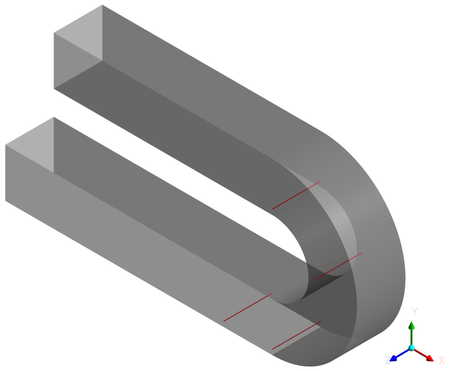

Figure 30 – Sampling lines for the w component of the velocity.

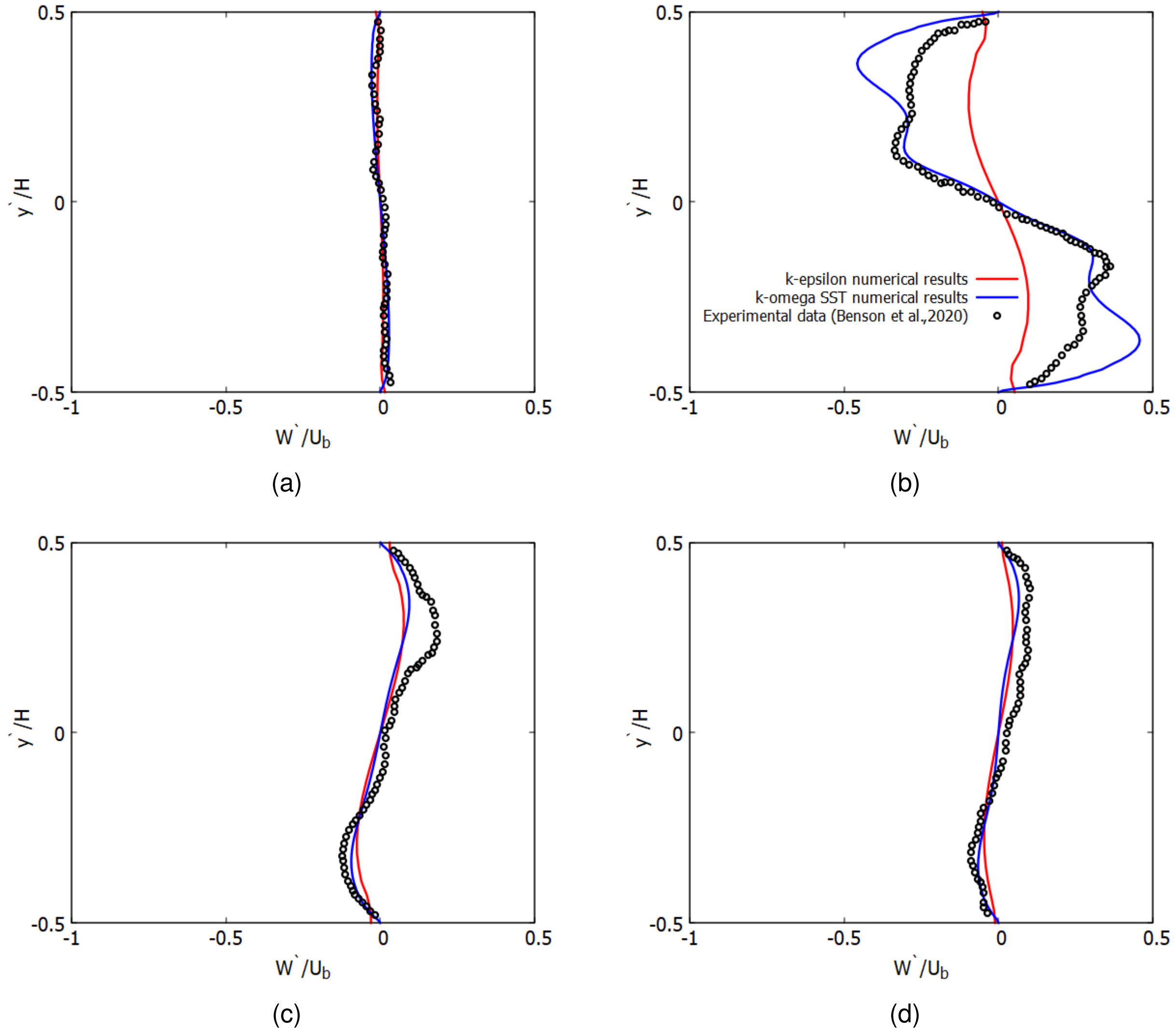

Figure 31 – Benson *et al.* (2020) U bend validation for both turbulence models - w component of the velocity profiles at the positions: (a)$z = 55\ mm$; (b)$z = 75\ mm$; (c) $z = 94\ mm$ and (d) $z = 104\ mm$

.

5.1.2 Comparison between the numerical simulations results and JIANG, BLISS E SCHULZ (1995) and WU (2007) portable wind tunnel data

Numerical simulation of the fluid flow inside the Jiang, Bliss and Schulz (1995) PWT were performed to be compared with the experimental data presented by these authors. As discussed earlier, the Jiang, Bliss and Schulz (1995) PWT geometry is not entirely identical to the UFES-PWT, but as there is very little and low quality experimental data available in the literature, the Jiang, Bliss and Schulz (1995) PWT geometry was simulated to validate the numerical model proposed in the present work, following the methodology presented in Section 4.7.

Figure 32 shows the comparison between the vertical profiles obtained by the numerical simulations for $\overline{u}$ and the experimental data, while Figure 33 shows the correlation coefficients. It can be seen that, despite the problems related to the Jiang, Bliss and Schulz (1995) experiments and data, already discussed in Section 3.2, a good correspondence between the numerical and experimental data was achieved. Ratner (2009) points out that correlation coefficient (R^2) values between 0.7 and 1.0 indicates a strong relation.

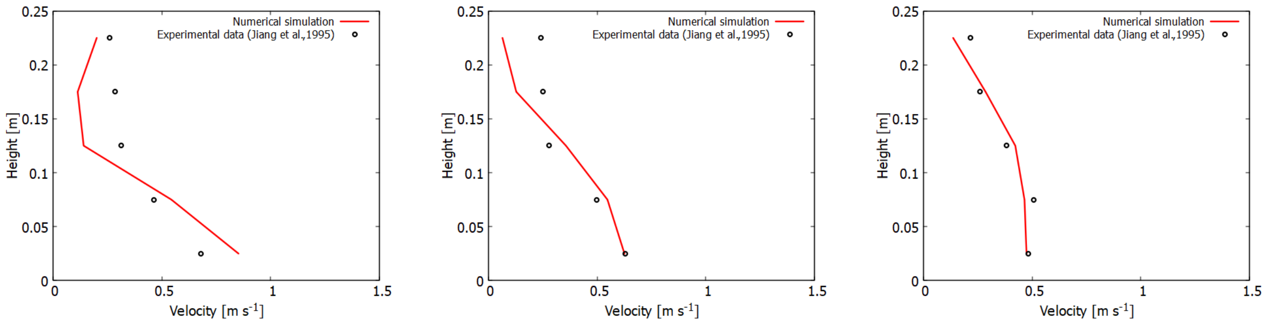

(a) (b) (c)

Figure 32 – Vertical profiles for $\overline{u}$ - numerical results compared to the experimental data at the positions: (a) $z = 200\ mm$; (b) $z = 400\ mm$ and (c) $z = 600\ mm$.

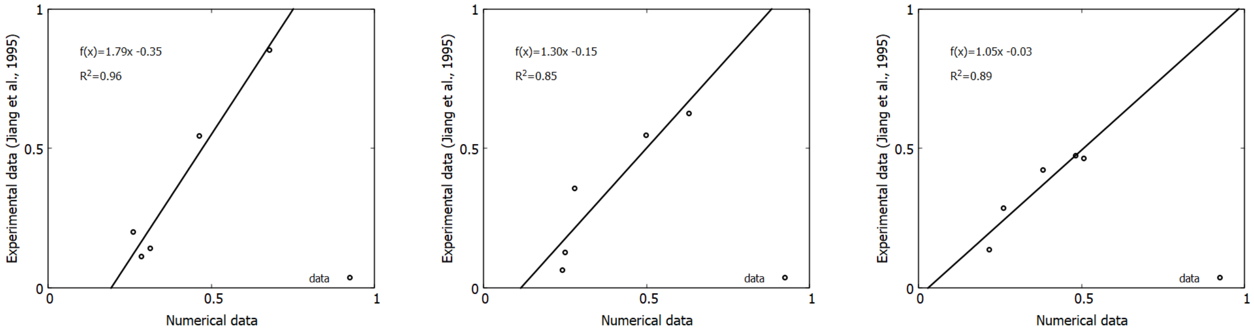

(a) (b) (c)

Figure 33 – Vertical profiles for $\overline{u}$ - Correlation coefficient for the numerical results compared to the experimental data: (a) $z = 200\,mm$; (b) $z = 400\,mm$ and (c) $z = 600\,mm$.

Figure 34 shows the horizontal profiles, for $\overline{u}$, obtained by the numerical simulations and Jiang, Bliss and Schulz (1995) experimental work. On contrary of the vertical profiles, the numerical horizontal profiles did not fit well with the experimental data. Such a result is intriguing, once that, as explained in Section 4.7, both results (vertical and horizontal) are calculated using the same database and methodology. Another work found in the literature that validates its numerical simulation of the flow inside the PWT using the Jiang, Bliss and Schulz (1995) data is the Perta *et al.* (2016), however not use the horizontal profile results. We suspect that the horizontal profile presented by Jiang, Bliss and Schulz (1995) has been calculated in a manner that is not well explained in the paper, as it is clear that the data is not the direct measurement, but a not well-explained combination of measurements in different positions.

A different source of experimental data that presents the results following the same methodology as Jiang, Bliss and Schulz (1995) is the work of Wu (2007), however as explained in Section 4.7 their geometry configuration and boundary conditions are a little different. In this way, this data will be used just to perform a qualitative comparison.

Figure 34 shows the horizontal profiles, for $\overline{u}$, for both the numerical and the Jiang, Bliss and Schulz (1995) and Wu (2007) experimental data. It can be seen that the Wu (2007) data tends to better fit with the tendency of the numerical results in comparison with the Jiang, Bliss and Schulz (1995) data. That is, higher velocity in the corner regions, width between $0.3\ to\ 0.4$ and $0.0\ to\ 0.2$, and lower velocity in the center region, width between $0.1\ to\ 0.3$.

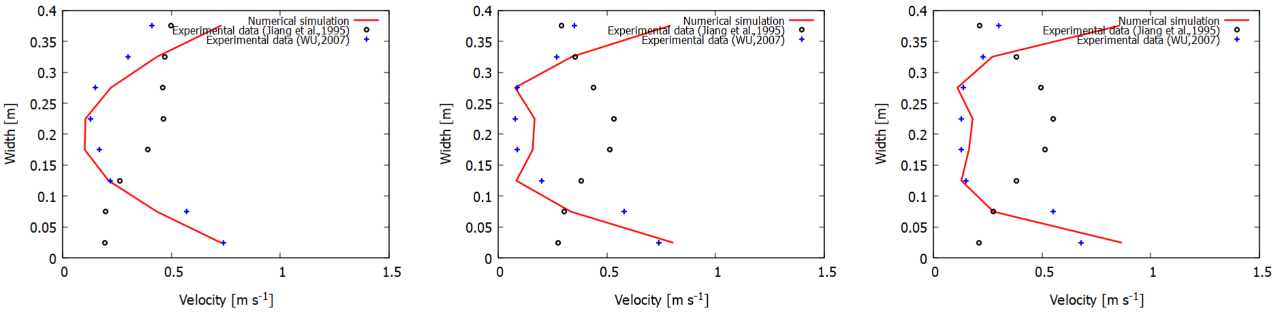

(a) (b) (c)

Figure 34 – Horizontal profiles for $\overline{u}$ - numerical results compared to the Jiang, Bliss and Schulz (1995) and Wu (2007) experimental data at the positions: (a) $z = 200\,mm$; (b) $z = 400\,mm$ and (c) $z = 600\,mm$.

The issues raised here bring the idea that it is necessary to carry out a hefty experimental work concerning the measurements of the flow structure inside the PWT, with open information regarding its details, such as the inlet velocity and the number of experiments. Also, a more sophisticated turbulence model such as Large Eddy Simulation, could be tested and it is recommended for future investigations. Or further investigating if the fluid flow is indeed turbulent inside the PWT for the usual operational conditions.

It is important to note that mesh sensitivity tests were performed to prove that the numerical simulations were correctly performed, the tests are presented in Apendix A.

5.2 ANALYSIS OF THE AIRFLOW PATTERNS INSIDE THE UFES-PWT FOR DIFFERENT INLET VELOCITIES

To study the airflow pattern inside the UFES-PWT and the influence of different inlet velocities, three numerical simulations of the airflow inside the UFES-PWT were conducted, using three different inlet velocities. Being the mean inlet velocities equal to: $3.82\,m\,s^{-1}$, $2.55\,m\,s^{-1}$ and $1.27\,m\,s^{-1}$.

The average velocity ($\overline{u}$) and TKE vertical profiles, plotted as it is shown in Section 4.7, are shown in Figures 35 and 36. It can be observed by analyzing both graphics that the flow patterns are similar for different inlet velocities, varying in intensity. This feature is more clearly seen through Figure 37, in where it is plotted the velocity profiles normalized by the inlet velocity for each case. Through Figure 35, it can be noted that for the higher inlet velocities, higher values of velocity in the main section are observed. In general, the observed profiles increases in its velocity values according to the inlet velocity, being the higher values observed for the inlet velocity equal to $3.82\,m\,s^{-1}$, followed by $2.55\,m\,s^{-1}$ and $1.27\,m\,s^{-1}$.

Analyzing the $\overline{u}$ velocity vertical profiles, it can be inferred that close to the beginning of the main section ($z = 200\,mm$), the bottom velocities (height 0 to $0.1\,m$) are higher. This is probably due to an acceleration provoked by the inlet duct curve. This higher velocity at the bottom remains, however, with less intensity at the profiles along the main section ($z = 400\,mm$ and $z = 600\,mm$).

By analyzing TKE profiles, it is noticeable that higher values are occurring close to the beginning of the main section ($z = 200\,mm$) at a bottom height (0 to $0.1\,m$). This tendency of a higher value close to the bottom height is braked at the sequence profiles ($z = 400\,mm$ and $z = 600\,mm$), where the higher values are occurring at a middle height (0.1 to $0.2\,m$). However, the TKE values at the highest heights (0.2 to $0.25\,m$) remain approximately constant along the profiles. This can indicate that there is a phenomenon (probably a reverse flow caused by a re-circulation zone) in the highest height that impact all the main section, however, in the bottom height, the change in the behavior of the TKE higher value can indicate that flow is not uniform along the bottom of the main section. Furthermore, higher values of TKE at the center and close to the end of the main section ($z = 400\,mm$ and $z = 600\,mm$) are occurring approximately at a middle height (0.1 to $0.2\,m$) which indicates a greater mixture in this region, probably provoked by the re-circulation zone.

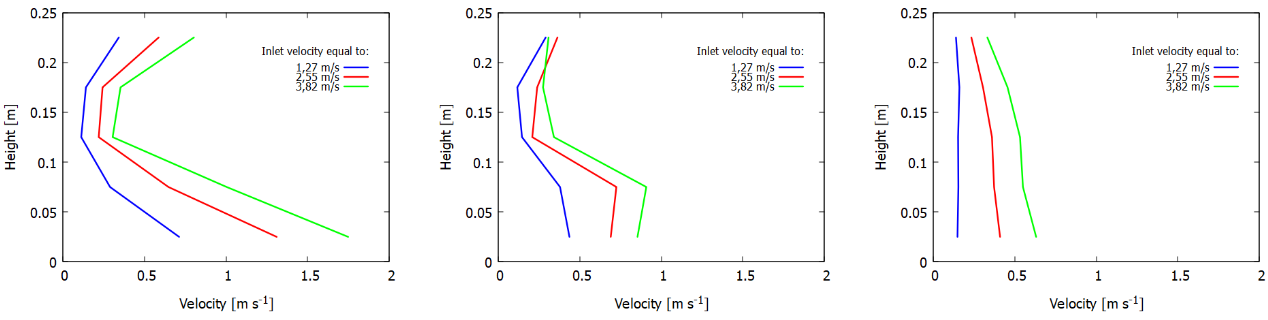

(a)

(b)

(c)

Figure 35 – Vertical velocity profiles for $\overline{u}$ for UFES PWT numerical simulations for the three tested velocities at the positions: (a) $z = 200\,mm$; (b) $z = 400\,mm$ and (c) $z = 600\,mm$.

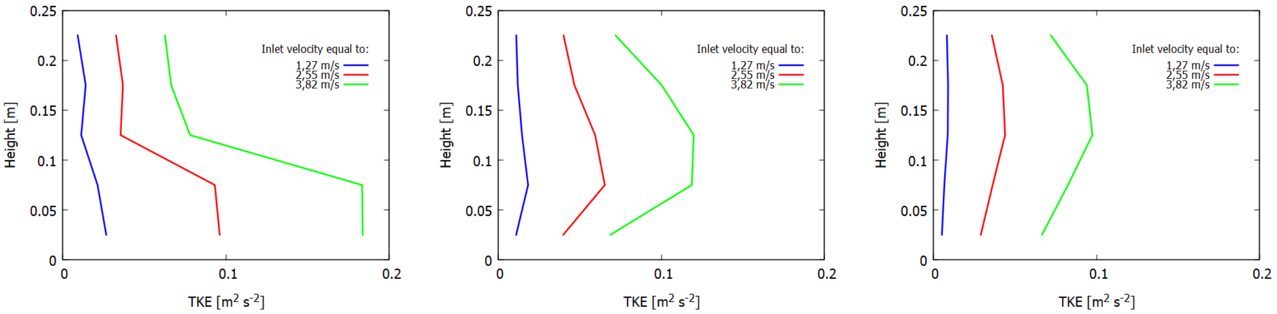

(a) (b) (c)

Figure 36 – Vertical TKE profiles for the UFES PWT numerical simulations for the three tested velocities at the positions: (a) $z = 200\ mm$; (b) $z = 400\ mm$ and (c) $z = 600\ mm$.

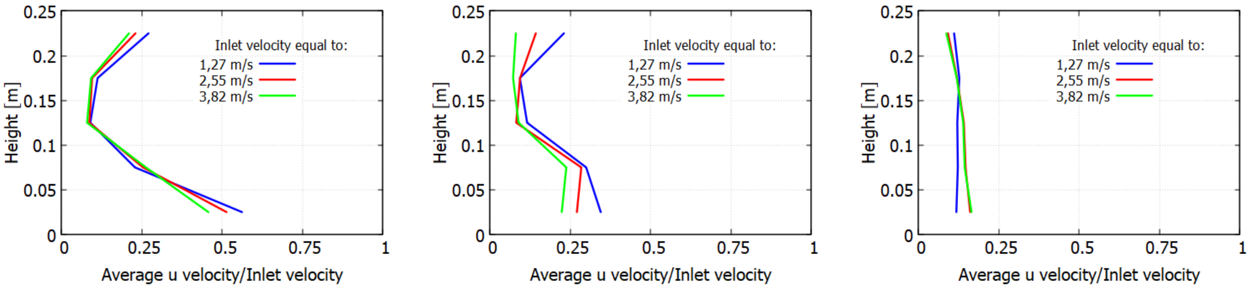

(a) (b) (c)

Figure 37 – Vertical velocity profiles for $\overline{u}$ normalized by the inlet velocity - UFES PWT numerical simulations for the three tested velocities at the positions: (a) $z = 200\ mm$; (b) $z = 400\ mm$ and (c) $z = 600\ mm$.

Figure 38 shows the velocity distribution top view, at half of the PWT height ($y = 125$), for the three simulations, it is possible no note, as happened for the vertical velocity profiles for $\overline{u}$, that the main flow behaves in general in the same way for the three velocities, diverging in its magnitude. It also can be noted that symmetry was achieved for all the simulations.

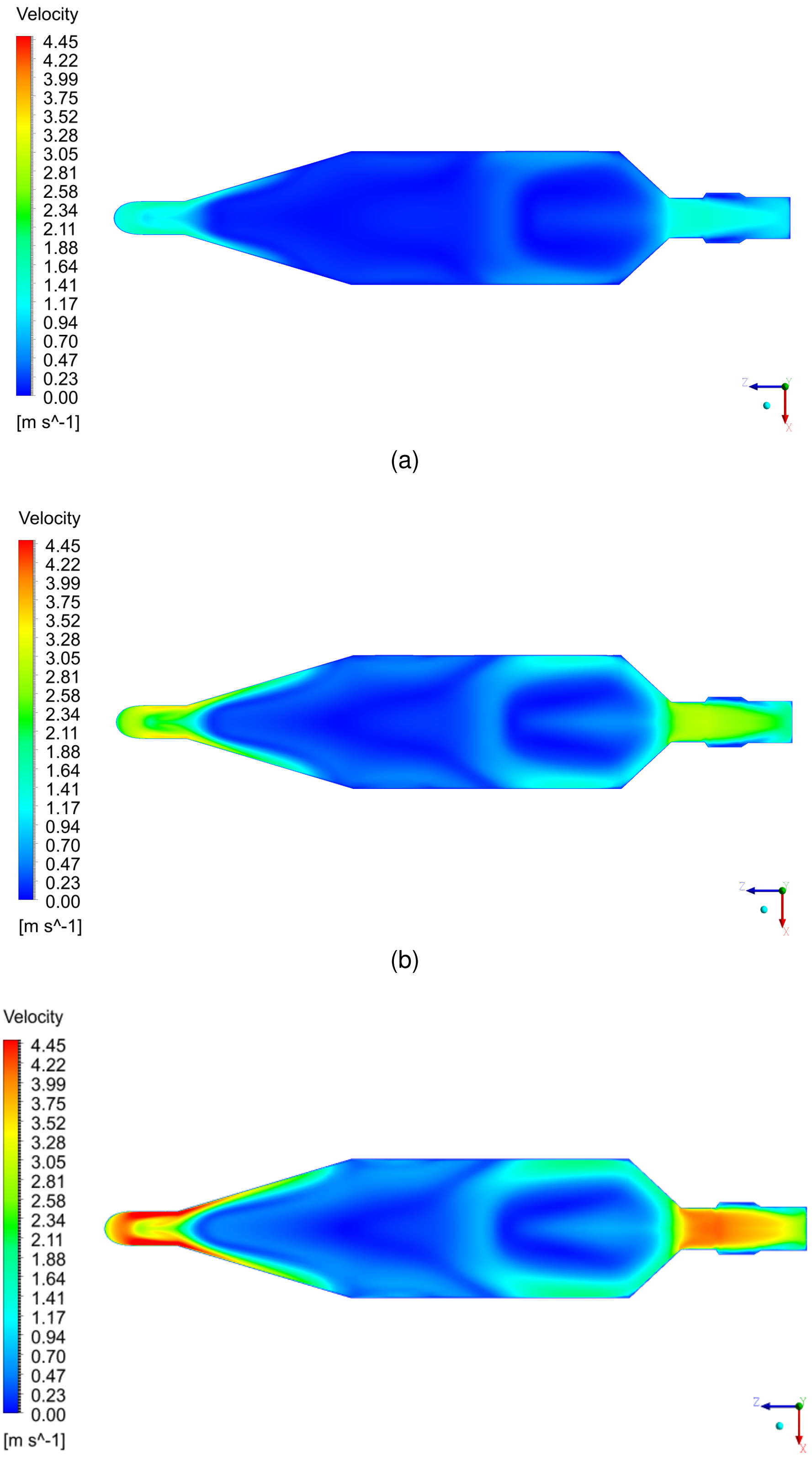

(a)

(b)

(c)

Figure 38 – Velocity distribution for $\overline{u}$ top view at half of the PWT height $(y = 125)$ - UFES PWT simlations for different inlet velocities: (a) $1.27\,m\,s^{-1}$; (b) $2.55\,m\,s^{-1}$ and (c) $3.82\,m\,s^{-1}$.

The lateral view of the streamlines is shown in Figure 39 for the three velocities.

Despite the noticeable average flow patterns similarities, it is interesting to note that the slightly bigger sizes of the recirculation zone are happening as opposed to the inlet velocity increase. That is, the bigger length of the recirculation appears to happen for inlet velocity equal to $1.27\,m\,s^{-1}$, followed by $2.55\,m\,s^{-1}$ and $3.82\,m\,s^{-1}$ as a last. That is more clearly seen through Figure 42-a, where it shows the w velocity component for a line placed at the center of the main section. The location of the line is shown in Figure 41. The passage of the w component of the velocity to a positive value marks the size of the recirculation zone that can be seen through the Figure 39, thus, the airflow with an inlet value of $1.27\,m\,s^{-1}$ presents a recirculation zone with size approximately equal to $0.55\,m$, for the airflow with inlet velocity equal to $2.55\,m\,s^{-1}$ $0.5\,m$ and for the airflow with inlet velocity equal to $3.82\,m\,s^{-1}$ $0.35\,m$. Through the graphics, it is also possible to note a second re-circulation zone with opposed velocity direction, which will be discussed in the next paragraphs.

The tendency break that happened along the TKE profiles can be more clearly seen through the image 39 plus the Figures 40, in which it is plotted the TKE distribution in a side view central plane, the bigger re-circulation zone goes until about the center of the main section and as a consequence, causes the behavior variation of the profiles (Figure 36) for close to the beginning of the main section and at the center and close to the end of the main section. In Figure 40, it is possible to see that the higher values of TKE were found for the case with inlet velocity equal to $3.82\,m/s$, i.e. the higher velocity. Was also possible to note through the TKE distribution, the presence of a major recirculation zone with size varying as opposed to the average inlet velocity and that appear to be caused by the curved inlet duct.

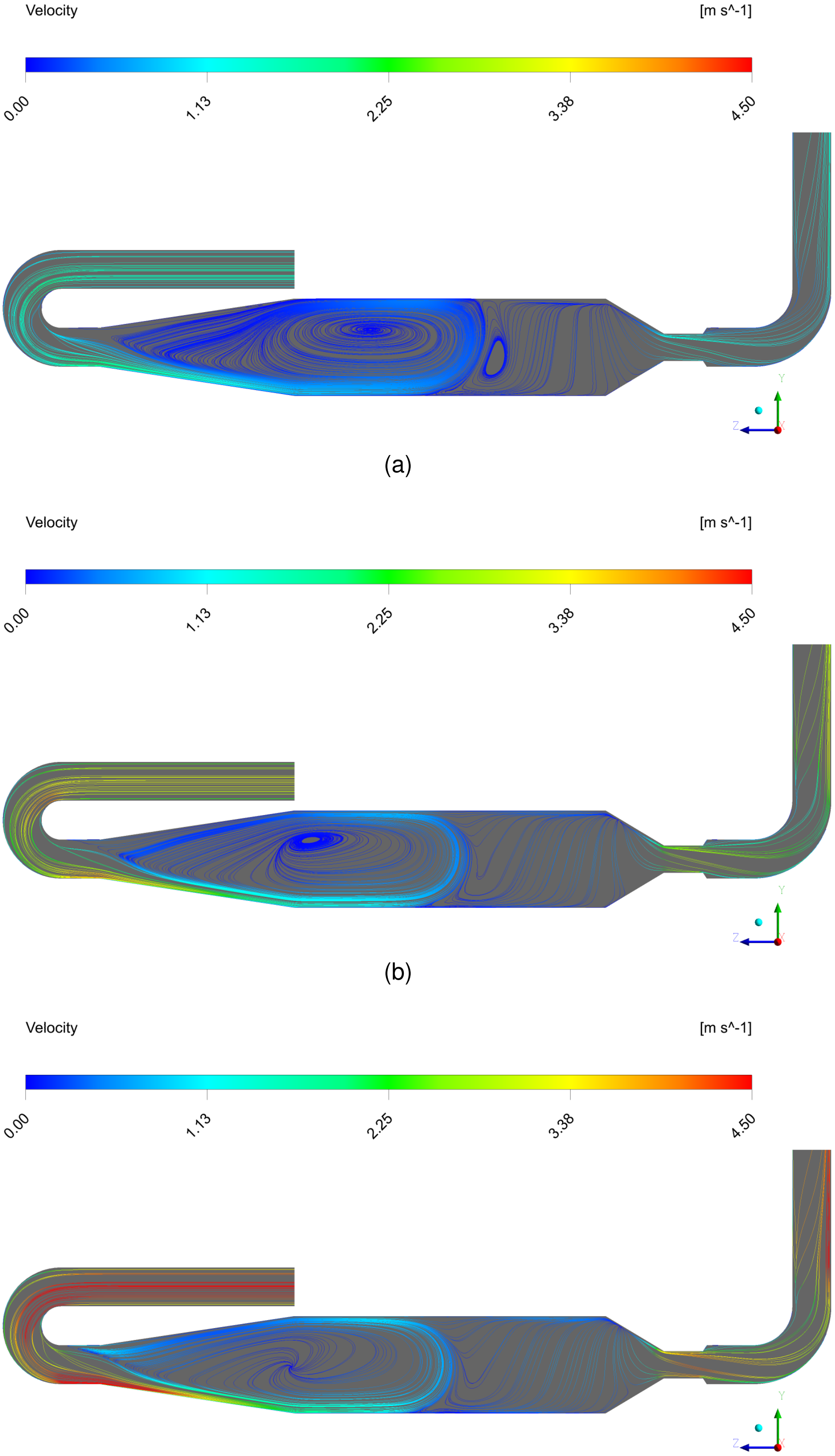
Velocity
[m s^-1]
0.00
1.13
2.25
3.38
4.50
Y
Z
X

(a)

(b)

(c)

Figure 39 – Streamlines side view - UFES PWT simlations for different inlet velocities: (a) $1.27\, m\, s^{-1}$; (b) $2.55\, m\, s^{-1}$ and (c) $3.82\, m\, s^{-1}$.

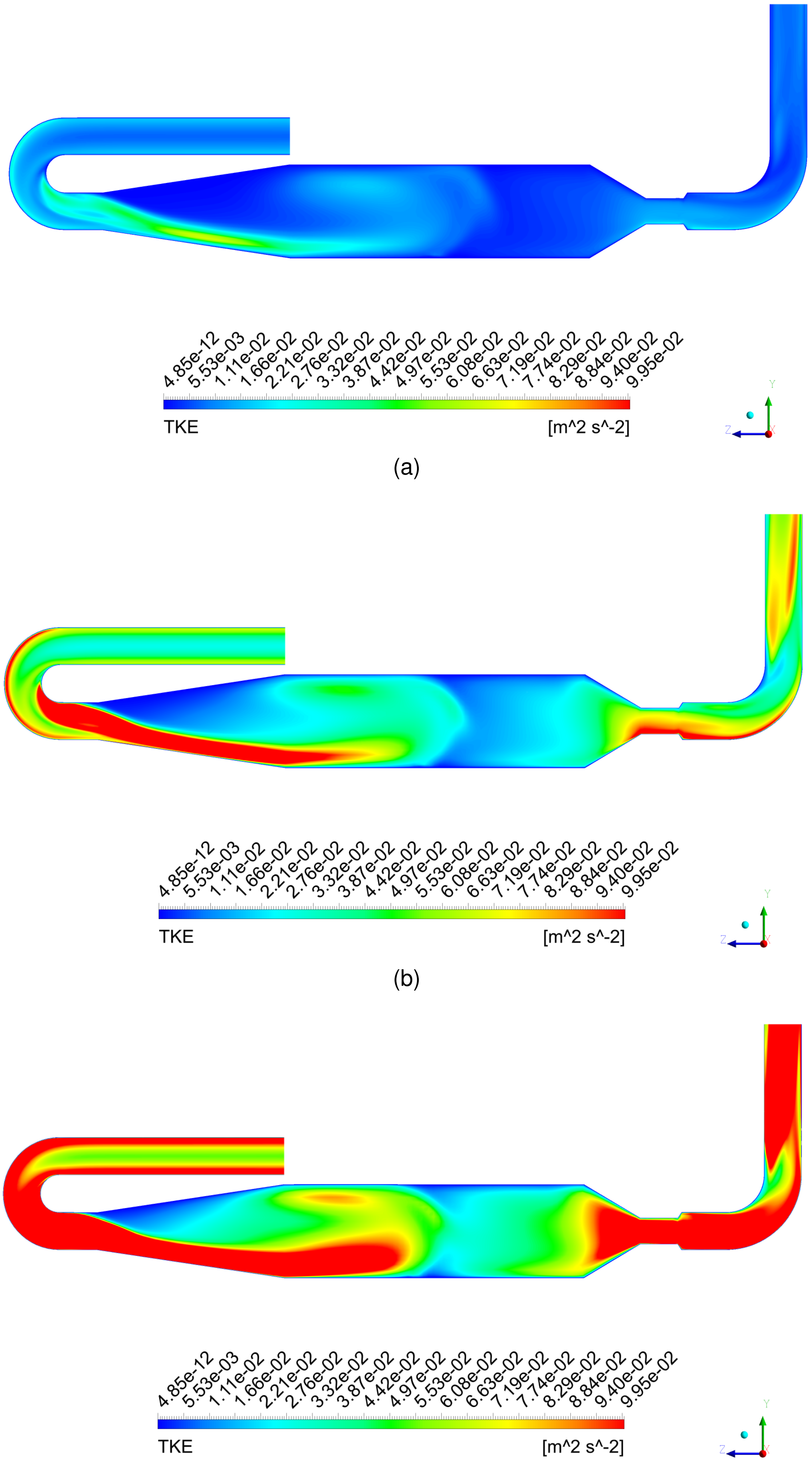

(a)

(b)

(c)

Figure 40 – TKE distribution side view - UFES PWT simlations for different inlet velocities: (a) $1.27\,m\,s^{-1}$; (b) $2.55\,m\,s^{-1}$ and (c) $3.82\,m\,s^{-1}$.

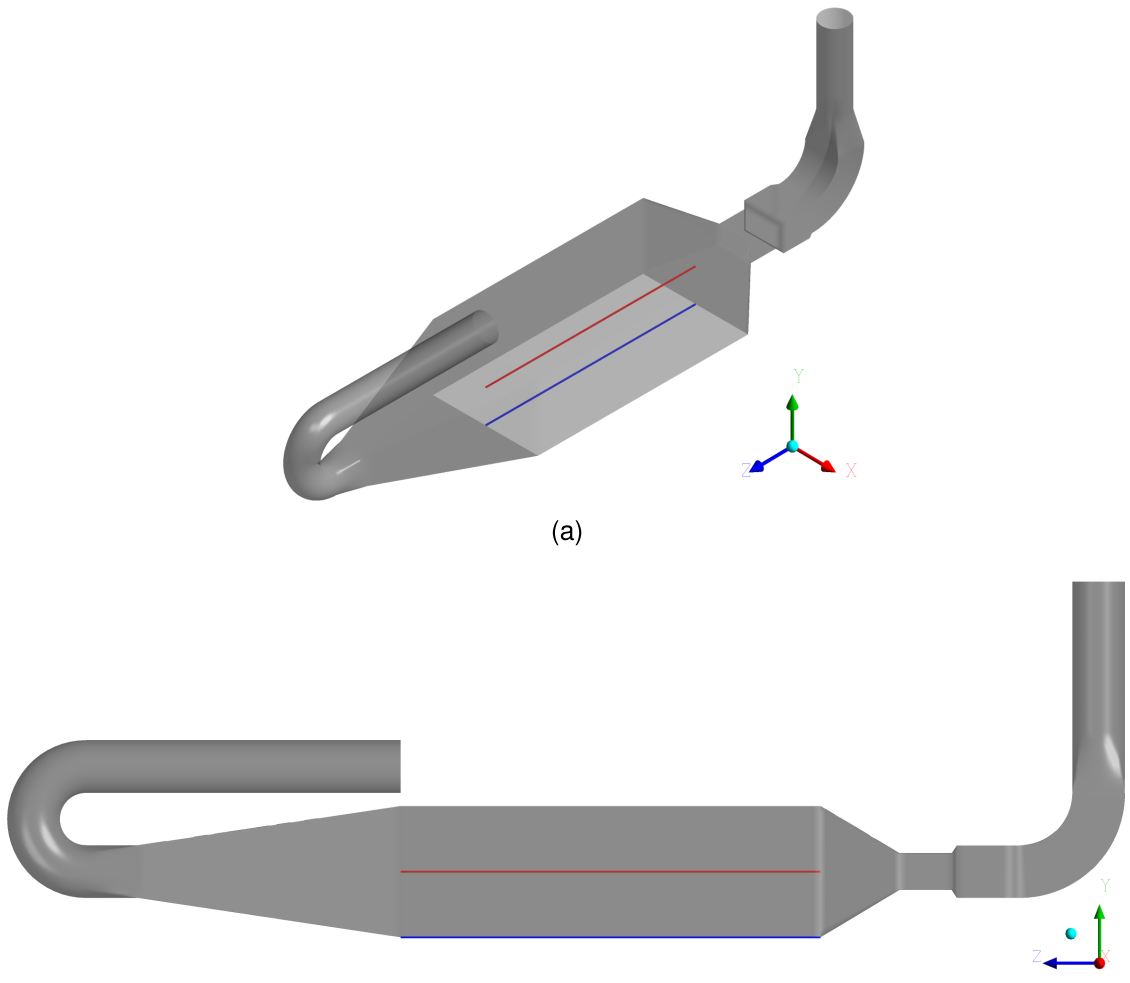

(a)

(b)

Figure 41 – Location of the lines used to study the size of the recirculation zone, red line: velocity and blue line: friction velocity: (a) Isometric view and (b) Lateral view.

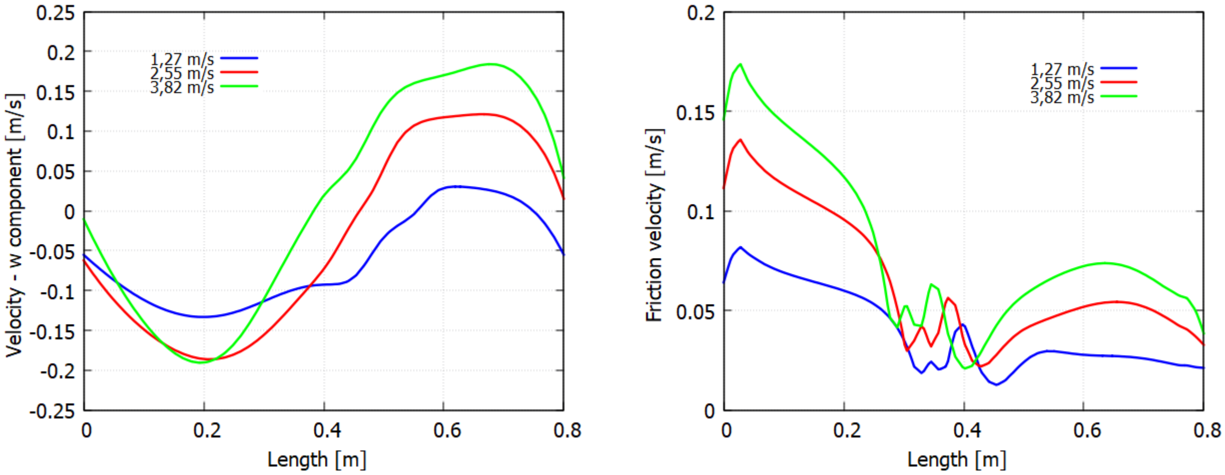

(a)

(b)

Figure 42 – Graphics used to analyze the size of a recirculation zone and its influence of the friction velocity: (a) Component w of the velocity for a line placed at the center of the main section; (b) Friction velocity for a line placed at the center of the gas-liquid interface.

The Figure 43 shows the velocity distributions at the outlet of the PWT. The sample of the air containing the odorant compounds is performed in a cross manner near the end of the outlet duct, that is, the samples are taken at five points in the outlet duct, one in the center and another four equidistant in itself and to the center point. In this way to obtain a representative sample, it would require a fully developed flow. In fact, one of the objectives of the proposal of this extended outlet duct, by Wang, Jiang and Kaye (2001), was that i.e. to let the flow achieve development on its inside. However, it is possible to note that the curve in the outlet duct provokes a nonuniform acceleration in its inside that is not fully attenuated along the duct and as a consequence, the flow along the outlet duct does not achieve development. The same behavior can be seen when looking the Figures 39 and 40, however in a different point of view (lateral view).

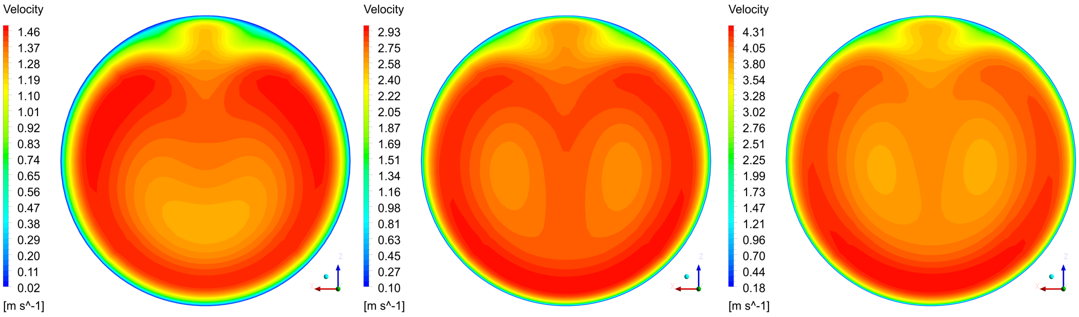

(a) (b) (c)

Figure 43 – Velocity distribution for $\overline{u}$ at the outlet of the UFES PWT for different inlet velocities: (a) $1.27\,m\,s^{-1}$; (b) $2.55\,m\,s^{-1}$ and (c) $3.82\,m\,s^{-1}$.

Figure 44 shows the friction velocity distribution in the gas-liquid interface plotted together with velocity vectors in a side view plane. The average values of the friction velocity in the gas-liquid interface ($\overline{u}^{*}$) are presented in Table 18 for each average inlet velocity. It seems that the average friction velocity grows linearly with the inlet velocity for this range of values. A re-circulation zone seen in Figure 44 is probably caused by the acceleration due to the curve in the inlet duct. This re-circulation remains until about the center of the main section. This same behavior can be seen in Figure 38. The friction velocity is higher at the beginning of the main section. The lowest friction velocity values are approximately at the center of the main section and then there is a little growth towards the end of the main section. This behavior appears to be related to the re-circulation that exists up to the center of the main section as can be seen more clearly in Figure 38. The straight relation of the friction velocity distribution with the re-circulation is more clearly seen through Figure 42-b, in where it is plotted the friction velocity on a line at the center of the gas-liquid interface (location shown in Figure 41) plus the Figure 42-a. It is possible to note that there are three different regions in the friction velocity. A first with the higher values of friction velocity, the values in these regions appear to be happening in the region influenced by the major re-circulation zone, also the size of this region appears to be straightly related to the size of the re-circulation zone. A second region happens in the transition of the two re-circulation zones and a third, with the lowest friction velocity values, appear to happen in a second re-circulation zone and with an opposed velocity direction.

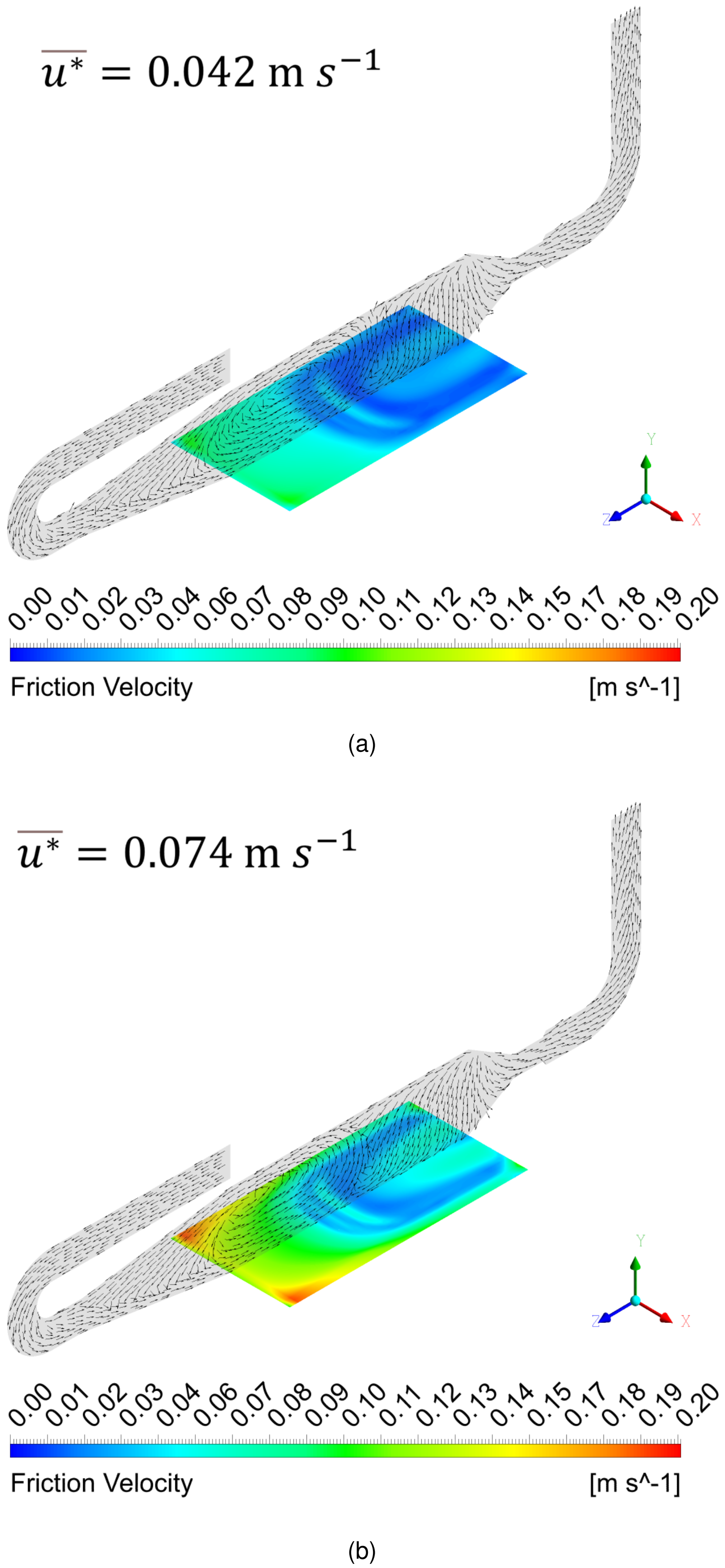

Figure 44 – Friction velocity distribution in the gas-liquid interface and velocity vectors in a side view plane - UFES PWT simulations for different inlet velocities: (a) $1.27\, m\, s^{-1}$; (b) $2.55\, m\, s^{-1}$ and (c) $3.82\, m\, s^{-1}$.

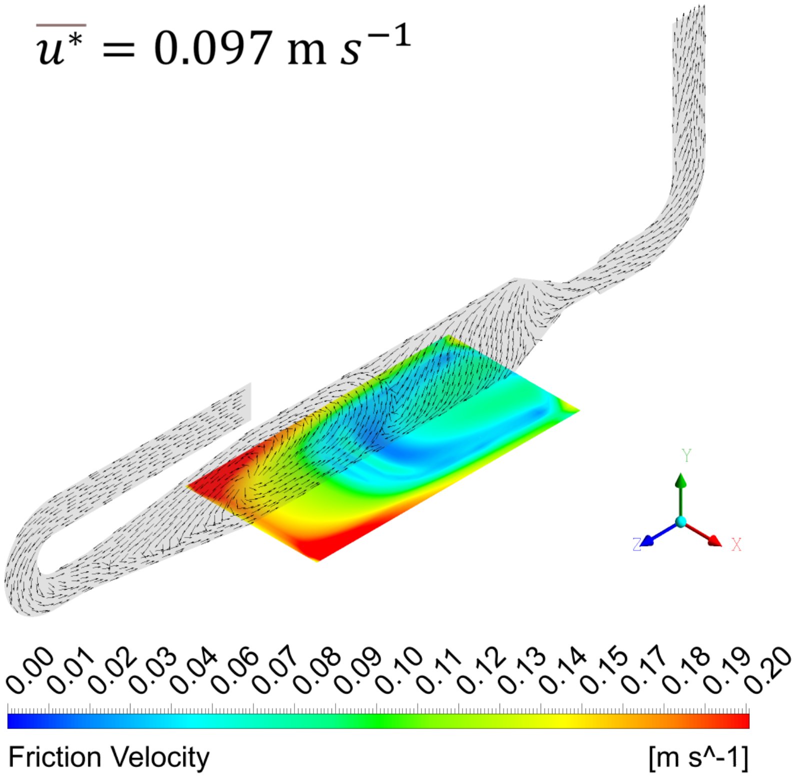

(c)

Figure 44 – Friction velocity distribution in the gas-liquid interface and velocity vectors in a side view plane - UFES PWT simulations for different inlet velocities: (a) $1.27\,m\,s^{-1}$; (b) $2.55\,m\,s^{-1}$ and (c) $3.82\,m\,s^{-1}$.

$\overline{u}\ [m\,s^{-1}]$	$\overline{u}^*\ [m\,s^{-1}]$
3.82	0.097
2.55	0.074
1.27	0.042

Table 18 – Average friction velocity ($\overline{u}^*$) in the gas-liquid interface for the different inlet velocities.

As it was previously discussed, there is the formation of a re-circulation zone in the central region of the PWT, that can be seen through the Figures 39 and 44. However, a closer look at the Figures 38, in where it is shown the velocity distribution for $\overline{u}$ in an top view plane, shows that the curved inlet duct not only seems to impose an acceleration near the bottom of the expansion section but also impose a lateral acceleration.

The lateral re-circulation zones can be seen more clearly through Figure 45, in where it is presented the $3D$ streamlines for all the velocities in a isometric perspective. In this Figure it is possible to note, for all inlet velocities, a lateral acceleration across the domain happening since the curved inlet duct.

Through Figure 46, in where it is shown the bottom view of the streamlines, it can be seen three re-circulation zones, one in the central region and two in the lateral regions, one at each side. Through these images it is also possible to note that the lateral accelaration is causing re-circulation zones directed to the main section as it encounter the contraction section walls. That re-circulation causes the occurrence of a reversed flow across a great part of the main section. This regions can be seen through velocity vectors at the Figure 48, in where it is plotted the velocity vectors with the same size for the central plane - side view. In this image it is possible to see, particularly in the main section, the central re-circulation zone followed by the reversed flow cause by lateral acceleration. The Figure 42-a also shows the presence of both re-circulation zones. In Section 5.3 it will be discussed the effects of this $3D$ and complex flow on the volatilization of the odorant compound.

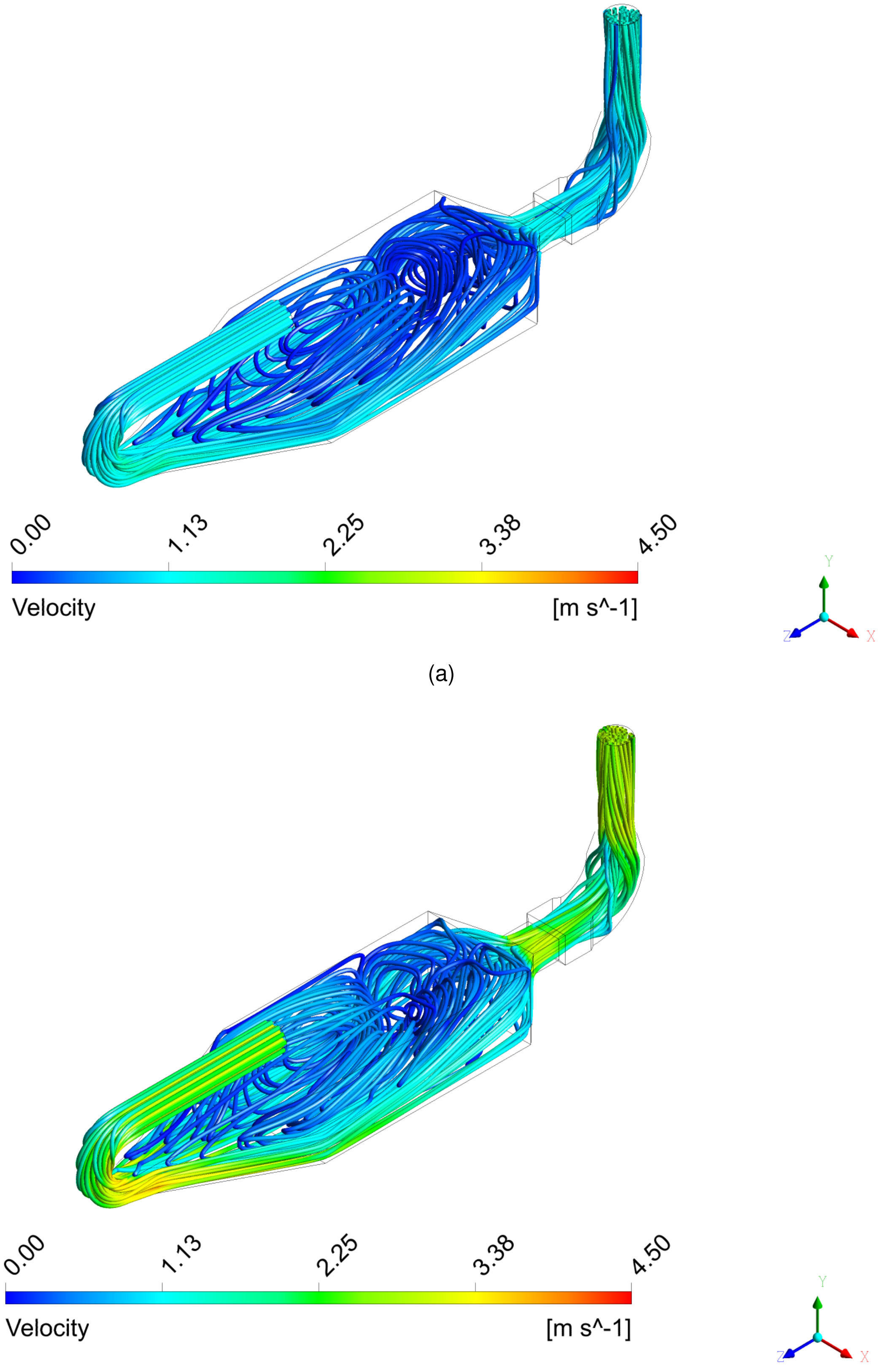
0.00
1.13
2.25
3.38
4.50
Velocity
[m s^-1]
Y
Z
X
0.00
1.13
2.25
3.38
4.50
Velocity
[m s^-1]
Y
Z
X

(a)

(b)

Figure 45 – $3D$ Streamlines isometric view - UFES PWT simulations for different inlet velocities: (a) $1.27\ m\,s^{-1}$; (b) $2.55\ m\,s^{-1}$ and (c) $3.82\ m\,s^{-1}$.

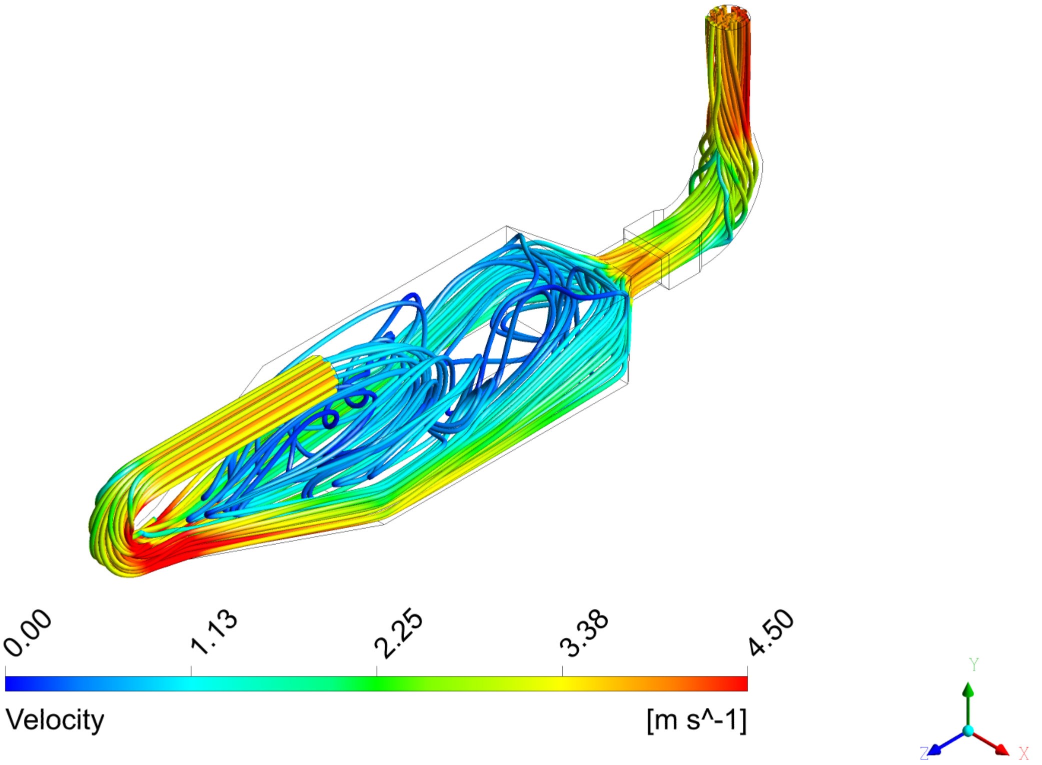
0.00
1.13
2.25
3.38
4.50
Velocity
[m s^-1]
Y
Z
X

(c)

Figure 45 – $3D$ Streamlines isometric view - UFES PWT simlations for different inlet velocities: (a) $1.27\,m\,s^{-1}$; (b) $2.55\,m\,s^{-1}$ and (c) $3.82\,m\,s^{-1}$.

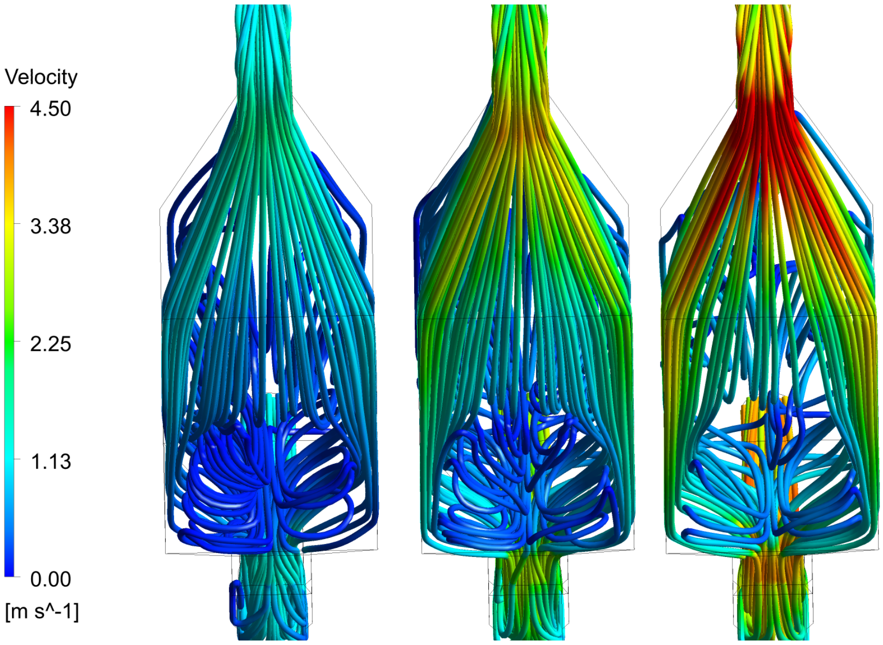
Velocity
4.50
3.38
2.25
1.13
0.00
[m s^-1]

(a) (b) (c)

Figure 46 – $3D$ Streamlines bottom view - UFES PWT simlations for different inlet velocities: (a) $1.27\,m\,s^{-1}$; (b) $2.55\,m\,s^{-1}$ and (c) $3.82\,m\,s^{-1}$.

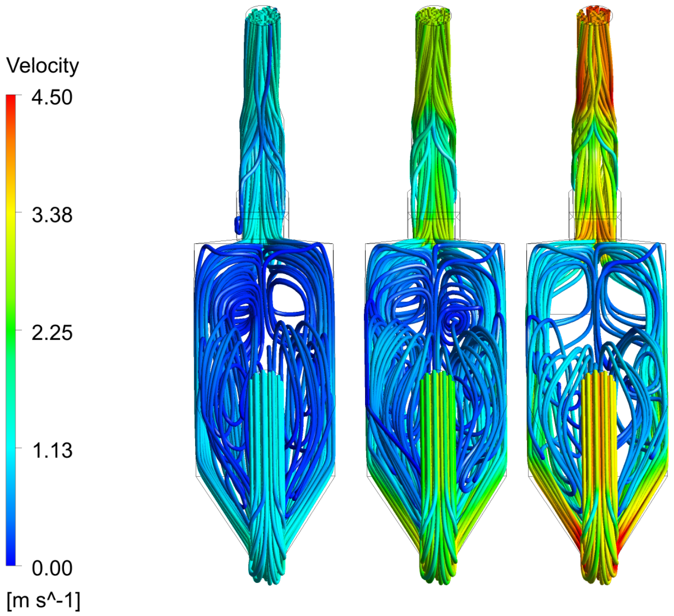
Velocity
4.50
3.38
2.25
1.13
0.00
[m s^-1]

(a) (b) (c)

Figure 47 – $3D$ Streamlines top view - UFES PWT simlations for different inlet velocities: (a) $1.27\ m\,s^{-1}$; (b) $2.55\ m\,s^{-1}$ and (c) $3.82\ m\,s^{-1}$.

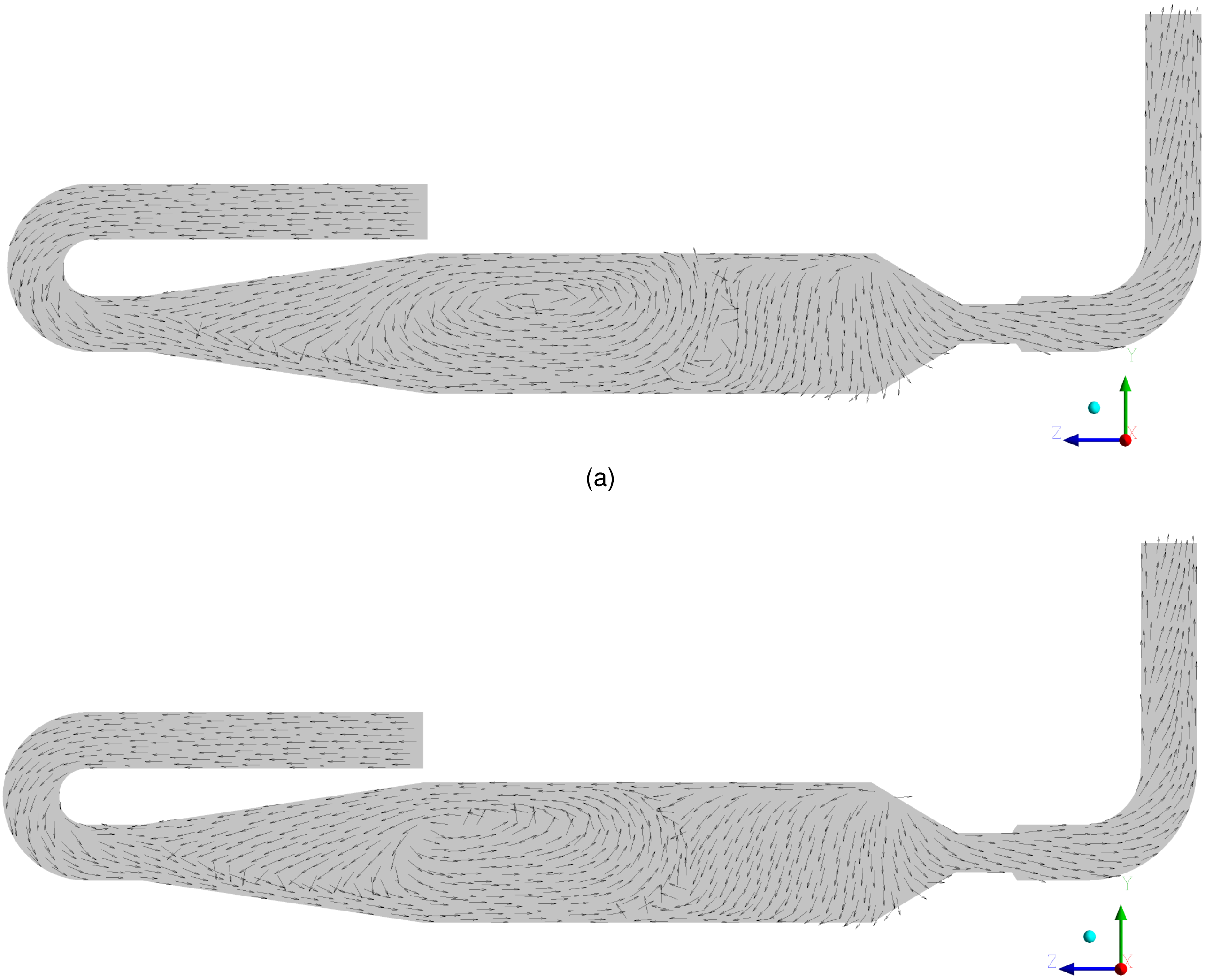

(a)

(b)

Figure 48 – Velocity vectors in a side view plane - UFES PWT simlations for different inlet velocities: (a) $1.27\,m\,s^{-1}$; (b) $2.55\,m\,s^{-1}$ and (c) $3.82\,m\,s^{-1}$.

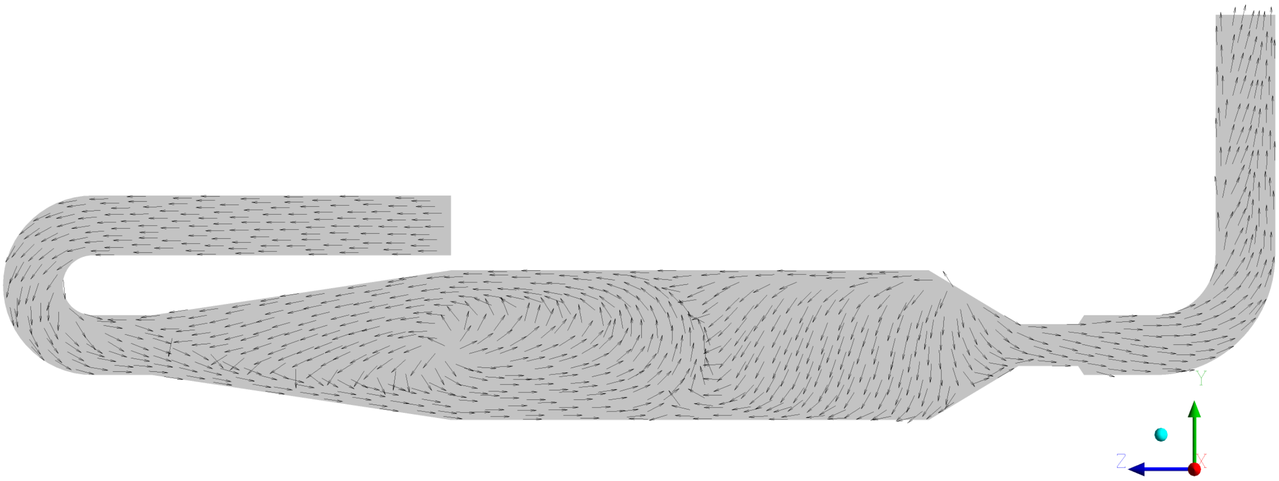

(c)

Figure 48 – Velocity vectors in a side view plane - UFES PWT simlations for different inlet velocities: (a) $1.27\,m\,s^{-1}$; (b) $2.55\,m\,s^{-1}$ and (c) $3.82\,m\,s^{-1}$.

As the numerical simulation of the fluid flow inside the Jiang, Bliss and Schulz (1995) PWT were presented in Section 5.1.2 to validate the numerical model proposed in the present work, it is also important to discuss here the impact of the geometry difference between the Jiang, Bliss and Schulz (1995) PWT and the UFES PWT on the fluid flow. The larger difference is in the outlet, as can be seen in Figure 49. However, another difference is encountered in the region that joints the inlet duct and the expansion section. This joint section in the Jiang, Bliss and Schulz (1995) geometry is a straight circular duct and in the UFES PWT is a duct that goes from a circular shape to a squared shape. The Figure 50 shows this difference in detail.

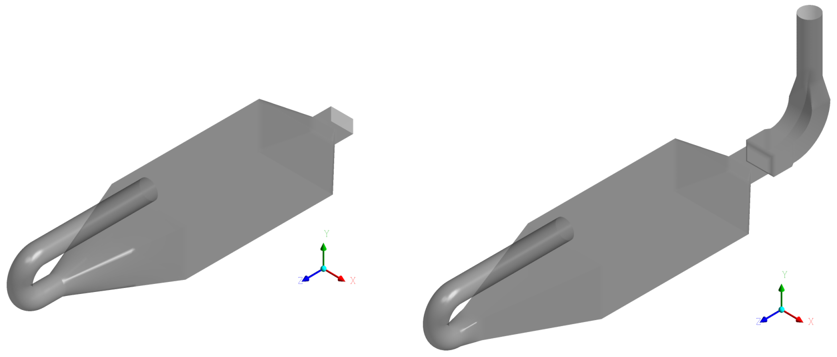

(a) (b)

Figure 49 – Difference in the outlet duct for the PWT geometries: (a) Jiang, Bliss and Schulz (1995) and (b) UFES PWT.

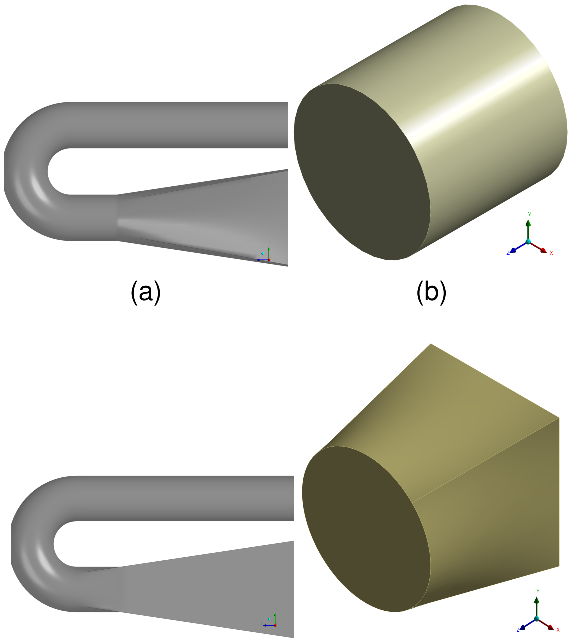

(a) (b)

(c) (d)

Figure 50 – Detail of the joint that connects the inlet duct and the expanse section of the PWT: (a) Jiang, Bliss and Schulz (1995) ; (b) Jiang, Bliss and Schulz (1995); (c) UFES pwt and (d) UFES PWT.

Figure 51 shows close details of the streamlines in the main section for the Jiang, Bliss and Schulz (1995) and the UFES PWTs simulations. Despite the difference in the velocity inlet (respectively, 2.82 and $2.55\,m\,s^{-1}$), the general behavior of the flow can be analyzed. It appears that, because of the difference in the joint section, the acceleration caused by the curve in the inlet duct is more pronounced in the UFES PWT and therefore the re-circulation zone in this geometry is larger. This kind of result points out that it seems that small changes in the geometry of the PWT have a great interference on the flow in its inside.

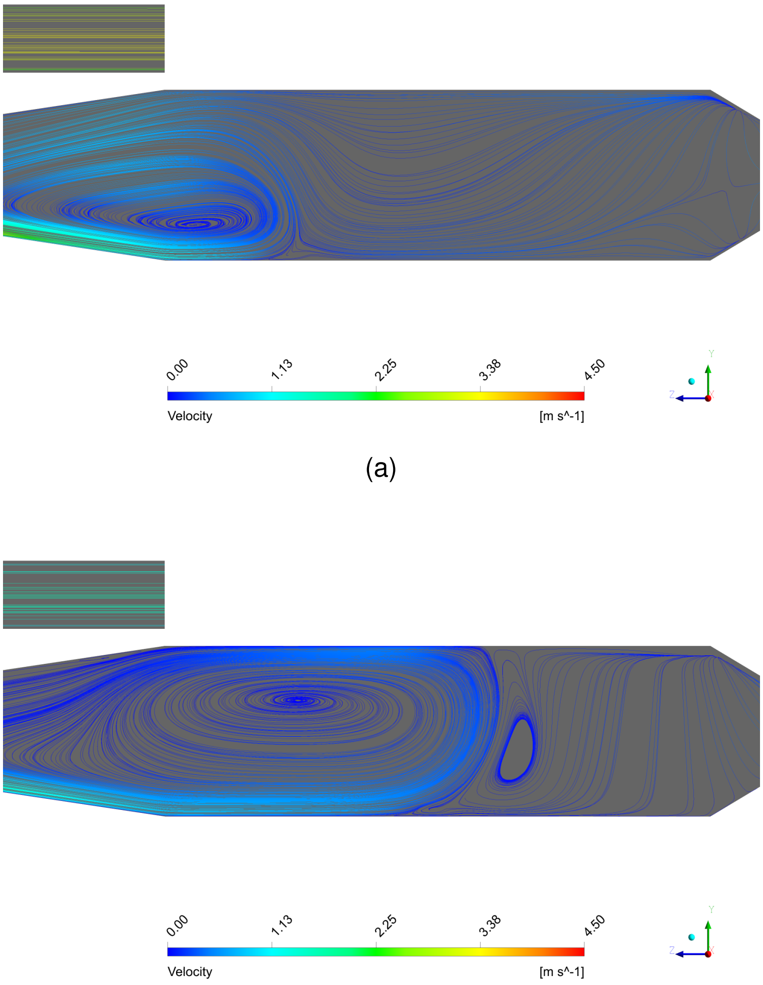

(a)

(b)

Figure 51 – Detail of the streamline in the main section for the: (a) Jiang, Bliss and Schulz (1995) PWT simulation and (b) UFES PWT simulation.

5.3 ANALYSIS OF THE MASS FRACTION PATTERNS INSIDE THE UFES-PWT FOR DIFFERENT INLET VELOCITIES

To study the mass fraction patterns inside the UFES PWT and its response to different inlet velocities, three numerical simulations of the mass fraction in its inside were conduced, using three different inlet velocities and for each velocity was considered two different odorant compounds, the hydrogen sulfide (H_2S) and the acetic acid (CH_3COOH). For both odorant compounds, it was considered as its boundary condition a prescribed concentration, however for the H_2S it was also conduced additional simulations using a constant mass flux as its boundary condition, to study the possible differences caused by the use of a different boundary condition. It should be noted that these two odorant compound was chosen to conduce the simulations due to their different response to the volatilization process, the hydrogen sulfide has its volatilization process dominated by the liquid phase and the acetic acid is dominated by the gas phase. More information and details on the simulations are given in Section 4.

The mass fraction pattern inside the UFES PWT will be analyzed first for the simulations considering a prescribed concentration at the gas-liquid interface. The differences that may occur caused by the consideration of a different boundary condition at the gas-liquid interface will be assessed following.

An important feature of the sampling of an odorant compound, whether it is performed (laboratory or field), and on the conduce of numerical simulations of this nature, is the stabilization time of the chemical compound. That is the time in which there are no significant changes in its concentration along with the geometry. To reach this time for the present numerical simulations, the mass fraction of both odorant compounds were sampled for each time step (approximately $0.01\ s$) at a point in the center of the outlet duct and distant $1\ mm$ of the outlet, shown in Figure 52.

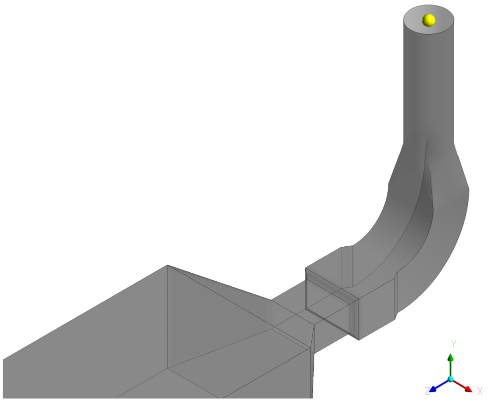

Figure 52 – Point selected to analyse the stabilization time for the mass-fraction numerical simulations.

Figure 53 presents the mass-fraction variation for both studied odorant compounds for the point shown in the Figure 52 along the simulated time, with the three studied velocities. For both cases, it is notable that the stabilization time is lower for the higher inlet velocity ($3.82\ m\ s^{-1}$) and slightly rises for the intermediate inlet velocity ($2.55\ m\ s^{-1}$), a greater increase occur for the lower inlet velocity ($1.27\ m\ s^{-1}$). As a stabilization time reference value valid for all the studied velocities, after approximately 75 seconds of simulation, the mass fraction achieved a stable value.

The higher stabilization time required by the lower inlet velocity simulations can indicate an improvement in the mixture of the odorant compound inside the apparatus, once the odorant compound stays inside the equipment for a longer time. Further, discuss about this topic will be made in the sequence.

A comparison of the stabilization time for the PWT and the US-EPA DFC can be performed using the data presented by Andreão *et al.* (2019), which is a result of the numerical simulations performed by the author using a similar methodology and using the same odorant compounds, H_2S and acetic acid, however for the US-EPA DFC. It appears that, due to the much lower airflow rate, the stabilization time for the US-EPA DFC was much higher, being approximately equal to $15\,min$, $30\,min$ and $50\,min$, respectively to the airflow rate of $2\,L\,min^{-1}$, $5\,L\,min^{-1}$ and $10\,L\,min^{-1}$. To compare, the average airflow rate for the UFES-PWT numerical simulations was $600\,L\,min^{-1}$, $1200\,L\,min^{-1}$ and $1800\,L\,min^{-1}$. As happened for the UFES-PWT, the stabilization time appears to be more connected with airflow rate that with odorant compound. The stabilization times for the same airflow rate and different odorant compound was very similar.

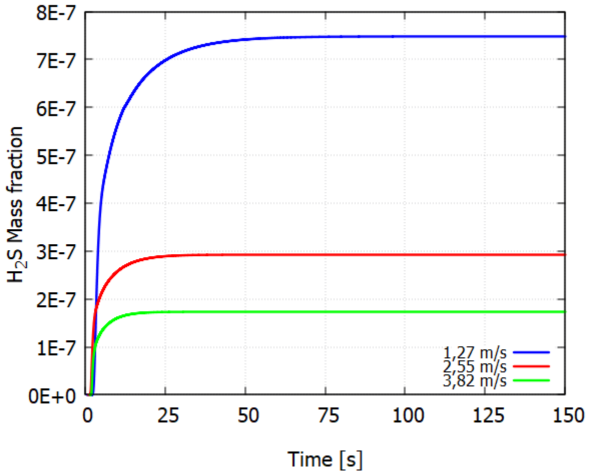

(a)

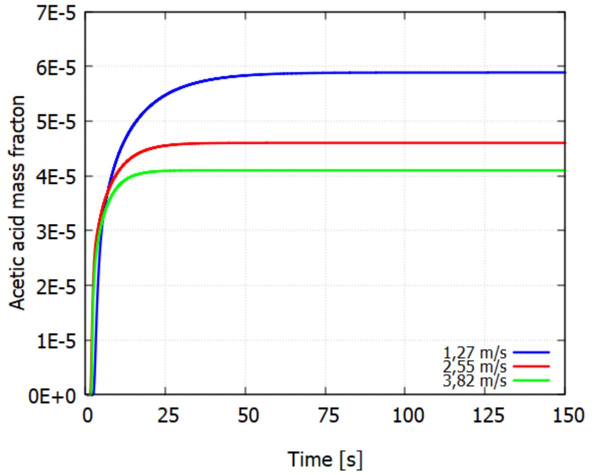

(b)

Figure 53 – Mass fraction variation for point shown in the Figure using the three different velocities for: (a) H_2S and (b) Acetic acid.

In Figures 54 and 55 is presented the mass fraction profiles plotted following the methodology shown in the Section 4.7, for both odorant compounds. However with different values, by analyzing the profiles, in general, the behavior of the mass fraction inside the apparatus was very similar, primarily in the profile at the beginning of the main section ($z = 200\,mm$). Looking at the profiles in sequence for both odorant compounds, it appears that the re-circulation zone that can be seen in the Figure 39 is sweeping the beginning of a greater odorant emission more forward, close to the middle of the main section ($z = 400$).

The variation of the inlet velocity seems to have a great influence on the mass fraction for both cases. The mass fraction rises as opposing to the increase in the inlet velocity, i.e the higher values in the mass fraction happen for the inlet velocity equal to $1.27\ m\ s^{-1}$ followed by $2.55\ m\ s^{-1}$ and $3.82\ m\ s^{-1}$. The plotted profiles cover a height range from 0.025 to $0.225\ m$, this result can show that the odorant compound emitted by the higher velocity goes directly to the outlet and is not captured by this range. This feature can be analyzed with more details looking for mass fractions distribution, plot in the Figures 57 and 56.

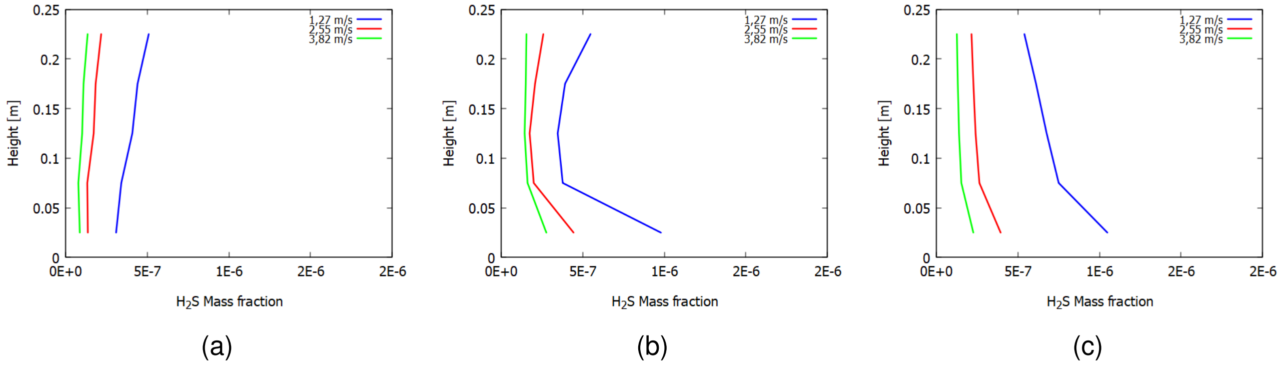

(a) (b) (c)

Figure 54 – $H2S$ mass fraction profiles for the UFES PWT numerical simulations for the three tested velocities at the positions: (a) $z = 200\ mm$; (b) $z = 400\ mm$ and (c) $z = 600\ mm$.

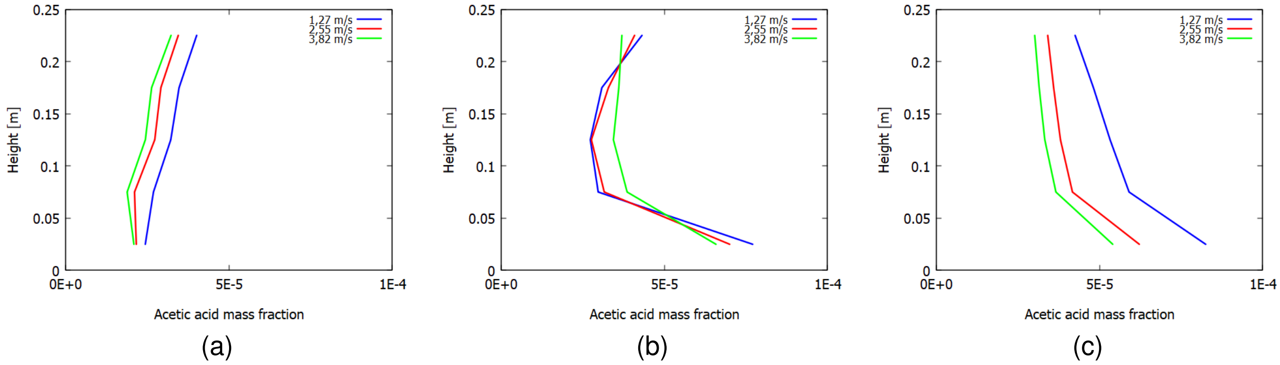

(a) (b) (c)

Figure 55 – Acetic acid mass fraction profiles for the UFES PWT numerical simulations for the three tested velocities at the positions: (a) $z = 200\ mm$; (b) $z = 400\ mm$ and (c) $z = 600\ mm$.

The Figures 57 and 56 shows the mass fractions distribution, respectively for the H_2S and acetic acid, for a side view plane for the three tested velocities. For both compounds, the transport appears to be greater for the lowest inlet velocity The H_2S emission appears to be more sensitive than the acetic acid to the velocity variations, which can be seen by both the mass fraction distribution and profiles.

To explain the difference in the sensitivity of both odorant compounds to the velocity variance, a first analysis is performed using the Schmidt number. The Schmidt number is defined by the ratio of the momentum and mass diffusivity of a certain compound in a certain medium and thus provides relative effectiveness of the mass transport(BERGMAN *et al.*, 2011). The Schmidt number (S_C) is defined in Equation 5.1, in where v is the kinematic viscosity $[m^2\ s^{-1}]$ and D is the molecular diffusivity of the solute A in the medium B $(m^2\ s^{-1})$. In this way, for the same medium, the lower values indicate a higher diffusivity and thus a higher mass transport. The Schmidt number in the air for the H_2S is equal to 1.01 and for the acetic acid is equal to 1.37 . Therefore, the observed behavior of the mass transport of H_2S, i.e. its higher sensitivity to velocity variations and its higher concentration gradients, can be explained in part when comparing the physical characteristics of both odorant compounds.

$$S_C = \frac{v}{D_{AB}} \tag{5.1}$$

Another factor that contributes to the difference in the sensitivity of both odorant compounds to the velocity variation, is the methodology used to calculate the gas-liquid interface boundary condition, i.e. the prescribed concentration. The H_2S prescribed concentration was calculated based on a liquid phase mass transfer coefficient (K_L) experimentally obtained by Siqueira (2022), with the K_L value plus the inlet airflow rate it was calculated as a H_2S mass fraction to be set as a boundary condition at the gas-liquid interface. To perform a similar calculation for the acetic acid it was necessary to obtain its gas phase mass transfer coefficient (K_G), however, according to the literature review, this value is not available in this case. Therefore, the acetic acid mass fraction was calculated using a constant acetic acid concentration in the liquid phase (PRATA JR *et al.*, 2018), with this value it was calculated the acetic acid mass fraction to be set as a boundary condition at the gas-liquid interface, however, this value does take into account the airflow rate. In such a manner, the interface boundary for the H_2S varied with inlet airflow rate, and for the acetic acid doesn't. These values, for both odorant compounds, and the calculations are presented in Section 4.4.3.

To this extent, it shows every sign that both factors, i.e. the nature of the odorant compounds plus the methodology used to calculate the interface boundary condition, contribute to the difference in the sensitivity of both odorant compounds to the velocity variation observed through the mass fraction distribution and profiles.

Another feature that can be observed through the mass fraction distribution, Figures 56 and 57, is that at the outlet duct, it can be seen a mass fraction gradient for all cases. As discussed in Section 5.2, the presence of this gradient causes a problem with the accuracy of the samples taken with the apparatus.

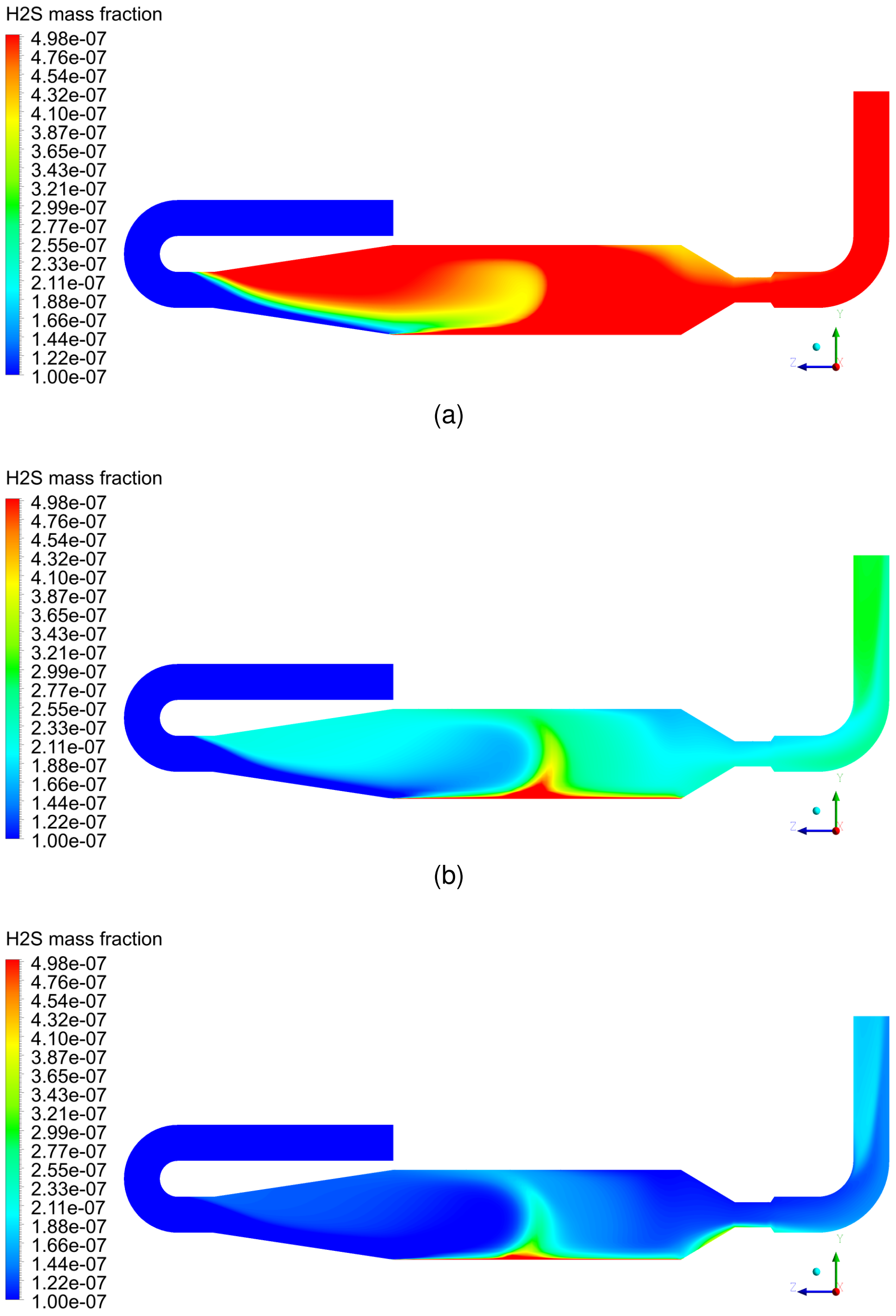

(a)

(b)

(c)

Figure 56 – H_2S mass fraction distribution side view - UFES PWT simlations: (a) $1.27\,m\,s^{-1}$; (b) $2.55\,m\,s^{-1}$ and (c) $3.82\,m\,s^{-1}$.

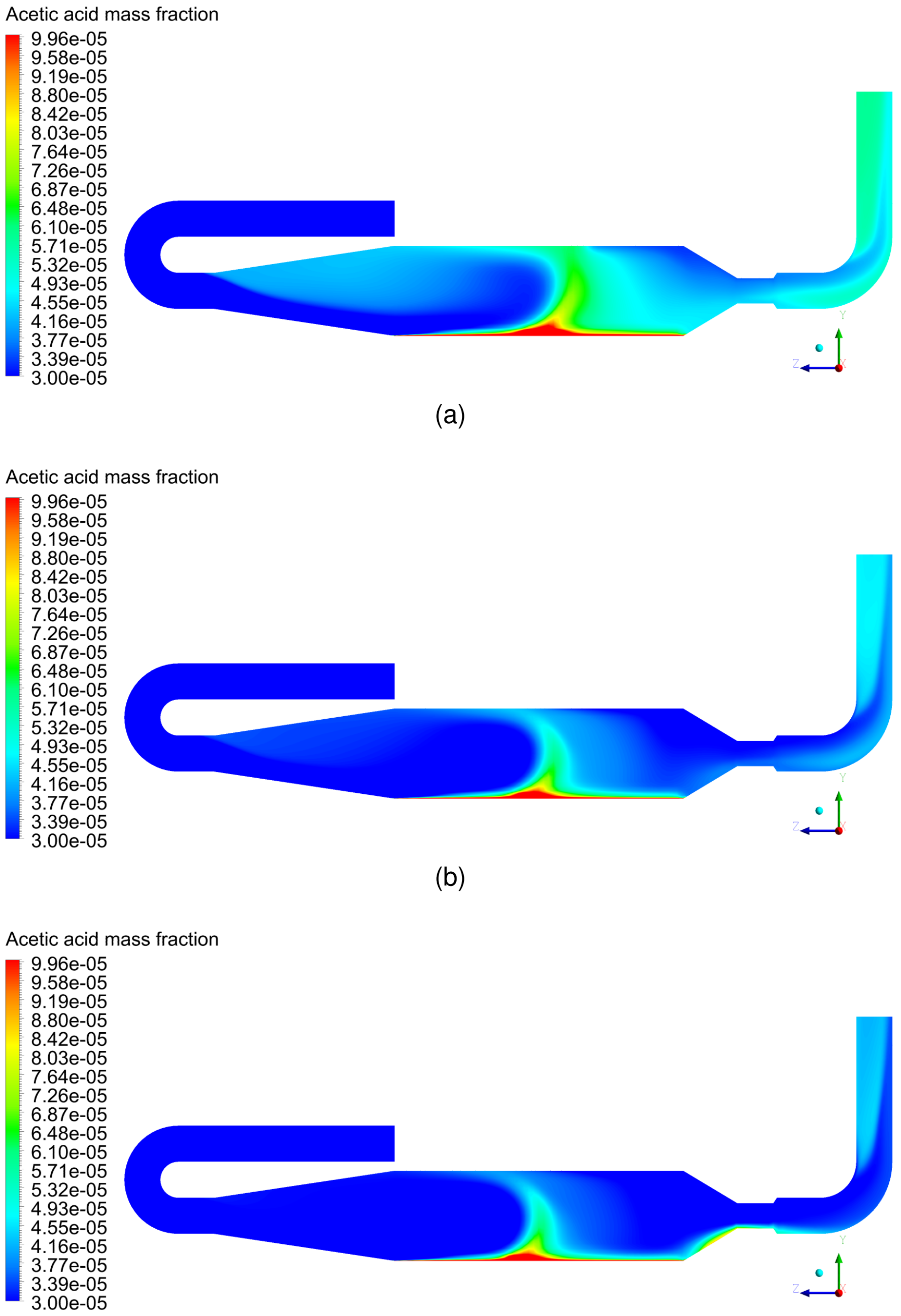

(c)

Figure 57 – Acetic acid mass fraction distribution side view - UFES PWT simlations: (a) $1.27\,m\,s^{-1}$; (b) $2.55\,m\,s^{-1}$ and (c) $3.82\,m\,s^{-1}$.

For a plane parallel and distant $1\,mm$ of the gas-liquid interface, it was calculated a gradient mass fraction (GMF) for the H_2 and acetic acid following the Equation 5.2. That is, the average mass fraction in the gas-liquid interface was subtracted from the mass fraction on a point in the plane and then divided by the distance of this plane to the gas-liquid interface. This calculation was performed for all the nodal points of the plane and is shown as gradient mass fraction contour coupled with the velocity vectors side by side with the friction velocity in Figure 58 and 59. Through these graphics it will be evaluated the effect of the airflow, via friction velocity, on the volatilization of the odorous compounds.

$$GMF = -\frac{(pontual\ mass\ fraction) - (average\ mass\ fraction\ in\ the\ gas - liquid\ interface)}{distance\ of\ the\ plane\ to\ the\ gas - liquid\ interface} \tag{5.2}$$

As it was discussed in Section 5.2, the flow in the main section of the apparatus is $3D$ and complex, with several re-circulation zones. This feature has a direct impact on the friction velocity distribution in the gas-liquid interface and thus on the volatilization of the odorant compound. Through the Figure 58 it is possible to note the direct relationship between the two variables, where the gradient mass fraction is higher when the mass fraction is also higher. The same behavior can be seen for the acetic acid, as shown in Figure 59.

Another important feature that can be seen through the Figures 58 and 59, is that there is a reversed flow in a great portion of the gas-liquid interface. Thus, it seems that the odorant compound that is being volatilized in this region does not follow immediately the main flow direction, in an opposite way it goes in the reversed flow and it is conduced to the main flow direction once it achieves the center recirculation zone, especially through the lateral accelerations. Thus, the idea that the PWT promotes a flow parallel to the gas-liquid interface or that the atmospheric flow is somehow reproduced inside its main section does not appear to be true for the studied geometries, Jiang, Bliss and Schulz (1995) and UFES-PWT. On the contrary, the flow inside the main section is complex and has a significant impact on the volatilization of the odorant compound.

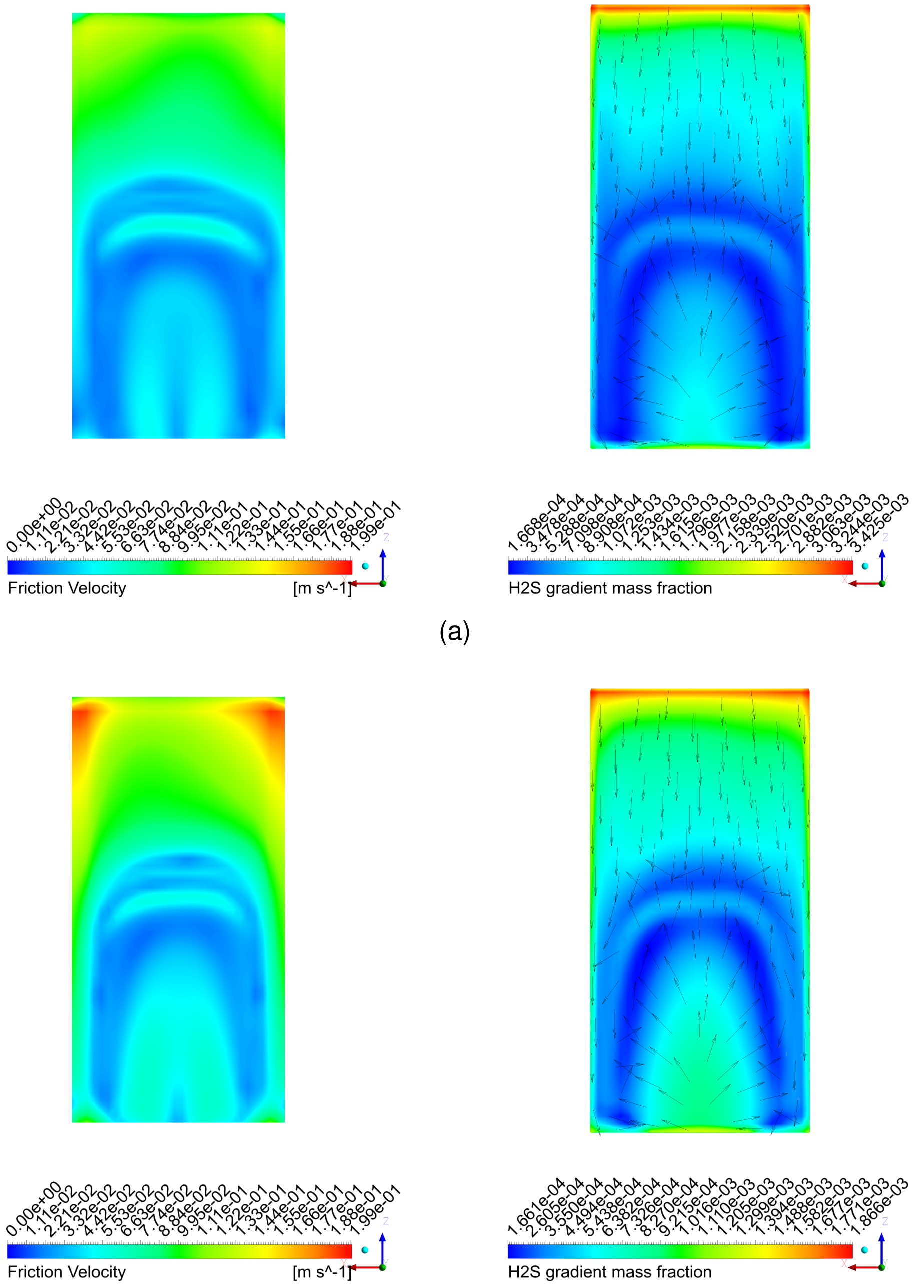

(a)

(b)

Figure 58 – H_SS gradient mass fraction contour side by side with the friction velocity - UFES PWT simlations: (a) $1.27\ m\,s^{-1}$; (b) $2.55\ m\,s^{-1}$ and (c) $3.82\ m\,s^{-1}$.

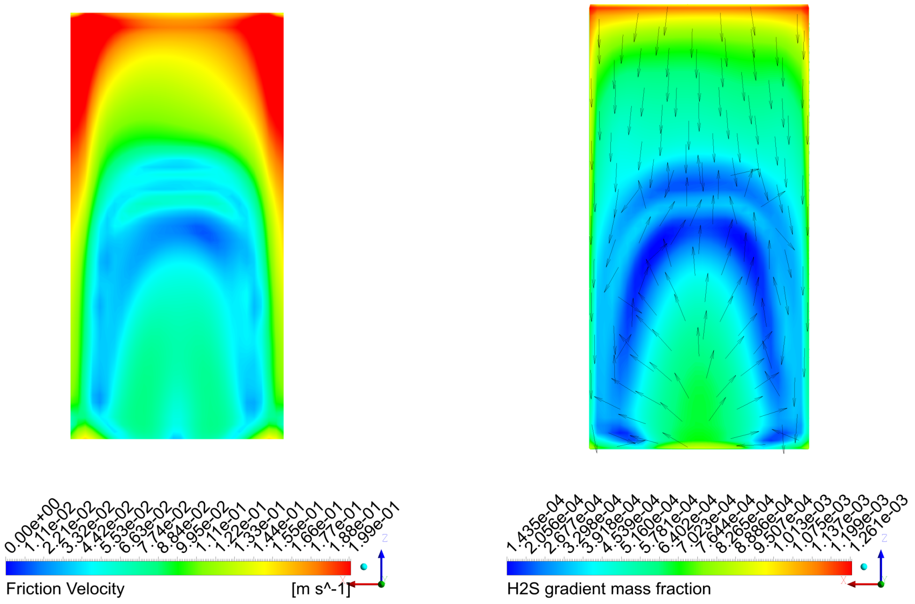

(c)

Figure 58 – H_SS gradient mass fraction contour side by side with the friction velocity - UFES PWT simlations: (a) $1.27\,m\,s^{-1}$; (b) $2.55\,m\,s^{-1}$ and (c) $3.82\,m\,s^{-1}$.

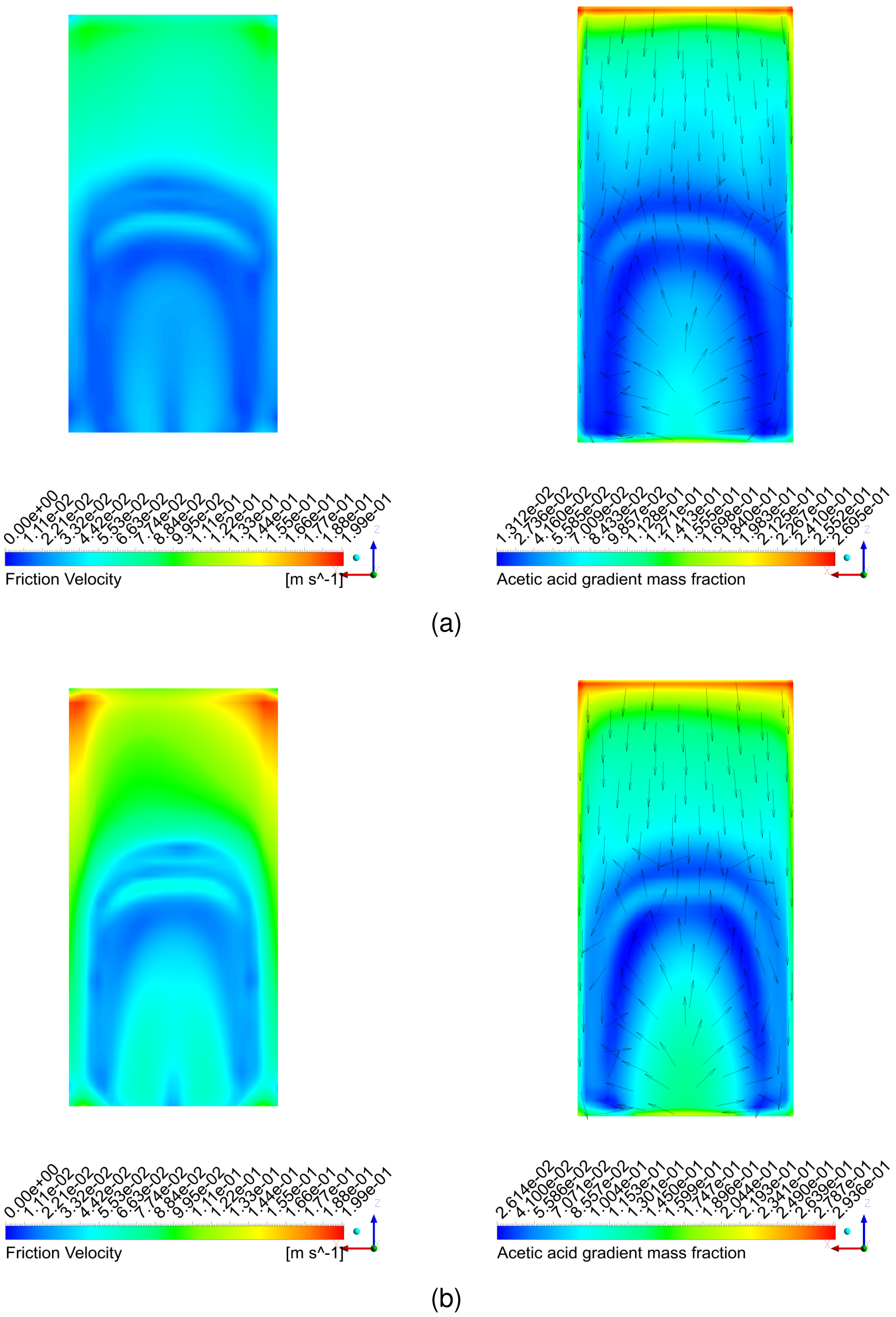

(a)

(b)

Figure 59 – Acetic acid gradient mass fraction contour side by side with the friction velocity - UFES PWT simlations: (a) $1.27\ m\,s^{-1}$; (b) $2.55\ m\,s^{-1}$ and (c) $3.82\ m\,s^{-1}$.

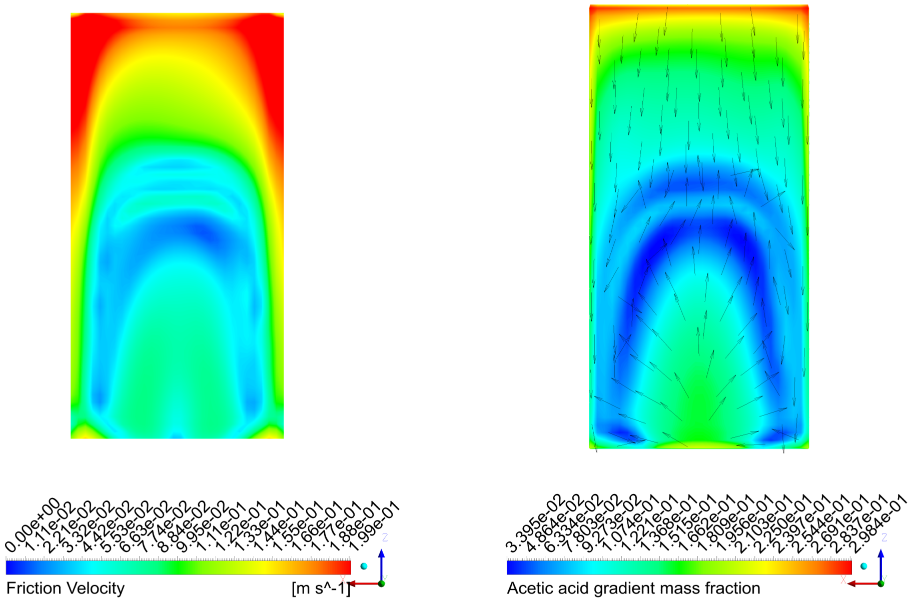

(c)

Figure 59 – Acetic acid gradient mass fraction contour side by side with the friction velocity - UFES PWT simlations: (a) $1.27\,m\,s^{-1}$; (b) $2.55\,m\,s^{-1}$ and (c) $3.82\,m\,s^{-1}$.

The Figures 61 and 62 show the mass fraction profiles for four lines located at the outlet duct of the UFES PWT. The location of the lines, distant 1 and $152\,mm$ from the outlet, is shown in Figure 60. The lines distant $152\,mm$ of the outlet are called group one and the lines distant $1\,mm$ of the outlet are called group two. Through these profiles is more clear that the mass fraction at the outlet duct isn't fully developed, nor distant or close to the outlet duct. However, analyzing the profiles for the same position at a different distance from the outlet, for example, Figures 61 a and c, it seems that the profiles show the same mass fraction distribution pattern with different intensities. This result indicates the process of profile development. The same patterns can be seen through Figures 63 and 64, in where it is plotted the mass fraction distribution at the outlet section for both odorant compounds. The average mass fraction for both odorant compounds in the outlet section is presented in Figure 19.

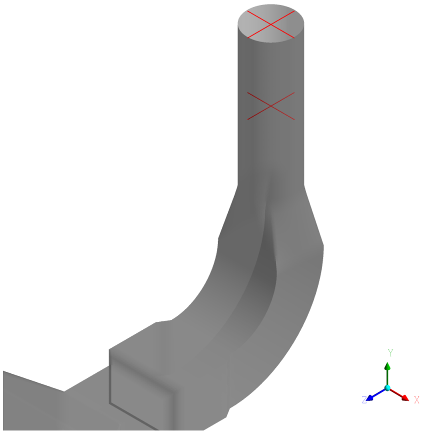

Figure 60 – Lines selected to analyze the mass fraction behavior at the outlet duct.

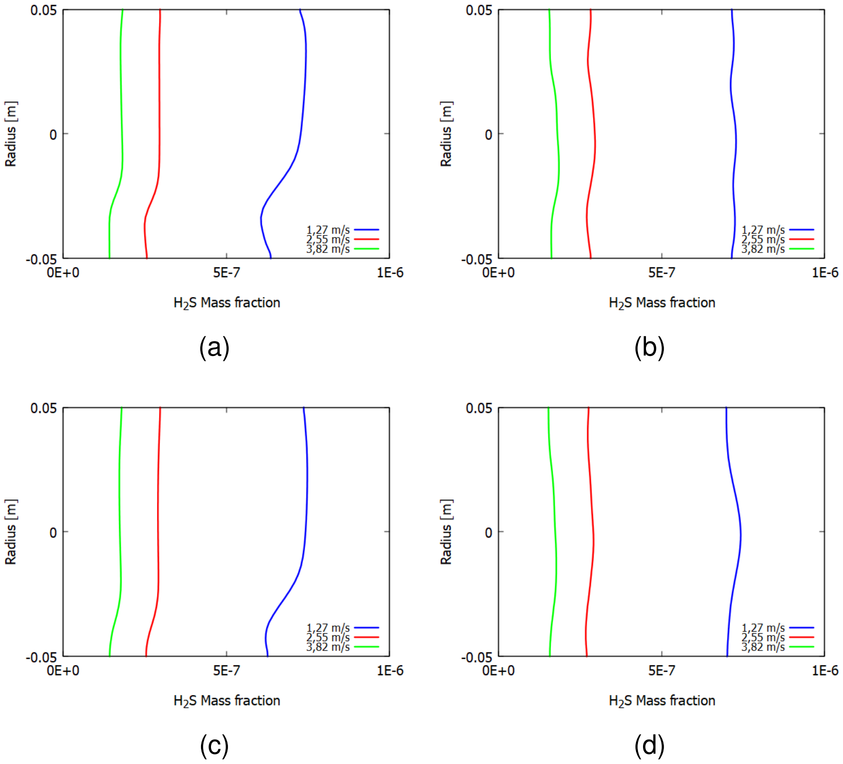

Figure 61 – $H2S$ mass fraction profiles for the UFES PWT numerical simulations at the outlet duct: (a) and (b): group one; (c) and (d) group two.

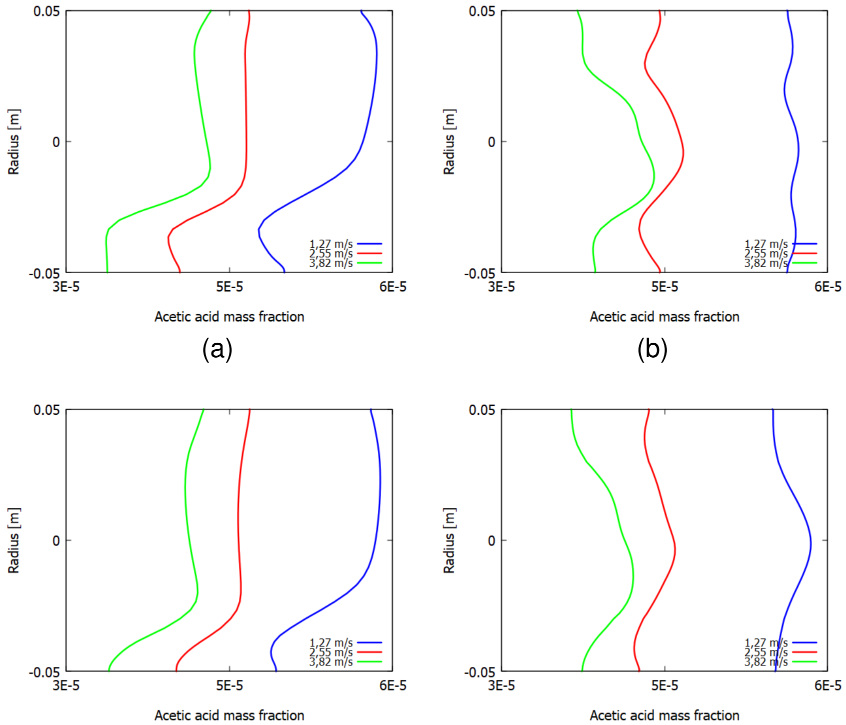

(a) (b)

(c) (d)

Figure 62 – Acetic acid mass fraction profiles for the UFES PWT numerical simulations at the outlet duct: (a) and (b): group one; (c) and (d) group two.

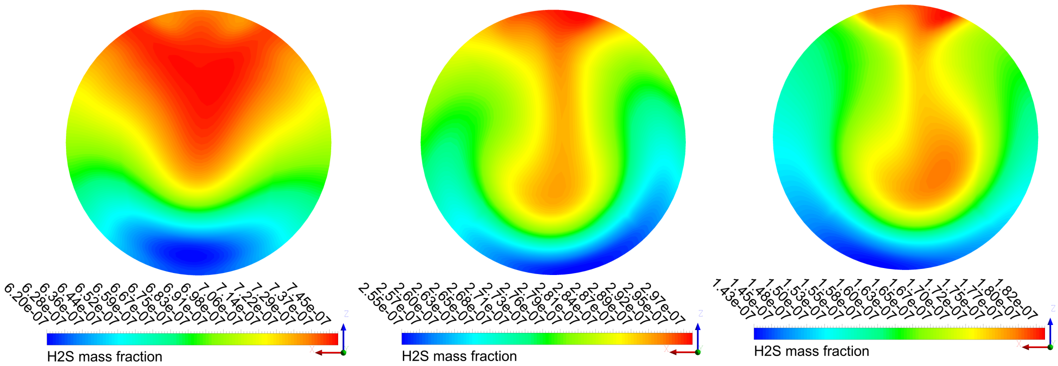

(a) (b) (c)

Figure 63 – H_2S mass fraction at the outlet section of the UFES PWT for different inlet velocities: (a) $1.27\ m\ s^{-1}$; (b) $2.55\ m\ s^{-1}$ and (c) $3.82\ m\ s^{-1}$.

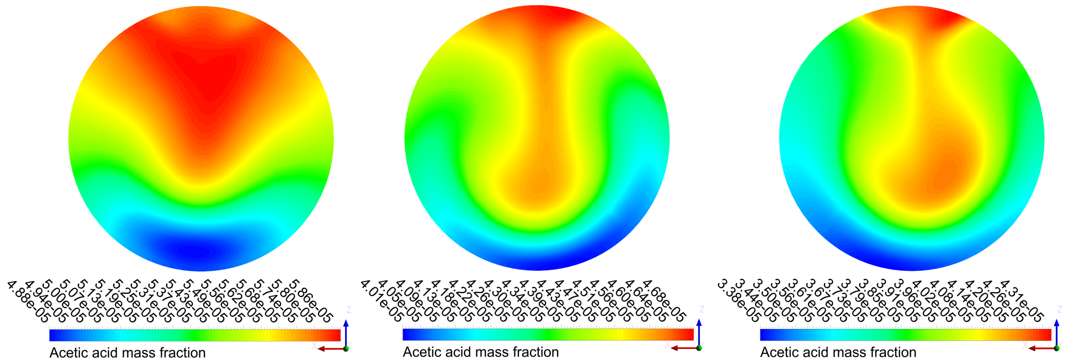

(a) (b) (c)

Figure 64 – Acetic acid mass fraction at the outlet section of the UFES PWT for different inlet velocities: (a) $1.27\ m\,s^{-1}$; (b) $2.55\ m\,s^{-1}$ and (c) $3.82\ m\,s^{-1}$.

Average velocity inlet	Average $H2S$ mass fraction - outlet section	Average acetic acid mass fraction - outlet section
$1.27\ m\,s^{-1}$	$7.05E-07$	$5.55E-05$
$2.55\ m\,s^{-1}$	$2.80E-07$	$4.40E-05$
$3.82\ m\,s^{-1}$	$1.65E-07$	$3.91E-05$

Table 19 – Average mass fraction in the outlet section for both odorant compounds and inlet velocities.

5.3.1 Analyze of a different boundary condition at the gas-liquid interface

To study the possible differences caused by the use of a different boundary condition to characterize the interface gas-liquid emission inside the UFES PWT. The UFES PWT simulations with H_2S were additionally conduced considering a constant mass flux at the interface. More details of the calculation and the application of this boundary condition are given at the Topic 4.4.3.

The Figure 65 shows the H_2S mass fraction distribution plotted in a side view plane when using a constant mass flux as interface boundary condition. When comparing the mass fraction distribution for the two different boundary conditions it seems that the influence of the re-circulation is attenuated when using the constant mass flux boundary condition, it was observed a lower gradient for all inlet velocities. The odorant compound seems to go directly to the outlet duct. That same pattern can be seen through the Figure 66, where its plotted the H_2S mass fraction profiles for the simulations using a constant mass flux as boundary conditions and obtained as it is shown in the Section 4.7. That is, the higher values of H_2S mass fraction were concentrated close to the interface (height 0 to $0.1\ m$), and also, as opposed to what happened when using the prescribed concentration, the profiles along the main section showed in generally the same behavior, growing in its intensity.

It also seems that because of the nature of the constant mass flux boundary condition, i.e. a constant amount of the odorant being injected into the domain, the H_2S mass fraction values were particularly higher. This feature can be seen more clearly through Figure 67, where its plotted the profile of the ratio of mass fraction obtained by the two boundary conditions. The H_2S mass fraction when using a constant mass flux has achieved a value close to 3000 time higher for the same point when compared to the ones found using the prescribed concentration. The values varied from 100 to 2810 times higher for the same point.

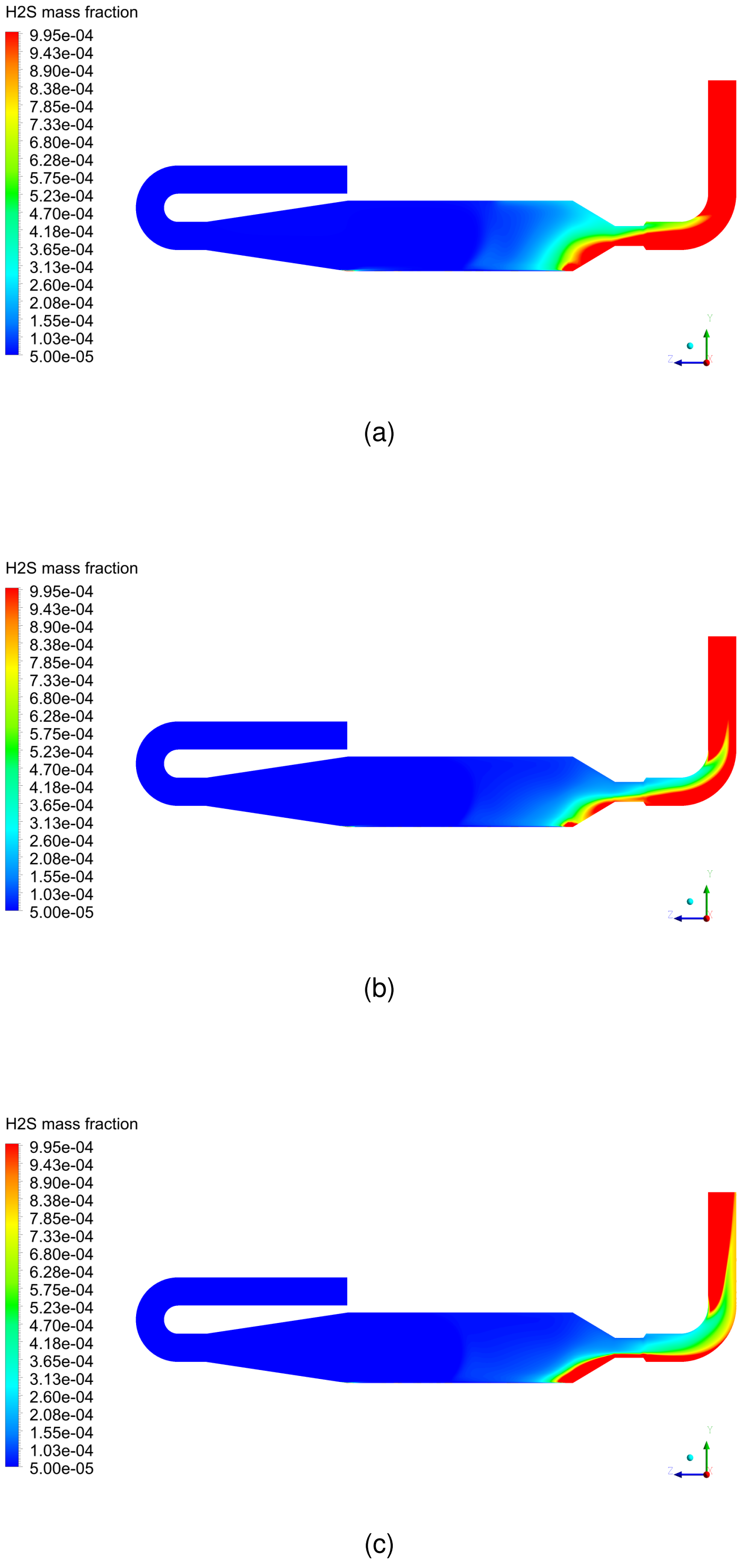

Figure 65 – H_2S mass fraction distribution side view when using a constant mass flux as interface boundary condition - UFES PWT simlations: (a) $1.27\ m\ s^{-1}$; (b) $2.55\ m\ s^{-1}$ and (c) $3.82\ m\ s^{-1}$.

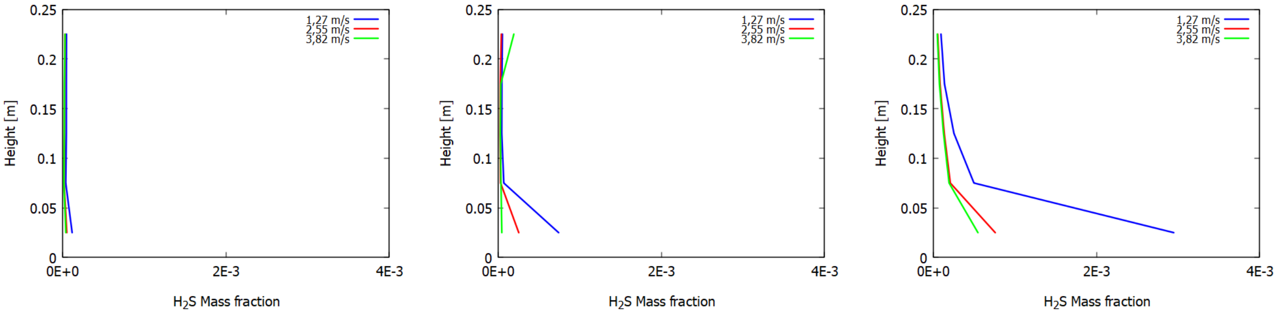

(a) (b) (c)

Figure 66 – H_2S mass fraction for the UFES PWT numerical simulations using a constant mass flux as interface boundary condition for the three tested velocities at the positions: (a) $z = 200\ mm$; (b) $z = 400\ mm$ and (c) $z = 600\ mm$.

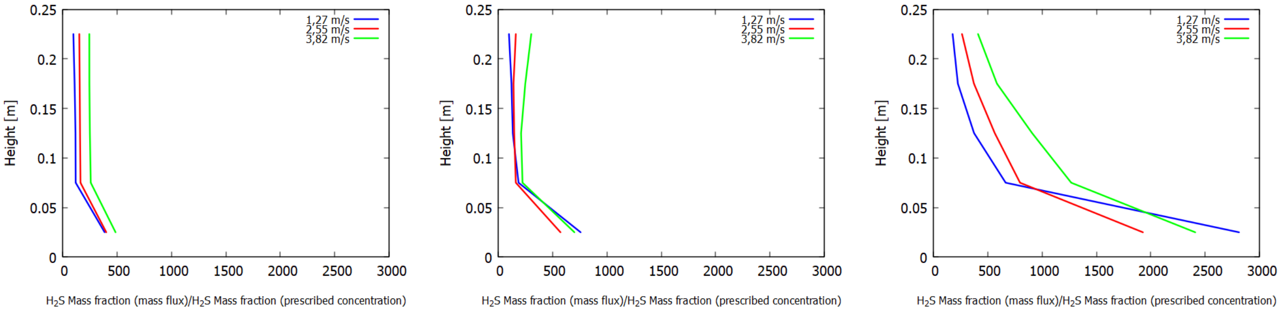

(a) (b) (c)

Figure 67 – Ratio of H_2S mass fraction obtained by the use of two boundary conditions for the UFES PWT numerical simulations for the three tested velocities at the positions: (a) $z = 200\ mm$; (b) $z = 400\ mm$ and (c) $z = 600\ mm$.

Furthermore, when looking the Figure 68, in where it is plotted the gradient mass fraction contour coupled with the velocity vectors side by side with the friction velocity, it seems that the use of the mass flux boundary condition attenuates the friction velocity effects on the gas-liquid interface. Although, the friction velocity distribution for both boundary conditions was very similar, its effect on the gradient mass fraction was not. In this case, the volatilization of the odorant compound is almost equal along the gas-liquid interface, being higher in lateral regions at the end of the main section, close to the contraction section.

Thus, it seems that an overlap of effects contributes to the higher H_2S mass fraction values and its different behavior when compared to the prescribed concentration, i.e. the nature of the boundary condition (a constant inlet mass-flow rate) and the attenuation of the friction velocity effects on the gas-liquid interface.

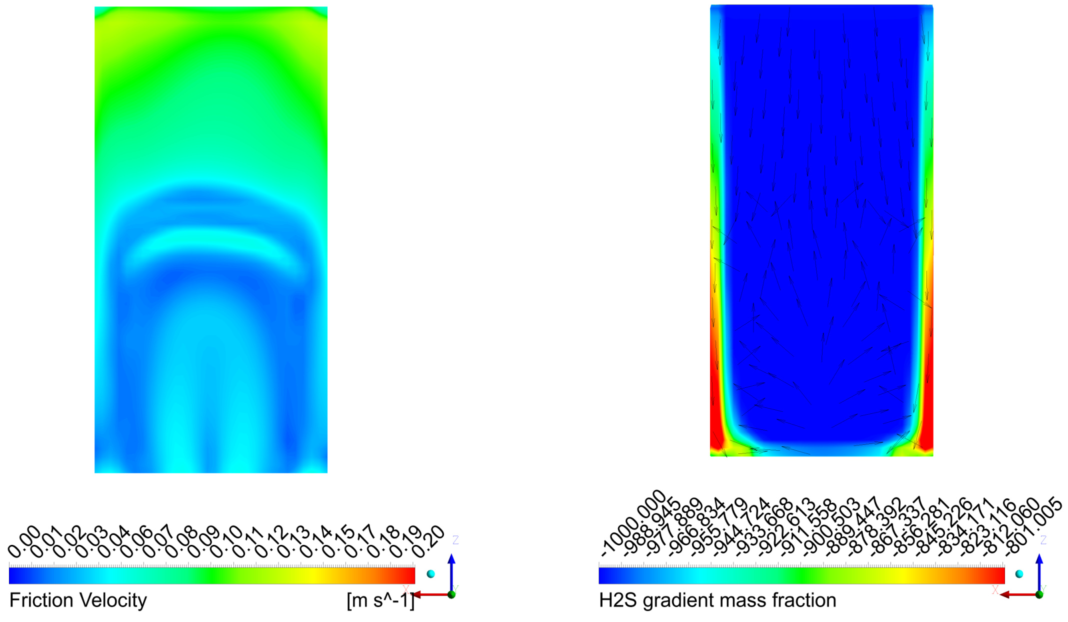

(a)

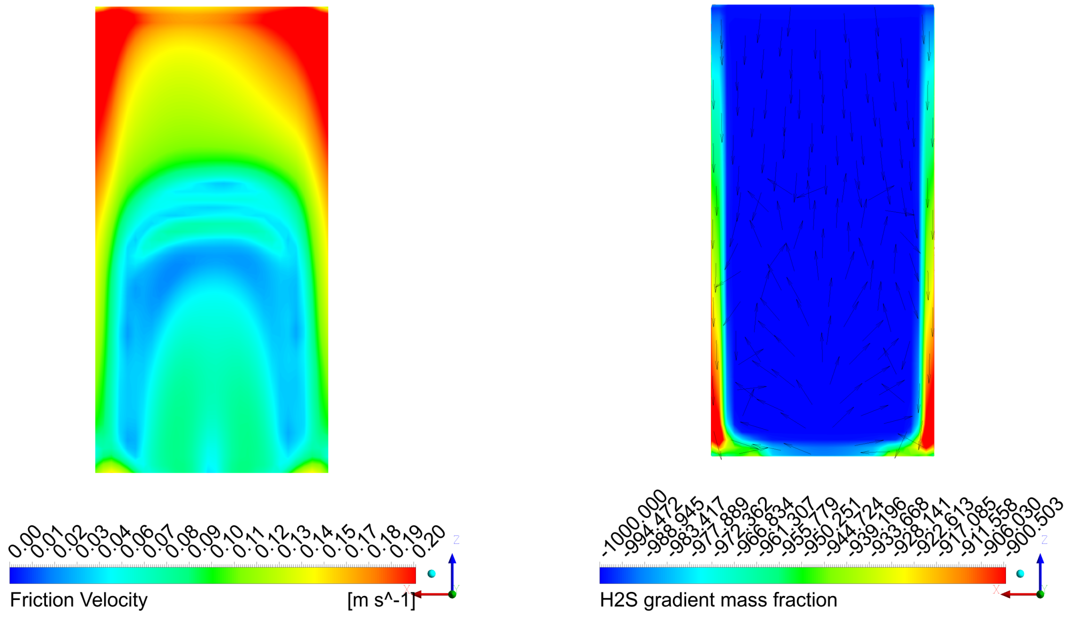

(b)

Figure 68 – H_2S gradient mass fraction distribution side by side with the friction velocity for the simulations with constant mass flux boundary condition - UFES PWT: (a) $1.27\,m\,s^{-1}$; (b) $2.55\,m\,s^{-1}$ and (c) $3.82\,m\,s^{-1}$.

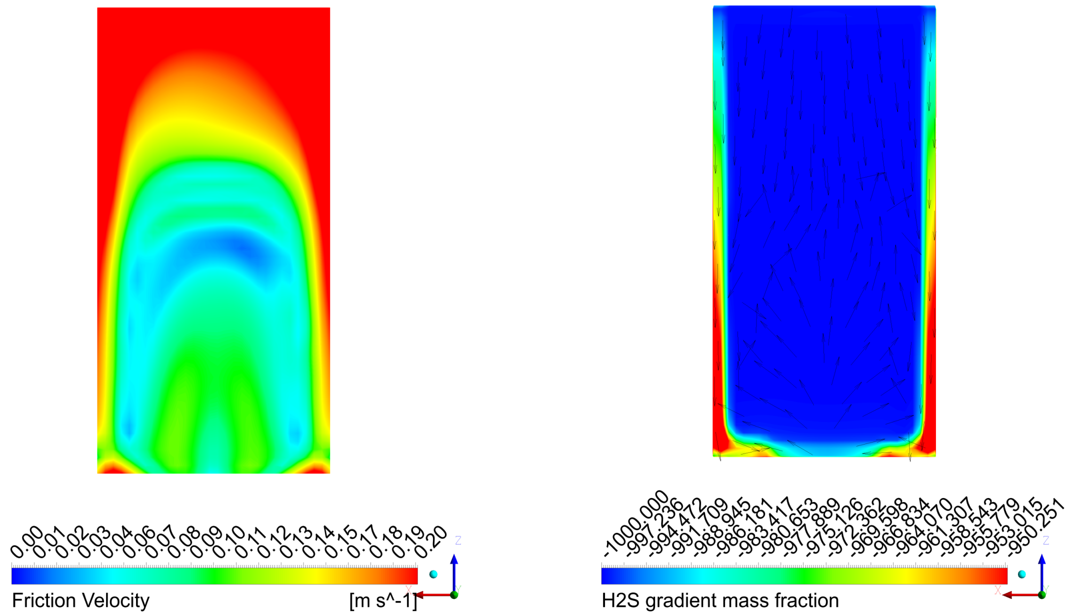

(c)

Figure 68 – H_2S gradient mass fraction distribution side by side with the friction velocity for the simulations with constant mass flux boundary condition - UFES PWT: (a) $1.27\,m\,s^{-1}$; (b) $2.55\,m\,s^{-1}$ and (c) $3.82\,m\,s^{-1}$.

About the gradient concentration at the outlet, as it is shown in Figure 69 it showed a similar behavior.

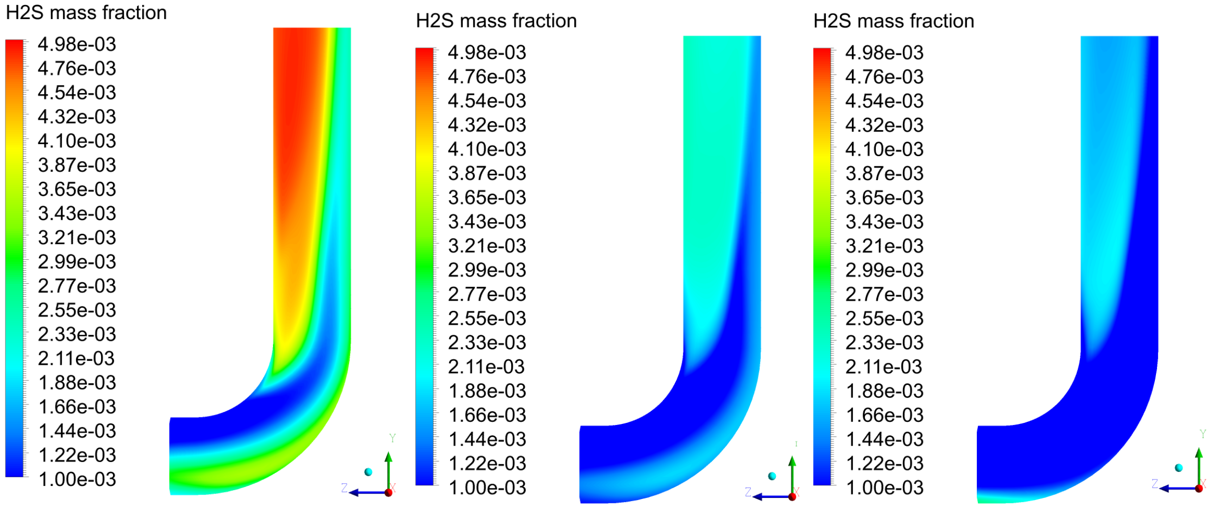

(a) (b) (c)

Figure 69 – H_2S mass fraction distribution side view in the outlet duct when using a constant mass flux as interface boundary condition - UFES PWT simlations: (a) $1.27\,m\,s^{-1}$; (b) $2.55\,m\,s^{-1}$ and (c) $3.82\,m\,s^{-1}$.

6 CONCLUSIONS

6.1 CONCLUSIONS

The main objective of the present work was to evaluate the influence of portable wind tunnel design and operational conditions on the airflow and mass transfer phenomena of odorous gases measured over passive liquid surfaces. It was simulated the airflow and mass transfer inside the UFES PWT for three different inlet average velocities, two different odorant compounds, and two different methodologies to set the gas-liquid interface boundary conditions. For the validation and mesh sensitivity test, it was simulated the airflow and mass transfer of H_2S inside the Jiang, Bliss and Schulz (1995) PWT. Thus, it was also evaluated the airflow and mass transfer variations caused by the geometrical differences between the two PWT designs. Furthermore, the flow inside the Benson *et al.* (2020) U-bend curved duct was simulated as a complementary validation and turbulence model analysis, between the $\kappa-\omega\ SST$ and standard $\kappa-\varepsilon$. For the PWT simulations it was used the $\kappa-\omega\ SST$ turbulence model.

All the numerical simulations were conduced using structured meshes, previous tests have demonstrated that the use of this type of mesh has conduced to a better numerical convergence for the PWT simulations. Due to the complexity of the geometry (i.e. with curves, expansion, contraction section, and so on) and thus the flow on its inside, it was necessary to run numerical simulations in an unsteady state and using a discretization blending factor. Through the validation step, it was faced problems concerning the Jiang, Bliss and Schulz (1995) experimental data, raising the necessity of robust experimental data concerning the $3D$ flow inside the device.

Through the PWT numerical simulations, both geometries, it was shown that for all the studied cases, the airflow inside the apparatus showed to be complex and $3D$, with several re-circulation zones and not showing a flow parallel to the liquid surface and nor the atmospheric flow in the liquid surface, seems to be represented. It was also shown that the airflow inside the device is straightly connected with the mass transfer behavior in its inside. However, analyzing the results obtained for the different configurations and different inlet velocities, it was possible to see that small geometrical changes impose a significant effect on the airflow inside the device. This led to the conclusion that geometrical changes, such as the implementation of honeycombs in the expansion section to uniform the flow, can lead to an improvement of the airflow inside the device.

The mass fraction stabilization time reference value valid for all the studied velocities was approximately 75 seconds. A value much lower than the obtained for the US-EPA DFC by Andreão *et al.* (2019), that varied from 15 to $50\,min$. It seems that this value is straightly connected with the airflow rate, that it is much higher for the PWT, ranging from $2\,L\,min^{-1}$ to $10\,L\,min^{-1}$ for US-EPA DFC and $600\,L\,min^{-1}$ to $1800\,L\,min^{-1}$, for the UFES-PWT.

As it was discussed in the last paragraph, the numerical simulations showed that the airflow is straightly connected with the friction velocity distribution on the gas-liquid interface and thus with the volatilization process inside the apparatus. Therefore, the volatilization process was also complex and not well behaved as previously expected when looking at the literature review. That feature was observed for all the average inlet velocities and odorant compounds. For both odorant compounds, higher concentration gradients in the main section were observed for the lowest inlet velocity ($\overline{U} = 1.27\,m\,s^{-1}$). Nonetheless, it was observed that the H_2S seems to be more sensitive to the velocity variation. It seems that this happens due to its different physical properties and the used methodology to obtain its boundary condition.

The use of the constant mass flow inlet leads to a great increase in the mass fraction values and a difference in its distribution along the main section, varying from 100 to 2810 times higher for the same point. It seems that this difference was caused by an overlap of effects, i.e. the nature of the mass flow inlet boundary condition, and also, it seems that this boundary condition attenuates the effect of the friction velocity on the volatilization process.

6.2 RECOMMENDATIONS FOR FUTURE WORKS

- Perform a experimental work concerning the $3D$ structures of the flow inside the PWT in order to allow validation of numerical simulation.
- Analyze via numerical simulation and experimental work different wind tunnel configurations.

- Conduce numerical simulation of the airflow and mass transfer inside the PWT using different turbulence models, such as the RSM and LES.

BIBLIOGRAPHY

ANDREÃO, W. L.; FERONI, R. de C. Cfd modeling of different mass transfer coefficients on hydrogen sulfide emission in a flux chamber. **Environmental Science and Pollution Research**, Springer, p. 1–14, 2021.

ANDREÃO, W. L. *et al.* Effects of flux chamber configuration on the sampling of odorous gases emissions. **International Journal of Heat and Mass Transfer**, Elsevier, v. 140, p. 918–930, 2019.

ANEJA, V. P. *et al.* Dynamic chamber system to measure gaseous compounds emissions and atmospheric-biospheric interactions. In: **Environmental simulation chambers: application to atmospheric chemical processes**. [S.l.]: Springer, 2006. p. 97–109.

BAI, M. *et al.* Comparing emissions from a cattle pen as measured by two micrometeorological techniques. **Environmental Pollution**, Elsevier, v. 230, p. 584–588, 2017.

BALÉO, J.; CLOIREC, P. L. Numerical-assisted design of a wind tunnel used in the estimation of volatilization from water, waste or soil. **Environmental technology**, Taylor & Francis, v. 27, n. 4, p. 403–409, 2006.

BARCLAY, J. J.; BORISSOVA, M. Potential problems using aermod to implement current odour regulations for wwtps. **Water Science and Technology**, 2013.

BATCHELOR, C. K.; BATCHELOR, G. **An introduction to fluid dynamics**. [S.l.]: Cambridge university press, 2000.

BEGHI, S. P. *et al.* Impact assessment of odours emitted by a wastewater treatment plant. **Water Science and Technology**, IWA Publishing, v. 66, n. 10, p. 2223–2228, 2012.

BENSON, M. J. *et al.* The 2019 mrv challenge: turbulent flow through a u-bend. **Experiments in Fluids**, Springer, v. 61, p. 1–17, 2020.

BERGMAN, T. L. *et al.* **Fundamentals of heat and mass transfer**. [S.l.]: John Wiley & Sons, 2011.

BLISS, P. J.; JIANG, K.; SCHULZ, T. J. The development of a sampling system for the determination of odor emission rates from areal surfaces: Part ii. mathematical model. **Journal of the Air & Waste Management Association**, Taylor & Francis, v. 45, n. 12, p. 989–994, 1995.

BOCKREIS, A.; STEINBERG, I. Measurement of odour with focus on sampling techniques. **Waste management**, Elsevier, v. 25, n. 9, p. 859–863, 2005.

BORHAN, M. *et al.* Effects of pen bedding and feeding high crude protein diets on manure composition and greenhouse gas emissions from a feedlot pen surface. **Journal of the Air & Waste Management Association**, Taylor & Francis, v. 63, n. 12, p. 1457–1468, 2013.

BRASCHKAT, J. *et al.* Measurement of ammonia emissions after liquid manure application: I. construction of a windtunnel system for measurements under field conditions. **Zeitschrift für Pflanzenernährung und Bodenkunde**, Wiley Online Library, v. 156, n. 5, p. 393–396, 1993.

CAO, S.-J.; MEYERS, J. Influence of turbulent boundary conditions on rans simulations of pollutant dispersion in mechanically ventilated enclosures with transitional slot reynolds number. **Building and Environment**, Elsevier, v. 59, p. 397–407, 2013.

CAPELLI, L.; SIRONI, S. Combination of field inspection and dispersion modelling to estimate odour emissions from an italian landfill. **Atmospheric Environment**, Elsevier, v. 191, p. 273–290, 2018.

CAPELLI, L. *et al.* Validation of a method for odor sampling on solid area sources. **Water Science and Technology**, IWA Publishing, v. 66, n. 8, p. 1607–1613, 2012.

CAPELLI, L.; SIRONI, S.; ROSSO, R. D. Odor sampling: techniques and strategies for the estimation of odor emission rates from different source types. **Sensors**, Multidisciplinary Digital Publishing Institute, v. 13, n. 1, p. 938–955, 2013.

CAPELLI, L. *et al.* Design and validation of a wind tunnel system for odour sampling on liquid area sources. **Water Science and Technology**, IWA Publishing, v. 59, n. 8, p. 1611–1620, 2009.

CAPELLI, L. *et al.* Predicting odour emissions from wastewater treatment plants by means of odour emission factors. **Water research**, Elsevier, v. 43, n. 7, p. 1977–1985, 2009.

CHAO, H.-P. *et al.* An alternative method for predicting organic solute volatilization rates under gas and liquid turbulence. **Chemosphere**, Elsevier, v. 59, n. 5, p. 711–720, 2005.

CHENG, W.-H.; HSU, S.-K.; CHOU, M.-S. Volatile organic compound emissions from wastewater treatment plants in taiwan: legal regulations and costs of control. **Journal of environmental management**, Elsevier, v. 88, n. 4, p. 1485–1494, 2008.

CHRISTENSEN, S. *et al.* Nitrous oxide emission from an agricultural field: Comparison between measurements by flux chamber and micrometerological techniques. **Atmospheric Environment**, Elsevier, v. 30, n. 24, p. 4183–4190, 1996.

CONEN, F.; SMITH, K. A re-examination of closed flux chamber methods for the measurement of trace gas emissions from soils to the atmosphere. **European Journal of Soil Science**, Wiley Online Library, v. 49, n. 4, p. 701–707, 1998.

DAELMAN, M. R. *et al.* Methane emission during municipal wastewater treatment. **Water research**, Elsevier, v. 46, n. 11, p. 3657–3670, 2012.

DEACON, E. Gas transfer to and across an air-water interface. **Tellus**, Taylor & Francis, v. 29, n. 4, p. 363–374, 1977.

DILLING, W. L. Interphase transfer processes. ii. evaporation rates of chloro methanes, ethanes, ethylenes, propanes, and propylenes from dilute aqueous solutions. comparisons with theoretical predictions. **Environmental Science & Technology**, ACS Publications, v. 11, n. 4, p. 405–409, 1977.

EÇA, L. *et al.* The pros and cons of wall functions. In: AMERICAN SOCIETY OF MECHANICAL ENGINEERS. **International Conference on Offshore Mechanics and Arctic Engineering**. [S.l.], 2015. v. 56482, p. V002T08A012.

EKLUND, B. Practical guidance for flux chamber measurements of fugitive volatile organic emission rates. **Journal of the Air & Waste Management Association**, Taylor & Francis, v. 42, n. 12, p. 1583–1591, 1992.

FANCHI, J. R. Improved recovery. In: **Shared Earth Modeling: Methodologies for Integrated Reservoir Simulations**. [S.l.]: Gulf Professional Publishing, 2002. cap. 16, p. 272–281.

FLUENT. Manual and user guide of fluent software. **Fluent Inc**, v. 597, 2005.

FLUENT, A. *et al.* Ansys fluent theory guide. **ANSYS Inc., USA**, v. 15317, p. 724–746, 2011.

GAO, F. *et al.* Design, fabrication, and application of a dynamic chamber for measuring gas emissions from soil. **Environmental science & technology**, ACS Publications, v. 31, n. 1, p. 148–153, 1996.

GHOLSON, A.; ALBRITTON, J. R.; JAYANTY, R. Evaluation of the flux chamber method for measuring volatile organic emissions from surface impoundments. **NTIS, SPRINGFIELD, VA(USA). 1989.**, 1989.

GHOLSON, A. R. *et al.* Evaluation of an enclosure method for measuring emissions of volatile organic compounds from quiescent liquid surfaces. **Environmental science & technology**, ACS Publications, v. 25, n. 3, p. 519–524, 1991.

GLAZ, P. *et al.* Greenhouse gas emissions from waste stabilisation ponds in western australia and quebec (canada). **Water research**, Elsevier, v. 101, p. 64–74, 2016.

GODOI, A. F. L. *et al.* Human exposure to hydrogen sulphide concentrations near wastewater treatment plants. **Science of the Total Environment**, Elsevier, v. 610, p. 583–590, 2018.

GOSTELOW, P. **The modelling of odours from sewage treatment works**. Tese (Doutorado) — Cranfield University, 2002.

GOSTELOW, P.; PARSONS, S. Sewage treatment works odour measurement. **Water science and technology**, IWA Publishing, v. 41, n. 6, p. 33–40, 2000.

GOSTELOW, P.; PARSONS, S.; COBB, J. Development of an odorant emission model for sewage treatment works. **Water science and technology**, IWA Publishing, v. 44, n. 9, p. 181–188, 2001.

GOSTELOW, P.; PARSONS, S.; STUETZ, R. Odour measurements for sewage treatment works. **Water research**, Elsevier, v. 35, n. 3, p. 579–597, 2001.

HACKBUSCH, W. **Multi-grid methods and applications**. [S.l.]: Springer Science & Business Media, 2013. v. 4.

HARPER, L.; DENMEAD, O.; FLESCH, T. Micrometeorological techniques for measurement of enteric greenhouse gas emissions. **Animal Feed Science and Technology**, Elsevier, v. 166, p. 227–239, 2011.

HAYES, J.; STEVENSON, R.; STUETZ, R. The impact of malodour on communities: A review of assessment techniques. **Science of the Total Environment**, Elsevier, v. 500, p. 395–407, 2014.

HENRY, C. G.; WATTS, P. J.; NICHOLAS, P. J. The development of industry-specific odor impact criteria for feedlots using models. **Journal of the Air & Waste Management Association**, Taylor & Francis, v. 58, n. 9, p. 1177–1186, 2008.

HU, L.; DU, Y.; LONG, Y. Relationship between h2s emissions and the migration of sulfur-containing compounds in landfill sites. **Ecological Engineering**, Elsevier, v. 106, p. 17–23, 2017.

HUDSON, N.; AYOKO, G. A. Odour sampling 1: Physical chemistry considerations. **Bioresource Technology**, Elsevier, v. 99, n. 10, p. 3982–3992, 2008.

HUDSON, N.; AYOKO, G. A. Odour sampling. 2. comparison of physical and aerodynamic characteristics of sampling devices: a review. **Bioresource technology**, Elsevier, v. 99, n. 10, p. 3993–4007, 2008.

HUDSON, N.; AYOKO, G. A. Comparison of emission rate values for odour and odorous chemicals derived from two sampling devices. **Atmospheric Environment**, Elsevier, v. 43, n. 20, p. 3175–3181, 2009.

HUDSON, N. *et al.* Comparison of odour emission rates measured from various sources using two sampling devices. **Bioresource technology**, Elsevier, v. 100, n. 1, p. 118–124, 2009.

INVERNIZZI, M. *et al.* Assessment of the chemical-physical variables affecting the evaporation of organic compounds from aqueous solutions in a sampling wind tunnel. **Chemosphere**, Elsevier, v. 220, p. 353–361, 2019.

JIANG, K.; BLISS, P. J.; SCHULZ, T. J. The development of a sampling system for determining odor emission rates from areal surfaces: Part i. aerodynamic performance. **Journal of the Air & Waste Management Association**, Taylor & Francis, v. 45, n. 11, p. 917–922, 1995.

JIANG, K.; KAYE, R. Comparison study on portable wind tunnel system and isolation chamber for determination of vocs from areal sources. **Water Science and Technology**, IWA Publishing, v. 34, n. 3-4, p. 583, 1996.

KIM, M.-S. *et al.* Applicability of the dynamic chamber-capture system (dcs) for estimating the flux of ammonia emission during liquid fertilizer spreading. **Atmospheric Pollution Research**, Elsevier, 2020.

KLENBUSCH, M. **Measurement of gaseous emission rates from land surfaces using an emission-isolation flux chamber. User's guide**. [S.l.], 1986.

LAUBACH, J. *et al.* A micrometeorological technique for detecting small differences in methane emissions from two groups of cattle. **Atmospheric environment**, Elsevier, v. 98, p. 599–606, 2014.

LAUBACH, J.; KELLIHER, F. M. Measuring methane emission rates of a dairy cow herd by two micrometeorological techniques. **Agricultural and Forest Meteorology**, Elsevier, v. 125, n. 3-4, p. 279–303, 2004.

LEBRERO, R. *et al.* Odor assessment and management in wastewater treatment plants: a review. **Critical Reviews in Environmental Science and Technology**, Taylor & Francis, v. 41, n. 10, p. 915–950, 2011.

LEWIS, W.; WHITMAN, W. Principles of gas absorption. **Industrial & Engineering Chemistry**, ACS Publications, v. 16, n. 12, p. 1215–1220, 1924.

MACKAY, D.; YEUN, A. T. Mass transfer coefficient correlations for volatilization of organic solutes from water. **Environmental Science & Technology**, ACS Publications, v. 17, n. 4, p. 211–217, 1983.

MARTINS, R. *et al.* Evaluating the flow inside of portable wind tunnels for odour measurements. **Chemical Engineering Transactions**, v. 68, p. 55–60, 2018.

MENTER, F. Zonal two equation kw turbulence models for aerodynamic flows. In: **23rd fluid dynamics, plasmadynamics, and lasers conference**. [S.l.: s.n.], 1993. p. 2906.

MENTER, F. R. Two-equation eddy-viscosity turbulence models for engineering applications. **AIAA journal**, v. 32, n. 8, p. 1598–1605, 1994.

National Research Council *et al.* Hydrogen sulfide acute exposure guideline levels. In: **Acute Exposure Guideline Levels for Selected Airborne Chemicals**. [S.l.]: National Academies Press (US), 2010. v. 9, cap. 4, p. 173–219.

NF X 43-104. **Qualité de l'air, atmosphères odorantes, méthodes de prélèvement**. Paris, 1995.

NI, K. *et al.* Field measurement of ammonia emissions after nitrogen fertilization—a comparison between micrometeorological and chamber methods. **European Journal of Agronomy**, Elsevier, v. 71, p. 115–122, 2015.

PAPADAKIS, G.; BERGELES, G. A locally modified second order upwind scheme for convection terms discretization. **International Journal of Numerical Methods for Heat & Fluid Flow**, MCB UP Ltd, 1995.

PARKER, D. *et al.* Standardization of flux chamber and wind tunnel flux measurements for quantifying volatile organic compound and ammonia emissions from area sources at animal feeding operations. **Atmospheric Environment**, Elsevier, v. 66, p. 72–83, 2013.

PARKER, D. B. *et al.* Effect of wind tunnel air velocity on voc flux rates from cafo manure and wastewater. In: AMERICAN SOCIETY OF AGRICULTURAL AND BIOLOGICAL ENGINEERS. **2008 Providence, Rhode Island, June 29–July 2, 2008**. [S.l.], 2008. p. 1.

PATANKAR, S. **Numerical heat transfer and fluid flow**. [S.l.]: CRC press, 2018.

PERTA, E. S. di *et al.* Study of aerodynamic performances of different wind tunnel configurations and air inlet velocities, using computational fluid dynamics (cfd). **Computers and Electronics in Agriculture**, Elsevier, v. 125, p. 137–148, 2016.

PERTA, E. S. di *et al.* Prolonged sampling time increases correlation between wind tunnel and integrated horizontal flux method. **Agricultural and forest meteorology**, Elsevier, v. 265, p. 48–55, 2019.

PI, H.; SHARRATT, B. Evaluation of the rweq and sweep in simulating soil and pm10 loss from a portable wind tunnel. **Soil and Tillage Research**, Elsevier, v. 170, p. 94–103, 2017.

POPE, S. B. **Turbulent flows**. [S.l.]: IOP Publishing, 2001.

PRATA, A. A. *et al.* A critical review on liquid-gas mass transfer models for estimating gaseous emissions from passive liquid surfaces in wastewater treatment plants. **Water research**, Elsevier, v. 130, p. 388–406, 2018.

Prata Jr, A. A. **Analysis of methods for estimating the emission rate of odorous compounds from passive liquid surfaces**. Tese (Doutorado) — The University of New South Wales, 2017.

PRATA JR, A. *et al.* Use of computational fluid dynamics in the analysis of a portable wind tunnel for sampling of odorous emissions at liquid surfaces. **Chemical Engineering Transactions**, v. 40, p. 145–150, 2014.

PRATA JR, A. A. *et al.* Mass transfer inside a flux hood for the sampling of gaseous emissions from liquid surfaces–experimental assessment and emission rate rescaling. **Atmospheric environment**, Elsevier, v. 179, p. 227–238, 2018.

PRATA JR, A. A. *et al.* Dynamic flux chamber measurements of hydrogen sulfide emission rate from a quiescent surface–a computational evaluation. **Chemosphere**, Elsevier, v. 146, p. 426–434, 2016.

QIANG, N.; LI, Z.; LIU, T. On odour emission rate from the working area of a municipal solid waste landfill in china. **Revista Internacional de Contaminación Ambiental**, v. 35, p. 149–158, 2019.

RATNER, B. The correlation coefficient: Its values range between+ 1/- 1, or do they? **Journal of targeting, measurement and analysis for marketing**, Springer, v. 17, n. 2, p. 139–142, 2009.

SANTOS, J. *et al.* Modelling hydrogen sulphide emission in a wwtp with uasb reactor followed by aerobic biofilters. **Water science and technology**, IWA Publishing, v. 54, n. 9, p. 173–180, 2006.

SANTOS, J. M. **Flow and dispersion around isolated buildings**. Tese (Doutorado) — The University of Manchester Institute of Science and Technology, 2000.

SANTOS, J. M. *et al.* Analysis of the aerodynamic performance of a portable wind tunnel for odour measurements. In: **AIR POLLUTION CONFERENCE BRAZIL 4th CMAS SOUTH AMERICA – Belo Horizonte: UFMG, 2019**. Belo Horizonte: [s.n.], 2019. v. 1, p. 424–428.

SANTOS, J. M. *et al.* Numerical simulation of flow and dispersion around an isolated cubical building: The effect of the atmospheric stratification. **Atmospheric Environment**, Elsevier, v. 43, n. 34, p. 5484–5492, 2009.

SANTOS, J. M. *et al.* An experimental determination of the h2s overall mass transfer coefficient from quiescent surfaces at wastewater treatment plants. **Atmospheric environment**, Elsevier, v. 60, p. 18–24, 2012.

SANTOS, J. M. *et al.* Mathematical modelling of hydrogen sulphide emission and removal in aerobic biofilters comprising chemical oxidation. **water research**, Elsevier, v. 43, n. 14, p. 3355–3364, 2009.

SCHÄFER, M. **Computational engineering: Introduction to numerical methods**. [S.l.]: Springer, 2006. v. 321.

SCHIFFMAN, S. S.; WILLIAMS, C. M. Science of odor as a potential health issue. **Journal of environmental quality**, American Society of Agronomy, Crop Science Society of America, Soil Science . . . , v. 34, n. 1, p. 129–138, 2005.

SCHWARZENBACH, R. P.; GSCHWEND, P. M.; IMBODEN, D. M. **Environmental organic chemistry**. [S.l.]: John Wiley & Sons, 2003.

SIQUEIRA, P. U. **ESTUDO EXPERIMENTAL DE TRANSFERÊNCIA DE MASSA ENTRE AS FASES LÍQUIDA E GASOSA NO INTERIOR DE UM TÚNEL DE VENTO PORTÁTIL UTILIZADO PARA ESTIMATIVA DAS TAXAS DE EMISSÃO PARA COMPOSTOS ODORANTES**. Dissertação (Mestrado) — Universidade Federal do Espírito Santo, 2022.

SMITH, J. H.; BOMBERGER, D. C.; HAYNES, D. L. Prediction of the volatilization rates of high-volatility chemicals from natural water bodies. **Environmental science & technology**, ACS Publications, v. 14, n. 11, p. 1332–1337, 1980.

SMITH, R.; WATTS, P. Determination of odour emission rates from cattle feedlots: Part 1, a review. **Journal of Agricultural Engineering Research**, Elsevier, v. 57, n. 3, p. 145–155, 1994.

SPRINGER, C.; LUNNEY, P.; VALSARAJ, K. Emission of hazardous chemicals from surface and near surface impoundments to air. **US Environmental Protection Agency, Solid and Hazardous Waste Research Division. Cincinnati, OH. Project**, n. 808161-02, p. 3–4, 1984.

STUETZ, R. M.; FRECHEN, F.-B. **Odours in wastewater treatment**. [S.l.]: IWA publishing, 2001.

VERSTEEG, H. K.; MALALASEKERA, W. **An introduction to computational fluid dynamics: the finite volume method**. [S.l.]: Pearson education, 2007.

WANG, T. *et al.* Comparison of two dynamic measurement methods of odor and odorant emission rates from freshly dewatered biosolids. **Journal of Environmental Monitoring**, Royal Society of Chemistry, v. 13, n. 6, p. 1746–1752, 2011.

WANG, X.; JIANG, J.; KAYE, R. Improvement of a wind-tunnel sampling system for odour and vocs. **Water science and technology**, IWA Publishing, v. 44, n. 9, p. 71–77, 2001.

WESSELING, P. The role of incomplete lu-factorization in multigrid methods. In: SPRINGER. **Incomplete Decomposition (ILU)—Algorithms, Theory, and Applications: Proceedings of the Eighth GAMM-Seminar, Kiel, January 24–26, 1992**. [S.l.], 1993. p. 202–214.

WILCOX, D. C. *et al.* **Turbulence modeling for CFD**. [S.l.]: DCW industries La Canada, CA, 1998. v. 2.

WILSON, J. *et al.* Estimation of the rate of gaseous mass transfer from a surface source plot to the atmosphere. **Atmospheric Environment (1967)**, Elsevier, v. 16, n. 8, p. 1861–1867, 1982.

WU, W. **Evaluation of a wind tunnel for measurement of odour emission from area sources**. Dissertação (Mestrado) — University of Manitoba, 2007.

YANG, W.-B. *et al.* Comparative assessments of voc emission rates and associated health risks from wastewater treatment processes. **Journal of Environmental Monitoring**, Royal Society of Chemistry, v. 14, n. 9, p. 2464–2474, 2012.

APPENDIX A – MESH SENSITIVITY TEST

A.1 PORTABLE WIND TUNNEL

To evaluate the sensitivity of the meshes, five meshes with different resolutions was constructed to simulate the airflow. The coarser mesh have 150.968 elements, the coarse mesh have 282.576 elements, the medium mesh have 434.112 elements, the fine mesh have 932.640 elements and the finer mesh have $1.808.940$ elements. The Table 20 presents the number of nodes and elements of the different meshes, the Figures 70 to 74 shows all the different meshes in three different perspectives. The meshes sensitivity will be evaluated to the $velocity$, tke, average friction velocity in gas-liquid interface and the $H_2Smassfraction$.

Mesh graduation	Nodes	Elements
Coarser	155.736	150.968
Coarse	290.700	282.576
Medium	445.735	434.112
Fine	954.576	932.640
Finer	1.846.854	1.808.940

Table 20 – Number of elements and nodes of the meshes used to perform the mesh sensitivity test of the Jiang, Bliss and Schulz (1995) pwt simulations.

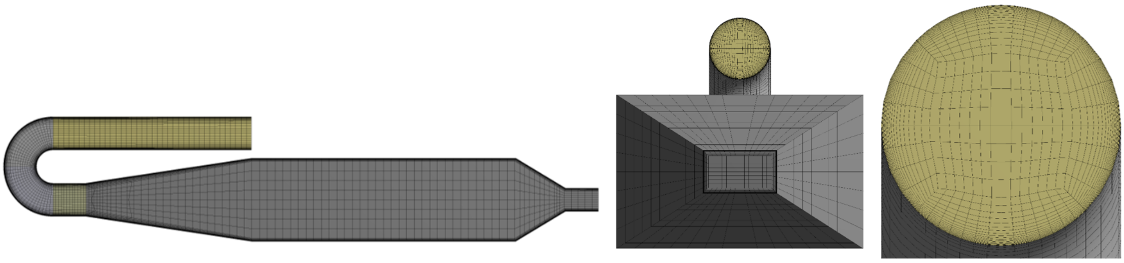
(a) (b) (c)

Figure 70 – Different views of the coarser mesh (150.968) used to perform the mesh sensitivity test of the Jiang, Bliss and Schulz (1995) pwt simulations: (a)Lateral, (b)Back and (c)Inlet duct zoom.

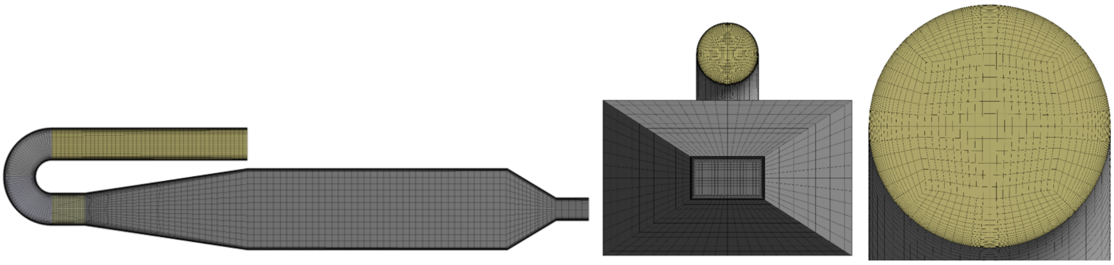

(a) (b) (c)

Figure 71 – Different views of the coarse mesh (282.576) used to perform the mesh sensitivity test of the Jiang, Bliss and Schulz (1995) pwt simulations: (a)Lateral, (b)Back and (c)Inlet duct zoom.

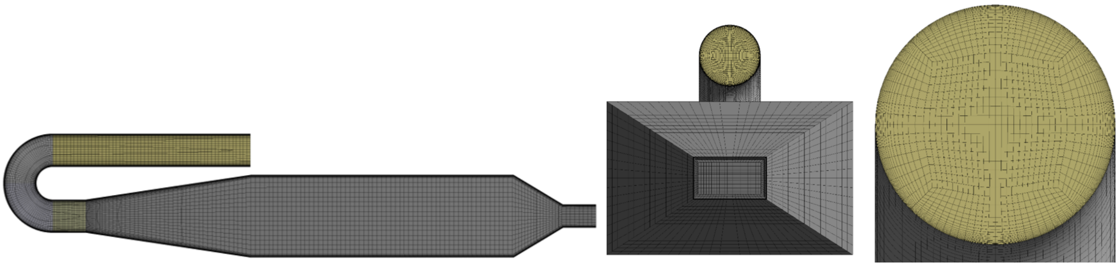

(a) (b) (c)

Figure 72 – Different views of the medium mesh (434.112) used to perform the mesh sensitivity test of the Jiang, Bliss and Schulz (1995) pwt simulations: (a)Lateral, (b)Back and (c)Inlet duct zoom.

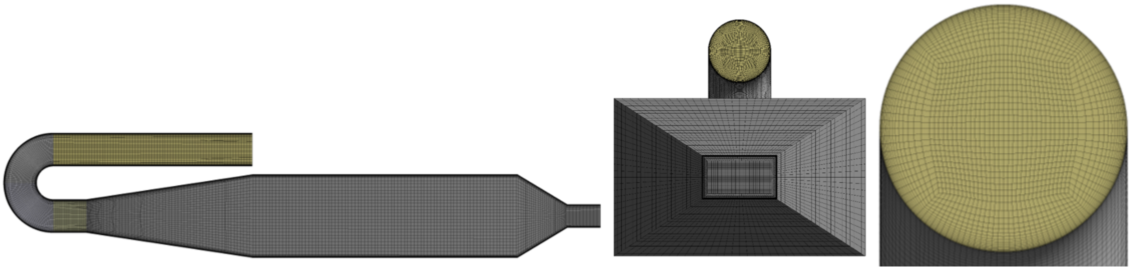

(a) (b) (c)

Figure 73 – Different views of the fine mesh (932.640) used to perform the mesh sensitivity test of the Jiang, Bliss and Schulz (1995) pwt simulations: (a)Lateral, (b)Back and (c)Inlet duct zoom.

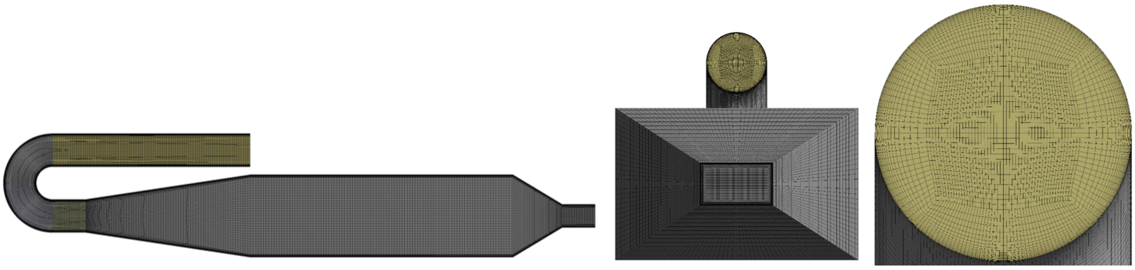

(a) (b) (c)

Figure 74 – Different views of the finer mesh (1.808.940) used to perform the mesh sensitivity test of the Jiang, Bliss and Schulz (1995) pwt simulations: (a)Lateral, (b)Back and (c)Inlet duct zoom.

Between the different meshes the first element size and the number of layers closest to the wall was fixed. It was changed the size of elements in all the three dimensions, e.g. for the coarser mesh, the size of the element in the main section was: $26\ mm$ in the longitudinal direction and $25x31\ mm$ in the transversal direction, for the coarse mesh mesh was: $20\ mm$ in the longitudinal direction and $20x21\ mm$ in the transversal direction. The Table 21 presents the size of elements in the longitudinal and transversal direction for all the meshes. It should be noted that the same pattern of mesh growth was reproduced in all the pwt geometry parts, i.e. inlet duct, expansion, contraction and measure section.

Mesh graduation	Transversal element size $[mm]$	Longitudinal size $[mm]$	Elements
Coarser	$25x31$	26	150.968
Coarse	$20x21$	20	282.576
Medium	$17x16$	14	434.112
Fine	$12x10$	10	932.640
Finer	$8x8$	8	1.808.940

Table 21 – Number of elements and nodes of the meshes used to perform the mesh sensitivity test of the Jiang, Bliss and Schulz (1995) pwt simulations.

About the quality of the meshes, the Fluent (2005) presents a quality spectrum for the two of the principal mesh metrics, the skewness and the orthogonal quality. The skewness is set as primary quality metric for a mesh, and it evaluates the difference between the cell shape and an equilateral cell of equivalent volume or area. The orthogonal quality evaluates the angle deviation between the vector that connects the centroid of the adjacent elements and the vector normal to the face. The excellent values for the skewness are in the range of $0-0.25$ and for the orthogonal quality, in the range of $0.95-1.00$ (FLUENT, 2005). The complete quality spectrums are shown in the Figure 75.

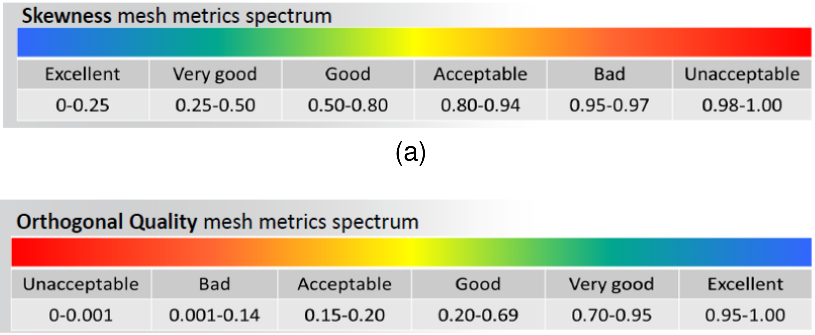

Skewness mesh metrics spectrum

Excellent	Very good	Good	Acceptable	Bad	Unacceptable
0-0.25	0.25-0.50	0.50-0.80	0.80-0.94	0.95-0.97	0.98-1.00

(a)

Orthogonal Quality mesh metrics spectrum

Unacceptable	Bad	Acceptable	Good	Very good	Excellent
0-0.001	0.001-0.14	0.15-0.20	0.20-0.69	0.70-0.95	0.95-1.00

(b)

Figure 75 – Quality spectrum for the mesh metrics: (a) Skewness and (b) Orthogonal quality Fluent (2005).

It was evaluated the worst values for both mesh metrics, i.e. the highest value for the skewness and the lowest value for the orthogonal quality. The coarser mesh and the coarse mesh presented a lowest value for orthogonal quality within the range of bad and acceptable, respectively. However, this did not have conduced to any problems in the simulations, as it will be shown. All the other meshes presented good values for both mesh metrics in its respective worst cases. The Table 22 present all the worst values for the skewness and orthogonal quality for all the meshes and its evaluation according to the quality spectrum.

Mesh graduation	Skewness		Orthogonal Quality	
	Value	Evaluation	Value	Evaluation
Coarser	0.54	Good	0.11	Bad
Coarse	0.56	Good	0.20	Acceptable
Medium	0.57	Good	0.30	Good
Fine	0.58	Good	0.46	Good
Finer	0.59	Good	0.54	Good

Table 22 – Number of elements and nodes of the meshes used to perform the mesh sensitivity test of the Jiang, Bliss and Schulz (1995) pwt simulations.

To perform first a qualitative analysis, the distribution of velocity and friction velocity are plotted respectively in the central plane - top view and in the gas-liquid interface and shown in Figures 76 and 77. It can be seen that was no significant changes between the flow structure captured by different meshes was found.

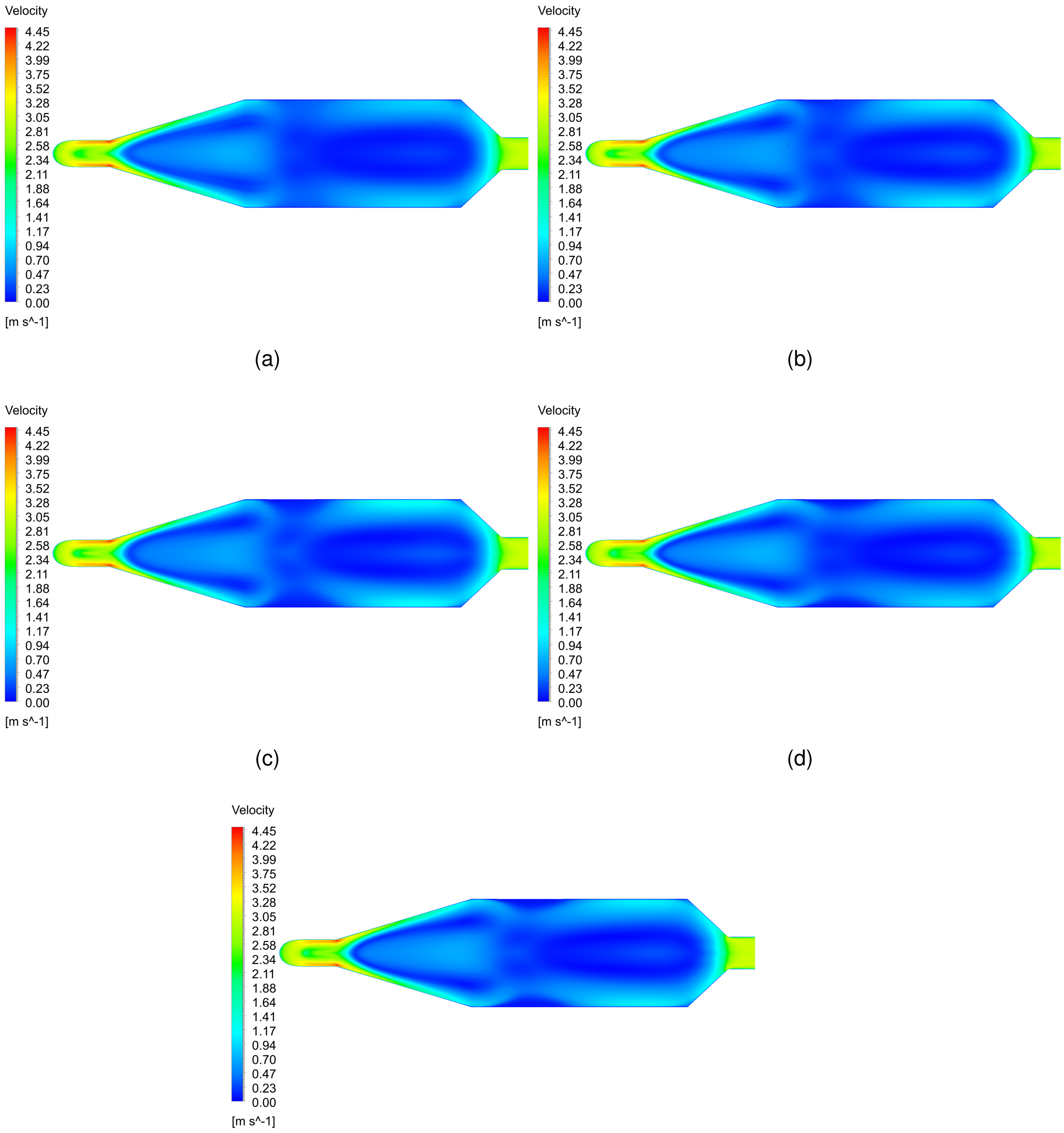

(a)

(b)

(c)

(d)

(e)

Figure 76 – Velocity distribution - central plane - top view: (a) Coarser mesh; (b) Coarse mesh (c) Medium mesh; (d) Fine mesh and (e) Finer mesh.

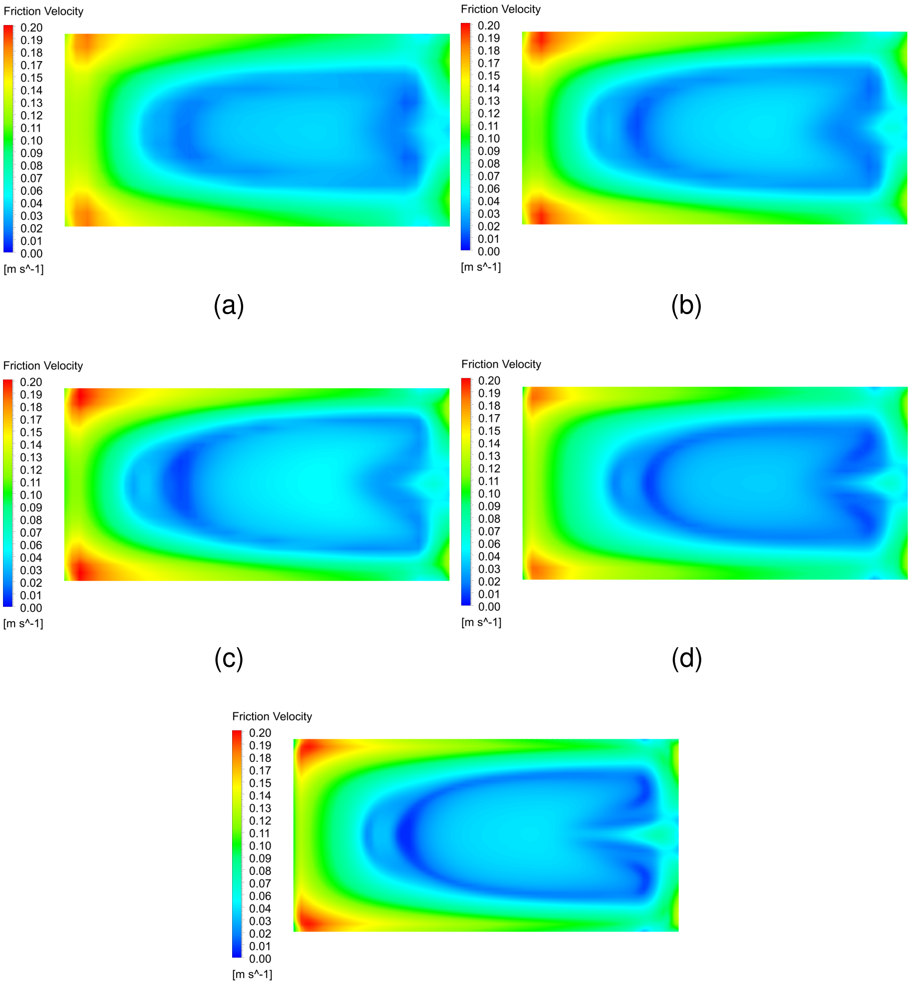

(a) (b)

(c) (d)

(e)

Figure 77 – Friction velocity distribution - gas liquid-interface: (a) Coarser mesh; (b) Coarse mesh (c) Medium mesh; (d) Fine mesh and (e) Finer mesh.

The vertical profiles used to perform the mesh sensitivity test in it self were obtained following the methodology presented at the Section 4.7. The $velocity$, tke and $H_2S\, massfraction$ profiles are shown in the Figures 78, 79 and 80. The average friction velocity in gas-liquid interface were approximately x and is presented in Table 23. It is possible to see that, as happen for the qualitative analysis, no significant modification between the profiles obtained for the different parameters was found when changing the mesh resolution to approximately 150.000 to $1.800.000$ i.e. multiplying the mesh resolution by twelve. However, as an attempt to run the simulations with less computational effort and paying attention to the minimum changes in the results that were observed between the meshes, the medium mesh (434.112 elements) was chosen to carry out the simulations.

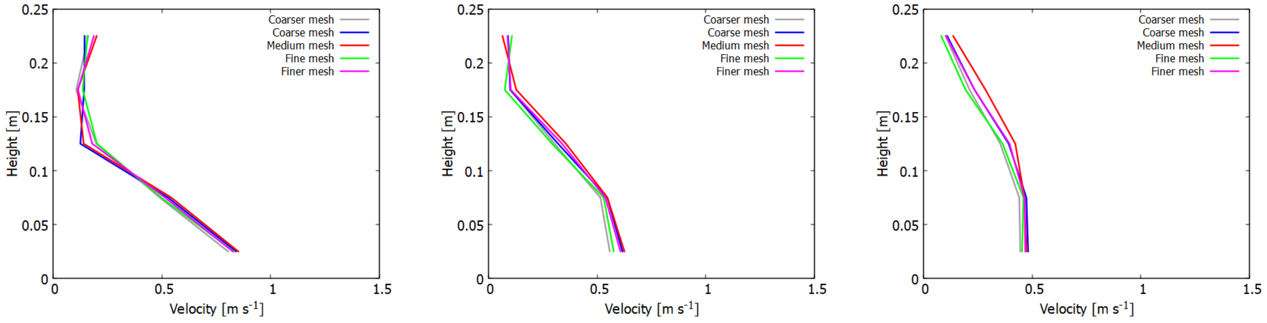

(a) (b) (c)

Figure 78 – Velocity vertical profiles - mesh sensitivity test at the positions: (a)$z = 200\ mm$; (b)$z = 400\ mm$ and (c) $z = 600\ mm$.

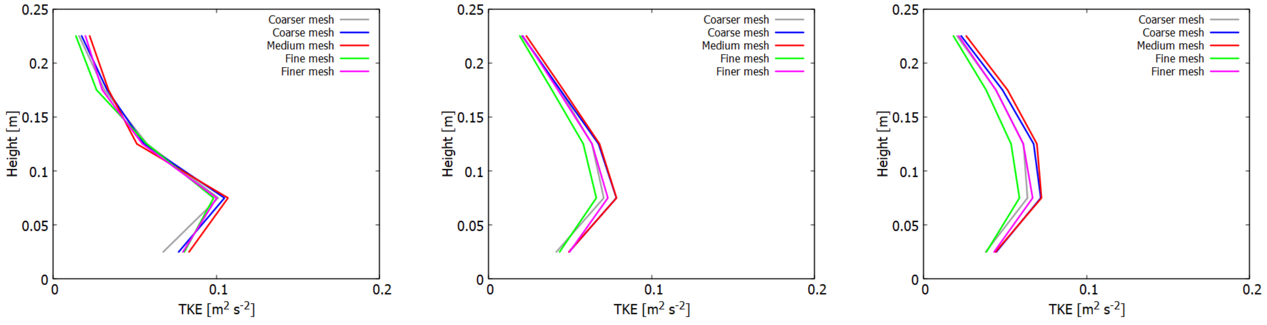

(a) (b) (c)

Figure 79 – TKE vertical profiles - mesh sensitivity test at the positions: (a)$z = 200\ mm$; (b)$z = 400\ mm$ and (c) $z = 600\ mm$.

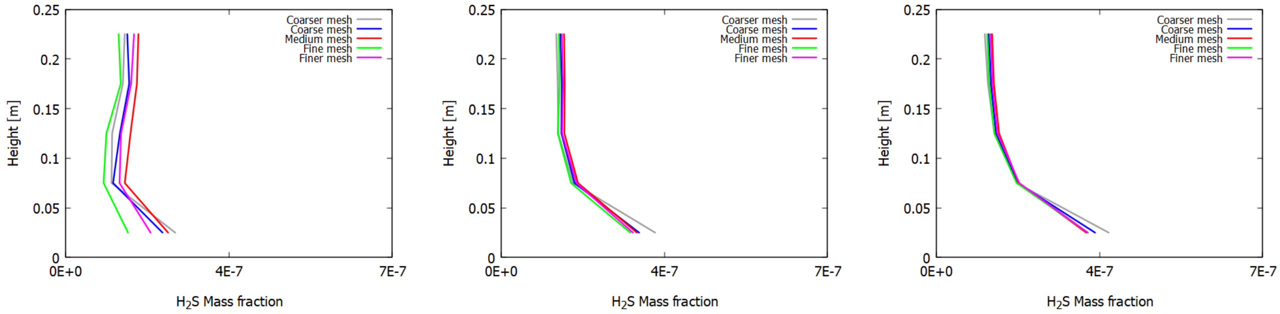

(a) (b) (c)

Figure 80 – $H_2Smassfraction$ vertical profiles - mesh sensitivity test at the positions: (a)$z = 200\ mm$; (b)$z = 400\ mm$ and (c) $z = 600\ mm$.

Mesh graduation	$\overline{u}^*$
Coarser	0.067
Coarse	0.067
Medium	0.068
Fine	0.063
Finer	0.066

Table 23 – Average friction velocity ($\overline{u}^*$) in the gas-liquid interface for the different mesh resolutions.

A.2 U-BEND

To evaluate the sensitivity of the meshes, six meshes with different resolutions was constructed to simulate the airflow using the $\kappa-\omega\ SST$ model and three using the $\kappa-\varepsilon$ model.

For the simulations using the $\kappa-\omega\ SST$ model, the coarsest mesh have 190.464 elements, the coarser mesh have 465.320 elements, the coarse mesh have 761.484 elements, the medium mesh have $1.436.180$ elements, the fine mesh have $3.381.360$ elements and the finer mesh have $7.122.720$ elements. For the simulations using the $\kappa-\varepsilon$ model, the coarse mesh have 33.792 elements, the medium mesh have 93.328 and the fine mesh have 280.575. The Tables 24 and 25 presents the number of nodes and elements of the different meshes, the Figures 81 and 82 shows all the different meshes in two different perspectives. The meshes sensitivity will be evaluated to the $velocity$ and tke.

Mesh graduation	Nodes	Elements
Coarsest	196.281	190.464
Coarser	477.432	465.320
Coarse	779.920	761.484
Medium	1.467.705	1.436.180
Fine	3.448.353	3.381.360
Finer	7.245.642	7.122.720

Table 24 – Number of elements and nodes of the meshes used to perform the mesh sensitivity test of the Benson *et al.* (2020) U bend simulations using the $\kappa-\omega\ SST$ model.

Mesh graduation	Nodes	Elements
Coarse	38.793	33.792
Medium	103.796	93.328
Fine	280.575	301.088

Table 25 – Number of elements and nodes of the meshes used to perform the mesh sensitivity test of the Benson *et al.* (2020) U bend simulations using the $\kappa-\varepsilon$ model.

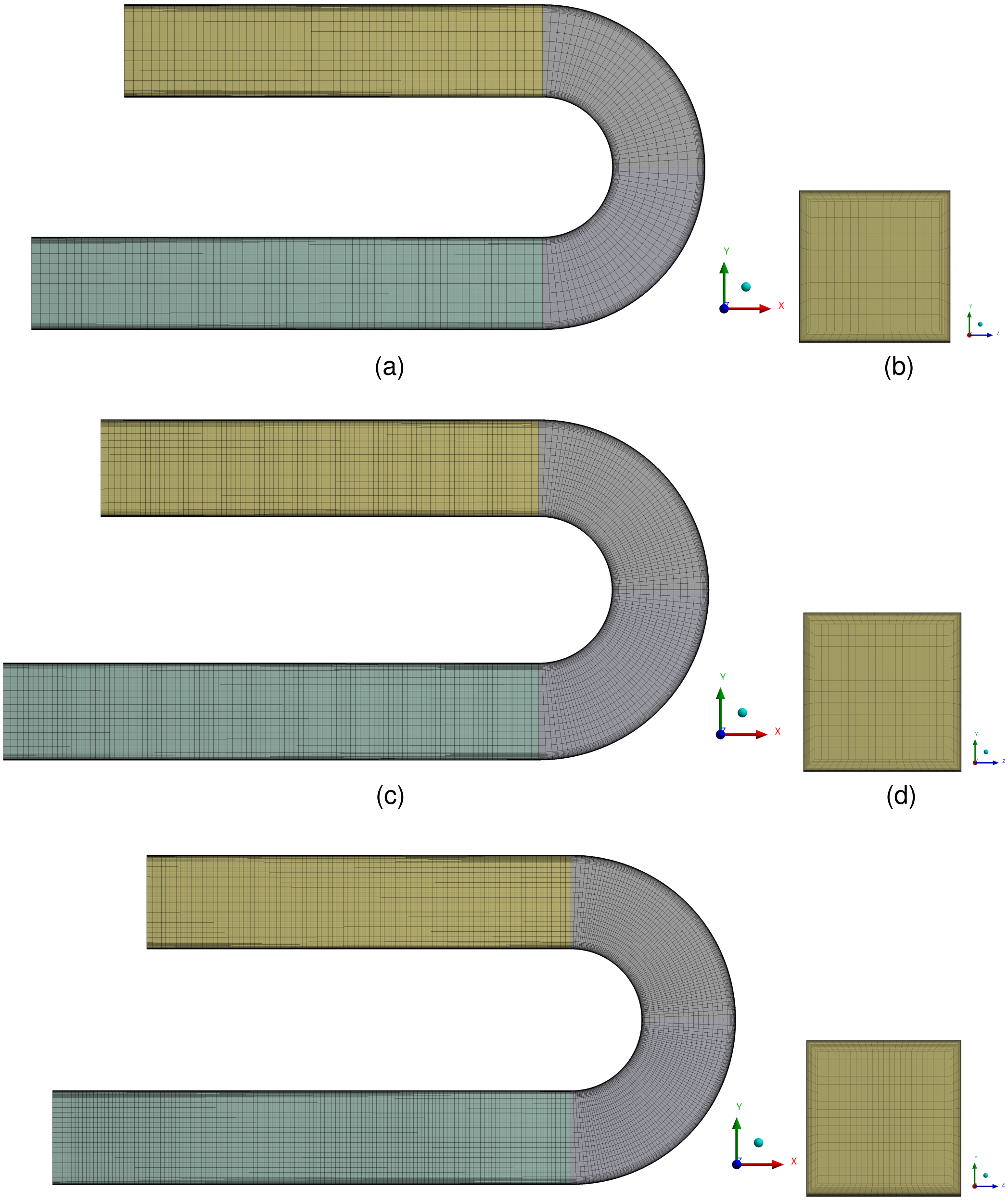

(a) (b)

(c) (d)

(e) (f)

Figure 81 – Different views of the meshes used to perform the mesh sensitivity test of the Benson *et al.* (2020) U bend using the $\kappa-\omega$ SST model: Coarsest mesh:(a)Lateral and (b)Frontal; Coarser mesh:(c)Lateral and (d)Frontal; Coarse mesh:(e)Lateral and (f)Frontal; Medium mesh:(g)Lateral and (h)Frontal; Fine mesh:(i)Lateral and (j)Frontal; Finer mesh:(k)Lateral and (l)Frontal;.

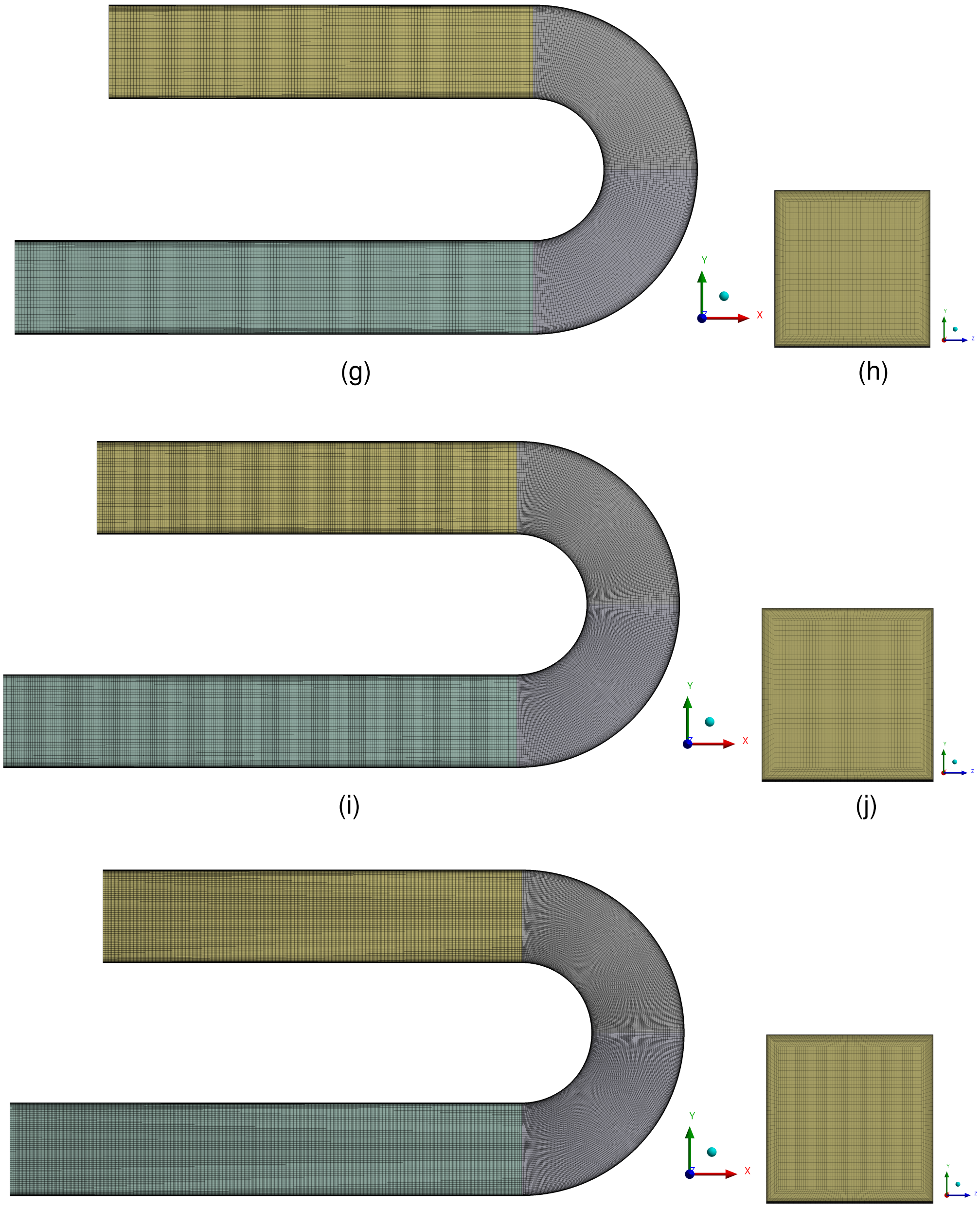

(g) (h)

(i) (j)

(k) (l)

Figure 81 – Different views of the meshes used to perform the mesh sensitivity test of the Benson *et al.* (2020) U bend using the $\kappa - \omega$ SST model: Coarsest mesh:(a)Lateral and (b)Frontal; Coarser mesh:(c)Lateral and (d)Frontal; Coarse mesh:(e)Lateral and (f)Frontal; Medium mesh:(g)Lateral and (h)Frontal; Fine mesh:(i)Lateral and (j)Frontal; Finer mesh:(k)Lateral and (l)Frontal;.

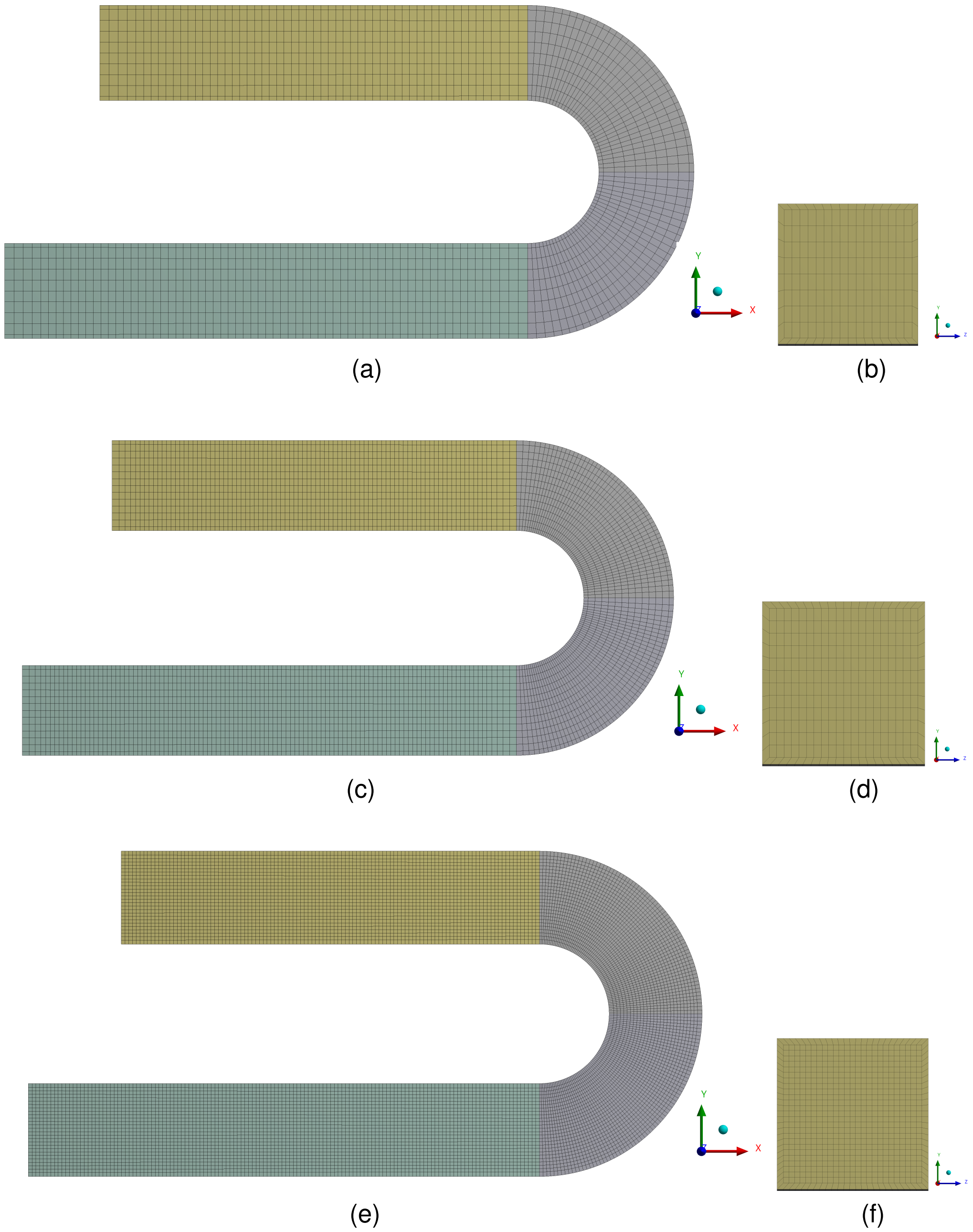

Figure 82 – Different views of the meshes used to perform the mesh sensitivity test of the Benson *et al.* (2020) U bend using the $\kappa - \varepsilon$ model: Coarse mesh:(a)Lateral and (b)Frontal; Medium mesh:(c)Lateral and (d)Frontal; Fine mesh:(e)Lateral and (f)Frontal.

The variation of the element size in the U bend geometry was performed following the same methodology as presented for the PWT geometries. That is,between the different meshes the first element size and the number of layers closest to the wall was fixed. It was changed the size of elements in all the three dimensions, e.g. for the coarsest mesh ($\kappa - \omega \;\; SST$ model) , the size of the element in the main section was: $2\, mm$ in the longitudinal direction and $1.56x3.13\; mm$ in the transversal direction, for the coarser mesh

mesh was: $1.25\ mm$ in the longitudinal direction and $1.25x2.08\ mm$ in the transversal direction. The Table 26 and 27 presents the size of elements in the longitudinal and transversal direction for all the meshes.

In order to guaranty that in the PWT and the U-bend airflow simulations similar structures are being captured, it was used a factor that relates the element size of both meshes when it was constructed, specially for the $\kappa-\omega\ SST$ model. The relation were constructed based on the diameter of the inlet duct, i.e. the diameter inlet duct of the PWT is four times larger that the U-bend edge, respectively 100 and $25\ mm$. In this way, the element size of the U-bend meshes is four times smaller than the PWT meshes element size.

Mesh graduation	Transversal element size $[mm]$	Longitudinal size $[mm]$	Elements
Coarsest	$1.56x3.13$	2	190.464
Coarser	$1.25x2.08$	1.25	465.320
Coarse	$1.04x1.56$	1	761.484
Medium	$0.78x1.04$	0.78	$1.436.180$
Fine	$0.50x0.83$	0.5	$3.381.360$
Finer	$0.37x0.60$	0.37	$7.245.642$

Table 26 – Number of elements and nodes of the meshes used to perform the mesh sensitivity test of the Benson *et al.* (2020) U bend using the $\kappa-\omega\ SST$ model.

Mesh graduation	Transversal element size $[mm]$	Longitudinal size $[mm]$	Elements
Coarse	$1.56x2$	2	38.793
Medium	$1.25x2.08$	1.25	93.328
Fine	$1.04x1.56$	2	301.088

Table 27 – Number of elements and nodes of the meshes used to perform the mesh sensitivity test of the Benson *et al.* (2020) U bend using the $\kappa-\varepsilon$ model.

To perform first a qualitative analysis for both turbulence models, the distribution of velocity are plotted in a lateral view and shown in Figures 83 and 84. For each turbulence model, it can be seen that was no significant changes between the flow structures captured by the different meshes.

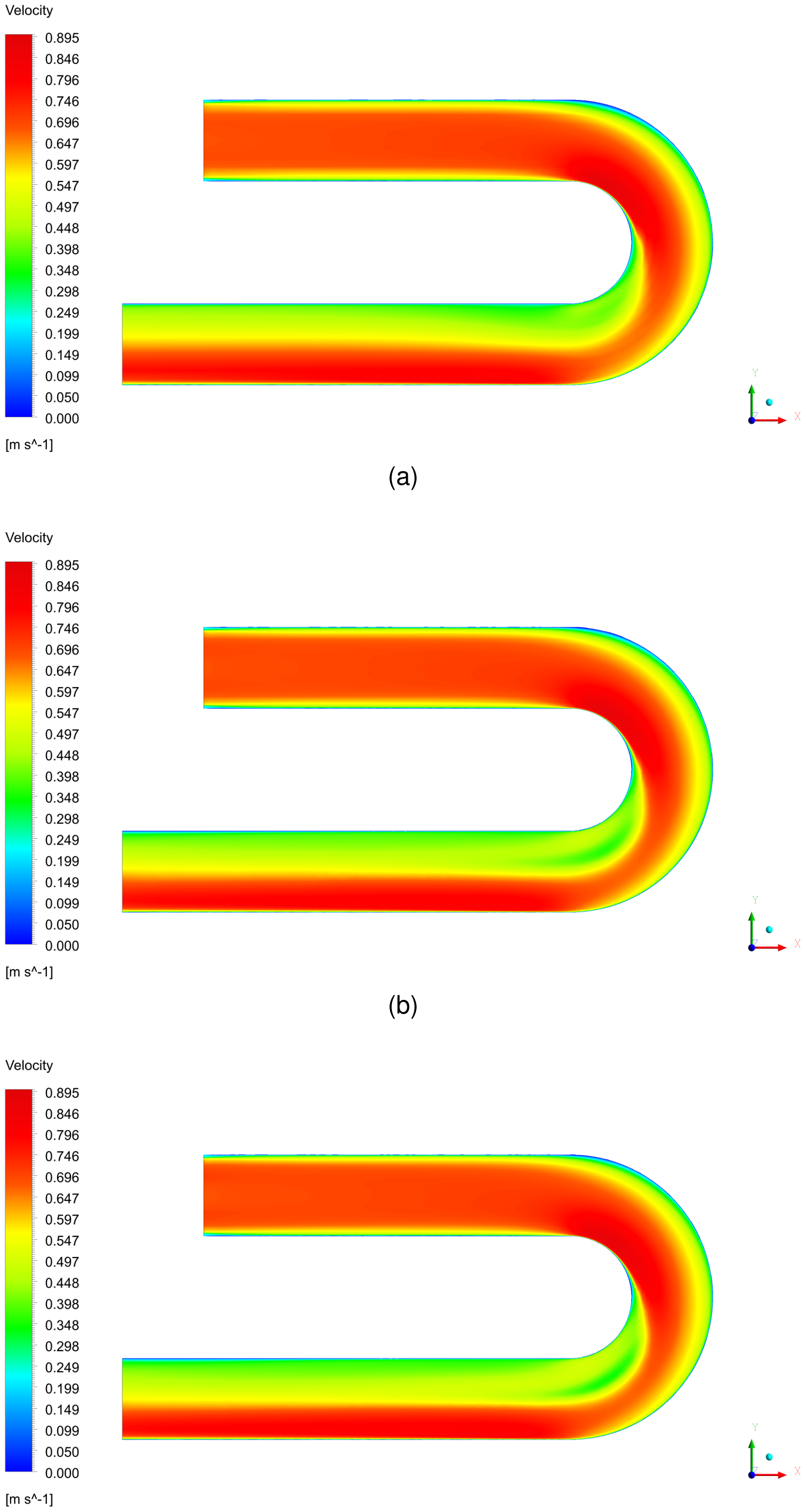

(a)

(b)

(c)

Figure 83 – Velocity distribution - Lateral view ($\kappa - \omega$ SST model): (a) Coarsest mesh; (b) Coarser mesh; (c) Coarse mesh (d) Medium mesh; (e) Fine mesh and (f) Finer mesh.

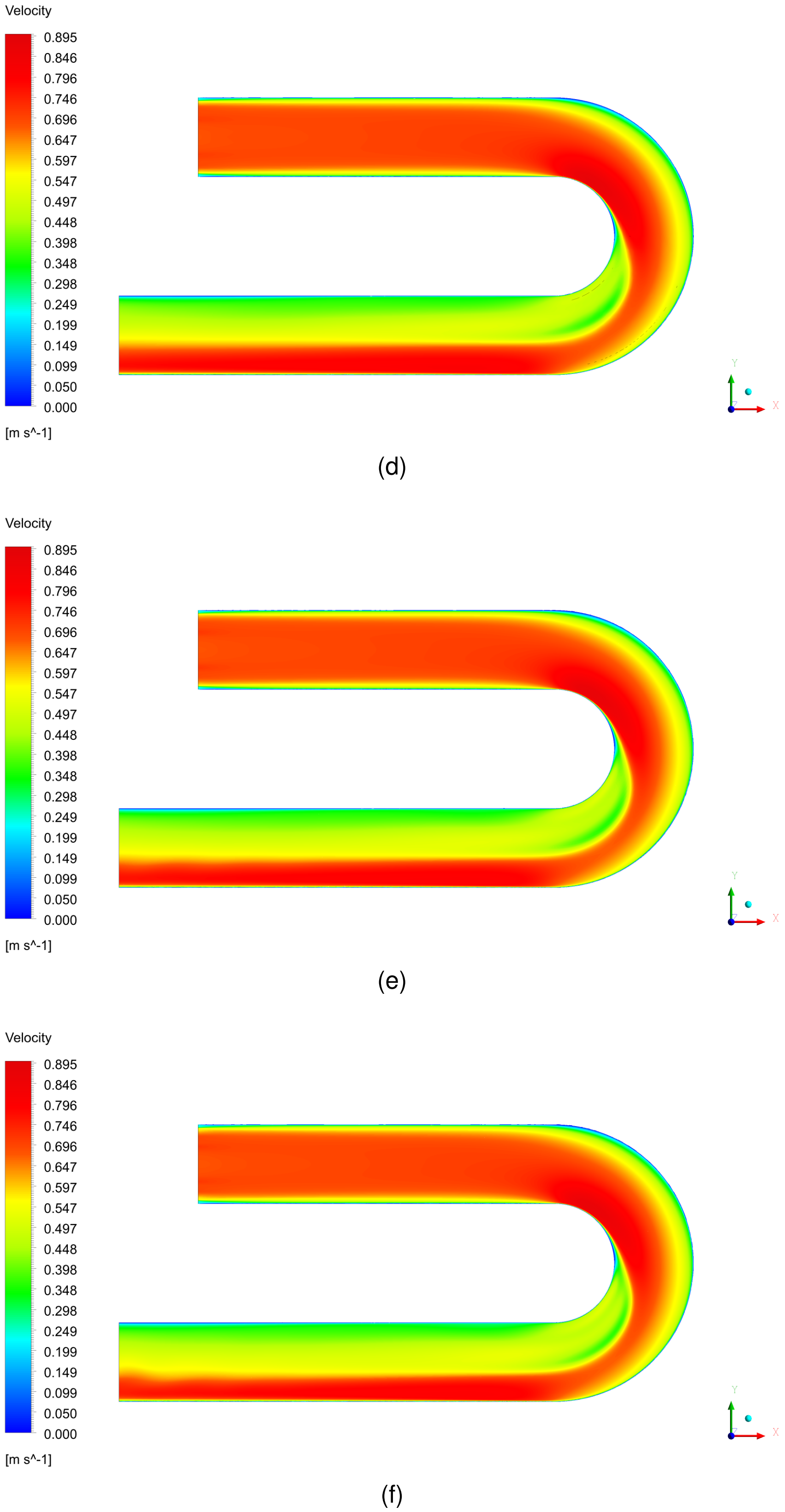

Figure 83 – Velocity distribution - Lateral view ($\kappa-\omega\ SST$ model): (a) Coarsest mesh; (b) Coarser mesh; (c) Coarse mesh (d) Medium mesh; (e) Fine mesh and (f) Finer mesh.

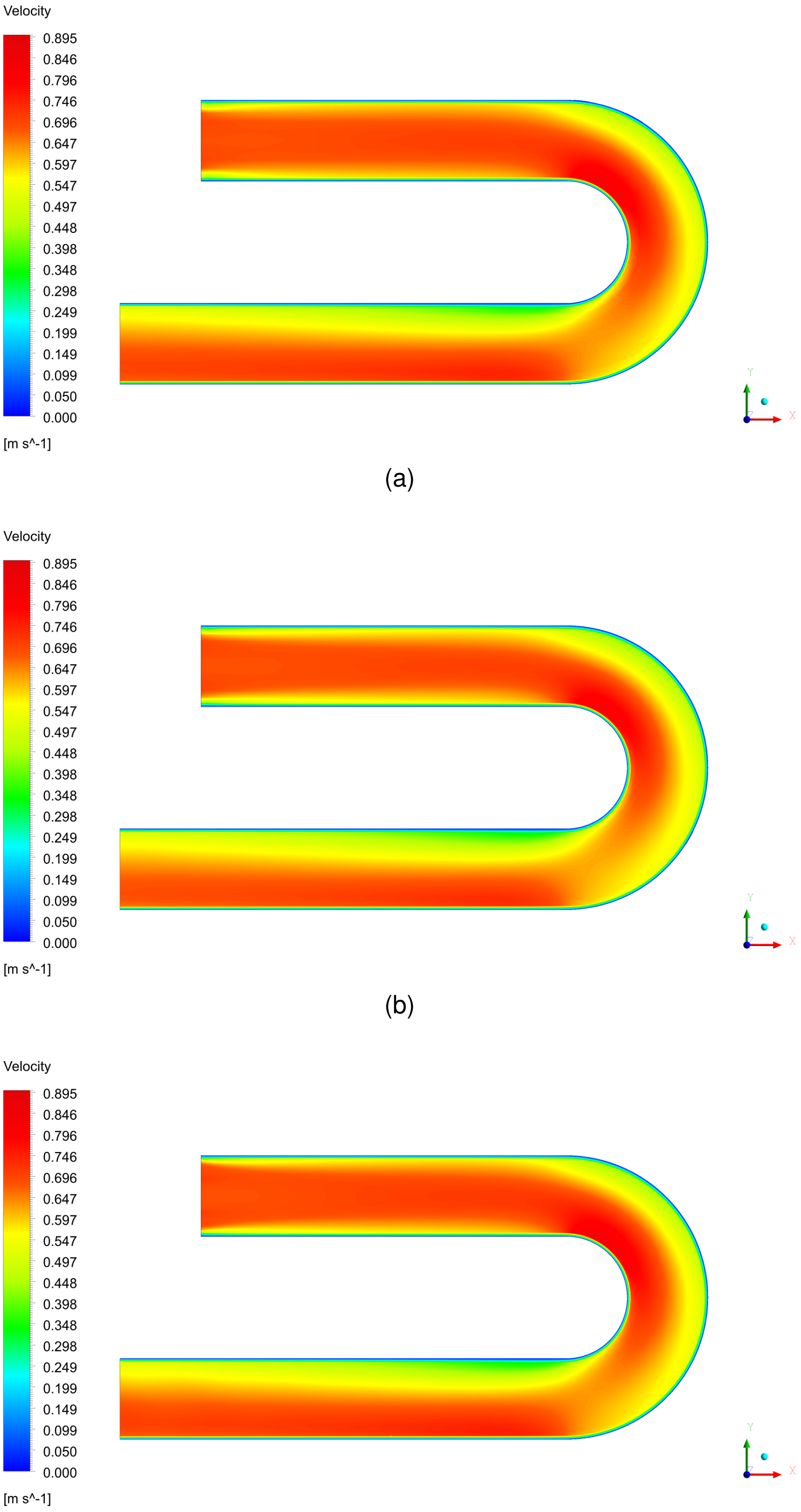

(a)

(b)

(c)

Figure 84 – Velocity distribution - Lateral view ($\kappa - \varepsilon$ model): (a) Coarse mesh (b) Medium mesh and (c) Fine mesh.

The profiles used to perform the mesh sensitivity test in it self were obtained following the methodology presented at the Section 4.7. The $velocity$ components and tke profiles are shown in the Figures 85 to 96. There was a difference in the results obtained by the different mesh resolutions for the TKE (Figure 88-c). Despite this difference, it can be seen that the same pattern was captured between the different meshes and furthermore, as the mesh resolution became finer this TKE gradient seems to be better captured and thus, lead to convergence. However, primarly because of the involved computational cost a more refined mesh was not simulated and possible errors are considered acceptable. The finer mesh have seven million elements and it is approximately 36 times finer than the coarsest. Further differences between the results, as can be seen in the Figure 87-b fall in the same behave as the explained earlier. For both turbulence models, the more refined meshes was selected to carry the results analysis (Section 5.1.1).

It is important to be aware that the primal objective of the U-bend simulations is to show that the PWT inlet curve are being well simulated and to explore the turbulence model that better simulate it ($\kappa-\omega\ SST$ or $\kappa-\varepsilon$), the presented results are considered highly acceptable to accomplish these objectives.

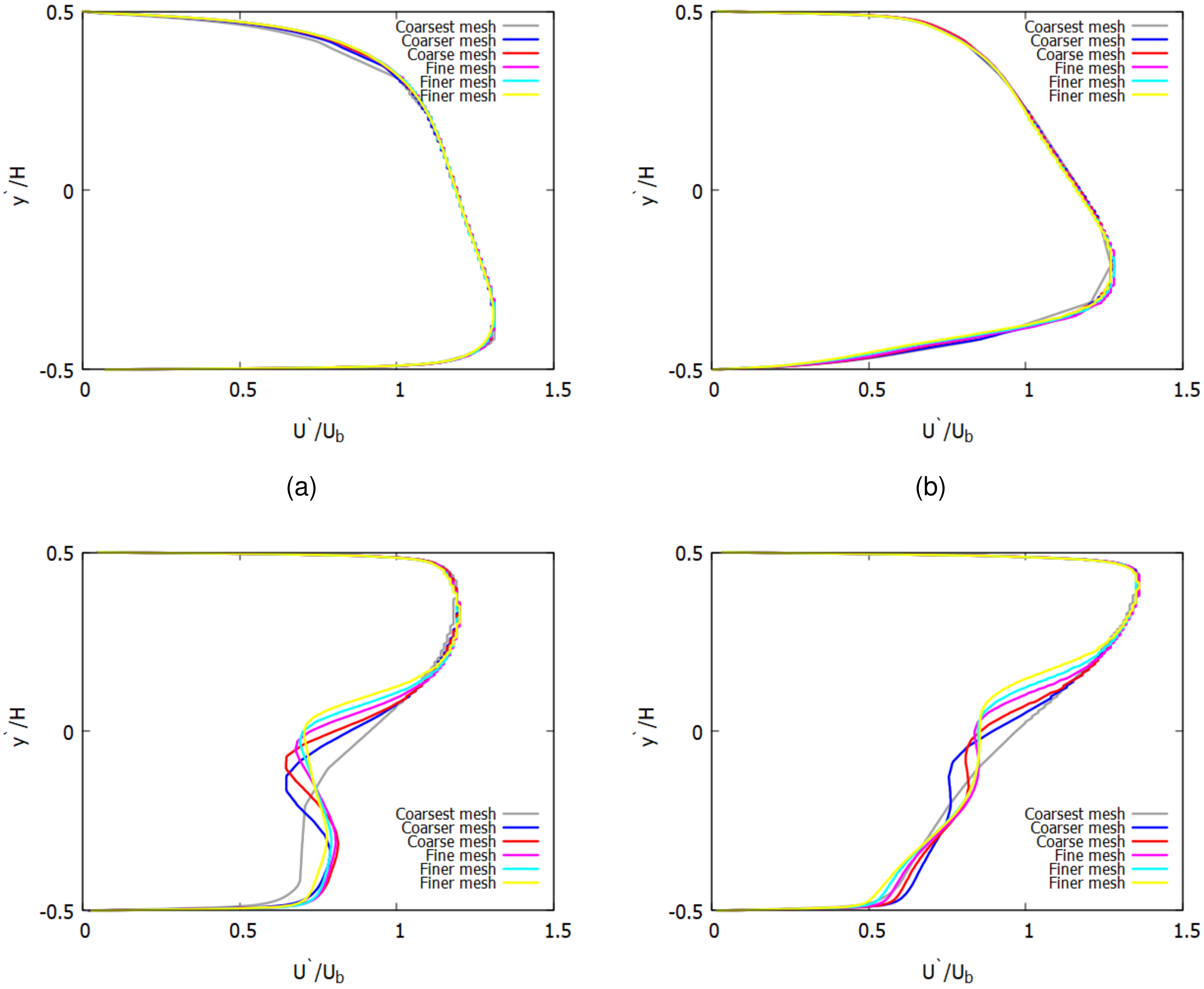

(a)

(b)

(c)

(d)

Figure 85 – Benson *et al.* (2020) U bend mesh sensitivity test ($\kappa - \omega \ \ SST$ model) - u component of the velocity profiles at the positions: (a)$z = 55\ mm$; (b)$z = 75\ mm$; (c) $z = 94\ mm$ and (d) $z = 104\ mm$
.

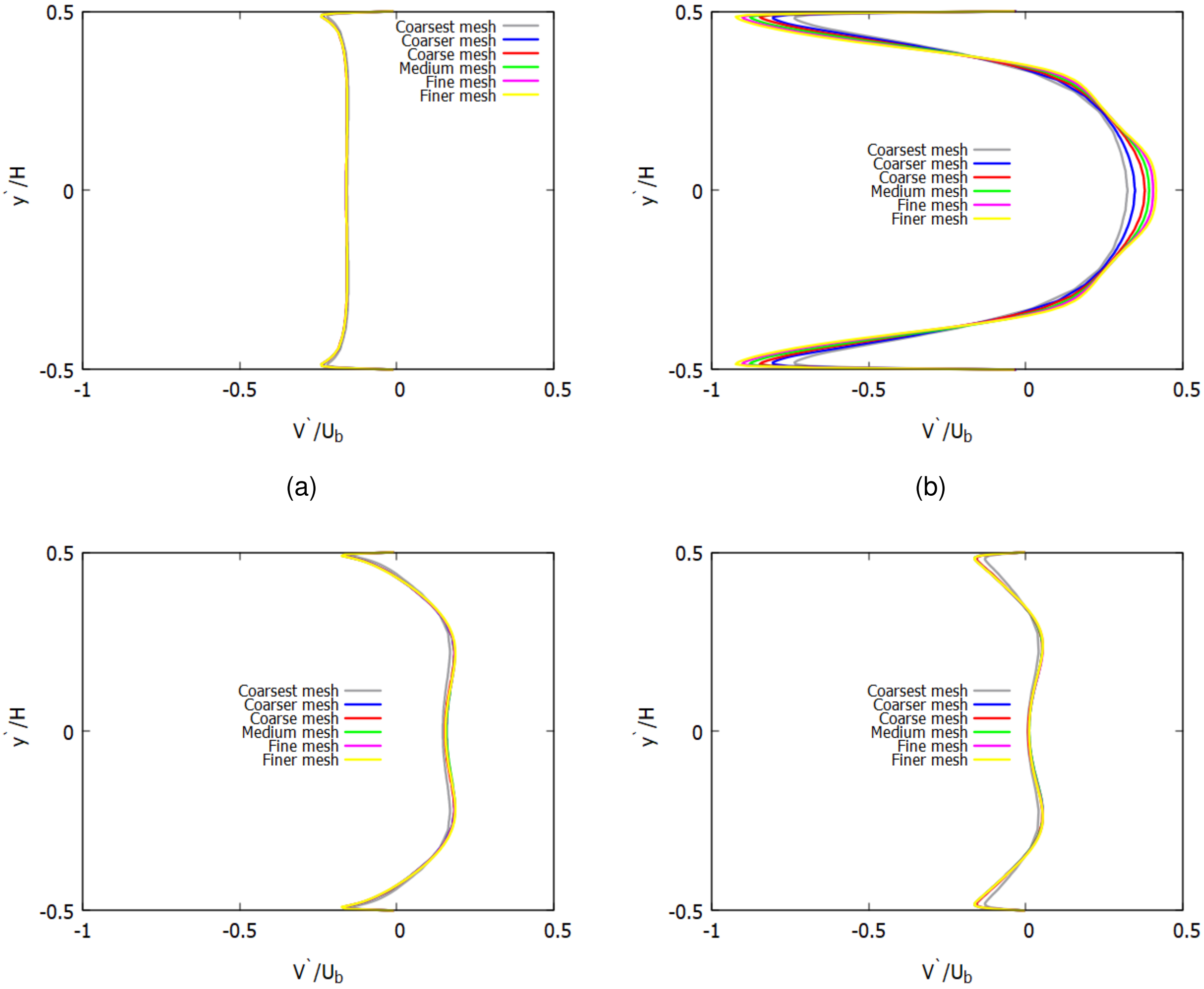

(a)

(b)

(c)

(d)

Figure 86 – Benson *et al.* (2020) U bend mesh sensitivity test ($\kappa - \omega \;\; SST$ model) - u component of the velocity profiles at the positions: (a)$z = 55\ mm$; (b)$z = 75\ mm$; (c) $z = 94\ mm$ and (d) $z = 104\ mm$.

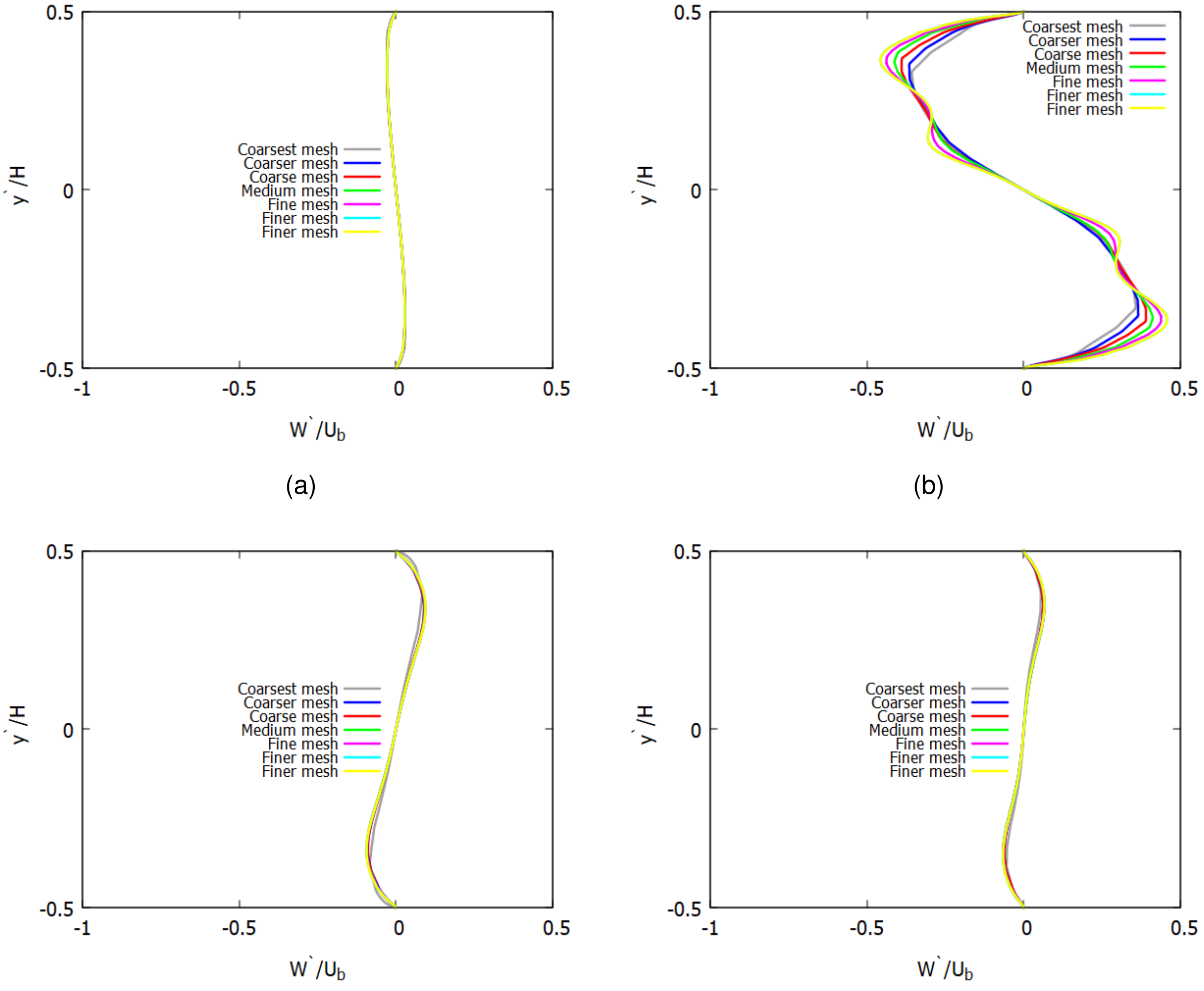

(a)

(b)

(c)

(d)

Figure 87 – Benson *et al.* (2020) U bend mesh sensitivity test ($\kappa-\omega\ \ SST$ model) - u component of the velocity profiles at the positions: (a)$z=55\ mm$; (b)$z=75\ mm$; (c) $z=94\ mm$ and (d) $z=104\ mm$

.

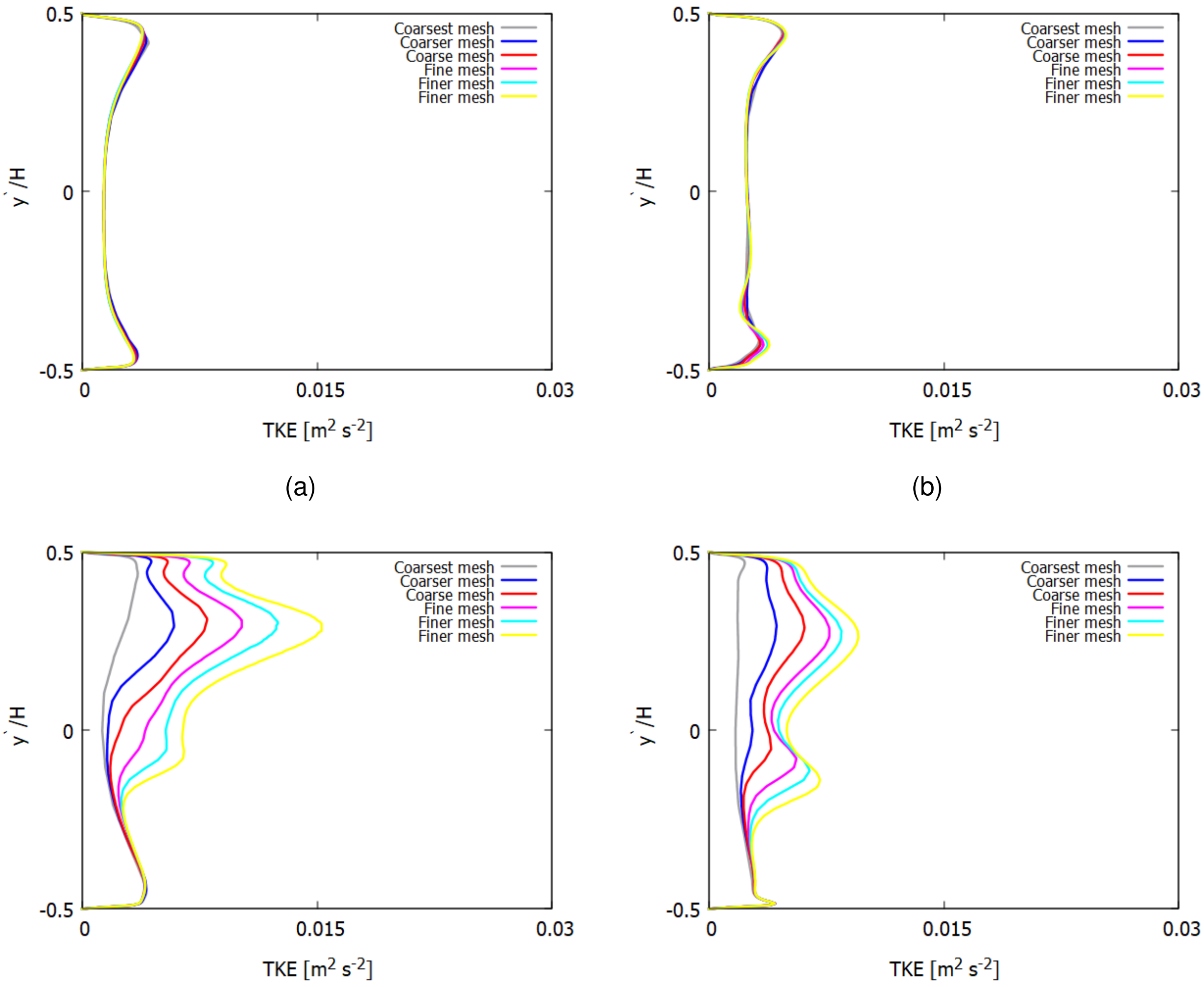

(a) (b) (c) (d)

Figure 88 – Benson *et al.* (2020) U bend mesh sensitivity test ($\kappa - \omega \;\; SST$ model) - TKE line 1 at posisions: (a)$z = 55 \; mm$; (b)$z = 75 \; mm$; (c) $z = 94 \; mm$ and (d) $z = 104 \; mm$.

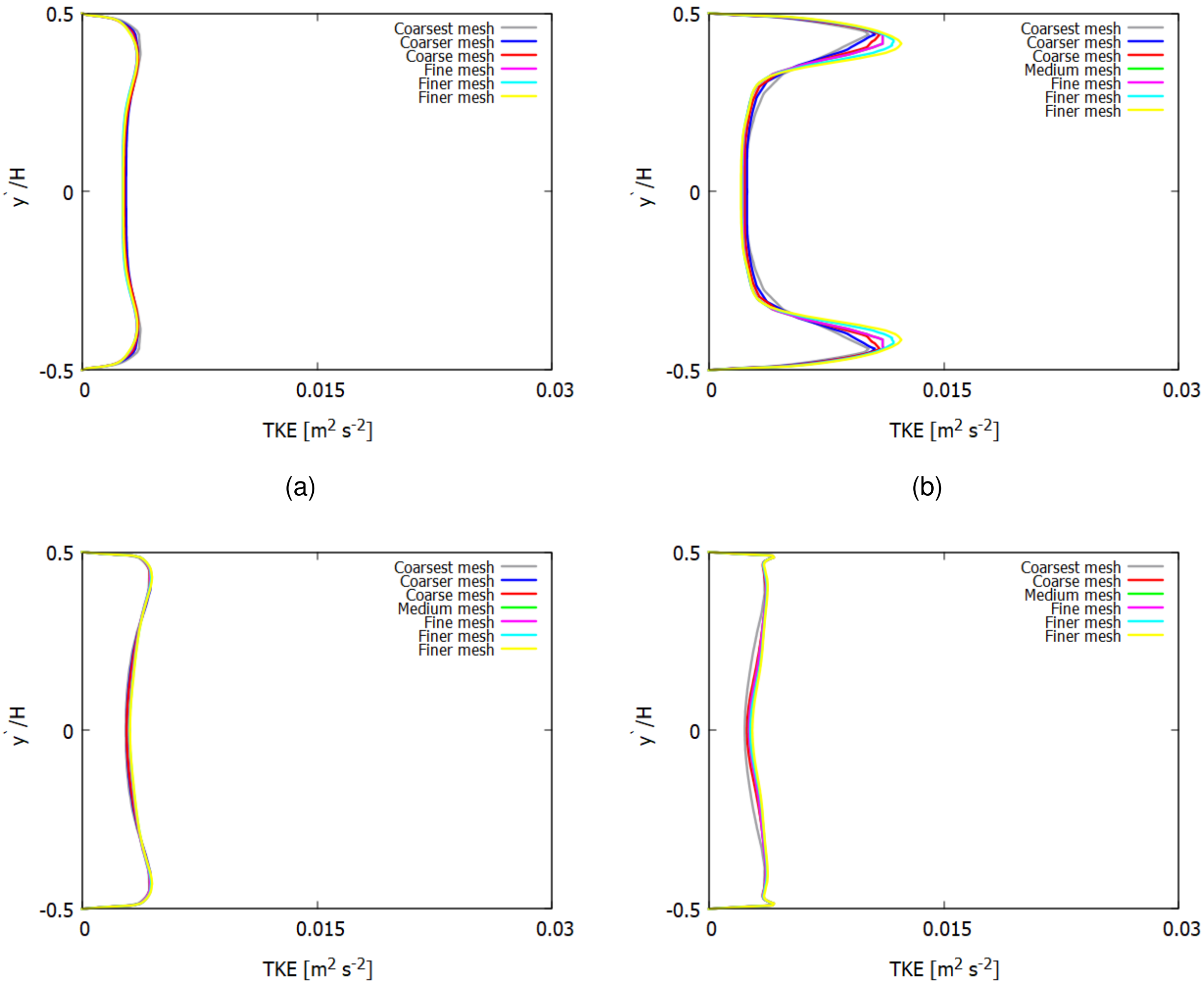

(a)

(b)

(c)

(d)

Figure 89 – Benson *et al.* (2020) U bend mesh sensitivity test ($\kappa-\omega\ \ SST$ model) - TKE line 2 at posisions: (a)$z=55\ mm$; (b)$z=75\ mm$; (c) $z=94\ mm$ and (d) $z=104\ mm$.

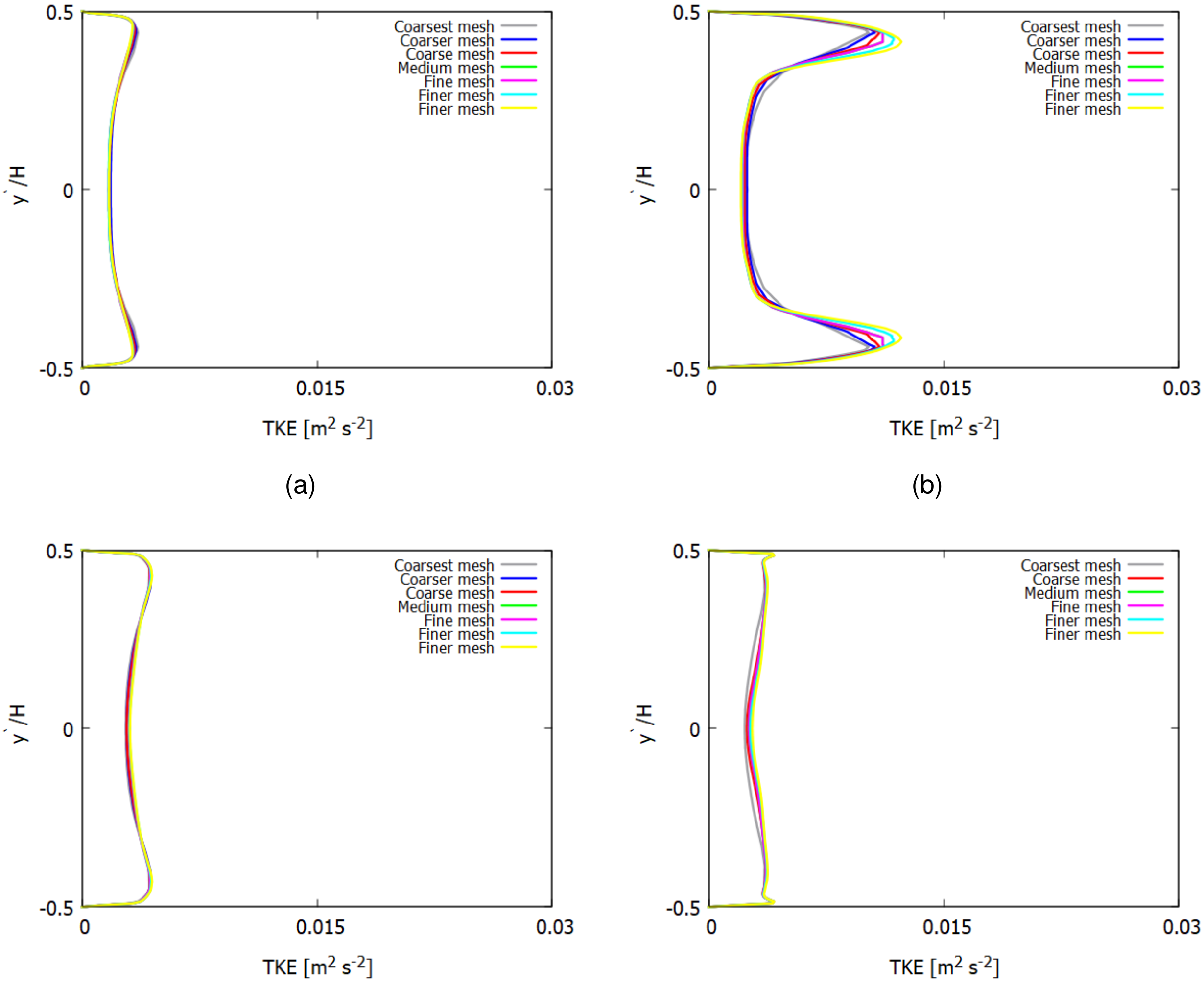

(a)

(b)

(c)

(d)

Figure 90 – Benson *et al.* (2020) U bend mesh sensitivity test ($\kappa-\omega\ \ SST$ model) - TKE line 3 at posisions: (a)$z = 55\ mm$; (b)$z = 75\ mm$; (c) $z = 94\ mm$ and (d) $z = 104\ mm$.

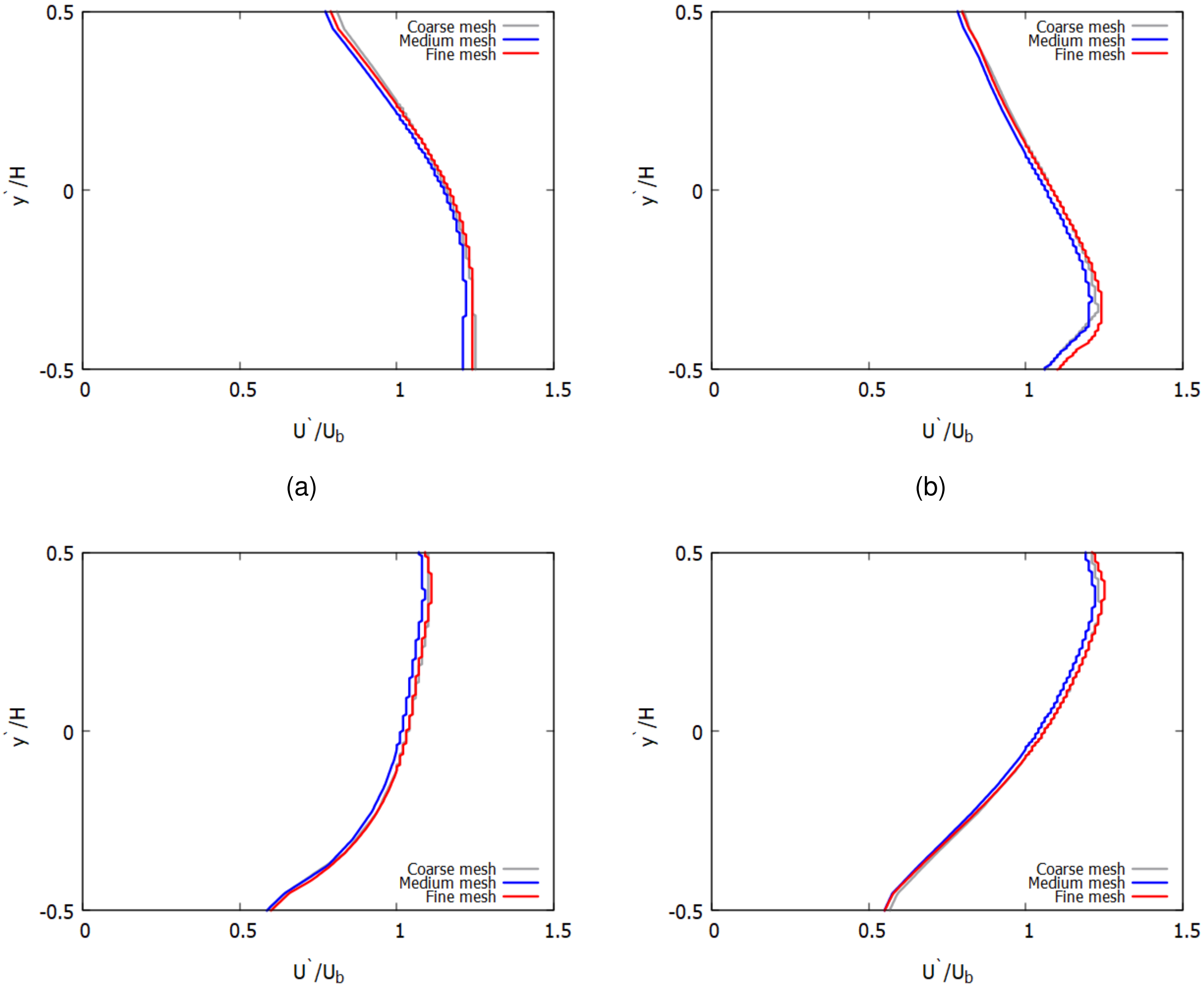

(a)

(b)

(c)

(d)

Figure 91 – Benson *et al.* (2020) U bend mesh sensitivity test ($\kappa - \varepsilon$ model) - u component of the velocity profiles at the positions: (a)$z = 55\ mm$; (b)$z = 75\ mm$; (c) $z = 94\ mm$ and (d) $z = 104\ mm$.

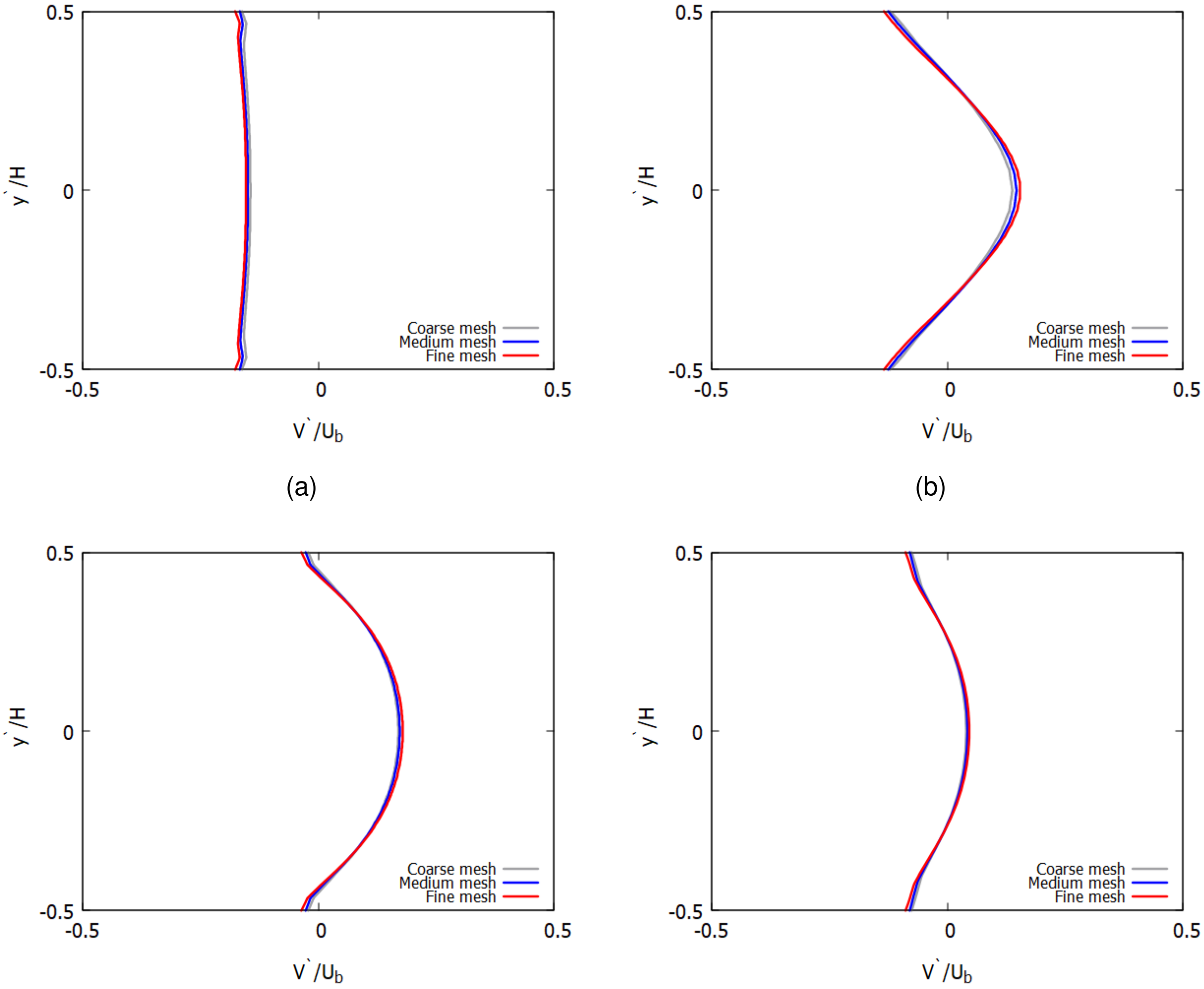

(a) (b)

(c) (d)

Figure 92 – Benson *et al.* (2020) U bend mesh sensitivity test ($\kappa - \varepsilon$ model) - v component of the velocity profiles at the positions: (a)$z = 55\ mm$; (b)$z = 75\ mm$; (c) $z = 94\ mm$ and (d) $z = 104\ mm$.

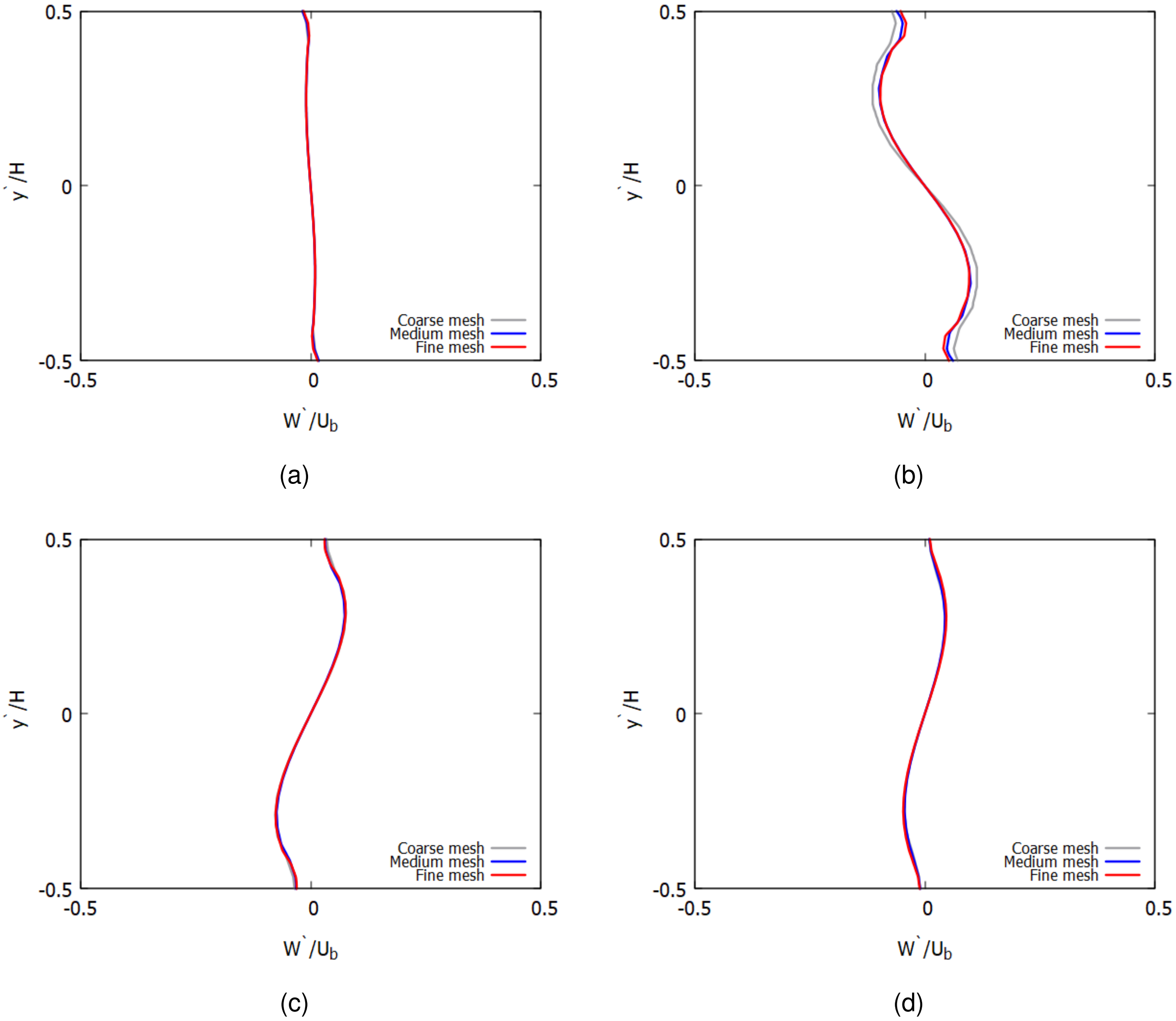

(a) (b) (c) (d)

Figure 93 – Benson *et al.* (2020) U bend mesh sensitivity test ($\kappa-\varepsilon$ model) - w component of the velocity profiles at the positions: (a)$z = 55\ mm$; (b)$z = 75\ mm$; (c) $z = 94\ mm$ and (d) $z = 104\ mm$.

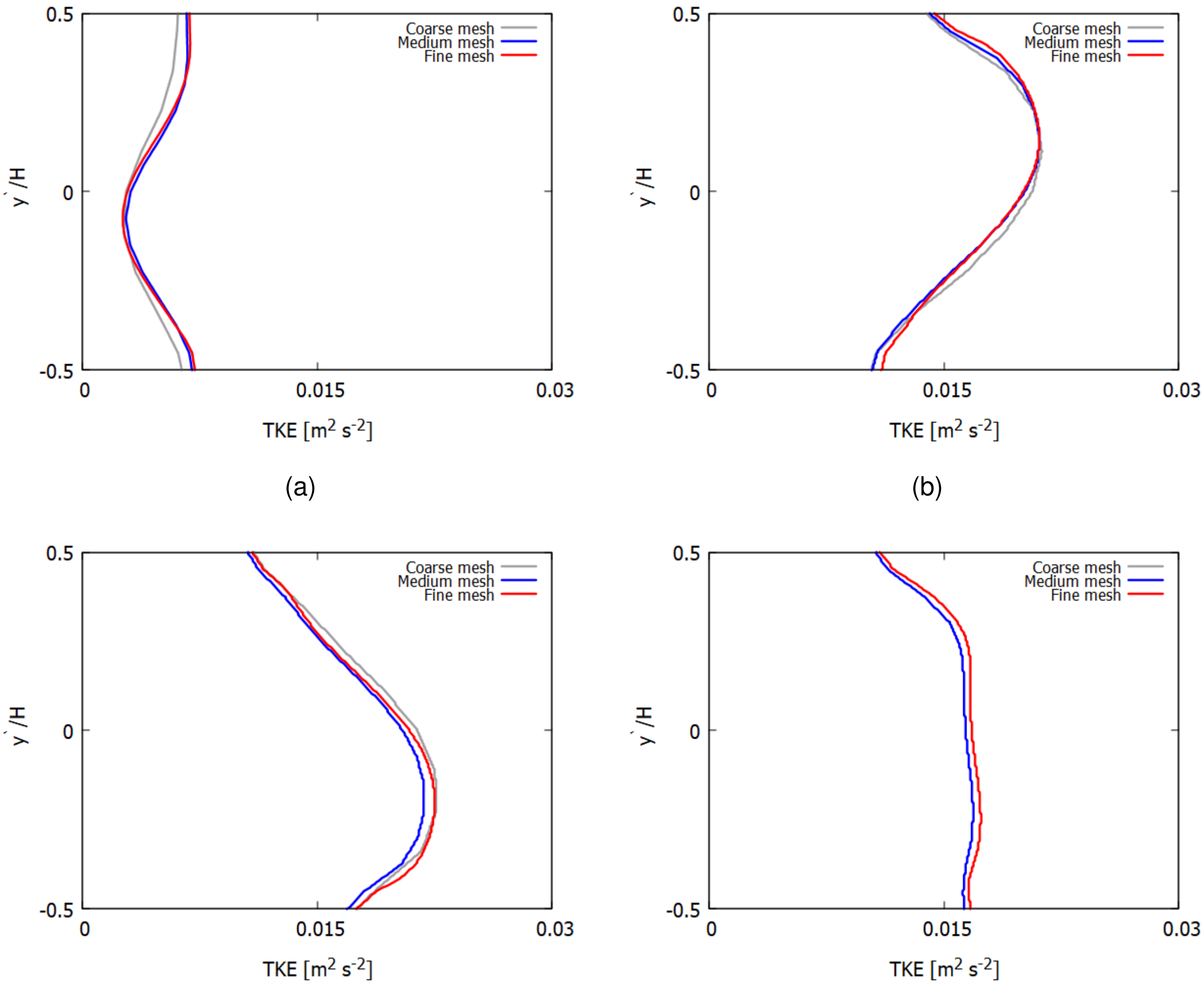

(a) (b) (c) (d)

Figure 94 – Benson *et al.* (2020) U bend mesh sensitivity test ($\kappa - \varepsilon$ model) - - TKE line 1 at posisions: (a)$z = 55\ mm$; (b)$z = 75\ mm$; (c) $z = 94\ mm$ and (d) $z = 104\ mm$.

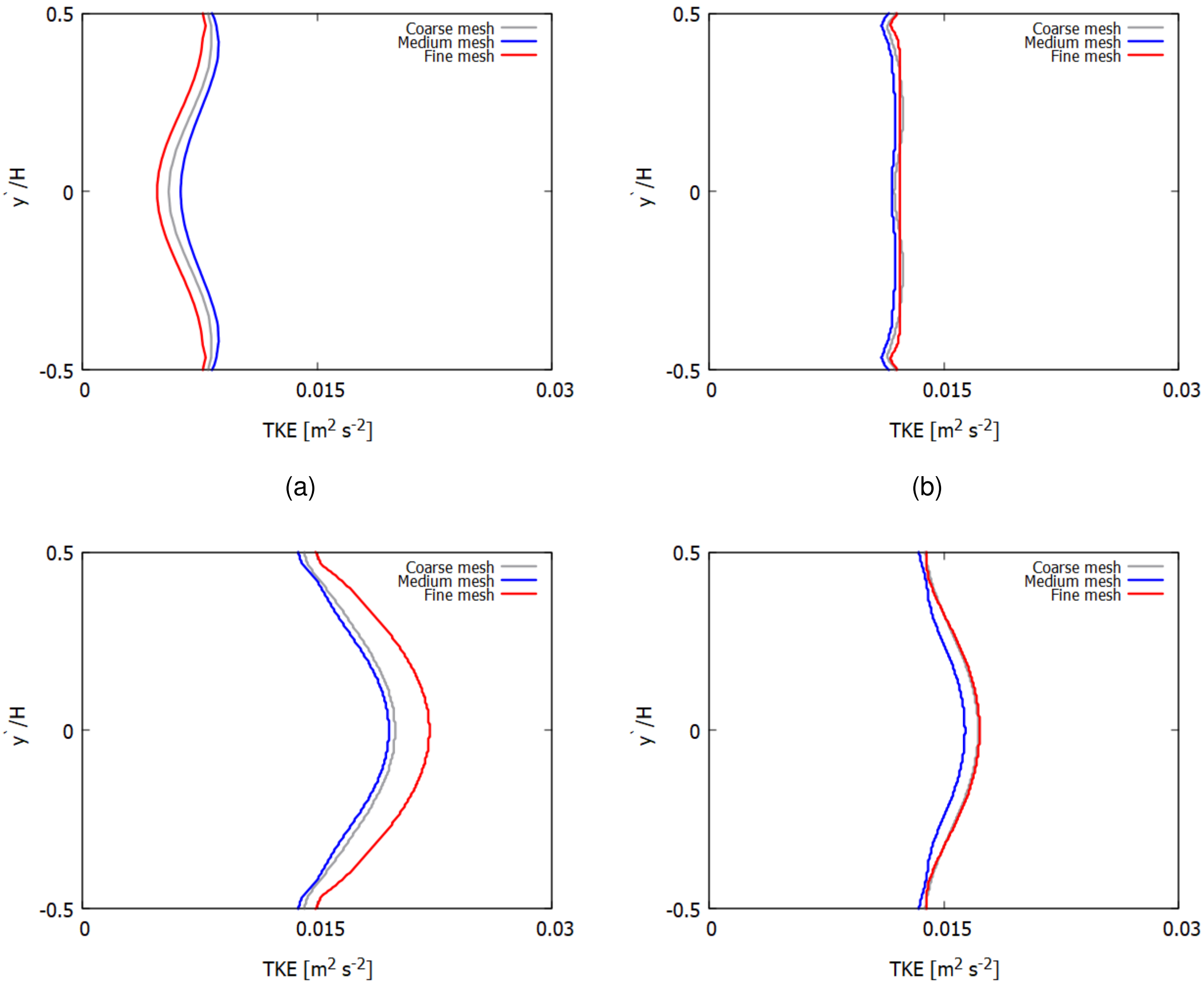

(a) (b) (c) (d)

Figure 95 – Benson *et al.* (2020) U bend mesh sensitivity test ($\kappa-\varepsilon$ model) - - TKE line 2 at posisions: (a)$z = 55\ mm$; (b)$z = 75\ mm$; (c) $z = 94\ mm$ and (d) $z = 104\ mm$.

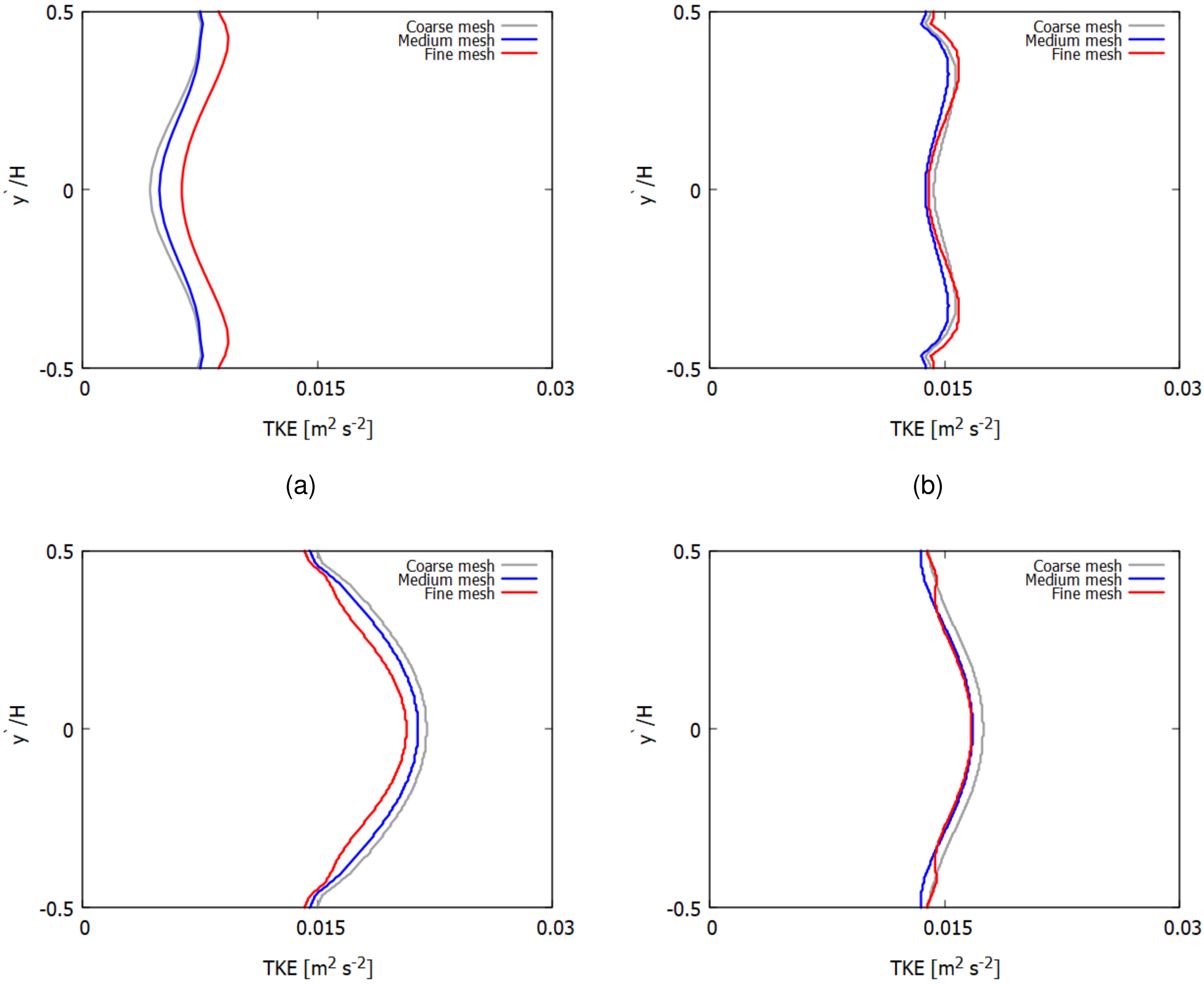

(a) (b) (c) (d)

Figure 96 – Benson *et al.* (2020) U bend mesh sensitivity test ($\kappa-\varepsilon$ model) - - TKE line 3 at posisions: (a)$z = 55\ mm$; (b)$z = 75\ mm$; (c) $z = 94\ mm$ and (d) $z = 104\ mm$.